BEILSTEIN JOURNAL OF NANOTECHNOLOGY

Nanogenerators and flexible electronics

Edited by Yanchao Mao

Imprint

Beilstein Journal of Nanotechnology
www.bjnano.org
ISSN 2190-4286
Email: journals-support@beilstein-institut.de

The *Beilstein Journal of Nanotechnology* is published by the Beilstein-Institut zur Förderung der Chemischen Wissenschaften.

Beilstein-Institut zur Förderung der
Chemischen Wissenschaften
Trakehner Straße 7–9
60487 Frankfurt am Main
Germany
www.beilstein-institut.de

BEILSTEIN JOURNAL OF NANOTECHNOLOGY

Triboelectric nanogenerator based on Teflon/vitamin B1 powder for self-powered humidity sensing

Liangyi Zhang[1,2], Huan Li[3], Yiyuan Xie*[1,2], Jing Guo*[1,2] and Zhiyuan Zhu[1,2]

Full Research Paper

Open Access

Address:
[1]Chongqing Key Laboratory of Nonlinear Circuits and Intelligent Information Processing, College of Electronic and Information Engineering, Southwest University, Chongqing, China, [2]Key Laboratory of Networks and Cloud Computing Security of Universities in Chongqing, College of Electronic and Information Engineering, Southwest University, Chongqing, China and [3]Ocean College, Zhejiang University, Zhejiang, China

Email:
Yiyuan Xie* - yyxie@swu.edu.cn; Jing Guo* - poem24@swu.edu.cn

* Corresponding author

Keywords:
humidity sensor; self-powered system; triboelectric nanogenerators (TENGs); triboelectrification; vitamin B1

Beilstein J. Nanotechnol. **2020,** *11,* 1394–1401.
https://doi.org/10.3762/bjnano.11.123

Received: 26 June 2020
Accepted: 18 August 2020
Published: 11 September 2020

This article is part of the thematic issue "Nanogenerators and flexible electronics".

Guest Editor: Y. Mao

Abstract

Recently, there has been growing interest in triboelectric nanogenerators (TENGs) that can effectively convert various forms of mechanical energy input into electrical energy. In the present study, a novel Teflon/vitamin B1 powder based triboelectric nanogenerator (TVB-TENG) is proposed. Paper is utilized as a supporting platform for triboelectrification between a commercial Teflon tape and vitamin B1 powder. The measured open-circuit voltage was approximately 340 V. The TVB-TENG can be applied as a humidity sensor and exhibits a linear and reversible response to the relative humidity of the environment. Moreover, the change in relative humidity is also indicated by the change in luminosity of a set of light-emitting diodes (LEDs) integrated in the TVB-TENG system. The TVB-TENG proposed in this study illustrates a cost-effective method for portable power supply and sensing devices.

Introduction

Recently, there has been unprecedented advancement in the internet of things (IoT) technology, which includes environmental monitoring and intelligent community applications. Particularly, humidity sensing has been investigated in environmental monitoring, and in other sectors, such as agriculture, food safety, wearable electronics, and wireless sensor networks [1-4]. However, conventional power generation is needed to supply energy to these sensor networks, which leads to increased energy usage and adverse impacts on the environment. More specifically, the degradation of the urban environment has been increasing due to the current life habits of the population [5-7]. Moreover, a variety of sensors are often placed in severe environmental conditions, which might restrict their power supply options [8-12]. As a result, several lines of research have been focused on the development of methods for harvesting energy from the surrounding environment and converting it into electrical power. Through the design of portable electronics and wireless sensor systems [13-16], which harvest energy from the environment, the adverse environmental effects caused by battery-powered systems can be mitigated [17-21]. Hence, the investigation of self-powered sensors which harvest energy from the surrounding environment is highly sustainable.

Triboelectric nanogenerators (TENGs) have been growing in popularity for use as a novel technology to harvest energy. TENGs have a significant impact on the advancement of wearable electronics, intelligent robots, and the IoT [22-28]. Presently, TENGs are used to harvest various forms of mechanical energy from the surrounding environment, such as acoustic energy, wind, vibrations and human motion [29-33]. Recently, TENG-based sensors have attracted increased attention [34-41]. In 2014, Ga-doped ZnO was used for the fabrication of piezo-humidity sensors with a high sensitivity and a fast response [42]. In 2018, Vivekananthan et al. proposed sustainable energy harvesting and battery-free humidity sensors by using biocompatible collagen nanofibrils [43]. More recently, Zhang et al. developed a TENG-driven self-powered flexible humidity sensor based on a tin disulfide nanoflower/reduced graphene oxide (SnS_2/rGO) hybrid nanomaterial [44]. However, the large-scale application of TENGs for humidity sensing is hindered by the high costs involved in their complex production and the high facility costs for particular manufacturing process. Thus, intensive research is required for the design of TENGs based on commercially available, cost-effective and feasible materials. Furthermore, TENGs should be seamlessly integrated and fabricated using a simple process, particularly regarding multifunctional sensing applications.

In the present study, a novel Teflon/vitamin B1 powder based triboelectric nanogenerator (TVB-TENG) is proposed. Vitamin B1 is an essential water-soluble vitamin which stays in the human body for only a few hours. Vitamin B1 is a coenzyme involved in the metabolism of sugar, protein and fat, which is found in grains, beans, pork, and other sources. Since it is cost-effective, environmentally friendly, non-poisonous and soluble, vitamin B1 can be used as a lubricant to make a friction nanogenerator. Due to its sustainability and flexibility, paper can be used as a substrate and supporting structure. The conductive electrode is made of copper foil, while the triboelectric pair is comprised of Teflon tape and vitamin B1 powder. The approximate values of the output power density of the TVB-TENG can reach 120.13 $\mu W/cm^2$. In addition, the approximate values of the open-circuit voltage (V_{oc}) and short-circuit current (I_{sc}) of this device were 340 V and 46.3 μA, respectively. These results indicate that sufficient power can be supplied to systems with low power requirements. As an extension of previous work [45], the self-powered TVB-TENG designed in this study can be used to measure the relative humidity and exhibits good linearity and reversibility. In addition, the materials used in the manufacturing of the TENGs are nontoxic and degradable. Furthermore, light-emitting diodes (LEDs) are integrated with the humidity sensor and the luminosity is an indicator of the relative humidity (RH) from the surrounding environment.

Experimental

The conductive copper foil tape is used as the electrode, while the paper (manufacturer: Miao Ben) at the bottom serves as a supporting platform. The Teflon tape (manufacturer: RUIGUAN) is cut to the desired size (4 cm × 5 cm) and pasted to the bottom of the conductive copper foil tape, serving as one element of the triboelectric pair. In addition, ≈20 ± 5 mg of vitamin B1 powder (manufacturer: Huazhong Pharmaceutical Co. LTD) is pressed against the bottom of another conductive copper foil tape with double-sided tape, working as the other element in the triboelectric pair. The fabrication process of the TVB-TENG proposed in this study is illustrated in Figure 1 and the actual price of the material used to make the TENG is only approximately CN¥ 0.5. An oscilloscope (probe: 100 MΩ) was used to measure the voltage across the external load (a variable resistor) and a high-precision multifunctional electronic scale, with an accuracy of 0.001 g, was used to measure the required amount of vitamin B1 powder.

Results and Discussion

As shown in Figure 2, the working mechanism of TVB-TENG is based on contact triboelectrification and electrostatic induction. First, when the device is externally compressed, electrons are transferred from the B1 vitamin membrane to the Teflon membrane. The contact surface between the vitamin B1 membrane and the Teflon membrane is separated in the absence of an external force. There is a positive charge transfer from the conductive copper foil tape at the bottom of the TVB-TENG, to the conductive copper foil tape at the top, leading to an electric field equilibrium due to electrostatic induction. As a result, a potential difference between the electrodes is generated. Subsequently, when the TVB-TENG is pressed again, an opposite potential difference is produced due to the triboelectrification principle. As such, there is a positive charge transfer from the top of the conductive copper foil tape of the TVB-TENG to the bottom one [46]. Therefore, it is expected that TVB-TENGs can produce a stable output power under the sustained effect of an external force. The potential distribution is illustrated to obtain a comprehensive understanding of this phenomenon.

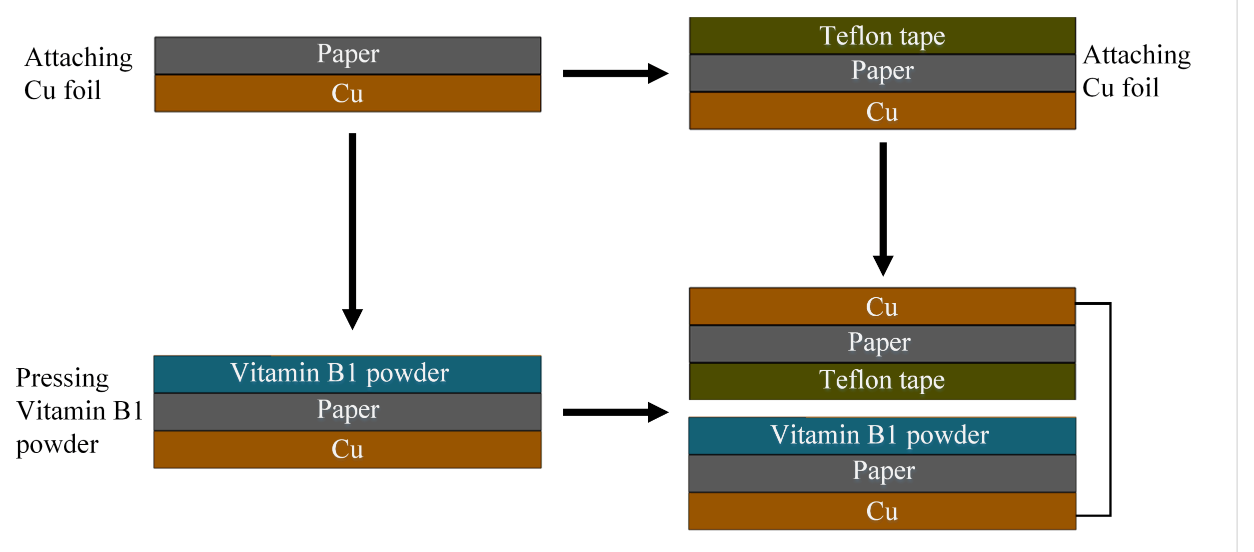

Figure 1: The manufacturing process of the TVB-TENG structure.

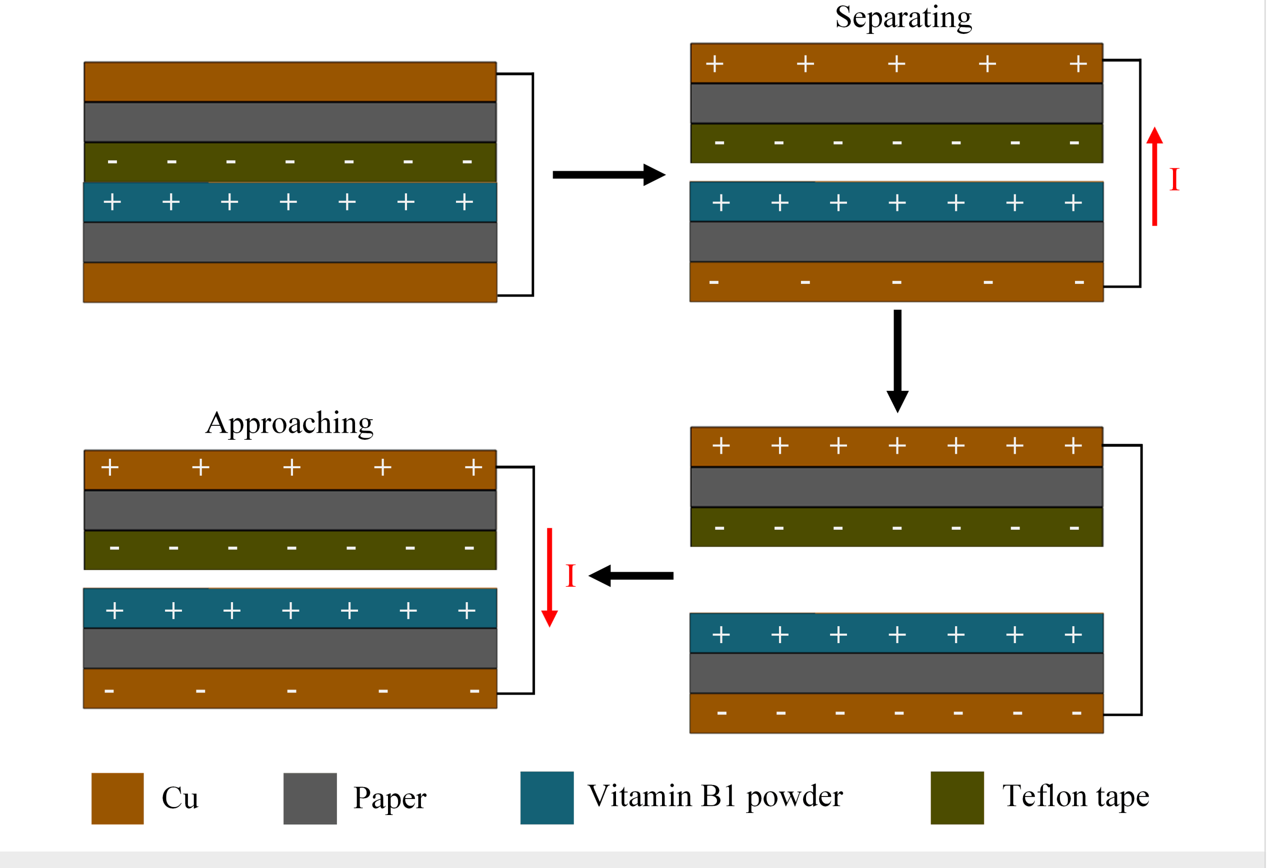

Figure 2: The working mechanism of the TVB-TENG structure.

An oscilloscope (probe: 100 MΩ) was used to measure the voltage across the external load (a variable resistor). The output current was calculated by using the measured voltage and the load resistance. As illustrated in Figure 3a and Figure 3b, the output voltage and the current reached a peak at 340 V and 46.3 µA, corresponding to a load resistance of 100 MΩ and 100 kΩ, respectively. As shown in Figure 3c, when the load resistance was increased from 100 kΩ to 100 MΩ, the measured

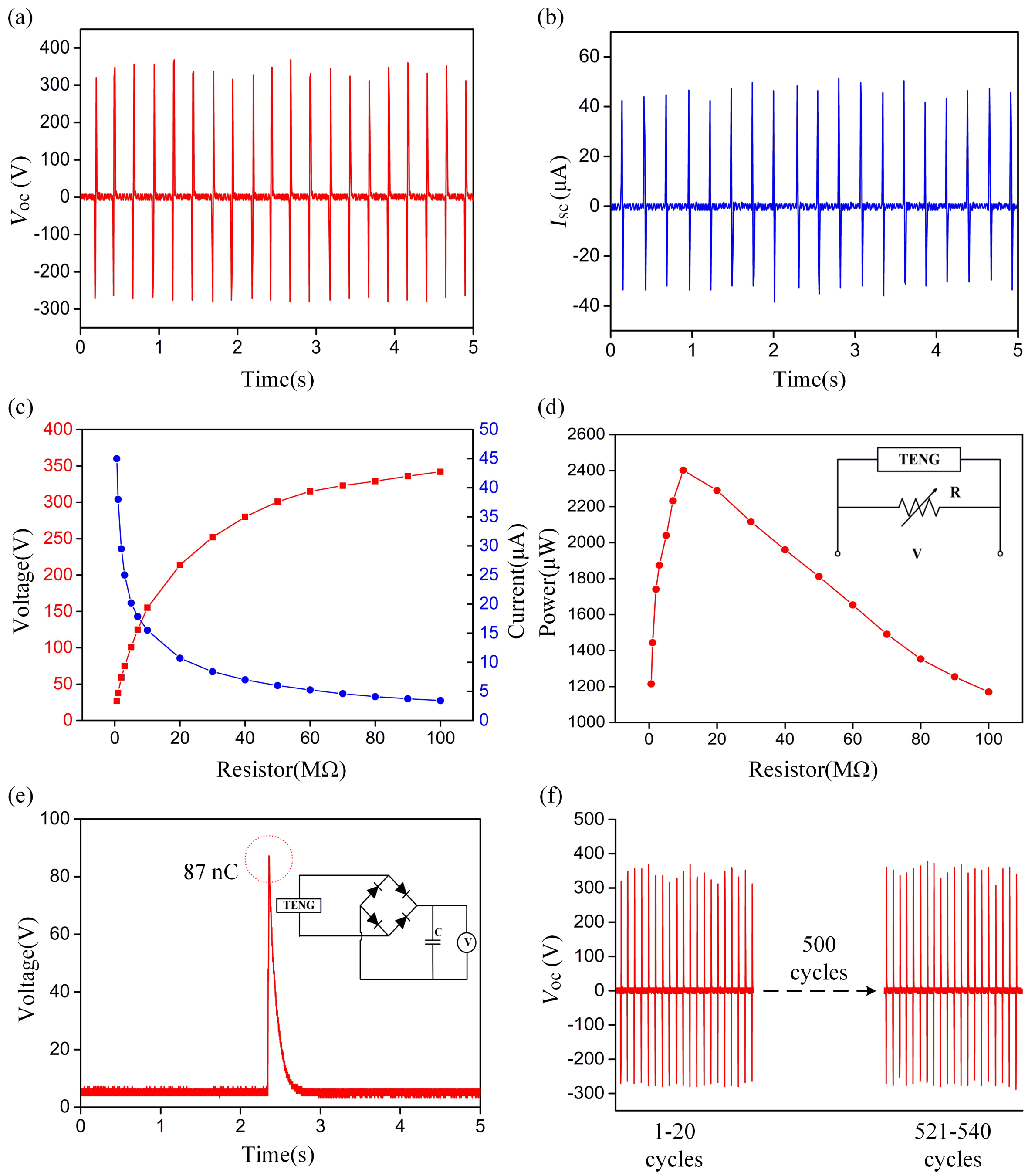

Figure 3: (a) The output voltage (matched load of 100 MΩ) and (b) short-circuit current (matched load of 100 kΩ) in a TENG. (c) The behavior of the output voltage and short-circuit current upon changing the load resistance. (d) The behavior of the output power density upon changing the load resistance. (e) TVB-TENG with a full-wave bridge rectifier for charging a 1 nF capacitor. In one cycle, 87 nC of charge is transferred. (f) The reliability of TVB-TENG was studied over 500 working cycles.

output voltage showed an increasing trend. As shown in Figure 3d, the output power reached its peak at 2402.5 µW at a loading resistance of 10 MΩ. Accordingly, the fabricated internal resistance of the TENGs was close to 10 MΩ. Consequently, considering the size of the fabricated TENG (4 cm × 5 cm), the maximum power density is 120.13 µW/cm^2. Since an external resistance of 100 MΩ is much higher than 10 MΩ (roughly equal to the internal resistance), the output voltage (at a 100 MΩ load) is approximated to be equal to the open circuit voltage. Similarly, for a load of 100 kΩ, the corresponding output current can be considered to be equal to the short circuit current. In addition, as shown in Figure 3e, the charging capacity of the prepared TVB-TENG was investigated by integrating a full-wave rectifier bridge to charge a 1 nF capacitor. The maximum capacitive voltage was 87 V, and in one cycle, a charge of 87 nC was transferred. The reliability of the manufactured TVB-TENG was also investigated. As shown in Figure 3f, the output voltage of the TENG remains steady even after 500 external force testing cycles.

The TENG output is affected by the humidity due to the triboelectric effect, and the preservation of the triboelectric charge at the surface is severely decreased by the humid environment [47]. It should be considered that the experiments with the TVB-TENG were performed in Chongqing, located in the southern region of China where it rains often and the annual relative humidity is usually above 40%. Thus, the humidity sensor response is limited due to a change in RH from 40 to 90% (Figure 4a–f). The dynamic change between the output voltage and the RH can be derived from the 2D graph. As the RH increased, there was a declining trend in the output signal. Figure 4 shows the output voltage of the TVB-TENG upon a change in RH. The output voltages of 371 V, 331 V, 247 V, 180 V, 137 V and 105 V corresponded to RH levels of 40%, 50%, 60%, 70%, 80% and 90%, respectively. As illustrated in Figure 5a, the output voltage as a function of RH has a linear

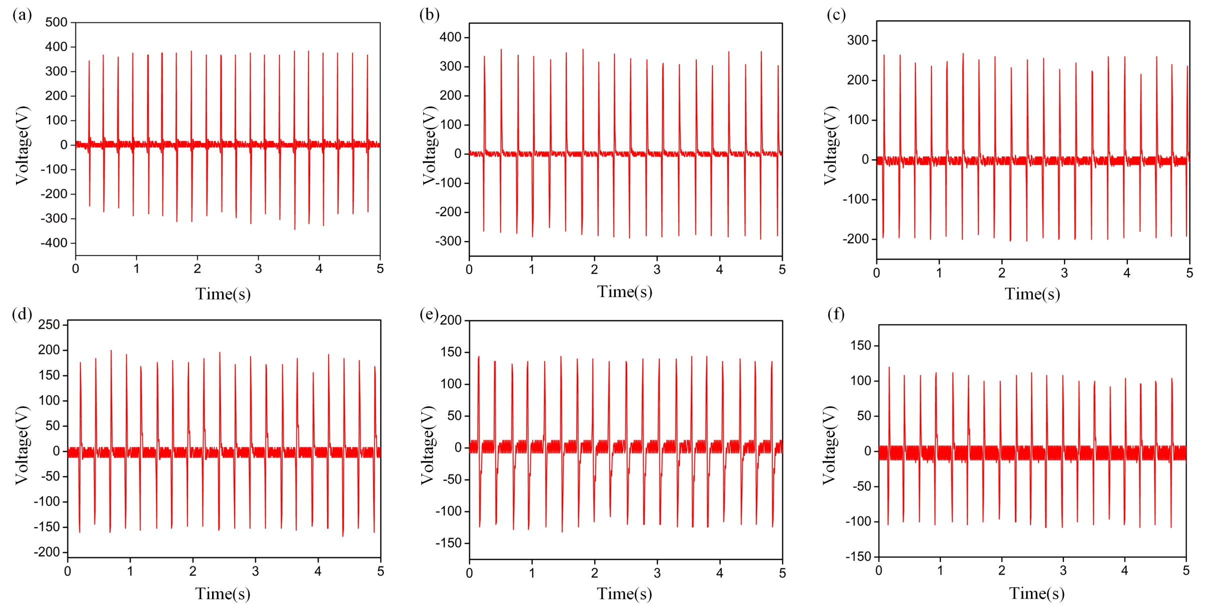

Figure 4: The output voltage sensor feedback at different humidity levels: 40% (a), 50% (b), 60% (c), 70% (d), 80% (e) and 90% (f).

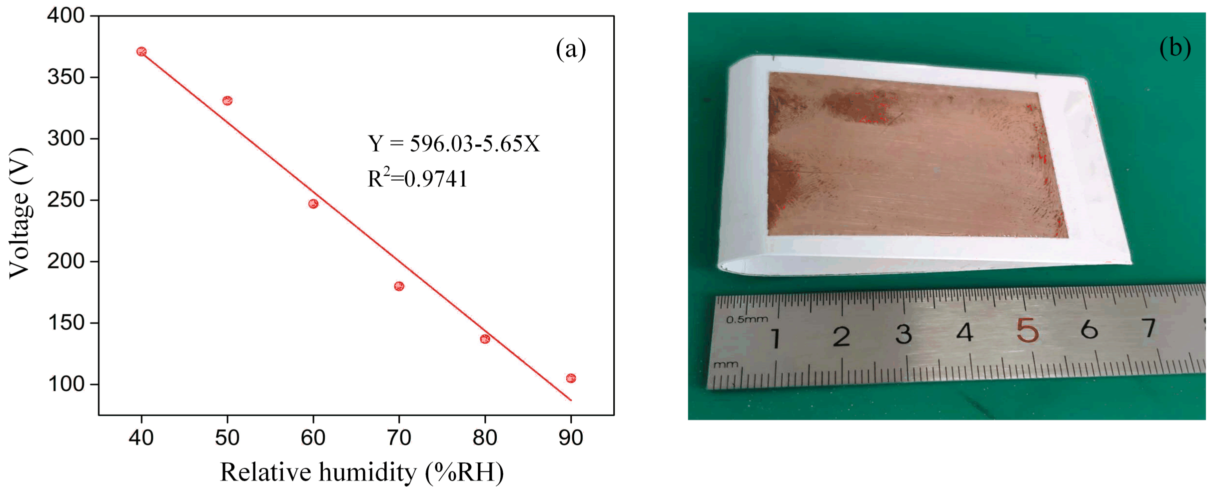

Figure 5: (a) The output voltage of the TVB-TENG as a function of RH (40–90%). (b) A representative photograph of the TVB-TENG.

fitting and the fitting equation for the output voltage (*Y*) and the relative humidity (*X*) can be represented as $Y = 596.03 - 5.65X$, with an *R*-squared value of 0.9741. A representative photograph of the TVB-TENG is shown in Figure 5b. Table 1 presents the humidity-sensing characteristics of the proposed humidity sensor in comparison with previously published studies [42-44,48,49]. The response and measurement range of the manufactured sensor are comparable to the sensor made from collagen–cotton fabric via the freeze-dried method [43].

Furthermore, the reversibility of the TVB-TENG in terms of humidity sensing characteristics was also studied, as shown in Figure 6a. Thirty blue LEDs (according to the product specification of these 3 mm LEDs the voltage range is 1.8–2.2 V) were connected to the TENG humidity sensor as a real-time indicator of changes in the RH. The tests were conducted in environments with different RHs, and the luminosity of the LEDs was an indicator of changes in the RH. As illustrated in Figure 6b, when the surrounding humidity changes drastically, the change in the LED system luminosity can act as an alarm.

Table 1: The results presented in this work are compared with previous studies for humidity detection.

Sensor type	Sensing material	Fabrication method	Measurement range	Response	Ref.
voltage-type	Ga-doped ZnO	hydrothermal method	45–80% RH	358	[42]
current-type	collagen–cotton fabric	freeze-dried method	50–90% RH	0.1287 μA/%RH	[43]
voltage-type	SnS_2/rGO	screen-printing method	0–97% RH	65	[44]
voltage-type	Al-doped ZnO	seed-assisted wet-chemical method	15–60% RH	1522	[48]
voltage-type	Fe-doped ZnO	seed-assisted wet-chemical method	5–65% RH	305	[49]
voltage-type	vitamin B powder	powder machine method	40–90% RH	5.65 V/%RH	current work

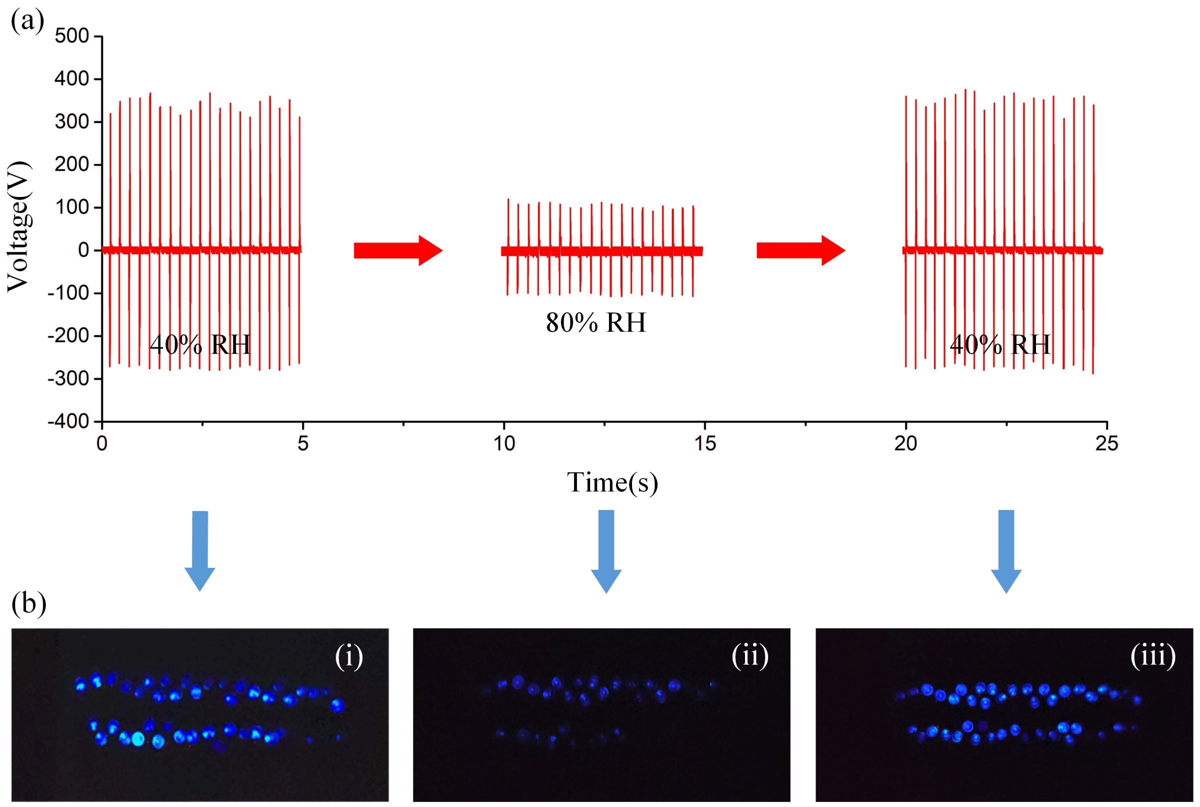

Figure 6: (a) Reversibility of a TVB-TENG-based humidity sensor. (b) The change in luminosity of thirty LEDs under different relative humidity conditions.

Conclusion

This study proposed a novel TVB-TENG using vitamin B1 powder and Teflon tape. The fabricated device integrates a self-powered energy supply with a sensing system, and the change in relative humidity of the surrounding environment is properly detected. According to the experimental analysis, the results show that the TVB-TENG has a distinct humidity response. Further, the change in RH was also illustrated via the luminosity changes of the integrated LEDs. The device proposed in this study has great application potential in the area of environmental monitoring.

Funding

This research was supported by Zhejiang Provincial Natural Science Foundation of China (Grant No. LY20F040004), the Fundamental Research Funds for the Central Universities (Grant No. SWU019040), National Natural Science Foundation of China (Grant No. 61804132) and Zhoushan Municipal Government.

References

1. Wang, J.; Zhang, H.; Xie, Y.; Yan, Z.; Yuan, Y.; Huang, L.; Cui, X.; Gao, M.; Su, Y.; Yang, W.; Lin, Y. *Nano Energy* **2017,** *33,* 418–426. doi:10.1016/j.nanoen.2017.01.055
2. Jiang, J.; Wang, Q.; Wang, B.; Dong, J.; Li, Z.; Li, X.; Zi, Y.; Li, S.; Wang, X. *Nano Energy* **2019,** *59,* 545–552. doi:10.1016/j.nanoen.2019.02.066
3. Wang, X.; Dai, Y.; Liu, R.; He, X.; Li, S.; Wang, Z. L. *ACS Nano* **2017,** *11,* 8339–8345. doi:10.1021/acsnano.7b03560
4. Tang, W.; Jiang, T.; Fan, F. R.; Yu, A. F.; Zhang, C.; Cao, X.; Wang, Z. L. *Adv. Funct. Mater.* **2015,** *25,* 3718–3725. doi:10.1002/adfm.201501331
5. Luo, J.; Xu, L.; Tang, W.; Jiang, T.; Fan, F. R.; Pang, Y.; Chen, L.; Zhang, Y.; Wang, Z. L. *Adv. Energy Mater.* **2018,** *8,* 1800889. doi:10.1002/aenm.201800889
6. Liu, D.; Bao, J.-F.; Chen, Y.-L.; Li, G.-K.; Zhang, X.-S. *Nano Energy* **2020,** *74,* 104770. doi:10.1016/j.nanoen.2020.104770
7. Ding, W.; Zhou, J.; Cheng, J.; Wang, Z.; Guo, H.; Wu, C.; Xu, S.; Wu, Z.; Xie, X.; Wang, Z. L. *Adv. Energy Mater.* **2019,** *9,* 1901320. doi:10.1002/aenm.201901320
8. Zhang, N.; Qin, C.; Feng, T.; Li, J.; Yang, Z.; Sun, X.; Liang, E.; Mao, Y.; Wang, X. *Nano Res.* **2020,** *13,* 1903–1907. doi:10.1007/s12274-020-2654-7
9. Lai, S.-N.; Chang, C.-K.; Yang, C.-S.; Su, C.-W.; Leu, C.-M.; Chu, Y.-H.; Sha, P.-W.; Wu, J. M. *Nano Energy* **2019,** *60,* 715–723. doi:10.1016/j.nanoen.2019.03.067
10. Li, X.; Lin, Z.-H.; Cheng, G.; Wen, X.; Liu, Y.; Niu, S.; Wang, Z. L. *ACS Nano* **2014,** *8,* 10674–10681. doi:10.1021/nn504243j
11. Yu, Y.; Wang, Y.; Zhang, S.; Zhang, P.; Xue, S.; Xie, Y.; Zhou, Z.; Li, J.; Kang, J. *Nano Energy* **2019,** *61,* 604–610. doi:10.1016/j.nanoen.2019.05.014
12. Mao, Y.; Geng, D.; Liang, E.; Wang, X. *Nano Energy* **2015,** *15,* 227–234. doi:10.1016/j.nanoen.2015.04.026
13. Ning, C.; Tian, L.; Zhao, X.; Xiang, S.; Tang, Y.; Liang, E.; Mao, Y. *J. Mater. Chem. A* **2018,** *6,* 19143–19150. doi:10.1039/c8ta07784c
14. Xie, L.; Chen, X.; Wen, Z.; Yang, Y.; Shi, J.; Chen, C.; Peng, M.; Liu, Y.; Sun, X. *Nano-Micro Lett.* **2019,** *11,* 39. doi:10.1007/s40820-019-0271-3
15. Su, Y.; Wang, J.; Wang, B.; Yang, T.; Yang, B.; Xie, G.; Zhou, Y.; Zhang, S.; Tai, H.; Cai, Z.; Chen, G.; Jiang, Y.; Chen, L.-Q.; Chen, J. *ACS Nano* **2020,** *14,* 6067–6075. doi:10.1021/acsnano.0c01804
16. Wang, S.; Jiang, Y.; Tai, H.; Liu, B.; Duan, Z.; Yuan, Z.; Pan, H.; Xie, G.; Du, X.; Su, Y. *Nano Energy* **2019,** *63,* 103829. doi:10.1016/j.nanoen.2019.06.025
17. Tang, Y.; Zhou, H.; Sun, X.; Diao, N.; Wang, J.; Zhang, B.; Qin, C.; Liang, E.; Mao, Y. *Adv. Funct. Mater.* **2020,** *30,* 1907893. doi:10.1002/adfm.201907893
18. He, Q.; Wu, Y.; Feng, Z.; Sun, C.; Fan, W.; Zhou, Z.; Meng, K.; Fan, E.; Yang, J. *Nano Energy* **2019,** *59,* 689–696. doi:10.1016/j.nanoen.2019.03.005
19. Zhang, B.; Tang, Y.; Dai, R.; Wang, H.; Sun, X.; Qin, C.; Pan, Z.; Liang, E.; Mao, Y. *Nano Energy* **2019,** *64,* 103953. doi:10.1016/j.nanoen.2019.103953
20. Wu, C.; Tetik, H.; Cheng, J.; Ding, W.; Guo, H.; Tao, X.; Zhou, N.; Zi, Y.; Wu, Z.; Wu, H.; Lin, D.; Wang, Z. L. *Adv. Funct. Mater.* **2019,** *29,* 1901102. doi:10.1002/adfm.201901102
21. Zhou, Z.; Li, X.; Wu, Y.; Zhang, H.; Lin, Z.; Meng, K.; Lin, Z.; He, Q.; Sun, C.; Yang, J.; Wang, Z. L. *Nano Energy* **2018,** *53,* 501–507. doi:10.1016/j.nanoen.2018.08.055
22. Mao, Y.; Zhang, N.; Tang, Y.; Wang, M.; Chao, M.; Liang, E. *Nanoscale* **2017,** *9,* 14499–14505. doi:10.1039/c7nr05222g
23. Zhang, Y.; Wu, M.; Zhu, Q.; Wang, F.; Su, H.; Li, H.; Diao, C.; Zheng, H.; Wu, Y.; Wang, Z. L. *Adv. Funct. Mater.* **2019,** *29,* 1904259. doi:10.1002/adfm.201904259
24. Li, Z.; Zhu, M.; Shen, J.; Qiu, Q.; Yu, J.; Ding, B. *Adv. Funct. Mater.* **2020,** *30,* 1908411. doi:10.1002/adfm.201908411
25. Cui, X.; Zhang, H.; Cao, S.; Yuan, Z.; Ding, J.; Sang, S. *Nano Energy* **2018,** *52,* 71–77. doi:10.1016/j.nanoen.2018.07.037
26. Jiang, C.; Li, X.; Ying, Y.; Ping, J. *Nano Energy* **2020,** *74,* 104863. doi:10.1016/j.nanoen.2020.104863
27. Zhang, Y.; Peng, M.; Liu, Y.; Zhang, T.; Zhu, Q.; Lei, H.; Liu, S.; Tao, Y.; Li, L.; Wen, Z.; Sun, X. *ACS Appl. Mater. Interfaces* **2020,** *12,* 19384–19392. doi:10.1021/acsami.9b22572
28. Ding, W.; Wang, A. C.; Wu, C.; Guo, H.; Wang, Z. L. *Adv. Mater. Technol. (Weinheim, Ger.)* **2019,** *4,* 1800487. doi:10.1002/admt.201800487
29. Luo, J.; Wang, Z.; Xu, L.; Wang, A. C.; Han, K.; Jiang, T.; Lai, Q.; Bai, Y.; Tang, W.; Fan, F. R.; Wang, Z. L. *Nat. Commun.* **2019,** *10,* 5147. doi:10.1038/s41467-019-13166-6
30. Wang, M.; Zhang, J.; Tang, Y.; Li, J.; Zhang, B.; Liang, E.; Mao, Y.; Wang, X. *ACS Nano* **2018,** *12,* 6156–6162. doi:10.1021/acsnano.8b02562
31. Chen, F.; Wu, Y.; Ding, Z.; Xia, X.; Li, S.; Zheng, H.; Diao, C.; Yue, G.; Zi, Y. *Nano Energy* **2019,** *56,* 241–251. doi:10.1016/j.nanoen.2018.11.041
32. Lin, H.; He, M.; Jing, Q.; Yang, W.; Wang, S.; Liu, Y.; Zhang, Y.; Li, J.; Li, N.; Ma, Y.; Wang, L.; Xie, Y. *Nano Energy* **2019,** *56,* 269–276. doi:10.1016/j.nanoen.2018.11.037
33. Wang, M.; Zhang, N.; Tang, Y.; Zhang, H.; Ning, C.; Tian, L.; Li, W.; Zhang, J.; Mao, Y.; Liang, E. *J. Mater. Chem. A* **2017,** *5,* 12252–12257. doi:10.1039/c7ta02680c
34. Xie, X.; Zhang, Y.; Chen, C.; Chen, X.; Yao, T.; Peng, M.; Chen, X.; Nie, B.; Wen, Z.; Sun, X. *Nano Energy* **2019,** *65,* 103984. doi:10.1016/j.nanoen.2019.103984

35. Cheng, P.; Sun, M.; Zhang, C.; Guo, H.; Shi, J.; Zhang, Y.; Liu, Y.; Wang, J.; Wen, Z.; Sun, X. *IEEE Trans. Nanotechnol.* **2020,** *19,* 230–235. doi:10.1109/tnano.2020.2976154
36. Chen, C.; Wen, Z.; Wei, A.; Xie, X.; Zhai, N.; Wei, X.; Peng, M.; Liu, Y.; Sun, X.; Yeow, J. T. W. *Nano Energy* **2019,** *62,* 442–448. doi:10.1016/j.nanoen.2019.05.029
37. Lin, H.; Liu, Y.; Chen, S.; Xu, Q.; Wang, S.; Hu, T.; Pan, P.; Wang, Y.; Zhang, Y.; Li, N.; Li, Y.; Ma, Y.; Xie, Y.; Wang, L. *Nano Energy* **2019,** *65,* 103944. doi:10.1016/j.nanoen.2019.103944
38. Su, Y.; Yao, M.; Xie, G.; Pan, H.; Yuan, H.; Yang, M.; Tai, H.; Du, X.; Jiang, Y. *Appl. Phys. Lett.* **2019,** *115,* 073504. doi:10.1063/1.5110334
39. Su, Y.; Xie, G.; Tai, H.; Li, S.; Yang, B.; Wang, S.; Zhang, Q.; Du, H.; Zhang, H.; Du, X.; Jiang, Y. *Nano Energy* **2018,** *47,* 316–324. doi:10.1016/j.nanoen.2018.02.031
40. Su, Y.; Xie, G.; Wang, S.; Tai, H.; Zhang, Q.; Du, H.; Zhang, H.; Du, X.; Jiang, Y. *Sens. Actuators, B* **2017,** *251,* 144–152. doi:10.1016/j.snb.2017.04.039
41. Su, Y.; Yang, T.; Zhao, X.; Cai, Z.; Chen, G.; Yao, M.; Chen, K.; Bick, M.; Wang, J.; Li, S.; Xie, G.; Tai, H.; Du, X.; Jiang, Y.; Chen, J. *Nano Energy* **2020,** *74,* 104941. doi:10.1016/j.nanoen.2020.104941
42. Zhao, T.; Fu, Y.; Zhao, Y.; Xing, L.; Xue, X. *J. Alloys Compd.* **2015,** *648,* 571–576. doi:10.1016/j.jallcom.2015.07.035
43. Vivekananthan, V.; Alluri, N. R.; Purusothaman, Y.; Chandrasekhar, A.; Selvarajan, S.; Kim, S.-J. *ACS Appl. Mater. Interfaces* **2018,** *10,* 18650–18656. doi:10.1021/acsami.8b02915
44. Zhang, D.; Xu, Z.; Yang, Z.; Song, X. *Nano Energy* **2020,** *67,* 104251. doi:10.1016/j.nanoen.2019.104251
45. Xia, K.; Zhu, Z.; Zhang, H.; Du, C.; Wang, R.; Xu, Z. *Microelectron. Eng.* **2018,** *199,* 114–117. doi:10.1016/j.mee.2018.08.002
46. Han, Y.; Han, Y.; Zhang, X.; Li, L.; Zhang, C.; Liu, J.; Lu, G.; Yu, H.-D.; Huang, W. *ACS Appl. Mater. Interfaces* **2020,** *12,* 16442–16450. doi:10.1021/acsami.0c01061
47. Nguyen, V.; Zhu, R.; Yang, R. *Nano Energy* **2015,** *14,* 49–61. doi:10.1016/j.nanoen.2014.11.049
48. Zang, W.; Wang, W.; Zhu, D.; Xing, L.; Xue, X. *RSC Adv.* **2014,** *4,* 56211–56215. doi:10.1039/c4ra10216a
49. Zhu, D.; Hu, T.; Zhao, Y.; Zang, W.; Xing, L.; Xue, X. *Sens. Actuators, B* **2015,** *213,* 382–389. doi:10.1016/j.snb.2015.02.119

License and Terms

The definitive version of this article is the electronic one which can be found at:
https://doi.org/10.3762/bjnano.11.123

BEILSTEIN JOURNAL OF NANOTECHNOLOGY

Walking energy harvesting and self-powered tracking system based on triboelectric nanogenerators

Mingliang Yao, Guangzhong Xie, Qichen Gong and Yuanjie Su*

Full Research Paper

Open Access

Address:
State Key Laboratory of Electronic Thin Films and Integrated Devices, School of Optoelectronic Science and Engineering, University of Electronic Science and Technology of China (UESTC), Chengdu 610054, PR China

Email:
Yuanjie Su* - yjsu@uestc.edu.cn

* Corresponding author

Keywords:
harvesting walking energy; internet of things; mechanical energy; pedestrian flow area; self-powered tracking system; triboelectric nanogenerator

Beilstein J. Nanotechnol. **2020,** *11,* 1590–1595.
https://doi.org/10.3762/bjnano.11.141

Received: 02 July 2020
Accepted: 18 September 2020
Published: 20 October 2020

This article is part of the thematic issue "Nanogenerators and flexible electronics".

Guest Editor: Y. Mao

Abstract

Due to the extensive energy consumption and high population density in modern cities, the collection and use of scattered walking energy from the stream of people is crucial for the development of a green ecological city. Herein, a flexible undulated electrode-based triboelectric nanogenerator (u-TENG) was integrated to the floor to scavenge walking energy from pedestrians, promoting the ordered collection of disordered and scattered energy. Driven by the steps of human walking, the output of the as-fabricated u-TENG are an open-circuit voltage of 86 V and a short-circuit current of 6.2 µA, which are able to continuously light up 110 light-emitting diode bulbs. In addition, a self-powered location-tracking system was prepared for pedestrian volume counting and passenger tracing with the purpose of reducing energy consumption in public areas. The proposed walking energy harvesting device is flexible, feasible, and unaffected by season, climate, or location. This work not only proposes a strategy for mechanical energy harvesting in public areas, including subway stations, hospitals, shopping malls, and business streets, but also offers a novel solution for smart cities and low-carbon transportation alternatives.

Introduction

With the fast progress in urbanization and commercialization, energy acquisition for powering wearable electronics [1-5] and wireless sensor networks is in high demand. Mechanical energy, which is widely distributed in the environment, is one of the most general power sources. The human body is a rich source of mechanical energy [6]. Muscle stretching, for example, converts biochemical energy into mechanical motion with a peak efficiency of ≈25%, which can easily deliver an output power of more than 100 W [7]. Even though the population maintains a sustainable growth, there is a high concentration of people in almost every public area. However, this universal and widespread form of energy has been neglected and wasted daily.

So far, in order to harvest the energy resulting from human motion, several mechanical energy scavenging methods have been invented, including devices based on electrostatic [8,9], electromagnetic [10,11], and piezoelectric effects [12-14]. Since the output power density of an electromagnetic generator (EMG) is proportional to the square of the frequency, it is not very efficient for an EMG to harvest low-frequency human motions, especially if they are below 5 Hz [15]. With respect to the piezoelectric generator, the relatively low-energy conversion efficiency and the fabrication complexity greatly hinder its potential application in large-scale energy conversion systems. Consequently, a small, lightweight, highly efficient, and cost-effective device for collecting disordered and scattered mechanical energy from the crowds in public locations is urgently needed.

Recently, triboelectric nanogenerators (TENGs) have been invented, which offer an innovative combination between electrostatic induction and contact electrification. These devices are able to harvest mechanical energy from a vast array of sources, such as body motion [16-19], vibration [20-23], rotation [24-27], sound wave [28], air flow [29-31], water wave, and rain drops [32-34]. Furthermore, since they are able to convert mechanical motion into electrical energy, TENGs have been widely used to successfully construct reliable self-powered sensing systems with an excellent performance, which can be used as motion [35-37] and temperature sensors [38,39], UV detectors [40], tactile sensors [41-43], sensors for healthcare [44-47], humidity sensors, and gas sensors [48-51], for example.

In this work, a flexible undulated electrode-based triboelectric nanogenerator (u-TENG) was proposed and fabricated to scavenge the walking energy from areas with a high pedestrian flow. The as-prepared u-TENG is composed of two copper-coated nanostructured poly(tetrafluoroethylene) (PTFE) thin films as the back electrodes and an elastic undulated electrode in between. The undulated electrode serves as a spacer and also as an induction electrode for energy collection. Triggered by the steps of human walking, the open-circuit voltage and short-circuit current reach values up to 86 V and 6.2 μA, respectively, which is sufficient to light up 110 light-emitting diode (LED) bulbs. In addition, by integrating the u-TENGs with six electrode channels, a self-powered location-tracking system was developed. This walking energy harvesting device is flexible, durable, and feasible, regardless of the time of the day, season, climate, and weather, which makes it an ideal candidate for harvesting walking energy from a high-flow pedestrian area. Although an undulated electrode with similar shape design and working mechanism has been proposed and demonstrated in our previous work [34], in which it was used to collect the impact from water waves, it has been used for the first time in this current work to build up a self-powered location-tracking system and to harvest mechanical energy from human walking. This work unravels the practicality of the u-TENG, which can be used as a device for harvesting energy from human motion, as a self-powered tracking system, for transportation control, and for environmental monitoring.

Experimental

Surface modification of a PTFE film

The surface modification of a PTFE film was performed in a similar manner as described previously [34]. Deep reactive ion etching was employed to construct PTFE nanowires aligned on the surface. Isopropyl and deionized water were used to clean 50 μm thick PTFE films, which were then dried with nitrogen. During the etching process, DC sputtering was used on the surface of the PTFE film as a mask to deposit Au particles for 45 s. Next, a gas mixture containing O_2, CF_4, and Ar was introduced to the inductively coupled plasma chamber, at corresponding flow rates of 10.0, 30.0, and 15.0 sccm, respectively. The nanowire structure was obtained on the surface by etching the PTFE film for 15 s. The high-density plasma was generated by a 500 W power source while the plasma ions were triggered by another 160 W.

Fabrication of the u-TENG

The u-TENG fabrication procedure was adapted, with modifications, from [34]. The back electrode was formed by depositing a Cu layer on the unmodified surface of a PTFE film via magnetron sputtering. A poly(dimethylsiloxane) (PDMS)-coated PTFE film was mounted onto a poly(ethylene terephthalate) (PET) substrate. The Kapton film was fixed with a row of steel rods and heated, for 4 h in an oven at 100 °C, to achieve a wavy configuration. Copper foils were deposited onto both sides of the Kapton film by electron beam evaporation to form the wave-shaped electrode. The lead was connected to the electrode as an output terminal.

Characterization and electrical measurement of the u-TENG

Field-emission scanning electron microscopy (FESEM, Hitachi SU-8020) was used to characterize the surface morphology of the modified PTFE film. A Stanford Research Systems equipment was used to measure the output performance of the u-TENG. Voltage and current were recorded using a Keithley 6514 electrometer.

Results and Discussion

The structured diagram of the fabricated undulated electrode-based triboelectric nanogenerator is shown in Figure 1a. This nanogenerator is composed of PET substrates, nanostructured PTFE thin films coated with copper foils (back electrodes), and an elastic undulated electrode in between. The internal wave-shaped electrode is obtained by depositing copper layers onto both sides of the wave-shaped Kapton film, as displayed in Figure 1a. Due to their huge difference in electron affinity [52], copper and PTFE were selected as the contact materials. The electrons flow between the undulated electrode and the planar electrode since the external mechanical impact repeatedly compresses the elastic corrugated electrode, shortening the distance between the PTFE film the undulated electrode. Through deep reactive ion etching, polymer nanowires (average diameter of ≈150 nm and length values ranging from 410 to 680 nm) were created to vertically align on the surface of the PTFE film, as shown in Figure 1b. This modification on the PTFE surface not only enhances the effective contact area with the undulated electrode but also promotes the triboelectric charge density on the friction surface. The prepared u-TENGs are flexible, rugged, light, and small devices, as revealed in Figure 1c. It is worth noting that the application of the undulated electrode structure in this work is totally different from its application in the previously reported work [34]. In the latter, the undulated elastic electrode configuration was utilized to harvest the impact from the water waves together with a solid–liquid interface generator to collect the electrostatic energy from the water body. In this manuscript, however, this design enables for an efficient approach for harvesting energy from the walking flow and for generating a self-powered pedestrian tracking system.

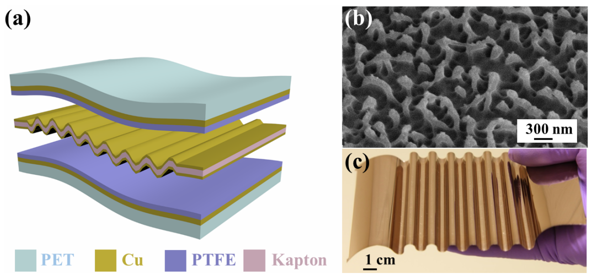

Figure 1: A flexible undulated electrode-based triboelectric nanogenerator. (a) Schematic diagram of the fabricated u-TENG. (b) FESEM image of an inductively coupled plasma-etched PTFE film. (c) Representative picture of the as-prepared undulated electrode.

The working principle of the u-TENG relies on the coupling between triboelectrification and electrostatic induction [34], as shown in Figure 2. The application and release of a stepping force during walking induces a periodical change between contact and separation the PTFE films and the undulated copper foils. This leads to the conversion of mechanical energy into electricity, as sketched in Figure 2.

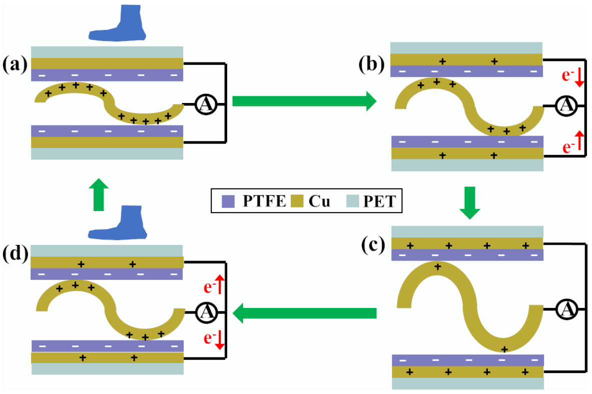

Figure 2: The working mechanism of the fabricated u-TENG in response to a stepping force. (a) The PTFE film and the undulated Cu electrode are brought into intimate contact by an external applied force. (b) When the force is released, free electrons flow from the Cu planar electrode to the undulated electrode. (c) The u-TENG reverts back to its unloaded position. (d) An external force compresses the u-TENG, driving the electrons move from the undulated electrode to the planar electrode.

To quantitatively characterize the u-TENG output performance, a linear motor was used to apply a periodical and controllable impact with tunable amplitude, frequency, and force. Triggered by an impact of 500 N at a frequency of 1 Hz, the as-prepared u-TENG delivered an output voltage of 86.0 V and an output current of 6.2 μA, as revealed in Figure 3a and Figure 3b, respectively. Output voltage and current both exhibit periodic behavior under repeated impact. In a frequency region of less than 5 Hz the output performance of the u-TENG is significantly higher than that of the EMG. Consequently, the frequency-dependent output behavior of the prepared u-TENG was investigated, as shown in Figure 3c and Figure 3d. As expected, the output current increased with an increasing frequency, while the output voltage remained almost constant. At an impact frequency of 5 Hz, the open-circuit voltage was 86.0 V and the short-circuit current was 10.8 μA. The impedance dependence of the fabricated u-TENG is shown in Figure 3e. The maximum output power of 0.279 mW can be observed at a loading resistance of 300 MΩ in Figure 3f. A long-term stability test did not exhibit a noticeable response decline after 10000 cycles (inset of Figure 3f), which indicates the robustness and repeatability of the prepared device.

To verify the capacity of harvesting human walking energy, the as-fabricated u-TENG was mounted as a floorboard to collect the mechanical energy from footsteps. The real-time dynamic signal profile of the output voltage for an adult man, an adult woman, and a child, respectively, was plotted in Figure 4a–c.

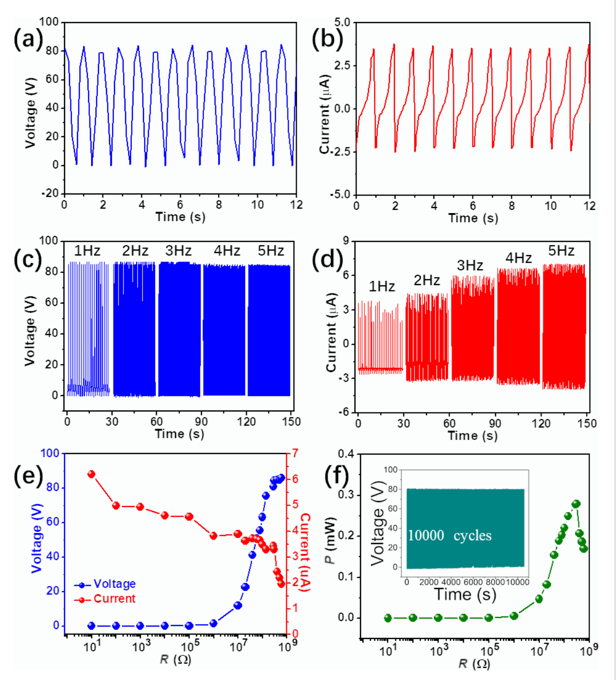

Figure 3: Electrical measurement results of the u-TENG. Open-circuit voltage (a) and short-circuit current (b) of the prepared u-TENG at an impact frequency of 1 Hz. Open-circuit voltage (c) and short-circuit current (d) of the prepared u-TENG under different frequencies ranging from 1 to 5 Hz. (e) Dependence of the output voltage and current on the external loading resistance. (f) Plot of the power density as a function of the loading resistance; inset: long-term stability.

These profiles show that our device is able to harvest a variety of walking motions from a wide range of people. It is evident that the walking steps can yield an electrical output. The output intensity is proportional to the pedestrian weight. This is because a more intense impact force causes a larger deformation of the undulated electrode, which contributes to larger separation (d) and thus a stronger output voltage.

To quantitatively study the dependence of the electric output on the force, the output voltage under various force values was plotted in Figure 4d. With an increasing force, the output voltage increases linearly at first and then it gradually saturates (Figure 4e). This can be explained by the combination of elastic and inelastic deformations. Under a relatively low external force, the induced elastic deformation increases almost linearly with the applied external force (region I). When the applied force increases, the elastic deformation is gradually converted into an inelastic deformation, which makes it harder to trigger a further deformation under an increasing force. According to the theoretical analysis of the TENG [53],

$$V_{\mathrm{OC}} = \frac{\sigma \cdot d}{\varepsilon_0 \cdot \varepsilon_r}, \qquad (1)$$

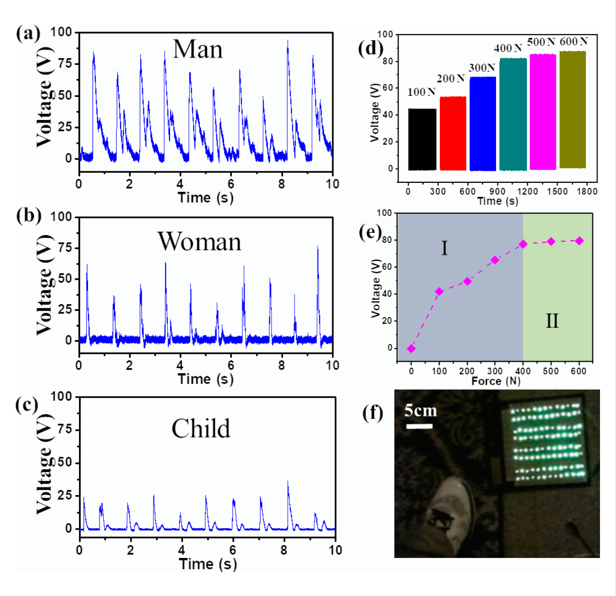

Figure 4: The ability of the u-TENG to harvesting energy from human walking. The electric output profile of a man (a), a woman (b), and a child (c). (d) The output voltage of u-TENG under different stress values. (e) The dependence of the output voltage on the impact force. (f) 110 LED bulbs are lit by stepping on a u-TENG.

where σ is the surface triboelectric charge density, d is the interlayer distance, ε_0 is the vacuum permittivity, and ε_r is the relative permittivity of the PTFE layer. The standstill deformation gives rise to the saturated output voltage in the inelastic deformation region (region II), as shown in Figure 4e. It was noted during the testing that the device was smaller than the sole of the feet of the participants. Therefore, only a part of the body weight was compressing the device. Hence, the applied force was smaller than the weight of a given participant. As a result, this feature leads to a larger difference in the output signal between a man (77 kg) and a woman (46 kg) according to Figure 4d.

To further demonstrate the device performance, 110 LED bulbs in series were linked to the as-fabricated u-TENG. As displayed in Figure 4f, all LED bulbs were simultaneously lit by a simple foot step, indicating the potential of the u-TENG as a sustainable power source.

To testify the feasibility of the fabricated u-TENG for a location-tracking system, six as-prepared u-TENGs were integrated into six floor blocks along a public aisle in order to detect and map the real-time position of a pedestrian, as shown in Figure 5a. Six channels were assigned via Labview to the corresponding six floorboards for real-time tracking. The output voltages from the six channels were recorded and instantly triggered the corresponding indicator on a monitor. When the pedestrian reached the first floorboard, a relevant voltage peak of 86.3 V was detected, as shown in Figure 5b. The signal triggered the first positioning indicator on a monitor, revealing that the pedestrian had just arrived at the first floorboard. The electric output also lit the LED bulb that was connected to the stepped floorboard and it emitted a visible light sign that indicated the instantaneous location of the pedestrian. It is important to mention that the LED light emission was powered by the triboelectric generator driven by the walking movements without any electric power source. Figure 5c and Figure 5d show the output voltage profile and the real-time mapping results when the pedestrian passes the third and the sixth floorboard, respectively. Therefore, the positional information of the pedestrian can be immediately displayed and directly observed, enabling pedestrian volume counting and passenger tracing. This design could be utilized in low-traffic areas or public passages at night to provide an alternative for energy harvesting and conservation in modern cities.

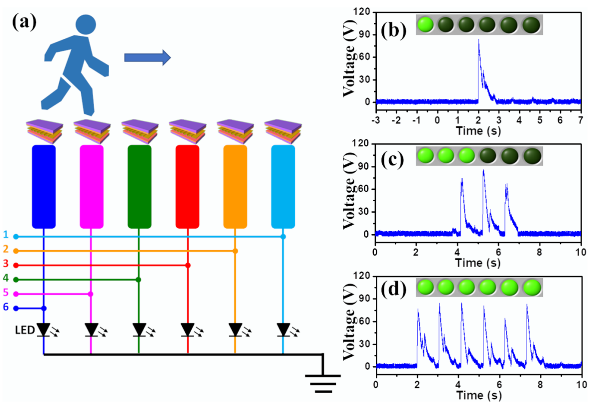

Figure 5: Self-powered u-TENG-based location-tracking system. (a) Circuit diagram of the fabricated u-TENG-based tracking system. (b–d) Measured output voltage and real-time location mapping when the pedestrian arrives at the (b) first, (c) third, and (d) sixth electrode.

Conclusion

In sum, we demonstrated that an undulated electrode-based TENG can be used to harvest walking energy from pedestrians. Triggered by the steps of human walking, an open-circuit voltage of 86 V and a short-circuit current of 6.2 μA were obtained from the as-fabricated u-TENG, which can continuously light up 110 LED bulbs. Moreover, the u-TENG can also harvest the mechanical energy from a variety of pedestrians, including men, women and children. In addition, integrated with six sensing channels along a public aisle, a self-powered location-tracking system was constructed for pedestrian volume counting and passenger tracing. This work paves the way for the application of triboelectric sensors in intelligent cities and for low-carbon transportation alternatives.

Funding

This work was partially supported by the Funds for Creative Research Groups of China (NO. 61421002), the National Natural Science Foundation of China (Grant Nos. 61571097, 61604033), and the National Postdoctoral Program for Innovative Talents (Grant No. BX201600026).

ORCID® iDs

Yuanjie Su - https://orcid.org/0000-0002-6851-4476

References

1. Chen, J.; Huang, Y.; Zhang, N.; Zou, H.; Liu, R.; Tao, C.; Fan, X.; Wang, Z. L. *Nat. Energy* **2016,** *1,* 16138. doi:10.1038/nenergy.2016.138
2. Jin, L.; Chen, J.; Zhang, B.; Deng, W.; Zhang, L.; Zhang, H.; Huang, X.; Zhu, M.; Yang, W.; Wang, Z. L. *ACS Nano* **2016,** *10,* 7874–7881. doi:10.1021/acsnano.6b03760
3. Zhang, B.; Chen, J.; Jin, L.; Deng, W.; Zhang, L.; Zhang, H.; Zhu, M.; Yang, W.; Wang, Z. L. *ACS Nano* **2016,** *10,* 6241–6247. doi:10.1021/acsnano.6b02384
4. Jin, L.; Xiao, X.; Deng, W.; Nashalian, A.; He, D.; Raveendran, V.; Yan, C.; Su, H.; Chu, X.; Yang, T.; Li, W.; Yang, W.; Chen, J. *Nano Lett.* **2020,** *20,* 6404–6411. doi:10.1021/acs.nanolett.0c01987
5. Ning, C.; Tian, L.; Zhao, X.; Xiang, S.; Tang, Y.; Liang, E.; Mao, Y. *J. Mater. Chem. A* **2018,** *6,* 19143–19150. doi:10.1039/c8ta07784c
6. Donelan, J. M.; Li, Q.; Naing, V.; Hoffer, J. A.; Weber, D. J.; Kuo, A. D. *Science* **2008,** *319,* 807–810. doi:10.1126/science.1149860
7. Margaria, R. *Int. Z. Angew. Physiol. Einschl. Arbeitsphysiol.* **1968,** *25,* 339–351. doi:10.1007/bf00699624
8. Lagomarsini, C.; Jean-Mistral, C.; Lombardi, G.; Sylvestre, A. *Smart Mater. Struct.* **2019,** *28,* 035003. doi:10.1088/1361-665x/aaf34e
9. Wang, F.; Hansenb, O. *Sens. Actuators, A* **2014,** *211,* 131–137. doi:10.1016/j.sna.2014.02.027
10. Rome, L. C.; Flynn, L.; Goldman, E. M.; Yoo, T. D. *Science* **2005,** *309,* 1725–1728. doi:10.1126/science.1111063
11. Xie, Z.; Huang, B.; Wang, S.; Zhou, X.; Gong, Y.; Huang, W. *Smart Mater. Struct.* **2020,** *29,* 075026. doi:10.1088/1361-665x/ab9147
12. Wang, Z. L.; Song, J. *Science* **2006,** *312,* 242–246. doi:10.1126/science.1124005
13. Gupta, K.; Brahma, S.; Dutta, J.; Rao, B.; Liu, C.-P. *Nano Energy* **2019,** *55,* 1–21. doi:10.1016/j.nanoen.2018.10.056
14. Gao, X.; Qiu, C.; Li, G.; Ma, M.; Yang, S.; Xu, Z.; Li, F. *Appl. Energy* **2020,** *271,* 115193. doi:10.1016/j.apenergy.2020.115193
15. Zi, Y.; Guo, H.; Wen, Z.; Yeh, M.-H.; Hu, C.; Wang, Z. L. *ACS Nano* **2016,** *10,* 4797–4805. doi:10.1021/acsnano.6b01569
16. Yang, H.; Deng, M.; Tang, Q.; He, W.; Hu, C.; Xi, Y.; Liu, R.; Wang, Z. L. *Adv. Energy Mater.* **2019,** *9,* 1901149. doi:10.1002/aenm.201901149
17. Tang, Y.; Zhou, H.; Sun, X.; Diao, N.; Wang, J.; Zhang, B.; Qin, C.; Liang, E.; Mao, Y. *Adv. Funct. Mater.* **2020,** *30,* 1907893. doi:10.1002/adfm.201907893
18. Yang, J.; Chen, J.; Yang, Y.; Zhang, H.; Yang, W.; Bai, P.; Su, Y.; Wang, Z. L. *Adv. Energy Mater.* **2014,** *4,* 1301322. doi:10.1002/aenm.201301322
19. Mao, Y.; Zhang, N.; Tang, Y.; Wang, M.; Chao, M.; Liang, E. *Nanoscale* **2017,** *9,* 14499–14505. doi:10.1039/c7nr05222g
20. Dai, Q.; Harne, R. L. *Smart Mater. Struct.* **2018,** *27,* 015011. doi:10.1088/1361-665x/aa9a13

21. Su, Y.; Yang, Y.; Zhong, X.; Zhang, H.; Wu, Z.; Jiang, Y.; Wang, Z. L. *ACS Appl. Mater. Interfaces* **2014,** *6,* 553–559. doi:10.1021/am404611h
22. Kumar, A.; Kumar, R.; Chandra Jain, S.; Vaish, R. *RSC Adv.* **2019,** *9,* 3918–3926. doi:10.1039/c8ra07887d
23. Hu, J.; Pu, X.; Yang, H.; Zeng, Q.; Tang, Q.; Zhang, D.; Hu, C.; Xi, Y. *Nano Res.* **2019,** *12,* 3018–3023. doi:10.1007/s12274-019-2545-y
24. Zhao, C.; Zhang, Q.; Zhang, W.; Du, X.; Zhang, Y.; Gong, S.; Ren, K.; Sun, Q.; Wang, Z. L. *Nano Energy* **2019,** *57,* 440–449. doi:10.1016/j.nanoen.2018.12.062
25. Mao, Y.; Geng, D.; Liang, E.; Wang, X. *Nano Energy* **2015,** *15,* 227–234. doi:10.1016/j.nanoen.2015.04.026
26. Su, Y.; Yang, Y.; Zhang, H.; Xie, Y.; Wu, Z.; Jiang, Y.; Fukata, N.; Bando, Y.; Wang, Z. L. *Nanotechnology* **2013,** *24,* 295401. doi:10.1088/0957-4484/24/29/295401
27. Wang, P.; Pan, L.; Wang, J.; Xu, M.; Dai, G.; Zou, H.; Dong, K.; Wang, Z. L. *ACS Nano* **2018,** *12,* 9433–9440. doi:10.1021/acsnano.8b04654
28. Qiu, W.; Feng, Y.; Luo, N.; Chen, S.; Wang, D. *Nano Energy* **2020,** *70,* 104543. doi:10.1016/j.nanoen.2020.104543
29. Su, Y.; Xie, G.; Xie, T.; Zhang, H.; Ye, Z.; Jing, Q.; Tai, H.; Du, X.; Jiang, Y. *J. Phys. D: Appl. Phys.* **2016,** *49,* 215601. doi:10.1088/0022-3727/49/21/215601
30. Su, Y.; Xie, G.; Xie, F.; Xie, T.; Zhang, Q.; Zhang, H.; Du, H.; Du, X.; Jiang, Y. *Chem. Phys. Lett.* **2016,** *653,* 96–100. doi:10.1016/j.cplett.2016.04.080
31. Zhang, L.; Zhang, B.; Chen, J.; Jin, L.; Deng, W.; Tang, J.; Zhang, H.; Pan, H.; Zhu, M.; Yang, W.; Wang, Z. L. *Adv. Mater. (Weinheim, Ger.)* **2016,** *28,* 1650–1656. doi:10.1002/adma.201504462
32. Zhong, W.; Xu, L.; Wang, H.; Li, D.; Wang, Z. L. *Nano Energy* **2019,** *66,* 104108. doi:10.1016/j.nanoen.2019.104108
33. Wu, Y.; Zeng, Q.; Tang, Q.; Liu, W.; Liu, G.; Zhang, Y.; Wu, J.; Hu, C.; Wang, X. *Nano Energy* **2020,** *67,* 104205. doi:10.1016/j.nanoen.2019.104205
34. Su, Y.; Wen, X.; Zhu, G.; Yang, J.; Chen, J.; Bai, P.; Wu, Z.; Jiang, Y.; Lin Wang, Z. *Nano Energy* **2014,** *9,* 186–195. doi:10.1016/j.nanoen.2014.07.006
35. Zhang, B.; Zhang, L.; Deng, W.; Jin, L.; Chun, F.; Pan, H.; Gu, B.; Zhang, H.; Lv, Z.; Yang, W.; Wang, Z. L. *ACS Nano* **2017,** *11,* 7440–7446. doi:10.1021/acsnano.7b03818
36. Wen, Z.; Yang, Y.; Sun, N.; Li, G.; Liu, Y.; Chen, C.; Shi, J.; Xie, L.; Jiang, H.; Bao, D.; Zhuo, Q.; Sun, X. *Adv. Funct. Mater.* **2018,** *28,* 1803684. doi:10.1002/adfm.201803684
37. Su, Y.; Zhu, G.; Yang, W.; Yang, J.; Chen, J.; Jing, Q.; Wu, Z.; Jiang, Y.; Wang, Z. L. *ACS Nano* **2014,** *8,* 3843–3850. doi:10.1021/nn500695q
38. Wen, X.; Su, Y.; Yang, Y.; Zhang, H.; Wang, Z. L. *Nano Energy* **2014,** *4,* 150–156. doi:10.1016/j.nanoen.2014.01.001
39. Su, Y.; Chen, J.; Wu, Z.; Jiang, Y. *Appl. Phys. Lett.* **2015,** *106,* 013114. doi:10.1063/1.4905553
40. Cheng, G.; Zheng, H.; Yang, F.; Zhao, L.; Zheng, M.; Yang, J.; Qin, H.; Du, Z.; Wang, Z. L. *Nano Energy* **2018,** *44,* 208–216. doi:10.1016/j.nanoen.2017.11.062
41. Chen, C.; Chen, L.; Wu, Z.; Guo, H.; Yu, W.; Du, Z.; Wang, Z. L. *Mater. Today* **2020,** *32,* 84–93. doi:10.1016/j.mattod.2019.10.025
42. Wang, J.; Qian, S.; Yu, J.; Zhang, Q.; Yuan, Z.; Sang, S.; Zhou, X.; Sun, L. *Nanomaterials* **2019,** *9,* 1304. doi:10.3390/nano9091304
43. Yang, J.; Chen, J.; Su, Y.; Jing, Q.; Li, Z.; Yi, F.; Wen, X.; Wang, Z.; Wang, Z. L. *Adv. Mater. (Weinheim, Ger.)* **2015,** *27,* 1316–1326. doi:10.1002/adma.201404794
44. Zhang, N.; Tao, C.; Fan, X.; Chen, J. *J. Mater. Res.* **2017,** *32,* 1628–1646. doi:10.1557/jmr.2017.162
45. Meng, K. Y.; Chen, J.; Li, X. S.; Wu, Y. F.; Fan, W. J.; Zhou, Z. H.; He, Q.; Wang, X.; Fan, X.; Zhang, Y. X.; Yang, J.; Wang, Z. L. *Adv. Funct. Mater.* **2018,** *29,* 1806388. doi:10.1002/adfm.201806388
46. Zhang, B.; Tang, Y.; Dai, R.; Wang, H.; Sun, X.; Qin, C.; Pan, Z.; Liang, E.; Mao, Y. *Nano Energy* **2019,** *64,* 103953. doi:10.1016/j.nanoen.2019.103953
47. Wang, M.; Zhang, J.; Tang, Y.; Li, J.; Zhang, B.; Liang, E.; Mao, Y.; Wang, X. *ACS Nano* **2018,** *12,* 6156–6162. doi:10.1021/acsnano.8b02562
48. Su, Y.; Yang, T.; Zhao, X.; Cai, Z.; Chen, G.; Yao, M.; Chen, K.; Bick, M.; Wang, J.; Li, S.; Xie, G.; Tai, H.; Du, X.; Jiang, Y.; Chen, J. *Nano Energy* **2020,** *74,* 104941. doi:10.1016/j.nanoen.2020.104941
49. Su, Y.; Xie, G.; Wang, S.; Tai, H.; Zhang, Q.; Du, H.; Zhang, H.; Du, X.; Jiang, Y. *Sens. Actuators, B* **2017,** *251,* 144–152. doi:10.1016/j.snb.2017.04.039
50. Su, Y.; Xie, G.; Tai, H.; Li, S.; Yang, B.; Wang, S.; Zhang, Q.; Du, H.; Zhang, H.; Du, X.; Jiang, Y. *Nano Energy* **2018,** *47,* 316–324. doi:10.1016/j.nanoen.2018.02.031
51. Su, Y.; Wang, J.; Wang, B.; Yang, T.; Yang, B.; Xie, G.; Zhou, Y.; Zhang, S.; Tai, H.; Cai, Z.; Chen, G.; Jiang, Y.; Chen, L.-Q.; Chen, J. *ACS Nano* **2020,** *14,* 6067–6075. doi:10.1021/acsnano.0c01804
52. Wang, Z. L. *ACS Nano* **2013,** *7,* 9533–9557. doi:10.1021/nn404614z
53. Niu, S.; Wang, S.; Lin, L.; Liu, Y.; Zhou, Y. S.; Hu, Y.; Wang, Z. L. *Energy Environ. Sci.* **2013,** *6,* 3576–3583. doi:10.1039/c3ee42571a

License and Terms

The definitive version of this article is the electronic one which can be found at:
https://doi.org/10.3762/bjnano.11.141

BEILSTEIN JOURNAL OF NANOTECHNOLOGY

A self-powered, flexible ultra-thin Si/ZnO nanowire photodetector as full-spectrum optical sensor and pyroelectric nanogenerator

Liang Chen‡[1,2], Jianqi Dong‡[1], Miao He*[2] and Xingfu Wang*[1]

Full Research Paper

Open Access

Address:
[1]Institute of Semiconductor Science and Technology, South China Normal University, Guangzhou 510631, China and [2]School of Physics and Optoelectronic Engineering, Guangdong University of Technology, Guangzhou 510006, China

Email:
Miao He* - herofate@126.com; Xingfu Wang* - xfwang@scnu.edu.cn

* Corresponding author ‡ Equal contributors

Keywords:
flexible; full-spectrum; photodetector; pyroelectric nanogenerator (PENG); self-powered

Beilstein J. Nanotechnol. **2020,** *11,* 1623–1630.
https://doi.org/10.3762/bjnano.11.145

Received: 13 July 2020
Accepted: 01 October 2020
Published: 27 October 2020

This article is part of the thematic issue "Nanogenerators and flexible electronics".

Guest Editor: Y. Mao

Abstract

In this work, a new type of self-powered, high-performance ultra-thin p-Si/n-ZnO nanowire (NW) flexible photodetector (PD) and its application as full-spectrum optical sensor and pyroelectric nanogenerator (PENG) are demonstrated. The working mechanism of PDs for PENGs is carefully investigated and systematically analyzed. The self-powered PDs exhibit high responsivity (1200 mA/W), high detectivity (10^{13} Jones) and fast response (τ_r = 18 μs, τ_f = 25 μs) under UV illumination. High and stable short-circuit output currents at each wavelength from ultraviolet (UV) to near-infrared (NIR) demonstrates that the device can realize full-spectrum optical communication. An experiment in which the PENG powers other devices is designed to further demonstrate the proposed working mechanism. This work provides an effective approach to realize self-powered, high-performance PDs for full-spectrum communication. Also, the fabrication of the PENG utilizing a simple and low-cost method shows its potential applications in self-powered flexible electronic devices.

Introduction

Full-spectrum photodetectors (PDs) that can detect light from ultraviolet to near-infrared have attracted widespread attention in recent years for a variety of applications in industry and technology, such as optical sensing/communication, environmental monitoring, biomedicine, and the "internet of things" [1-4]. Especially full-spectrum PDs applied in flexible wearable electronic devices have been extensively researched [5]. The majority of the reported full-spectrum PDs, which are based on perovskites, quantum dots, or organic materials are costly, complicated to prepare, and difficult to integrate into flexible electronic devices. This limits their application in the field of flexible electronics. Recently, the design of flexible devices with Si membranes as building blocks has been explored. These devices have become promising candidates for the use as flexible PDs due to many advantages, such as good compatibility, working in a harsh environment, low cost, and easy preparation [6-9]. However, the energy supply system of traditional Si-based flexible PDs utilizes an external battery, which will affect the portability, comfort, and durability of wearable devices due to large volume, and limited capacity. Therefore, it is necessary to develop a new type of full-spectrum flexible PDs with a special working mechanism to further improve their performance and expand the practical application.

Pyroelectric polarization can be achieved by changing the temperature of a pyroelectric material [10]. ZnO is an ideal pyroelectric material with a wide bandgap (3.2 eV), which absorbs UV light and can be easily prepared [11,12]. A pyroelectric potential will be generated in ZnO when the temperature changes upon illumination. The internal electric field can effectively drive the flow of electrons through an external circuit, yielding a short-circuit current output that can be used as a power generator [13,14]. Pyroelectric nanogenerators (PENGs) based on a pyroelectric material have been demonstrated as an effective approach that could avoid the waste of energy by converting temperature fluctuations induced by photoabsorption into electric energy. This is achieved by utilizing the temperature dependence of electric displacement of polar materials, which are already applied in solar cells, photodetectors, temperature sensors, and stretchable electronics [15-18]. It means that the PENGs could serve as a power source to power PDs by harvesting energy from the working environment instead of a battery. Comparing with another emerging nanogenerators (triboelectric nanogenerators) [19,20], the PENGs benefit from not requiring external mechanical energy and can make full use of the energy in their own environment. This self-powered system can greatly improve the portability and durability of the flexible PDs.

In this work, a new type of self-powered high-performance full-spectrum flexible PDs consisting of ultra-thin p-Si/n-ZnO nanowires (NWs) is fabricated. The working mechanism of PDs based on p-Si/n-ZnO heterojunctions for PENGs is carefully investigated and systematically analyzed. Also, the impact of the periodic frequency of the illumination and the optical power density on the short-circuit current and performance of PDs is analyzed carefully. This self-powered PDs show a full-spectrum response range from UV (325 nm) to near-infrared (NIR) (1064 nm) under zero bias with fast response speed at each wavelength. The self-power PDs exhibit high responsivity (1200 mA/W), high detectivity (10^{13} Jones) and fast response speed (τ_r = 18 μs, τ_f = 25 μs) under UV illumination. The pyroelectric output current can drive a LED by harvesting thermal energy induced by photoabsorption. This work provides an effective approach to realize self-powered, high-performance full-spectrum PDs utilizing a simple and low-cost method.

Results and Discussion

Preparation and characterization of the flexible PDs

The schematic of a self-powered full-spectrum PD based on a p-Si/n-ZnO NWs heterojunction is illustrated in Figure 1a. A typical cross-sectional scanning electron microscopy (SEM) image of the as-grown Si/ZnO NWs heterojunction is shown in Figure 1b. The uniformly grown ZnO NWs are conducive to a stable short-circuit current output. The detailed process of device preparation is shown in the Experimental section. The 45 μm ultrathin p-Si layer is obtained by isotropic chemical etching to realize a flexible device. Importantly, a previous study has shown that the performance of PDs (regarding, e.g., transient current and response speed) of PDs is significantly improved by reducing the thickness of Si [21]. In order to investigate the performance of self-powered PDs, a dynamic response curve *I–t* was measured under periodic 325 nm ultraviolet (UV) illumination and zero bias (Figure 1c). The photoresponsivity is calculated by Equation 1 [21]:

$$R = \frac{i_{\text{py}} - i_{\text{dark}}}{P_{\text{in}}}, \tag{1}$$

where i_{py}, i_{dark}, and P_{in} represent the pyroelectric current, the dark current, and the input power, respectively. The calculated photoresponsivity R is up to 1200 mA/W, which is more ten times than that of Perovskite/ZnO and Si/ZnO PDs [22,23]. The detectivity D^* is one of the key parameters of a PD, which usually describes the ability to detect weak signals. The photoresponsivity is calculated by Equation 2 [3]:

$$D^* = R\left(\frac{S}{2qI_{\text{dark}}}\right)^{1/2}, \tag{2}$$

where R, S, q, and I_{dark} represent responsivity, illuminated area, electronic charge, and dark current, respectively. The calculated detectivity D^* of our device is as high as 10^{13} Jones. A one-cycle dynamic response curve extracted from Figure 1c is shown in Figure 1d, indicating that the PD possesses a fast response speed (rising time τ_r = 18 μs, falling time τ_f = 25 μs). It is obvious that the p-Si/n-ZnO NWs heterojunction PDs exhibit excellent detection capability and work well without an external power source.

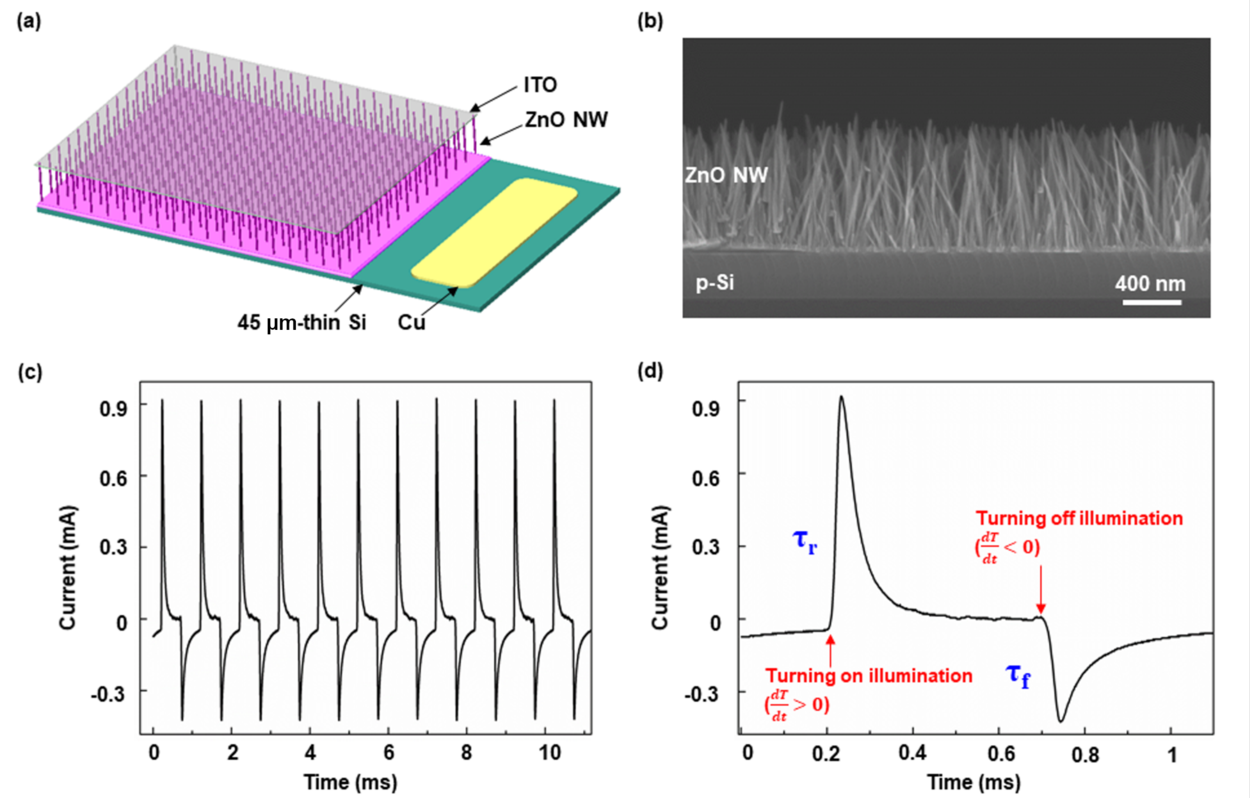

Figure 1: (a) Structure diagram of p-Si/n-ZnO NWs PDs. (b) Cross-sectional SEM image of the as-grown Si/ZnO NWs heterojunction. (c) Dynamic response curve *I*–*t* under 325 nm ultraviolet illumination and zero bias. (d) One typical cycle of short-circuit *I*–*t* curve.

Working mechanism of a PENG based on p-Si/n-ZnO NWs heterojunctions

To illustrate the working mechanism of self-powered PDs, schematic diagrams for the different conditions are presented in Figure 2. In the dark, a depletion layer is formed at the heterojunction interface due to carrier diffusion, and a corresponding intrinsic electric field (E_b) is formed in the depletion zone (Figure 2, left). Under this circumstance, the electron diffusion current and drift current are equal in magnitude and opposite in direction in the heterojunction. Therefore, the net current flowing through the heterojunction is zero, and no current flows through the external circuit. However, upon illumination, a photothermally induced instantaneous temperature increase ($\frac{dT}{dt} > 0$) will lead to the generation of a pyroelectric polarization potential and pyroelectric polarization charges at both ends of the *c*-axis of the ZnO NWs (Figure 2, middle). Because the direction of the pyroelectric electric field (E_{py}) is the same as E_b and the barrier height decreases at the heterojunction interface due to the generation of a negative polarization potential, the total electric field in the depletion zone increases instantly. The electric field in the depletion zone drives electrons to flow from Si to ZnO and produces a transient short-circuit output current in the external circuit. According to the pyroelectric theory, the pyroelectric current can be determined by Equation 3 [24]:

$$i_{py} = PA\frac{dT}{dt}, \quad (3)$$

where P, A, and T represent pyroelectric coefficient, effective area, and temperature, respectively. The corresponding open-circuit voltage can be determined by Equation 4 [25]:

$$V_{py} = PA\frac{\Delta T}{C}, \quad (4)$$

where P, A, C, and T represent pyroelectric coefficient, effective area, equivalent capacitance of device, and temperature, respectively. A large transient pyroelectric current occurs in the moment when the illumination is turned on (Figure 1d). When the illumination is turned off, the photothermallly induced instantaneous temperature decrease ($\frac{dT}{dt} < 0$) will lead to the generation of a pyroelectric polarization potential and pyroelectric polarization charges opposite to those before, when the illumination was turned on (Figure 2, right). The depletion zone width and corresponding electric field will decrease due to the generation of the reverse pyroelectric field (E_{py}) in the opposite direction of E_b. The total electric field in the depletion zone

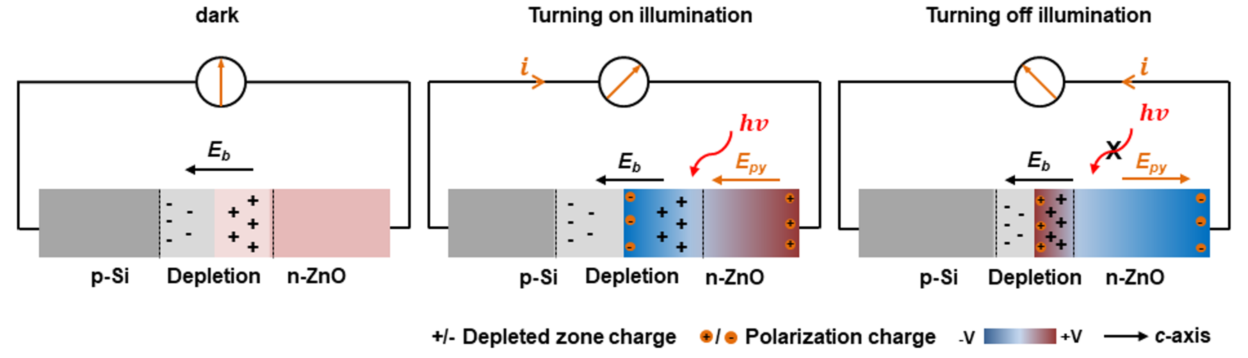

Figure 2: Working mechanism of PENGs. under zero bias, a depletion zone and corresponding built-in electric field are formed without illumination (left). Upon illumination, the pyroelectric electric field and transient output current are generated (middle). Reverse pyroelectric field and reverse transient output current are generated at the moment of turning off illumination (right).

decreases instantly. The electric field drives electrons to flow from ZnO to Si and produces a transient short-circuit output current in the external circuit. Therefore, the device based on p-Si/n-ZnO NWs heterojunction can serve as a PENG, and the self-powered full-spectrum PD can work at zero bias without any power sources.

Dependence of the short-circuit current on periodic frequency and power density of the illumination

The impact of UV illumination with different periodic frequencies and power densities on the performance of the self-powered PDs is studied and summarized carefully in Figure 3.

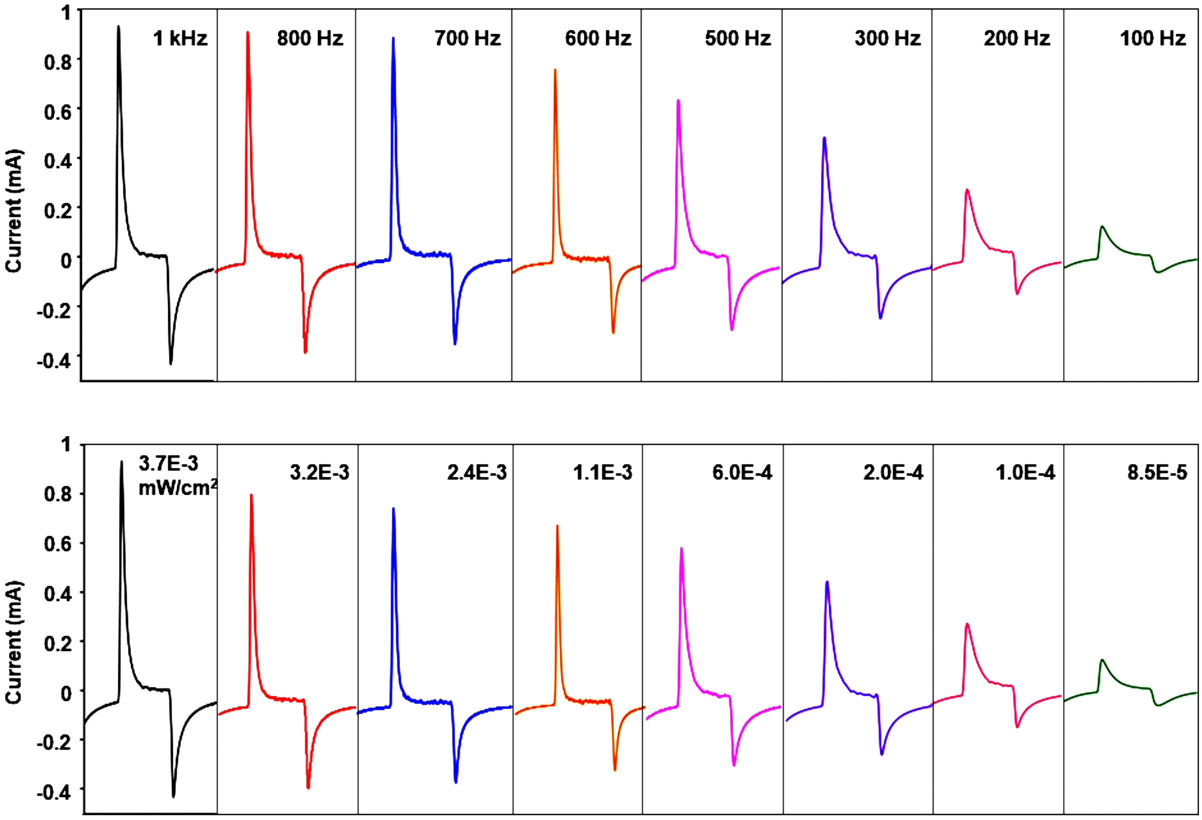

Figure 3: Impact of the incident optical power density and periodic frequency on the short-circuit current. *I–t* characteristics of a PD under zero bias and 325 nm UV illumination with different periodic frequencies ranges from 100 Hz to 1 kHz (top row). *I–t* characteristics of a PD under zero bias and 325 nm UV illumination with different power densities ranges from 8.5 × 10^{-5} to 3.7 × 10^{-3} mW/cm^2 (bottom row).

The short-circuit current response of PDs to 325 nm UV illumination under different frequencies ranging from 100 Hz to 1 kHz is shown in the top row of Figure 3. Obviously, the short-circuit current increases with increasing the frequency, indicating that the higher the frequency, the stronger the pyroelectric effect and the pyroelectric current. The reason for this phenomenon is mainly that the pyroelectric current induced by the pyroelectric effect is proportional to $\frac{\mathrm{d}T}{\mathrm{d}t}$ (i.e., $i_{\mathrm{py}} \propto \frac{\mathrm{d}T}{\mathrm{d}t}$), that is, inversely proportional to Δt. The short-circuit current response to UV illumination under zero bias is also measured and systematically investigated by varying the power density from 8.5×10^{-5} to 3.7×10^{-3} mW/cm^2. The light-induced temperature difference ΔT increases with the increase of incident optical power density. Therefore, a larger short-circuit current will be generated because the pyroelectric current is proportional to ΔT. At the moment of turning off the illumination, the transient temperature decreases and the corresponding temperature change rate is less than zero ($\frac{\mathrm{d}T}{\mathrm{d}t} < 0$). Therefore, there is an negative transient current. As in the case of turning on the illumination, the transient current gradually increases with the increase of periodic frequency. According to the above analysis, incident optical power density and periodic frequency play an important role in the performance of PDs and output current as a PENG.

Full spectrum response

To further investigate the performance of PDs in the illumination range from UV to NIR, the laser was operated at 325, 442, 532, 635, 808, and 1064 nm as an excitation source. The dynamic characteristic curves *I*–*t* of a PD under zero bias and at different laser wavelengths are shown in Figure 4. It is obvious that there are large short-circuit currents at all wavelengths, indicating that the self-powered PDs yields full-spectrum (UV–visible–NIR) detection. The broad spectral photoresponse from UV to NIR is related to two different bandgap materials (wide bandgap $E_{\mathrm{g}}^{\mathrm{ZnO}}$ = 3.2 eV and narrow bandgap $E_{\mathrm{g}}^{\mathrm{Si}}$ = 1.1 eV). Remarkably, the photoresponse current is significantly enhanced by introducing the pyroelectric effect based on the ZnO pyroelectric material. Moreover, response time and high sensitivity are almost the same at each wavelength, and the device exhibits excellent stability and repeatability in the UV–visible–NIR range. Therefore, the self-powered p-Si/n-ZnO NWs heterojunction device can be applied in full-spectrum optical sensing or optical communication.

Powering external circuits as a PENG

In structure design of the device, ultra-thin (45 μm) p-Si is prepared by isotropic chemical etching to fabricate flexible electronic devices and enhance the performance of the PDs. The structure diagram of a flexible device based on p-Si/n-ZnO NWs heterojunction is shown in Figure 5a, with a corresponding optical image of the sample shown in Figure 5b. The device can work well under repeated bending, ensuring the practicality of the device. The short-circuit output current to 325 nm UV illumination is measured under zero bias by periodically turning

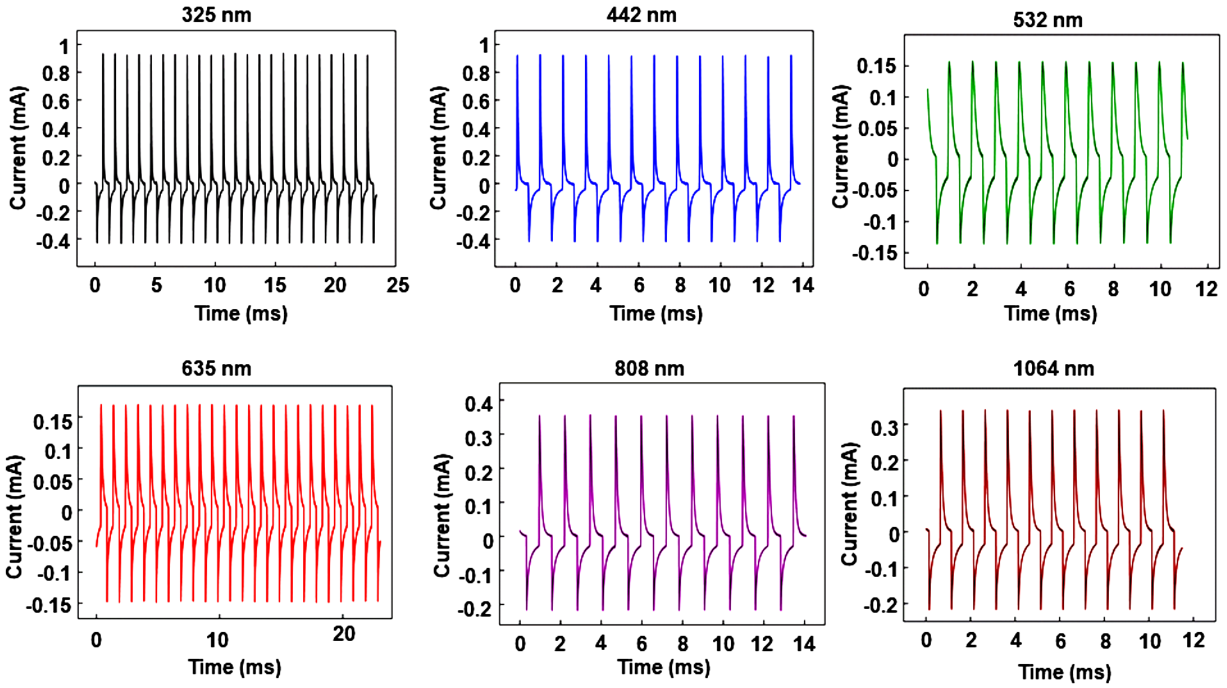

Figure 4: Dynamic response characteristics *I*–*t* characteristics of PDs under zero bias and different incident optical wavelengths in the range from UV to NIR.

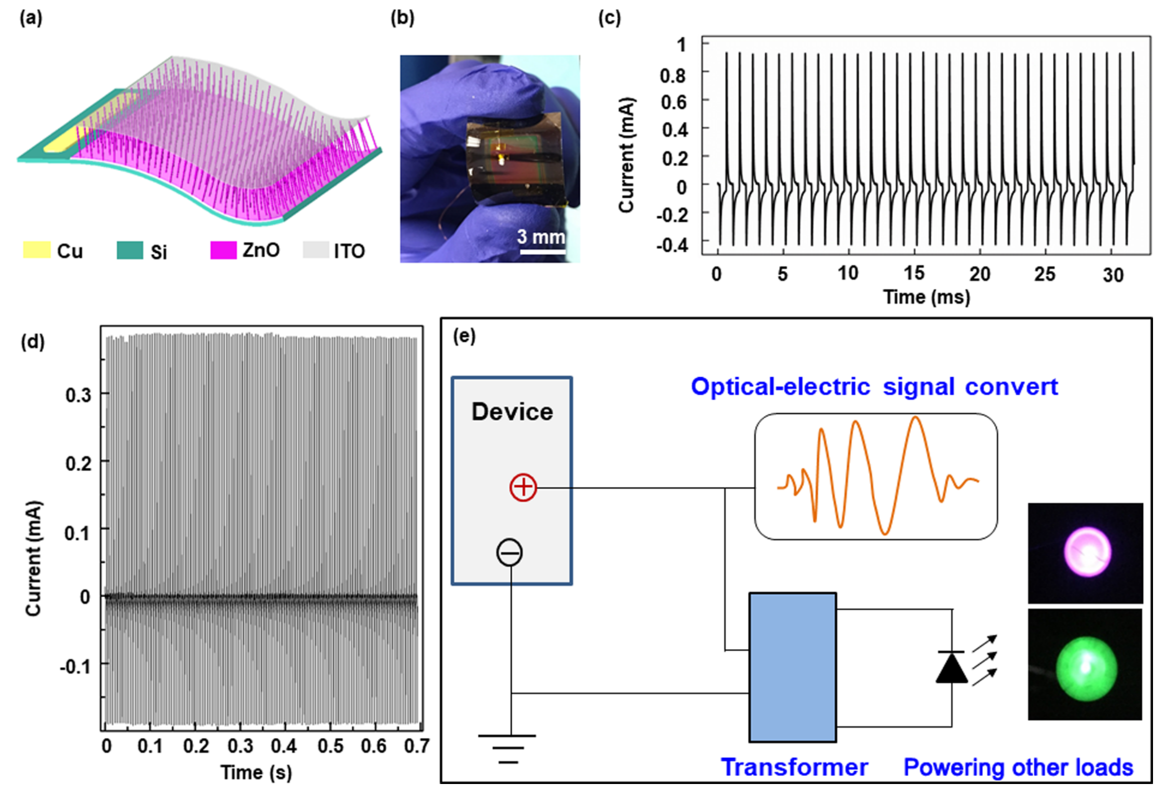

Figure 5: (a) Structure diagram of an ultra-thin (45 µm) p-Si/n-ZnO heterojunction device. (b) Optical image of the flexible PD. (c) Short-circuit photoresponse current of the ultra-thin (45 µm) p-Si/n-ZnO heterojunction device under zero bias by periodically turning on/off 325 nm UV illumination with a frequency of 1 kHz. (d) Dynamic response characteristics under 1064 nm NIR illumination. (e) Schematic diagram of a PENG powering different loads.

on/off illumination with a 1 kHz frequency as plotted in Figure 5c. A stable output is necessary for a power source to ensure the load can work stably. Moreover, the maximum output current is up to 1.5 mA with a corresponding voltage of up to 0.5 mV. The data about shown in Figure 5d indicates the stability and repeatability of device. To demonstrate the p-Si/n-ZnO NWs heterojunction PDs as a PENG can be used as a direct power source, a schematic diagram of the PENG powering the load is shown in Figure 5e. The output current through the transformer can be used to power LEDs (inset in Figure 5e). The rated power of the green LED is 0.06 W and the corresponding rated current is 20 mA. The rated power of the red LED is about 0.04 W and the corresponding rated current is also 20 mA. Based on the investigation of directly powering the LEDs, we can conclude that the p-Si/n-ZnO NWs heterojunction device not only can realize self-powered full-spectrum (UV–visible–NIR) optical sensing but can also serve as a power source (PENG) transforming thermal energy into electrical energy to power other loads.

Conclusion

We have fabricated a high-performance self-powered flexible p-Si/n-ZnO NWs heterojunction PDs for full-spectrum optical sensing and as a pyroelectric nanogenerator. The working mechanism of PDs for PENGs is carefully investigated and systematically analyzed. By changing the periodic frequency and the power density of the illumination the short-circuit current and the performance of PDs are notably improved. The self-powered PDs exhibit high responsivity (1200 mA/W), high detectivity (10^{13} Jones) and fast response speed (τ_r = 18 µs, τ_f = 25 µs) under UV illumination. High and stable short-circuit output currents at each wavelength illumination range from UV to NIR demonstrate that the device can realize full-spectrum optical communication. The experiment in which the PENG powers other loads is designed to further demonstrate the proposed working mechanism. Therefore, this work provides an effective approach to realize self-powered, high-performance PDs for full-spectrum communication and PENGs utilizing a simple and low-cost method, which offer potential applications in self-powered flexible electronic devices.

Experimental

Fabrication process of the device: Firstly, the ultra-thin (45 µm) p-Si substrate was prepared by isotropic chemical etching. More specifically, a 500 µm p-type high conductivity Si substrate was dipped into potassium hydrate (KOH) solution with a concentration of 50% at 130 °C for 6–8 h. Then, the obtained 45 μm p-Si was washed with acetone, isopropanol, and deionized water. Secondly, a thin ZnO seed layer was deposited onto 45 μm p-Si by radio frequency (RF) magnetron sputtering. Next, the sample was placed into a solution of 0.877 g hexamethylenetetramine, 1.372 g $Zn(CH_3COO)_2$, and 13 mL ammonium hydroxide to grow ZnO NWs for half an hour via a hydrothermal method in a mechanical convection oven at 90 °C. Finally, by RF magnetron sputtering, a 200 nm thick layers of ITO and Cu were deposited on ZnO NWs and p-Si, respectively.

Electrical measurements: the measurement setup includes a source meter, an optical platform, a chopper, sample, and a light source. Sample, chopper and light source must be in the same straight line. The voltage of source meter is set as 0 V. When controlling the frequency of the chopper, the incident light power density and the wavelength of the incident light, the transient response current, the different light power density, and the wavelength of the incident light are measured.

Instruments: The scanning electron microscope is a Hitachi SU8010. The *I–t* characteristic curves are measured by a source table (SR570, DS345). The optical input stimuli are provided by a He–Cd dual-color laser (MCLS1, Thorlabs Inc.). The light power density used in this work was measured and obtained by a thermopile power meter (Newport 818P-001-12).

Funding

This research also supported by the National Natural Science Foundation of China (Grant No. 11804103 and 61874161), Guangdong Natural Science Foundation for Distinguished Young Scholars (Grant No. 2018B030306048), and Zhongshan Science and Technology Planning Project of Guangdong Province, China (2019A4008).

ORCID® iDs

Liang Chen - https://orcid.org/0000-0003-4229-0707
Xingfu Wang - https://orcid.org/0000-0001-7450-6723

References

1. Zhou, X.; Yang, D.; Ma, D. *Adv. Opt. Mater.* **2015,** *3,* 1570–1576. doi:10.1002/adom.201500224
2. Wu, G.; Fu, R.; Chen, J.; Yang, W.; Ren, J.; Guo, X.; Ni, Z.; Pi, X.; Li, C.-Z.; Li, H.; Chen, H. *Small* **2018,** *14,* 1802349. doi:10.1002/smll.201802349
3. Gong, X.; Tong, M.; Xia, Y.; Cai, W.; Moon, J. S.; Cao, Y.; Yu, G.; Shieh, C.-L.; Nilsson, B.; Heeger, A. J. *Science* **2009,** *325,* 1665–1667. doi:10.1126/science.1176706
4. Dong, R.; Bi, C.; Dong, Q.; Guo, F.; Yuan, Y.; Fang, Y.; Xiao, Z.; Huang, J. *Adv. Opt. Mater.* **2014,** *2,* 549–554. doi:10.1002/adom.201400023
5. Chen, Y.; Zhang, Y.; Yuan, F.; Ding, F.; Schmidt, O. G. *Adv. Electron. Mater.* **2017,** *3,* 1600540. doi:10.1002/aelm.201600540
6. Kim, S.-Y.; Bong, J. H.; Kim, C.; Hwang, W. S.; Kim, T.-S.; Cho, B. J. *Adv. Mater. Interfaces* **2017,** *4,* 1700618. doi:10.1002/admi.201700618
7. Sarkar, A.; Katiyar, A. K.; Das, A. K.; Ray, S. K. *Flexible Printed Electron.* **2018,** *3,* 025004. doi:10.1088/2058-8585/aac127
8. Yoo, J.; Jeong, S.; Kim, S.; Je, J. H. *Adv. Mater. (Weinheim, Ger.)* **2015,** *27,* 1712–1717. doi:10.1002/adma.201404945
9. Wu, X.; Zhou, B.; Zhou, J.; Chen, Y.; Chu, Y.; Huang, J. *Small* **2018,** *14,* 1800527. doi:10.1002/smll.201800527
10. Whatmore, R. W. *Rep. Prog. Phys.* **1986,** *49,* 1335–1386. doi:10.1088/0034-4885/49/12/002
11. Wang, Z.; Yu, R.; Wang, X.; Wu, W.; Wang, Z. L. *Adv. Mater. (Weinheim, Ger.)* **2016,** *28,* 6880–6886. doi:10.1002/adma.201600884
12. Dong, J.; Wang, Z.; Wang, X.; Wang, Z. L. *Nano Today* **2019,** *29,* 100798. doi:10.1016/j.nantod.2019.100798
13. Yang, Y.; Wang, S.; Zhang, Y.; Wang, Z. L. *Nano Lett.* **2012,** *12,* 6408–6413. doi:10.1021/nl303755m
14. Yang, Y.; Guo, W.; Pradel, K. C.; Zhu, G.; Zhou, Y.; Zhang, Y.; Hu, Y.; Lin, L.; Wang, Z. L. *Nano Lett.* **2012,** *12,* 2833–2838. doi:10.1021/nl3003039
15. Peng, L.; Hu, L.; Fang, X. *Adv. Funct. Mater.* **2014,** *24,* 2591–2610. doi:10.1002/adfm.201303367
16. Yang, Y.; Zhang, H.; Zhu, G.; Lee, S.; Lin, Z.-H.; Wang, Z. L. *ACS Nano* **2013,** *7,* 785–790. doi:10.1021/nn305247x
17. Liao, X.; Liao, Q.; Zhang, Z.; Yan, X.; Liang, Q.; Wang, Q.; Li, M.; Zhang, Y. *Adv. Funct. Mater.* **2016,** *26,* 3074–3081. doi:10.1002/adfm.201505223
18. Lee, J.-H.; Lee, K. Y.; Gupta, M. K.; Kim, T. Y.; Lee, D.-Y.; Oh, J.; Ryu, C.; Yoo, W. J.; Kang, C.-Y.; Yoon, S.-J.; Yoo, J.-B.; Kim, S.-W. *Adv. Mater. (Weinheim, Ger.)* **2014,** *26,* 765–769. doi:10.1002/adma.201303570
19. Tang, Y.; Zhou, H.; Sun, X.; Diao, N.; Wang, J.; Zhang, B.; Qin, C.; Liang, E.; Mao, Y. *Adv. Funct. Mater.* **2020,** *30,* 1907893. doi:10.1002/adfm.201907893
20. Zhang, B.; Tang, Y.; Dai, R.; Wang, H.; Sun, X.; Qin, C.; Pan, Z.; Liang, E.; Mao, Y. *Nano Energy* **2019,** *64,* 103953. doi:10.1016/j.nanoen.2019.103953
21. Wang, X.; Dai, Y.; Liu, R.; He, X.; Li, S.; Wang, Z. L. *ACS Nano* **2017,** *11,* 8339–8345. doi:10.1021/acsnano.7b03560
22. Shao, D.; Zhu, W.; Xin, G.; Liu, X.; Wang, T.; Shi, S.; Lian, J.; Sawyer, S. *J. Mater. Chem. C* **2020,** *8,* 1819–1825. doi:10.1039/c9tc05940g
23. Alkis, S.; Tekcan, B.; Nayfeh, A.; Okyay, A. K. *J. Opt. (Bristol, U. K.)* **2013,** *15,* 105002. doi:10.1088/2040-8978/15/10/105002
24. Ryu, H.; Yoon, H.-J.; Kim, S.-W. *Adv. Mater. (Weinheim, Ger.)* **2019,** *31,* 1802898. doi:10.1002/adma.201802898
25. Sultana, A.; Alam, M. M.; Middya, T. R.; Mandal, D. *Appl. Energy* **2018,** *221,* 299–307. doi:10.1016/j.apenergy.2018.04.003

License and Terms

The definitive version of this article is the electronic one which can be found at:
https://doi.org/10.3762/bjnano.11.145

BEILSTEIN JOURNAL OF NANOTECHNOLOGY

Piezoelectric sensor based on graphene-doped PVDF nanofibers for sign language translation

Shuai Yang[1], Xiaojing Cui[1], Rui Guo[1], Zhiyi Zhang[2], Shengbo Sang*[1] and Hulin Zhang*[1]

Full Research Paper

Open Access

Address:
[1]Micro Nano System Research Center, College of Information and Computer, Taiyuan University of Technology, Taiyuan, 030024, China and [2]College of Textile Engineering, Taiyuan University of Technology, Taiyuan, 030024, China

Email:
Shengbo Sang* - sangshengbo@tyut.edu.cn; Hulin Zhang* - zhanghulin@tyut.edu.cn

* Corresponding author

Keywords:
motion sensor; piezoelectric; polyvinylidene fluoride (PVDF); self-powered; sign language translation

Beilstein J. Nanotechnol. **2020,** *11,* 1655–1662.
https://doi.org/10.3762/bjnano.11.148

Received: 30 August 2020
Accepted: 09 October 2020
Published: 02 November 2020

This article is part of the thematic issue "Nanogenerators and flexible electronics".

Guest Editor: Y. Mao

Abstract

The tracking of body motion, such as bending or twisting, plays an important role in modern sign language translation. Here, a subtle flexible self-powered piezoelectric sensor (PES) made of graphene (GR)-doped polyvinylidene fluoride (PVDF) nanofibers is reported. The PES exhibits a high sensitivity to pressing and bending, and there is a stable correlation between bending angle and piezoelectric voltage. The sensitivity can be adjusted by changing the doping concentration of GR. Also, when the PES contacts a source of heat, a pyroelectric signal can be acquired. The positive correlation between temperature and signal can be used to avoid burns. The integrated sensing system based on multiple PESs can accurately recognize the action of each finger in real time, which can be effectively applied in sign language translation. PES-based motion-tracking applications have been effectively used, especially in human–computer interaction, such as gesture control, rehabilitation training, and auxiliary communication.

Introduction

Sign language, as a communication method that works based on gestures, plays an important role for people who are hearing-impaired or unable to speak. With the development of society, the requirement to facilitate the communication with people with hearing or speaking impairments is increasing. Real-time translation systems based on gestures are gradually showing rich application prospects in sign language learning and daily communication. A recently reported yarn-based stretchable sensor can already translate a large number of gestures into speech signals [1-6]. However, traditional real-time sign language translation systems are limited by their bulky design and complex configurations, and always have limitations in terms of portability, comfort and cost [7-16]. A convenient and sensitive sign language translation system is urgently required to meet the needs of daily work and life.

Nowadays, pressure and bending angle sensors are mainly based on signals caused by a changing force [17-25]. Plenty of measurement methods, using different materials and different principles, have been proposed in recent years [26]. Although these sensors can detect various interactions between humans and machines, the indispensability of external power sources greatly narrow their application scopes [27-35]. Piezoelectric sensors generate self-responsive electrical signals based on external mechanical forces. As a self-powered sensing system, piezoelectric sensors show potential in wearable sensing applications [19,36-41]. However, traditional piezoelectric sensor devices such as piezoelectric ceramics have disadvantages in detecting bending, and their detection stability and measurement range need to be improved [18,42-48]. In the era of smart sensing, there is an increasing need for self-powered pressure and bending sensing systems [49-64].

In this study, we propose a flexible self-powered piezoelectric sensor (PES) based on graphene (GR)-doped PVDF nanofibers. The fiber properties after electrospinning were measured, and a potential application of the PES in the translation of sign language was successfully demonstrated. The designed PES shows a high sensitivity regarding both pressure and bending. In particular, a stable angle mapping under bending could be obtained. The amount of GR doping has an impact on sensitivity. In addition, the sensor will generate a large pyroelectric signal when it is touched with a hot object, which can be used to prevent burns of the hands. When the PES is integrated in a measuring circuit, it can accurately perceive the movement state of fingers in real time and output standardized sign language content. This work provides a novel solution for a portable and intelligent sign language translation system, which is considered to be an extremely valuable application to meet the requirements of future intelligent sensing.

Results and Discussion

The structural design of the self-powered PES based on GR-doped PVDF nanofibers is shown in Figure 1a. The cross section of the self-powered PES shows three parts, namely the GR-doped PVDF piezoelectric layer in the center, the electrode layer of Ti_3C_2 MXene and Ag NWs on both sides, and the PDMS protective layer on the outermost sides. Each PVDF fiber contains GR doping. Figure 1b shows a schematic diagram of a sign language translation system based on a self-powered PES. Sensors are separately integrated into the gloves at the joints of the fingers and the fingertips. When a hand gesture such as “Hello” is made, the signal acquisition and processing module will process the recorded sensor signal. The corresponding sign language content is wirelessly transmitted to a screen for convenient recognition. To further study the performance of this piezoelectric material, a bending-induced piezoelectric model was constructed, and the calculated stress and potential distribution were obtained through finite element analysis, as shown in Figure 1c and Figure 1d. Figure 1c shows the

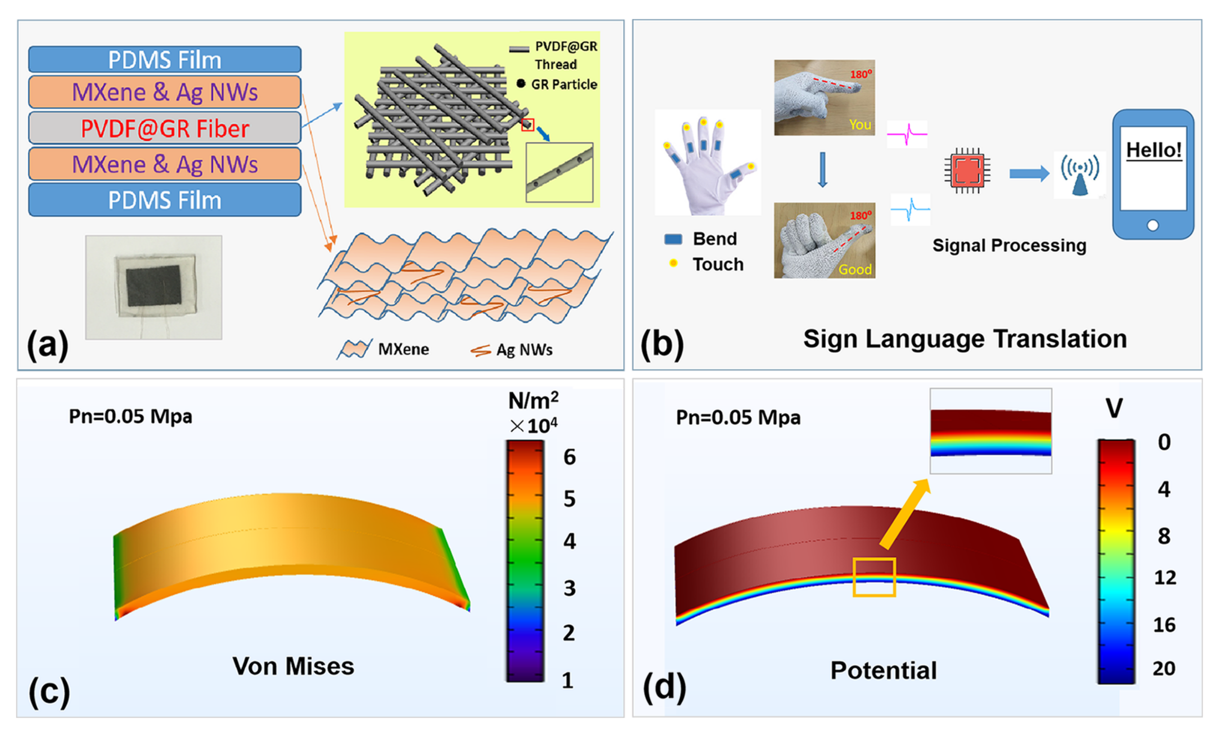

Figure 1: (a) Schematic diagram of a self-powered PES based on GR-doped PVDF. (b) Schematic diagram of an efficient sign language translation system using self-powered PESs. (c) Calculated stress in the PES during bending. (d) Potential distribution in the PES under bending.

stress distribution under bending. It can be clearly found that the stress is mainly concentrated in the bent part of the material, and the potential is generated on the opposite side of the device.

Electrospinning is used to manufacture GR-doped PVDF fibers. The overall process is shown in Figure 2a. Firstly, GR is dispersed in dimethylformamide (DMF). After ultrasonic treatment, PVDF powder is added under stirring to yield the spinning solution for electrospinning. After preparation of the fibers, an aqueous solution of Ti_3C_2 MXene and Ag NWs is sprayed on both sides of the material and then dried. Finally, the nanowire membrane is covered on both sides with PDMS to obtain the piezoelectric sensor. Ti_3C_2 MXene and Ag NWs maintain the good conductivity of the electrode and avoid possible short-circuit problems occurring after magnetron sputtering. Also, a stable flexibility of the structure is maintained. GR is added with six different mass fractions, that is, 0, 0.2, 0.4, 0.6, 0.8, and 1.0 wt %. Figure 2b shows SEM images after doping with different concentrations. It can be found that all spinning solutions yield a uniform fiber film without GR agglomeration after electrospinning. Figure 2c shows the FTIR spectra of samples with different doping concentrations.

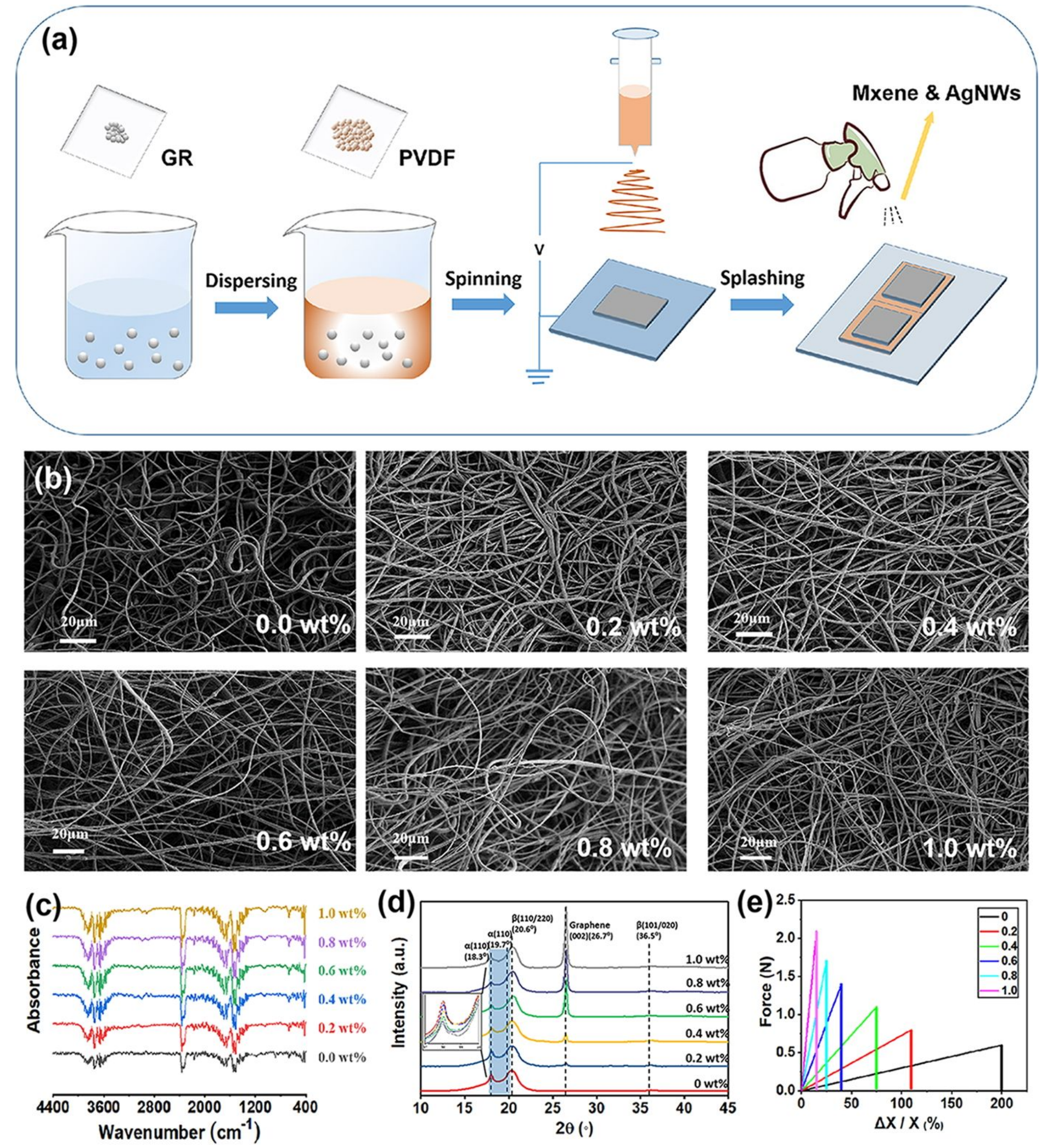

Figure 2: (a) Preparation of the self-powered GR-doped PVDF PES. (b) SEM images of PVDF fibers with different GR doping concentrations. (c) FTIR spectra of the PVDF fibers. (d) XRD patterns of the PVDF fibers. (e) Stress–strain curves of the PVDF fibers.

Further, XRD was used to characterize the material (Figure 2d). It was found that as the GR concentration increases, the fraction of the β-phase of PVDF also increases, which is considered to have a positive effect on the piezoelectricity of PVDF. The influence of the GR concentration on the tensile strength of the fibers is shown in Figure 2e. As the concentration increases, the tensile strength of the material increases.

The output of the self-powered PES was measured with a series of experiments. Figure 3a,b shows that when the pressure gradually increases, the generated piezoelectric voltage increases. The voltage also increases with increasing GR doping concentration, which is consistent with previous characterization results [24]. Figure 3c shows the measured waveform of the device with 1 wt % GR under pressure. After repeated pressing for thousands of times the output of the sensor shows no visible attenuation (Figure 3d). The output voltage increases with stronger bending, that is, smaller bending angles φ (Figure 3e). The effective working range of the sensor under bending is 120° to 60°, and its angular resolution can reach 0.006 V/° at 1 wt % GR. Figure 3g shows the measured waveform of a device with 1 wt % GR under different bending angles. The voltage in Figure 3h was measured while the sensor was gradually bent and shaken at different angles. The output voltage is stable and there is a good mapping relationship with the bending angle. In the upper left corner of Figure 3h, the voltage under repeated bending is shown. The output of the PES shows no obvious attenuation after a large number of bending tests. The PES was attached alternatively to a heater and a cooling fin to measure its pyroelectric voltage (Figure 3i). The heater was kept at a constant temperature of 50 °C. Figure 3j displays that the voltage increases with increasing doping concentration. The pyroelectric voltage of the PES as a function of the doping concentration is plotted in Figure 3k, showing that the measured waveform is stable and repeatable. When the temperature of the heater is changed, the voltage rises as the temperature is increased (Figure 3j).

The PES has great application potential in self-powered motion tracking. To examine its function in sign language translation, PESs were attached to all fingers and the wrists to realize motion tracking through the integrated sensor system. When the hand shows a sign language "Y", as shown in Figure 4a, the bent fingers produce an output signal and the system recog-

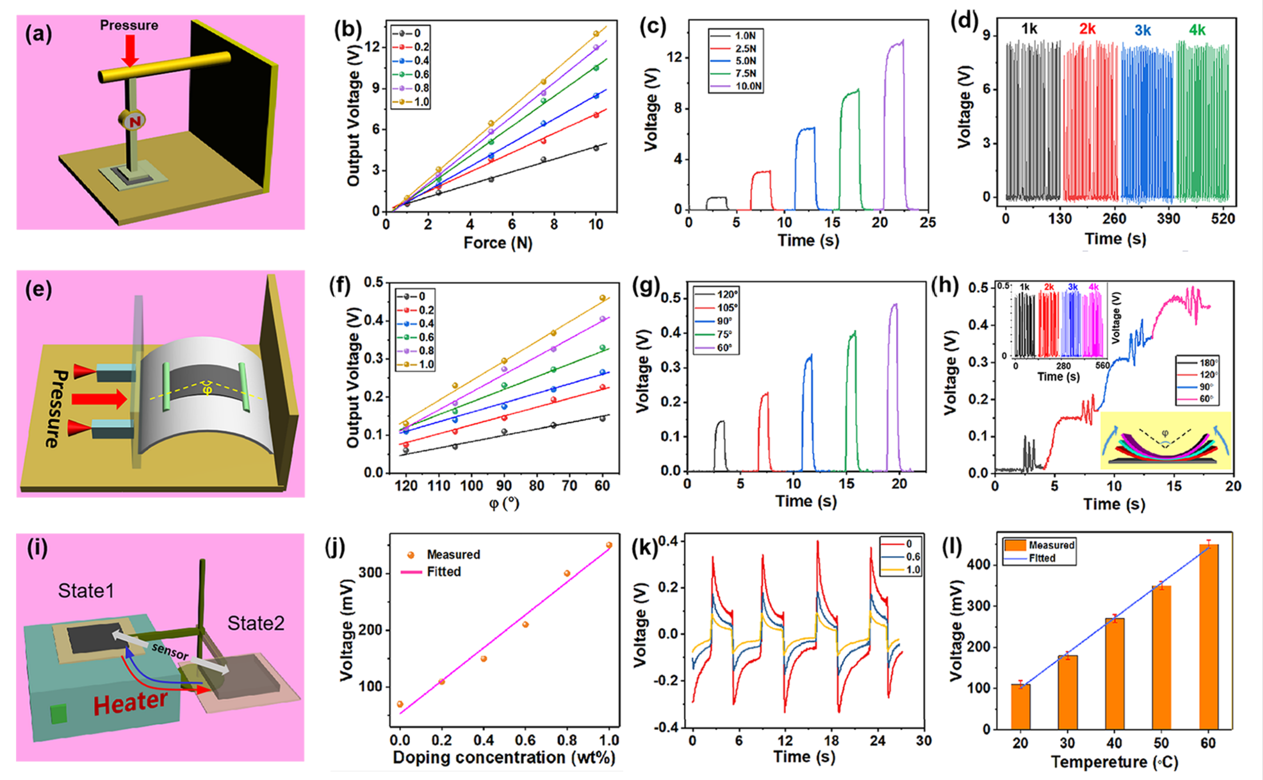

Figure 3: (a) Schematic diagram of the PES under external pressure. (b) Output voltage as a function of the applied pressure for different doping concentrations. (c) Waveforms corresponding to different pressures (1 wt % GR). (d) Waveforms after cyclic pressing. (e) Schematic diagram of the PES under bending. (f) Output voltage as a function of the bending angle for different doping concentrations. (g) Waveforms corresponding to different bending angles (1 wt % GR). (h) Waveforms when the PES is slightly shaken under increasing bending angles. (i) Schematic diagram of the PES contacting a heat source. (j) Output voltage during contact with the heat source for different doping concentrations. (k) Waveforms during contact with the heat source at different concentrations. (l) Output voltage at different temperatures (1 wt % GR).

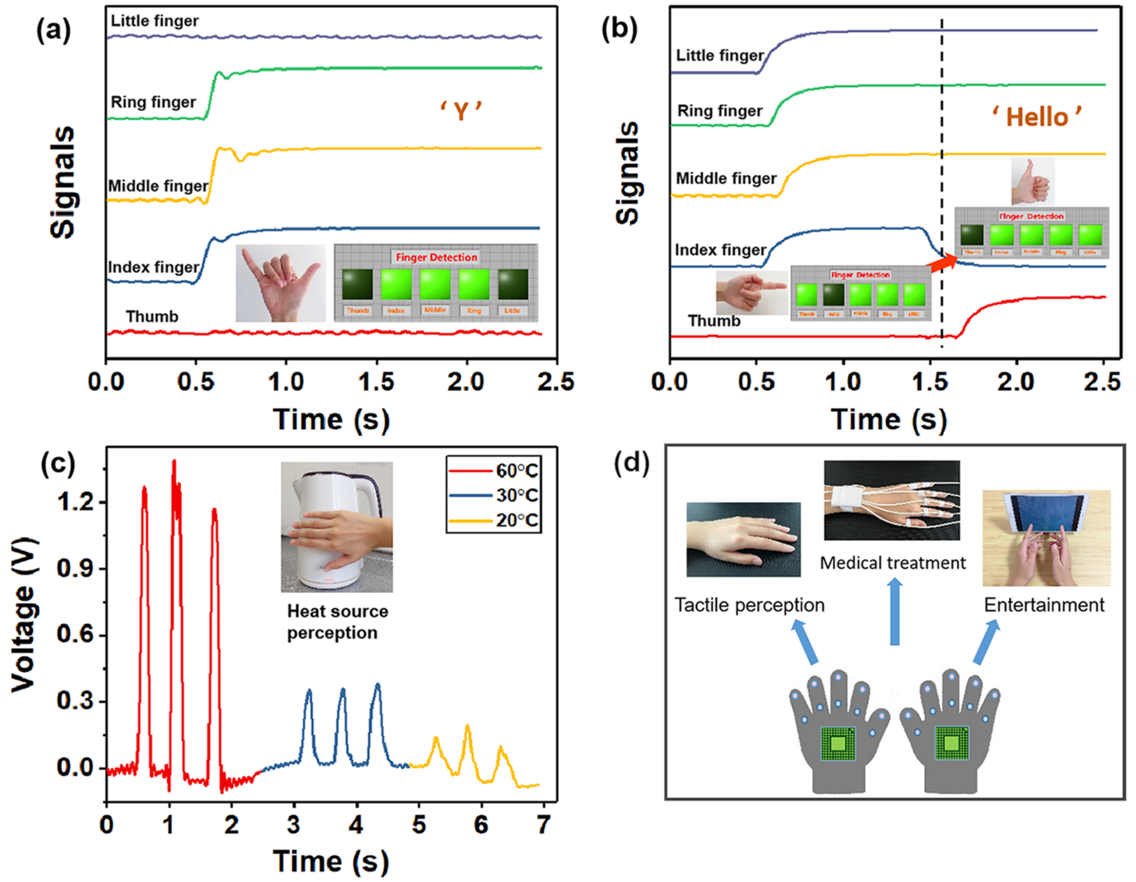

Figure 4: (a) Output signal when a sign language "Y" is shown. (b) Output signal when a sign language "Hello" is shown. (c) Output signal when PES touches a heat source. (d) Potential applications of smart gloves containing PESs.

nizes the corresponding sign. When the sign language "Hello" is shown, the corresponding finger action can be well recognized as the fingers move (Figure 4b). The output signal yields an accurate mapping relationship to the hand motion. The output voltage of the PES when it touches a heat source is plotted in Figure 4c. A temperature of 60 °C induces a high output voltage, which can be used to avoid burns of the hands. If PESs made of GR-doped PVDF are integrated into a smart glove, the self-powered sensor system can be used for other applications, such as tactile perception, medical rehabilitation, and gesture games (Figure 4d).

Conclusion

A self-powered PES based on GR-doped PVDF has been fabricated. Its sensitivity to pressure and bending was examined, especially regarding the reliable measurment of the bending angle. Also, the effect of different doping concentrations on the sensitivity is shown. The pyroelectric voltage can be used to prevent burns. The PES-based sign language recognition system has a good recognition effect for different actions. Our work has paved the way for wearable motion-tracking systems based on piezoelectric sensors, which are of great value in fields such as human–machine interaction, medical rehabilitation, and virtual reality.

Experimental

Chemicals: PVDF (M_w = 2.75 × 10^5 g/mol) powder was purchased from SOLEF (USA). *N*,*N*-Dimethylformamide (DMF) was provided by China National Pharmaceutical Group. Graphene powder was purchased from Suzhou Carbon Fung Graphene Technology Company. Ag NWs (60 nm in diameter) were purchased from Lit Nanotech. Ti_3C_2 MXene was purchased from Beijing Beike New Material Technology Company. Polydimethylsiloxane (PDMS) and curing agent were purchased from Shenzhen Oss Corporation.

Electrospinning process: First, GR is added to DMF and ultrasonically dispersed for 10 min. The dispersion is then heated to 60 °C. PVDF powder (18 wt %) is added under continuous heating and stirring for 6 h to obtain the spinning solution. The prepared solution is filled into a 10 mL syringe with an 18 gauge needle, the rotation speed of the plate is 50 min^{-1}, the distance between needle and plate is 15 cm, the injection speed is 0.5 mL/h, the applied voltage is 18 kV, and each sample is electrospun for 5 h.

Preparation of PES sensor: Ti_3C_2 powder (0.1 g) and Ag NWs (0.05 g) are ultrasonically dispersed in deionized water (10 mL) for 1 h to obtain the spray solution. The liquid is transferred into a spray can and sprayed evenly on the surface of the fiber membrane. Then, the fiber membrane is dried at 60 °C for 5 min. After attaching copper wires on both sides, the membrane is encapsulated with PDMS.

Thermoelectric test process: The PES unit is attached to a thin polyethylene plate and connected to the analogue signal test system via the copper wire electrodes. The surface of the plate heater is kept at a temperature of 50 °C. The polyethylene plate is fixed to a vertical rod on one side and can be rotated laterally. The PES is moved between the heating stage and the suspended cooling end in a cycle of approximately 7 s, and the output of the analogue signal is recorded.

Sign language translation system: The PESs were attached to five finger bending joints of a glove with double-sided tape. The thin copper wires were connected to the input terminals of the analogue measurement channels of a National Instruments BNC-2111 connector block. Voltage and current were measured with a Keithley 6514 electrometer (200 TΩ input impedance). The analogue signal of each channel is collected in real time. When the voltage exceeds the threshold, the corresponding Boolean indicator lights up, otherwise the indicator light goes out. Thus, the indicator lights can represent sign language gestures.

Funding

This work is supported by Scientific and Technological Innovation Programs of Higher Education Institutions in Shanxi (STIP) (No. 201802028), Research Project Supported by Shanxi Scholarship Council of China (HGKY2019022), Youth Foundation of Taiyuan University of Technology (2017QN61) and Youth Top Talent Program of Shanxi Province (2018).

ORCID® iDs

Hulin Zhang - https://orcid.org/0000-0003-4899-1491

References

1. Cai, Y.; Shen, J.; Ge, G.; Zhang, Y.; Jin, W.; Huang, W.; Shao, J.; Yang, J.; Dong, X. *ACS Nano* **2018,** *12,* 56–62. doi:10.1021/acsnano.7b06251
2. Cao, R.; Pu, X.; Du, X.; Yang, W.; Wang, J.; Guo, H.; Zhao, S.; Yuan, Z.; Zhang, C.; Li, C.; Wang, Z. L. *ACS Nano* **2018,** *12,* 5190–5196. doi:10.1021/acsnano.8b02477
3. Seminara, L.; Capurro, M.; Cirillo, P.; Cannata, G.; Valle, M. *Sens. Actuators, A* **2011,** *169,* 49–58. doi:10.1016/j.sna.2011.05.004
4. Zhou, Z.; Chen, K.; Li, X.; Zhang, S.; Wu, Y.; Zhou, Y.; Meng, K.; Sun, C.; He, Q.; Fan, W.; Fan, E.; Lin, Z.; Tan, X.; Deng, W.; Yang, J.; Chen, J. *Nat. Electron.* **2020,** *3,* 571–578. doi:10.1038/s41928-020-0428-6
5. Chang, J.; Dommer, M.; Chang, C.; Lin, L. *Nano Energy* **2012,** *1,* 356–371. doi:10.1016/j.nanoen.2012.02.003
6. Corres, J. M.; Garcia, Y. R.; Arregui, F. J.; Matias, I. R. *IEEE Sens. J.* **2011,** *11,* 2383–2387. doi:10.1109/jsen.2011.2123881
7. Deng, W.; Yang, T.; Jin, L.; Yan, C.; Huang, H.; Chu, X.; Wang, Z.; Xiong, D.; Tian, G.; Gao, Y.; Zhang, H.; Yang, W. *Nano Energy* **2019,** *55,* 516–525. doi:10.1016/j.nanoen.2018.10.049
8. Fuh, Y.-K.; Chen, P.-C.; Huang, Z.-M.; Ho, H.-C. *Nano Energy* **2015,** *11,* 671–677. doi:10.1016/j.nanoen.2014.10.038
9. He, Q.; Wu, Y.; Feng, Z.; Sun, C.; Fan, W.; Zhou, Z.; Meng, K.; Fan, E.; Yang, J. *Nano Energy* **2019,** *59,* 689–696. doi:10.1016/j.nanoen.2019.03.005
10. Liang, Y.; Cheng, S.; Zhao, J.; Zhang, C.; Sun, S.; Zhou, N.; Qiu, Y.; Zhang, X. *J. Power Sources* **2013,** *240,* 204–211. doi:10.1016/j.jpowsour.2013.04.019
11. Lim, S.; Son, D.; Kim, J.; Lee, Y. B.; Song, J.-K.; Choi, S.; Lee, D. J.; Kim, J. H.; Lee, M.; Hyeon, T.; Kim, D.-H. *Adv. Funct. Mater.* **2015,** *25,* 375–383. doi:10.1002/adfm.201402987
12. Lin, Z.; Yang, J.; Li, X.; Wu, Y.; Wei, W.; Liu, J.; Chen, J.; Yang, J. *Adv. Funct. Mater.* **2018,** *28,* 1704112. doi:10.1002/adfm.201704112
13. Liu, Z. H.; Pan, C. T.; Su, C. Y.; Lin, L. W.; Chen, Y. J.; Tsai, J. S. *Sens. Actuators, A* **2014,** *211,* 78–88. doi:10.1016/j.sna.2014.03.012
14. Meng, K.; Chen, J.; Li, X.; Wu, Y.; Fan, W.; Zhou, Z.; He, Q.; Wang, X.; Fan, X.; Zhang, Y.; Yang, J.; Wang, Z. L. *Adv. Funct. Mater.* **2018,** *29,* 1806388. doi:10.1002/adfm.201806388
15. Neppalli, R.; Wanjale, S.; Birajdar, M.; Causin, V. *Eur. Polym. J.* **2013,** *49,* 90–99. doi:10.1016/j.eurpolymj.2012.09.023
16. Shin, Y.-E.; Sohn, S.-D.; Han, H.; Park, Y.; Shin, H.-J.; Ko, H. *Nano Energy* **2020,** *72,* 104671. doi:10.1016/j.nanoen.2020.104671
17. Shirinov, A. V.; Schomburg, W. K. *Sens. Actuators, A* **2008,** *142,* 48–55. doi:10.1016/j.sna.2007.04.002
18. Zhang, Y.; Wu, M.; Zhu, Q.; Wang, F.; Su, H.; Li, H.; Diao, C.; Zheng, H.; Wu, Y.; Wang, Z. L. *Adv. Funct. Mater.* **2019,** *29,* 1904259. doi:10.1002/adfm.201904259
19. Wang, W.; Zhang, J.; Zhang, Y.; Chen, F.; Wang, H.; Wu, M.; Li, H.; Zhu, Q.; Zheng, H.; Zhang, R. *Appl. Phys. Lett.* **2020,** *116,* 023901. doi:10.1063/1.5134100
20. Tanaka, M.; Tanaka, Y.; Chonan, S. *J. Intell. Mater. Syst. Struct.* **2007,** *19,* 35–42. doi:10.1177/1045389x06072802
21. Yang, S.; Zhang, H.; Sang, S. *Energy Technol.* **2020,** *8,* 2000155. doi:10.1002/ente.202000155
22. Su, Y.; Wu, Z.; Wu, X.; Long, Y.; Zhang, H.; Xie, G.; Du, X.; Tai, H.; Jiang, Y. *Sens. Actuators, A* **2016,** *241,* 169–175. doi:10.1016/j.sna.2016.02.023
23. Yang, T.; Pan, H.; Tian, G.; Zhang, B.; Xiong, D.; Gao, Y.; Yan, C.; Chu, X.; Chen, N.; Zhong, S.; Zhang, L.; Deng, W.; Yang, W. *Nano Energy* **2020,** *72,* 104706. doi:10.1016/j.nanoen.2020.104706
24. Zhang, H.; Zhang, S.; Yao, G.; Huang, Z.; Xie, Y.; Su, Y.; Yang, W.; Zheng, C.; Lin, Y. *ACS Appl. Mater. Interfaces* **2015,** *7,* 28142–28147. doi:10.1021/acsami.5b10923
25. Bai, P.; Zhu, G.; Jing, Q.; Yang, J.; Chen, J.; Su, Y.; Ma, J.; Zhang, G.; Wang, Z. L. *Adv. Funct. Mater.* **2014,** *24,* 5807–5813. doi:10.1002/adfm.201401267

26. Chen, G.; Li, Y.; Bick, M.; Chen, J. *Chem. Rev.* **2020,** *120,* 3668–3720. doi:10.1021/acs.chemrev.9b00821
27. Chen, J.; Huang, Y.; Zhang, N.; Zou, H.; Liu, R.; Tao, C.; Fan, X.; Wang, Z. L. *Nat. Energy* **2016,** *1,* 16138. doi:10.1038/nenergy.2016.138
28. Chen, J.; Wang, Z. L. *Joule* **2017,** *1,* 480–521. doi:10.1016/j.joule.2017.09.004
29. Chen, X.; Iwamoto, M.; Shi, Z.; Zhang, L.; Wang, Z. L. *Adv. Funct. Mater.* **2015,** *25,* 739–747. doi:10.1002/adfm.201403577
30. Chen, X.; Jiang, T.; Yao, Y.; Xu, L.; Zhao, Z.; Wang, Z. L. *Adv. Funct. Mater.* **2016,** *26,* 4906–4913. doi:10.1002/adfm.201600624
31. Chen, X.; Liu, L.; Feng, Y.; Wang, L.; Bian, Z.; Li, H.; Wang, Z. L. *Mater. Today* **2017,** *20,* 501–506. doi:10.1016/j.mattod.2017.08.027
32. Chen, X.; Pu, X.; Jiang, T.; Yu, A.; Xu, L.; Wang, Z. L. *Adv. Funct. Mater.* **2017,** *27,* 1603788. doi:10.1002/adfm.201603788
33. Deng, W.; Zhou, Y.; Zhao, X.; Zhang, S.; Zou, Y.; Xu, J.; Yeh, M.-H.; Guo, H.; Chen, J. *ACS Nano* **2020,** *14,* 9050–9058. doi:10.1021/acsnano.0c04113
34. Jin, L.; Xiao, X.; Deng, W.; Nashalian, A.; He, D.; Raveendran, V.; Yan, C.; Su, H.; Chu, X.; Yang, T.; Li, W.; Yang, W.; Chen, J. *Nano Lett.* **2020,** *20,* 6404–6411. doi:10.1021/acs.nanolett.0c01987
35. Khan, A. U.; Kobayashi, K.; Tang, D.-M.; Yamauchi, Y.; Hasegawa, K.; Mitome, M.; Xue, Y.; Jiang, B.; Tsuchiya, K.; Golberg, D.; Bando, Y.; Mori, T. *Nano Energy* **2017,** *31,* 152–159. doi:10.1016/j.nanoen.2016.11.016
36. Li, Z.; Guo, L.; Yao, H.; Di, X.; Xing, K.; Tu, J.; Gu, C. *ACS Appl. Mater. Interfaces* **2020,** *12,* 33315–33324. doi:10.1021/acsami.0c10992
37. Lin, Z.; Chen, J.; Li, X.; Zhou, Z.; Meng, K.; Wei, W.; Yang, J.; Wang, Z. L. *ACS Nano* **2017,** *11,* 8830–8837. doi:10.1021/acsnano.7b02975
38. Lu, L.; Ding, W.; Liu, J.; Yang, B. *Nano Energy* **2020,** *78,* 105251. doi:10.1016/j.nanoen.2020.105251
39. Meng, K.; Zhao, S.; Zhou, Y.; Wu, Y.; Zhang, S.; He, Q.; Wang, X.; Zhou, Z.; Fan, W.; Tan, X.; Yang, J.; Chen, J. *Matter* **2020,** *2,* 896–907. doi:10.1016/j.matt.2019.12.025
40. Wu, M.; Zheng, T.; Zheng, H.; Li, J.; Wang, W.; Zhu, M.; Li, F.; Yue, G.; Gu, Y.; Wu, J. *J. Mater. Chem. A* **2018,** *6,* 16439–16449. doi:10.1039/c8ta05887c
41. Yan, C.; Deng, W.; Jin, L.; Yang, T.; Wang, Z.; Chu, X.; Su, H.; Chen, J.; Yang, W. *ACS Appl. Mater. Interfaces* **2018,** *10,* 41070–41075. doi:10.1021/acsami.8b14514
42. Yan, C.; Gao, Y.; Zhao, S.; Zhang, S.; Zhou, Y.; Deng, W.; Li, Z.; Jiang, G.; Jin, L.; Tian, G.; Yang, T.; Chu, X.; Xiong, D.; Wang, Z.; Li, Y.; Yang, W.; Chen, J. *Nano Energy* **2020,** *67,* 104235. doi:10.1016/j.nanoen.2019.104235
43. Yang, J.; Chen, J.; Su, Y.; Jing, Q.; Li, Z.; Yi, F.; Wen, X.; Wang, Z.; Wang, Z. L. *Adv. Mater. (Weinheim, Ger.)* **2015,** *27,* 1316–1326. doi:10.1002/adma.201404794
44. Zhang, C.; Fan, Y.; Li, H.; Li, Y.; Zhang, L.; Cao, S.; Kuang, S.; Zhao, Y.; Chen, A.; Zhu, G.; Wang, Z. L. *ACS Nano* **2018,** *12,* 4803–4811. doi:10.1021/acsnano.8b01534
45. Zhang, N.; Tao, C.; Fan, X.; Chen, J. *J. Mater. Res.* **2017,** *32,* 1628–1646. doi:10.1557/jmr.2017.162
46. Zhou, Z.; Padgett, S.; Cai, Z.; Conta, G.; Wu, Y.; He, Q.; Zhang, S.; Sun, C.; Liu, J.; Fan, E.; Meng, K.; Lin, Z.; Uy, C.; Yang, J.; Chen, J. *Biosens. Bioelectron.* **2020,** *155,* 112064. doi:10.1016/j.bios.2020.112064
47. Zou, Y.; Raveendran, V.; Chen, J. *Nano Energy* **2020,** *77,* 105303. doi:10.1016/j.nanoen.2020.105303
48. Mao, Y.; Geng, D.; Liang, E.; Wang, X. *Nano Energy* **2015,** *15,* 227–234. doi:10.1016/j.nanoen.2015.04.026
49. Mao, Y.; Zhang, N.; Tang, Y.; Wang, M.; Chao, M.; Liang, E. *Nanoscale* **2017,** *9,* 14499–14505. doi:10.1039/c7nr05222g
50. Ning, C.; Tian, L.; Zhao, X.; Xiang, S.; Tang, Y.; Liang, E.; Mao, Y. *J. Mater. Chem. A* **2018,** *6,* 19143–19150. doi:10.1039/c8ta07784c
51. Tang, Y.; Zhou, H.; Sun, X.; Diao, N.; Wang, J.; Zhang, B.; Qin, C.; Liang, E.; Mao, Y. *Adv. Funct. Mater.* **2020,** *30,* 1907893. doi:10.1002/adfm.201907893
52. Wang, L.; Lu, S.; Deng, Y.; Wu, W.; Wang, L.; Liu, Y.; Zhao, X. *J. Sci. Food Agric.* **2020,** in press. doi:10.1002/jsfa.10739
53. Wang, M.; Zhang, J.; Tang, Y.; Li, J.; Zhang, B.; Liang, E.; Mao, Y.; Wang, X. *ACS Nano* **2018,** *12,* 6156–6162. doi:10.1021/acsnano.8b02562
54. Wang, M.; Zhang, N.; Tang, Y.; Zhang, H.; Ning, C.; Tian, L.; Li, W.; Zhang, J.; Mao, Y.; Liang, E. *J. Mater. Chem. A* **2017,** *5,* 12252–12257. doi:10.1039/c7ta02680c
55. Zhang, B.; Tang, Y.; Dai, R.; Wang, H.; Sun, X.; Qin, C.; Pan, Z.; Liang, E.; Mao, Y. *Nano Energy* **2019,** *64,* 103953. doi:10.1016/j.nanoen.2019.103953
56. Tiwari, S.; Gaur, A.; Kumar, C.; Maiti, P. *Energy* **2019,** *171,* 485–492. doi:10.1016/j.energy.2019.01.043
57. Cui, X.; Zhang, H.; Cao, S.; Yuan, Z.; Ding, J.; Sang, S. *Nano Energy* **2018,** *52,* 71–77. doi:10.1016/j.nanoen.2018.07.037
58. Guo, R.; Zhang, H.; Cao, S.; Cui, X.; Yan, Z.; Sang, S. *Mater. Des.* **2019,** *182,* 108025. doi:10.1016/j.matdes.2019.108025
59. Wang, J.; Zhang, H.; Xie, Y.; Yan, Z.; Yuan, Y.; Huang, L.; Cui, X.; Gao, M.; Su, Y.; Yang, W.; Lin, Y. *Nano Energy* **2017,** *33,* 418–426. doi:10.1016/j.nanoen.2017.01.055
60. Zhang, H.; Yang, Y.; Su, Y.; Chen, J.; Adams, K.; Lee, S.; Hu, C.; Wang, Z. L. *Adv. Funct. Mater.* **2014,** *24,* 1401–1407. doi:10.1002/adfm.201302453
61. Zhao, T.; Cao, S.; Yang, S.; Guo, R.; Sang, S.; Zhang, H. *Nano Energy* **2019,** *65,* 104025. doi:10.1016/j.nanoen.2019.104025
62. Cui, X.; Zhao, T.; Yang, S.; Xie, G.; Zhang, Z.; Zhang, Y.; Sang, S.; Lin, Z.-H.; Zhang, W.; Zhang, H. *Nano Energy* **2020,** *78,* 105381. doi:10.1016/j.nanoen.2020.105381
63. Wang, M.; Zhang, J.; Tang, Y.; Li, J.; Zhang, B.; Liang, E.; Mao, Y.; Wang, X. *ACS Nano* **2018,** *12,* 6156–6162. doi:10.1021/acsnano.8b02562
64. Zhang, N.; Qin, C.; Feng, T.; Li, J.; Yang, Z.; Sun, X.; Liang, E.; Mao, Y.; Wang, X. *Nano Res.* **2020,** *13,* 1903–1907. doi:10.1007/s12274-020-2654-7

License and Terms

The definitive version of this article is the electronic one which can be found at:
https://doi.org/10.3762/bjnano.11.148

BEILSTEIN JOURNAL OF NANOTECHNOLOGY

Piezotronic effect in AlGaN/AlN/GaN heterojunction nanowires used as a flexible strain sensor

Jianqi Dong‡1, Liang Chen‡2, Yuqing Yang‡1 and Xingfu Wang*1

Full Research Paper

Open Access

Address:
[1]Institute of Semiconductor Science and Technology, South China Normal University, Guangzhou 510631, China and [2]School of Physics and Optoelectronic Engineering, Guangdong University of Technology, Guangzhou 510006, China

Email:
Xingfu Wang* - xfwang@scnu.edu.cn

* Corresponding author ‡ Equal contributors

Keywords:
AlGaN/AlN/GaN nanowires; flexible; piezotronic effect; strain sensors; strain tests; top-down method

Beilstein J. Nanotechnol. **2020,** *11,* 1847–1853.
https://doi.org/10.3762/bjnano.11.166

Received: 28 July 2020
Accepted: 10 November 2020
Published: 10 December 2020

This article is part of the thematic issue "Nanogenerators and flexible electronics".

Guest Editor: Y. Mao

Abstract

1D semiconductor nanowires (NWs) have been extensively studied in recent years due to the predominant mechanical flexibility caused by a large surface-to-volume ratio and unique electrical and optical properties induced by the 1D quantum confinement effect. Herein, we use a top-down two-step preparation method to synthesize AlGaN/AlN/GaN heterojunction NWs with controllable size. A single NW is transferred to a flexible poly(ethylene terephthalate) substrate and fixed by indium tin oxide electrodes to form an ohmic contact for the strain sensor. An external mechanical stress is introduced to study the performance of the fabricated piezotronic strain sensor. The gauge factor is as high as 30 under compressive or tensile stress, which indicates a high sensitivity of the strain sensor. Periodic strain tests show the high stability and repeatability of the sensor. The working mechanism of the strain sensor is investigated and systematically analyzed under compressive and tensile strain. Here, we describe a strain sensor that shows a great application potential in wearable integrated circuits, in health-monitoring devices, and in artificial intelligence.

Introduction

Due to the non-centrosymmetric structure of the group-III nitride semiconductor materials (e.g., GaN, AlN, and AlGaN), spontaneous polarization (P_{sp}) and piezoelectric polarization induced by lattice mismatch (P_{lm}) are inevitably introduced during the epitaxial growth process [1-3]. Furthermore, the analysis of the internal polarization of the AlGaN/AlN/GaN heterojunction showed the existence of a 2D electron gas (2DEG), which effectively suppresses the degradation of the carrier mobility caused by the scattering at charge impurity centers [4]. This is a widely discussed topic in the field of high electron mobility transistor (HEMT) research [5,6]. In order to further improve the physical properties of a 2DEG and optimize the performance of AlGaN/AlN/GaN-based HEMT devices, piezotronic effects are introduced to adjust the polarization distribution inside the heterojunction [7,8]. The piezotronic effect, described first by Zhong Lin Wang in 2007, is a combination of the piezoelectric effect and the properties of non-centrosymmetric semiconductor materials [9].

1D semiconductor nanowires (NWs) are more suitable candidates for the study of the piezotronic effect than nanofilms or bulk materials since the smaller physical size and larger surface-to-volume ratio of 1D NWs yields superior mechanical properties [4,10]. In addition, 1D semiconductor NWs can increase the electron mobility and achieve the confinement of light based on the 1D quantum confinement effect. Hence, the unique electrical and optical properties of 1D semiconductor NWs have attracted research interest from the field of nanogenerators [11-14] and NW-based strain sensors [15-19]. Strain sensors can convert mechanical deformation into electrical signals. They exhibit a potential for application in health-monitoring and motion-monitoring devices, and in artificial intelligence, for example [20-22]. However, high sensitivity (gauge factor ≥20) is key to detect a very small deformation of a given material [23,24]. Therefore, AlGaN/AlN/GaN NWs with high electron mobility, carrier density, and mechanical flexibility have become good candidates for highly sensitive and flexible strain sensors. In this work, we use a top-down two-step process, including inductively coupled plasma (ICP) dry etching and selective electrochemical (EC) wet etching, to prepare AlGaN/AlN/GaN heterojunction NWs with a controllable size. After the lift-off, a single NW is transferred to a flexible poly(ethylene terephthalate) (PET) substrate and is fixed by indium tin oxide (ITO) electrodes to form an ohmic contact for the strain sensor. Under different compressive and tensile strain values, *I–V* characteristic curves of the prepared piezotronic strain sensor show the ability of the sensor to detect strain. The gauge factor is calculated under different strain conditions. It is as high as 30 under either a −1.78% compressive strain or a 1.78% tensile strain, which shows its high sensitivity. Furthermore, the current increases with an increase in the tensile strain and decreases with an increase in the compressive strain along the *c*-axis. The current returns to its original value after release of the mechanical stress. At the same time, the multiple cycles of tensile and compressive strain testing also fully demonstrates the repeatability and stability of the strain sensors. The working principle of strain sensors is illustrated by the analysis of the polarized charge distribution under compressive and tensile strain modes. This work describes the fabrication of a highly sensitive and a highly stable strain sensor based on a new AlGaN/AlN/GaN NW structure, which has a great potential to be applied in wearable integrated circuits, health-monitoring devices, artificial intelligence, among other fields.

Results and Discussion

The epitaxial structures used in this study were synthesized by metal-organic chemical vapor deposition (MOCVD), as shown in Figure 1a. First, 1 µm of an unintentionally doped GaN layer was deposited onto a sapphire substrate. Then, 500 nm of n-type GaN, as a current-spreading layer, was deposited to increase the lateral spreading of the current. Next, 500 nm of an unintentionally doped GaN layer was deposited to protect the lower layer

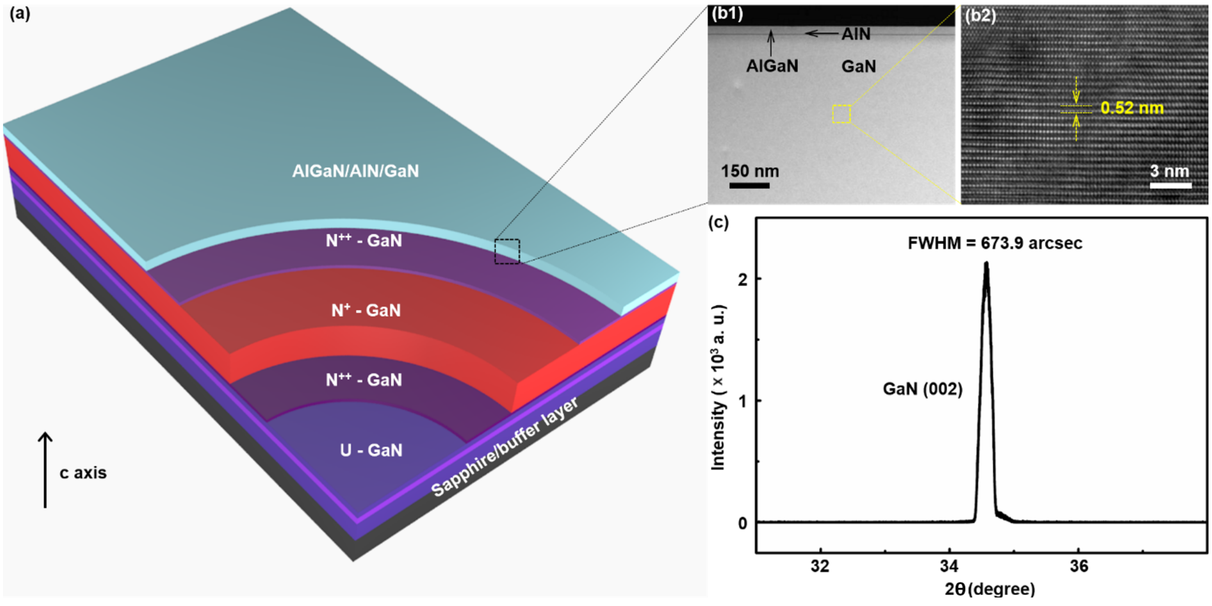

Figure 1: (a) Schematic diagram of the epitaxial structure. (b) STEM image taken of the AlGaN/AlN/GaN heterojunction (left panel, b1) and HRTEM image of the corresponding GaN layer (right panel, b2). (c) XRD 2θ scan of the epitaxial structure in the region of the (002) reflection.

during the selective EC etching. A heavily doped GaN (N^+-GaN) sacrificial layer, sandwiched by two thin N^{++}-GaN layers was inserted under the AlGaN/AlN/GaN layer to enhance the conductivity contrast. Detailed structural parameters are shown in the Experimental section.

Figure 1b shows a scanning transmission electron microscopy (STEM) image taken of the AlGaN/AlN/GaN heterojunction (left panel) and a corresponding high-resolution transmission electron microscopy (HRTEM) image of the GaN layer (right panel). It can be seen that there is a clear dividing line (ultrathin AlN layer) between AlGaN and GaN. An interplanar spacing of 0.52 nm was measured in the GaN layer along the [2] direction. Furthermore, an X-ray diffraction (XRD) scan of the epitaxial structure is shown in Figure 1c. The full width at half maximum (FWHM) of the GaN(002) reflection is approx. 673.9 arcsec, which is comparable to that of bulk GaN. These results unambiguously prove that the AlGaN/AlN/GaN heterojunction has an ultrahigh crystal quality, although it was grown onto a heavily doped GaN sacrificial layer.

The specific top-down two-step preparation process of freestanding AlGaN/AlN/GaN heterojunction NWs, including isotropic ICP dry etching and selective EC wet etching [25,26], is shown in Figure 2. First, a layer of photoresist was spin coated on the surface of the wafer from MOCVD, and advanced stepper lithography was used to form a striped pattern, which was used as a mask for ICP dry etching. The depth of the ICP dry etching needs to be greater than 1 µm (the thickness of the AlGaN/AlN/GaN heterojunction is 931.5 nm). The purpose is to expose the sacrificial layer for the subsequent EC wet etching. Then, the striped photoresist mask, which covers the surface, was removed with acetone to obtain the structure shown in Figure 2a. The settings for the stripe width (900 nm) and the interval between the stripes (3 µm) were controlled during stepper lithography.

After ICP dry etching, the sample was placed in an electrolytic cell containing 0.3 M oxalic acid solution for EC wet etching. The sacrificial layer (GaN) was dissolved during the EC wet etching to release the upper layer of the AlGaN/AlN/GaN heterojunction NWs (Figure 2b), which was transferred to the host substrate (Figure 2c). Under a suitable applied electric field, the mechanism of EC etching can be described by:

$$\mathrm{GaN} + 6h^+ \rightarrow 2\mathrm{Ga}^{3+} + \mathrm{N}_2 \uparrow .$$

The corresponding SEM images are shown in Figure 2d–f. After ICP dry etching, a regular stripe array was formed (Figure 2d) and the shape of the NWs was controlled in advance during stepper lithography. Because of its high conductivity, the heavily doped GaN preferentially reacts with the oxalic acid solution in an applied electric field. The lateral etching rates on both sides of N^+-GaN were approximately the same during EC wet etching (Figure 2e). Finally, a single NW was obtained to prepare the strain sensor (Figure 2f).

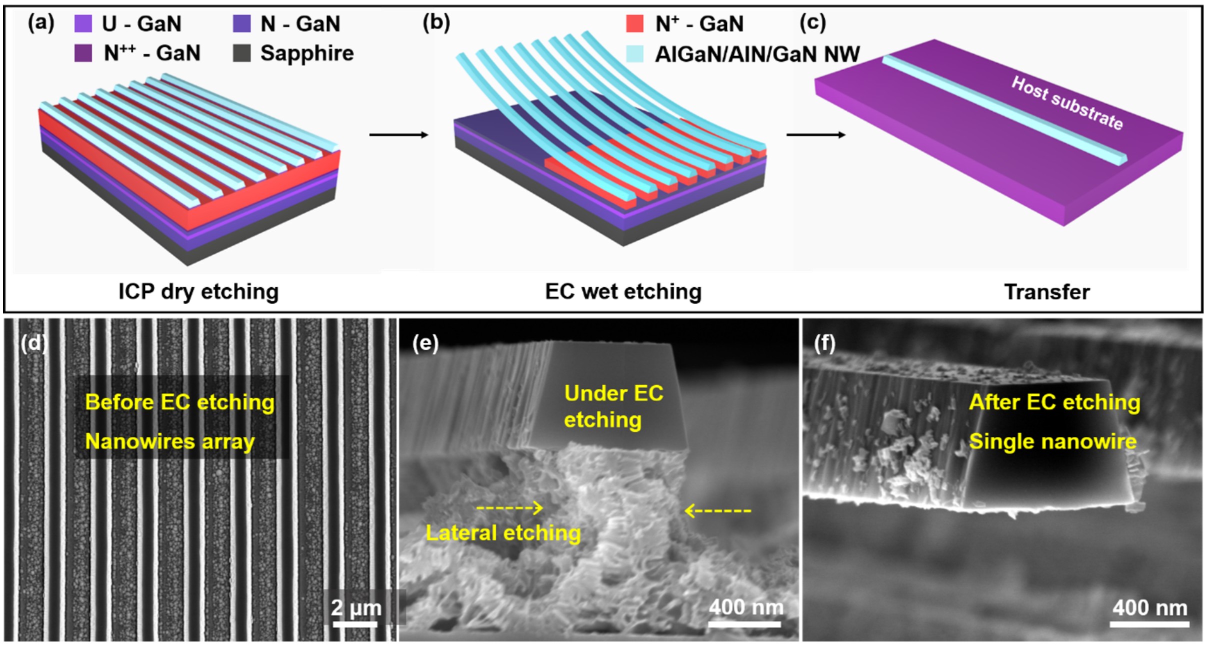

Figure 2: (a) Schematic diagrams after ICP dry etching, (b) during EC wet etching, (c) and of a single nanowire. (d) SEM image of a AlGaN/AlN/GaN heterojunction NW array after ICP dry etching. (e) SEM image during EC etching. (f) SEM image of the released NW after EC etching.

The ITO transparent electrodes were patterned and deposited onto the two ends of the AlGaN/AlN/GaN heterojunction NWs to eliminate the impact of the Schottky barrier. In addition, they fixed the NW to the flexible PET substrate. A schematic of the equipment (electric one-dimensional translation stage) for different values of compressive or tensile stress applied along the *c*-axis is shown in Figure 3a. The typical *I*–*V* curves were obtained for different strain values (Figure 3b). It can be clearly seen that, as the tensile strain increases along the *c*-axis, the current at a given voltage gradually increases. Conversely, when the compressive strain increases, the current at a given voltage gradually decreases. The mechanism regarding this behavior will be explained below. A characteristic strain–current curve was extracted from the *I*–*V* curves at a bias voltage of 1.9 V, as shown in Figure 3c. The results unambiguously show that there is a positive correlation between strain and current. Taking the current in the free state as the reference, the current increased by 53.55% at 1.78% tensile strain, whereas it decreased by approx. 53.49% at −1.78% compressive strain, showing superior strain detection ability.

The gauge factor is the key parameter describing the sensitivity of strain sensors and can be calculated using the following formula [25]:

$$\text{gauge factor} = \frac{I - I_0}{I_0 \cdot \Delta\varepsilon},$$

where I is the current in the compressive state or in the strained state and I_0 is the current when the sample is not strained. It can be seen from Figure 3d that, regardless of the strain, the gauge factor shows an increasing trend at a bias voltage of 1.9 V. At a strain of −1.78% (compressive strain) or 1.78% (tensile strain), the gauge factor is as high as 30, which enables the detection of a very small deformation. Compared with previous works [27-29], the AlGaN/AlN/GaN NW-based strain sensor has a higher

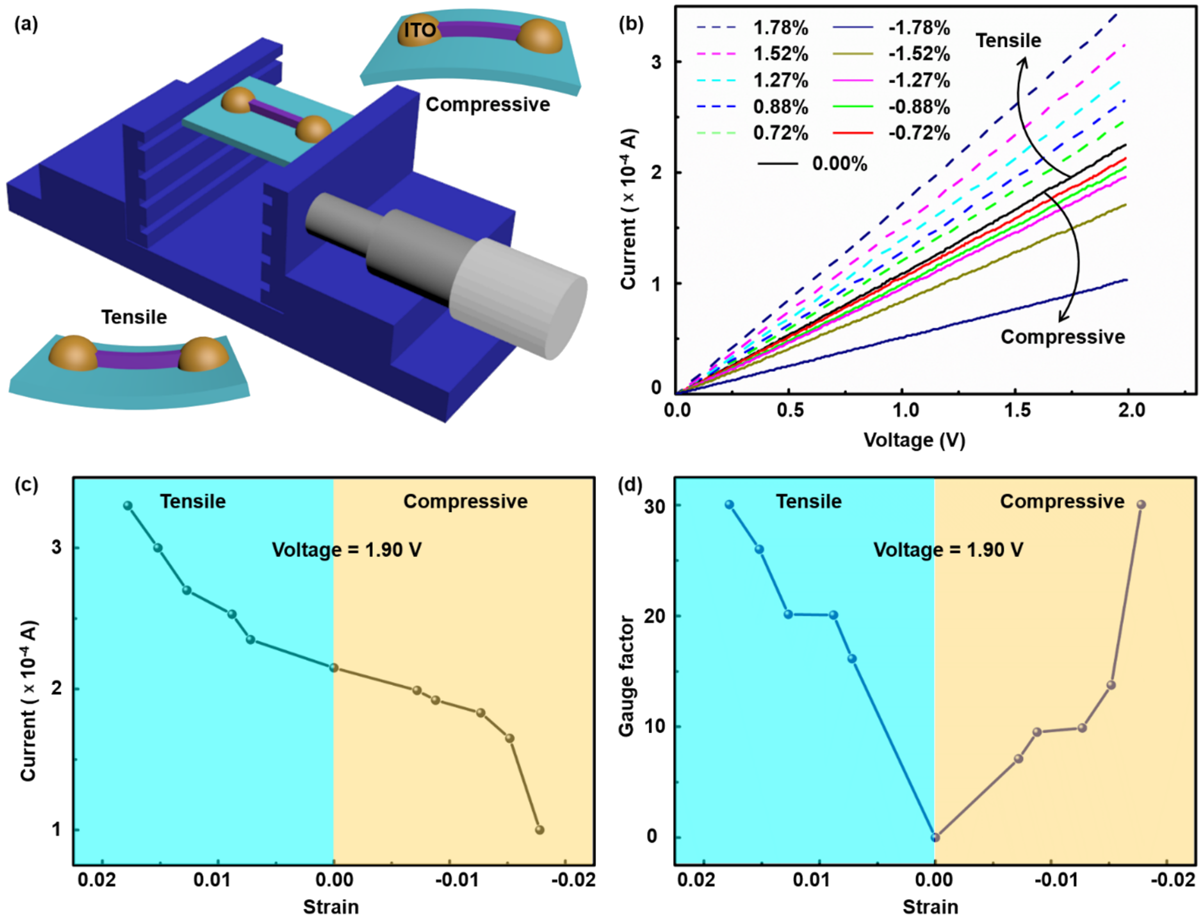

Figure 3: (a) Experimental setup showing the stress application on the AlGaN/AlN/GaN heterojunction NW-based strain sensor. (b) *I*–*V* characteristic curves at different compressive and tensile strain values along the *c*-axis. (c) The relation between current and strain at a bias voltage of 1.9 V. (d) The relation between gauge factor and strain at a bias voltage of 1.9 V.

sensitivity. The compressive strain and the tensile strain are converted to a normal strain ε by using the following formula [25,26]:

$$\varepsilon = \frac{h}{2R}.$$

Here, the PET substrate was bent to a radius R and the thickness h is based on the assumption that the strain of the PET substrate is considered as the strain of the AlGaN/AlN/GaN NW-based strain sensor.

The stability and repeatability of the AlGaN/AlN/GaN NW-based strain sensor is demonstrated in Figure 4. Tensile and compressive stress was repeatedly applied and released. At a bias voltage of 0.2 V, the output current increased with the increase in the tensile strain. The output current went back to the initial value when the stress was continuously released (Figure 4a). Conversely, at a bias voltage of 0.1 V, the output current continuously decreased until a −1.78% compressive strain value was reached. Then, it gradually returned to the initial value (Figure 4b). The results show that the strain influences the transmission of carriers and the output current signal even under small bias voltage and strain values, which further demonstrates the sensitivity and stability of the strain sensor. A test with five cycles of repetitive mechanical load and unload was carried out, as shown in Figure 4c. The results demonstrate that the strain sensor still has a superior performance after multiple cycles at 0.88% tensile strain, which indicates its stability.

The polarization charge distribution of the AlGaN/AlN/GaN heterojunction NW under different strain conditions is shown in Figure 5. This model depicts the working mechanism of the strain sensor. Due to the non-centrosymmetric structure of nitride semiconductor materials, P_{sp} and P_{lm} can occur. The direction of polarization (shown in Figure 5b), $P_{\mathrm{sp}}^{\mathrm{GaN}}$, $P_{\mathrm{sp}}^{\mathrm{AlGaN}}$, and P_{lm} are along the negative direction of the c-axis. That is, the positive polarization charges are gathered on the $-c$ plane whereas the negative polarization charges are generated on the $+c$ plane. At the heterojunction interface, the positive polarization charge on the bottom surface of AlGaN couples with the negative polarization charge on the top surface of GaN, resulting in a positive net polarization charge. This results in the attraction of free electrons in the GaN layer, which gather on the GaN side and form a 2DEG [4]. The 2DEG at the heterojunction interface has a higher electron mobility (1.2×10^3 cm^2·V^{-1}·s^{-1}) and sheet density (8.6×10^{12} cm^{-2}),

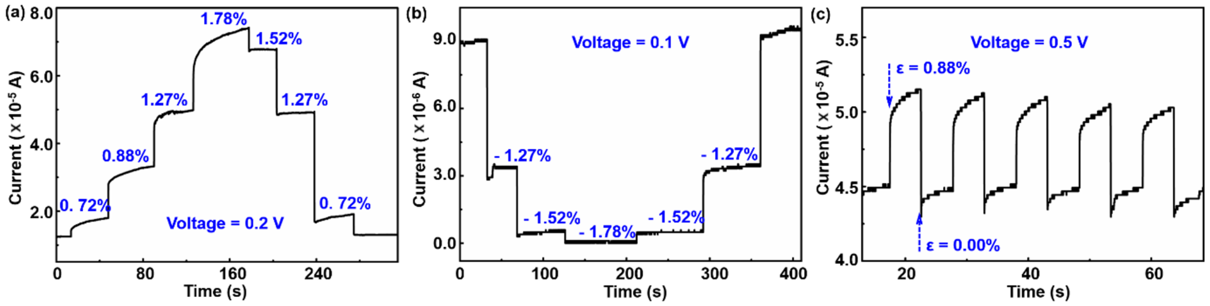

Figure 4: (a) *I*–*t* characteristic curve at a bias voltage of 0.2 V under tensile strain. (b) *I*–*t* characteristic curve at a bias voltage of 0.1 V under compressive strain. (c) *I*–*t* characteristic curve under periodic tensile straining to 0.88%.

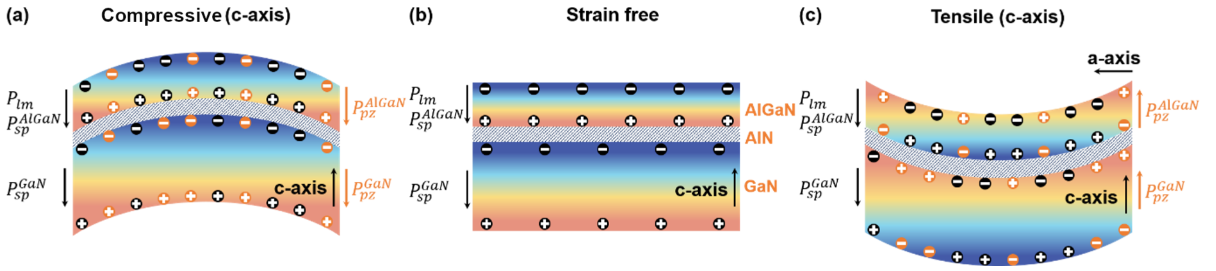

Figure 5: Structure diagram showing the charge distribution of the AlGaN/AlN/GaN heterojunction NW under compressive strain (a), without strain (b), and under tensile strain (c). The black color represents the inherent polarization and the charge generated by the inherent polarization, whereas the orange color represents the piezoelectric polarization and the charge generated by the piezoelectric polarization.

values obtained from the Hall test, which greatly improves the performance of the AlGaN/AlN/GaN heterojunction NW-based strain sensor.

In Figure 5a, the AlGaN/AlN/GaN heterojunction NW under compressive strain (c-axis) generated a piezoelectric polarization along the negative direction of the *c* axis, which resulted in a negative piezoelectric charge on the +*c*-plane of the GaN layer. The corresponding net polarization charge at the heterojunction interface decreases, resulting in a decrease in the density of the 2DEG. Therefore, as the compressive strain (c-axis) increases, the output current gradually decreases, which is consistent with the experimental results obtained (Figure 3). On the contrary, under tensile strain (*c*-axis), the direction of the piezoelectric polarization is along the positive direction of the *c*-axis, and positive piezoelectric polarization charges are generated on the +*c*-plane of GaN. Therefore, the net polarization charge at the heterojunction interface increases, resulting in an increase in the density of the 2DEG and a corresponding increase in the output current (Figure 5c and Figure 3). The results show that mechanical strain changes the concentration of the 2DEG at the heterojunction interface by changing the polarization charge distribution. This, in turn, influences the output current signal of the piezotronic strain sensor.

Conclusion

AlGaN/AlN/GaN heterojunction NWs with controllable size were prepared by a top-down two-step process, including ICP dry etching and selective EC wet etching. After the lift-off, a single NW was transferred to a flexible PET substrate and was fixed by ITO electrodes to form an ohmic contact for the strain sensor. We have introduced the piezotronic effect to adjust the carrier transmission and the output current under the action of an applied stress. The output current increased with an increasing tensile strain, decreased with an increasing compressive strain, and went back to the initial value after the release of either the compressive or the tensile strain, which shows the strain detection ability of the device. The gauge factor was calculated under different strain conditions. It was as high as 30 under either a −1.78% compressive strain or a 1.78% tensile strain, which shows the high sensitivity of the sensor. Furthermore, multiple cycles of tensile stress–release testing also fully demonstrated the repeatability and stability of the strain sensor. The working principle model of the strain sensor was illustrated by the polarized charge distribution under compressive or under tensile strain. This work describes a highly sensitive and a highly stable strain sensor based on a new AlGaN/AlN/GaN NW structure, which has shown great application potential in several fields, including wearable integrated circuits, health-monitoring devices, and artificial intelligence.

Experimental

Synthesis of the epitaxial structure

The epitaxial structure used in this study was grown by MOCVD (Thomas Swan). Trimethylgallium (TMGa), trimethylaluminum (TMAl), and ammonia (NH_3) were used as Ga, Al, and N sources, respectively. N_2 and H_2 were used as carrier gases in the growth process. A 1 μm layer of unintentionally doped GaN was deposited as the buffer layer on a sapphire substrate, followed by a 500 nm layer of Si-doped N-GaN (the doping concentration was $5 \times 10^{18} \cdot \mathrm{cm}^{-3}$). The thickness of the heavily doped GaN was 1.5 μm and the Si doping concentration was $1.0 \times 10^{19} \cdot \mathrm{cm}^{-3}$. The thickness of the two thin N^{++}-GaN layers was only 10 nm each with a Si concentration of 4.5×10^{19} cm^{-3}. The thickness values of U-GaN, U-AlN, and U-$Al_{0.3}Ga_{0.7}N$ were 900 nm, 1.5 nm, and 30 nm, respectively.

Preparation of the AlGaN/AlN/GaN NW-based strain sensor

First, stepper lithography was used to form NW stripes with a controllable size. Here, we set the stripe width to 900 nm and the stripe spacing to 3 μm. Then, the wafer was etched by ICP. The etching depth reached the heavily doped GaN to expose the sacrificial layer for EC wet etching. Next, the wafer was laser-cut into a rectangular sample, where the NWs were aligned parallel to the long sides. One end of the sample was coated with a silver paste and connected to the anode of the electrolytic cell, and the cathode was the Pt sheet. Oxalic solution (0.3 M) was used as the electrolyte. The applied voltage was 20 V and the duration of its application was 10 min. After selective EC wet etching, the sample with suspended NWs was placed in deionized water to remove the etching residues. Then, the cleaned and dried NWs were electrostatically adsorbed onto a PET substrate in order to print and fix on the pre-cured host substrate, such as another PET substrate or room-temperature-vulcanizing silicone (RTV) substrate. Herein, a single AlGaN/AlN/GaN NW was transferred to a flexible PET substrate, and ITO electrodes were prepared by magnetron sputtering on both ends of the NW to form an ohmic contact.

Measurements

The selective EC etching process and the morphology of the NWs were imaged using an optical microscope (Leica DM2500M), an SEM (ZEISS Ultra 55), and a TEM (JEM-2100HR, JEM-1400 PLUS). The *I–V* characteristic curves were measured using a source table including a SR570 low-noise current preamplifier and a DS345 function generator.

Funding

This research was supported by the Science and Technology Program of Guangzhou (No. 2019050001), the Innovation Project of Graduate School of South China Normal University (2019LKXM032), the National Natural Science Foundation of China (Grant No. 11804103), and the GuangdongNaturalScienceFoundation for DistinguishedYoungScholars (Grant No. 2018B030306048).

ORCID® iDs

Xingfu Wang - https://orcid.org/0000-0001-7450-6723

References

1. Leach, J. H.; Wu, M.; Ni, X.; Li, X.; Özgür, Ü.; Morkoç, H. *Phys. Status Solidi A* **2010,** *207,* 211–216. doi:10.1002/pssa.200925362
2. Tanaka, A.; Choi, W.; Chen, R.; Dayeh, S. A. *Adv. Mater. (Weinheim, Ger.)* **2017,** *29,* 1702557. doi:10.1002/adma.201702557
3. Shin, D.; Roy, S.; Watkins, T. R.; Shyam, A. *Comput. Mater. Sci.* **2017,** *138,* 149–159. doi:10.1016/j.commatsci.2017.06.021
4. Wang, X.; Yu, R.; Jiang, C.; Hu, W.; Wu, W.; Ding, Y.; Peng, W.; Li, S.; Wang, Z. L. *Adv. Mater. (Weinheim, Ger.)* **2016,** *28,* 7234–7242. doi:10.1002/adma.201601721
5. Lu, J. Y.; Grafendorfer, T.; Zhang, T.; Vasanawala, S.; Robb, F.; Pauly, J. M.; Scott, G. C. *IEEE Trans. Med. Imaging* **2016,** *35,* 2558–2567. doi:10.1109/tmi.2016.2586053
6. Liu, T.; Jiang, C.; Huang, X.; Du, C.; Zhao, Z.; Jing, L.; Li, X.; Han, S.; Sun, J.; Pu, X.; Zhai, J.; Hu, W. *Nano Energy* **2017,** *39,* 53–59. doi:10.1016/j.nanoen.2017.06.041
7. Zhu, J.; Zhou, X.; Jing, L.; Hua, Q.; Hu, W.; Wang, Z. L. *ACS Nano* **2019,** *13,* 13161–13168. doi:10.1021/acsnano.9b05999
8. Chang, T.-H.; Xiong, K.; Park, S. H.; Yuan, G.; Ma, Z.; Han, J. *Sci. Rep.* **2017,** *7,* 6360. doi:10.1038/s41598-017-06957-8
9. Wang, Z. L. *Adv. Mater. (Weinheim, Ger.)* **2007,** *19,* 889–892. doi:10.1002/adma.200602918
10. Zhang, B.; Tang, Y.; Dai, R.; Wang, H.; Sun, X.; Qin, C.; Pan, Z.; Liang, E.; Mao, Y. *Nano Energy* **2019,** *64,* 103953. doi:10.1016/j.nanoen.2019.103953
11. Mao, Y.; Geng, D.; Liang, E.; Wang, X. *Nano Energy* **2015,** *15,* 227–234. doi:10.1016/j.nanoen.2015.04.026
12. Mao, Y.; Zhang, N.; Tang, Y.; Wang, M.; Chao, M.; Liang, E. *Nanoscale* **2017,** *9,* 14499–14505. doi:10.1039/c7nr05222g
13. Wang, M.; Zhang, N.; Tang, Y.; Zhang, H.; Ning, C.; Tian, L.; Li, W.; Zhang, J.; Mao, Y.; Liang, E. *J. Mater. Chem. A* **2017,** *5,* 12252–12257. doi:10.1039/c7ta02680c
14. Tang, Y.; Zhou, H.; Sun, X.; Feng, T.; Zhao, X.; Wang, Z.; Liang, E.; Mao, Y. *J. Mater. Sci.* **2020,** *55,* 2462–2470. doi:10.1007/s10853-019-04095-2
15. Zhang, S.; Yen, S.-C.; Xiang, Z.; Liao, L.-D.; Kwong, D.-L.; Lee, C. *J. Microelectromech. Syst.* **2015,** *24,* 1303–1313. doi:10.1109/jmems.2015.2417678
16. Zhang, S. S.; Wang, T.; Lou, L.; Tsang, W. M.; Sawada, R.; Kwong, D.-L.; Lee, C. *J. Microelectromech. Syst.* **2014,** *23,* 1396–1407. doi:10.1109/jmems.2014.2313635
17. Lou, L.; Yan, H.; Park, W.-T.; Kwong, D.-L.; Lee, C. *IEEE Trans. Electron Devices* **2012,** *59,* 3097–3103. doi:10.1109/ted.2012.2214440
18. Lou, L.; Park, W.-T.; Zhang, S.; Lim, L. S.; Kwong, D.-L.; Lee, C. *IEEE Electron Device Lett.* **2011,** *32,* 1764–1766. doi:10.1109/led.2011.2169931
19. Tang, Y.; Zhou, H.; Sun, X.; Diao, N.; Wang, J.; Zhang, B.; Qin, C.; Liang, E.; Mao, Y. *Adv. Funct. Mater.* **2020,** *30,* 1907893. doi:10.1002/adfm.201907893
20. Choi, J.-H.; No, Y.-S.; So, J.-P.; Lee, J. M.; Kim, K.-H.; Hwang, M.-S.; Kwon, S.-H.; Park, H.-G. *Nat. Commun.* **2016,** *7,* 11569. doi:10.1038/ncomms11569
21. Wang, M.; Zhang, J.; Tang, Y.; Li, J.; Zhang, B.; Liang, E.; Mao, Y.; Wang, X. *ACS Nano* **2018,** *12,* 6156–6162. doi:10.1021/acsnano.8b02562
22. Zhao, X.; Hua, Q.; Yu, R.; Zhang, Y.; Pan, C. *Adv. Electron. Mater.* **2015,** *1,* 1500142. doi:10.1002/aelm.201500142
23. Yang, T.; Jiang, X.; Zhong, Y.; Zhao, X.; Lin, S.; Li, J.; Li, X.; Xu, J.; Li, Z.; Zhu, H. *ACS Sens.* **2017,** *2,* 967–974. doi:10.1021/acssensors.7b00230
24. Jiang, Y.; Liu, Z.; Matsuhisa, N.; Qi, D.; Leow, W. R.; Yang, H.; Yu, J.; Chen, G.; Liu, Y.; Wan, C.; Liu, Z.; Chen, X. *Adv. Mater. (Weinheim, Ger.)* **2018,** *30,* 1706589. doi:10.1002/adma.201706589
25. Chen, L.; Zhang, K.; Dong, J.; Wang, B.; He, L.; Wang, Q.; He, M.; Wang, X. *Nano Energy* **2020,** *72,* 104660. doi:10.1016/j.nanoen.2020.104660
26. Jiang, J.; Wang, Q.; Wang, B.; Dong, J.; Li, Z.; Li, X.; Zi, Y.; Li, S.; Wang, X. *Nano Energy* **2019,** *59,* 545–552. doi:10.1016/j.nanoen.2019.02.066
27. Duan, Z.; Jiang, Y.; Wang, S.; Yuan, Z.; Zhao, Q.; Xie, G.; Du, X.; Tai, H. *ACS Sustainable Chem. Eng.* **2019,** *7,* 17474–17481. doi:10.1021/acssuschemeng.9b04690
28. Yamada, T.; Hayamizu, Y.; Yamamoto, Y.; Yomogida, Y.; Izadi-Najafabadi, A.; Futaba, D. N.; Hata, K. *Nat. Nanotechnol.* **2011,** *6,* 296–301. doi:10.1038/nnano.2011.36
29. Cheng, Y.; Wang, R.; Sun, J.; Gao, L. *Adv. Mater. (Weinheim, Ger.)* **2015,** *27,* 7365–7371. doi:10.1002/adma.201503558

License and Terms

The definitive version of this article is the electronic one which can be found at:
https://doi.org/10.3762/bjnano.11.166

BEILSTEIN JOURNAL OF NANOTECHNOLOGY

Paper-based triboelectric nanogenerators and their applications: a review

Jing Han‡[1,2], Nuo Xu‡[1,3], Yuchen Liang[1,4], Mei Ding[5], Junyi Zhai[1,2,3], Qijun Sun*[1,2,3] and Zhong Lin Wang*[1,2,6]

Review

Open Access

Address:
[1]Beijing Institute of Nanoenergy and Nanosystems, Chinese Academy of Sciences, Beijing, 101400, P. R. China, [2]School of Nanoscience and Technology, University of Chinese Academy of Sciences, Beijing, 100049, P. R. China, [3]Center on Nanoenergy Research, School of Physical Science and Technology, Guangxi University, Nanning, 530004, P. R. China, [4]Qichen (Shanghai) Medical Co., Ltd., Shanghai 201319, P. R. China, [5]College of Materials Science and Engineering, Changsha University of Science & Technology, Changsha, 410114, P. R. China and [6]School of Materials Science and Engineering, Georgia Institute of Technology, Atlanta, Georgia 30332-0245, United States

Email:
Qijun Sun* - sunqijun@binn.cas.cn;
Zhong Lin Wang* - zhong.wang@mse.gatech.edu

* Corresponding author ‡ Equal contributors

Keywords:
energy harvesting; interaction; Internet of Things (IoT); paper-based sensors; self-powered devices; P-TENGs; triboelectric nanogenerator

Beilstein J. Nanotechnol. **2021,** *12,* 151–171.
https://doi.org/10.3762/bjnano.12.12

Received: 29 October 2020
Accepted: 30 December 2020
Published: 01 February 2021

This article is part of the thematic issue "Nanogenerators and flexible electronics".

Guest Editor: Y. Mao

Abstract

The development of industry and of the Internet of Things (IoTs) have brought energy issues and huge challenges to the environment. The emergence of triboelectric nanogenerators (TENGs) has attracted wide attention due to their advantages, such as self-powering, lightweight, and facile fabrication. Similarly to paper and other fiber-based materials, which are biocompatible, biodegradable, environmentally friendly, and are everywhere in daily life, paper-based TENGs (P-TENGs) have shown great potential for various energy harvesting and interactive applications. Here, a detailed summary of P-TENGs with two-dimensional patterns and three-dimensional structures is reported. P-TENGs have the potential to be used in many practical applications, including self-powered sensing devices, human–machine interaction, electrochemistry, and highly efficient energy harvesting devices. This leads to a simple yet effective way for the next generation of energy devices and paper electronics.

Introduction

Environmental pollution is an undeniable fact in our daily lives. The air pollution caused by industrial waste generation (gases/toxins) and by the combustion of fossil fuels is getting more and more serious [1,2]. Meanwhile, with the rapid growth of the Internet of Things (IoTs), the explosive growth of sensors has led to the massive use of batteries, which have also resulted in severe environmental issues in virtue of their short lifetime. In this regard, renewable energy sources, such as wind, wave, and solar power, appear to be the most efficient and effective solutions [3-10]. However, the infrastructure constructions for harvesting energy from renewable sources (e.g., wind power stations and solar photovoltaic energy systems) are huge, expensive, and take a long time to be built. Even worse, harvested wind and solar energy cannot be incorporated into the power grid, which inevitably calls for additional energy storage facilities [11-13]. Therefore, there are still increasing demands for the development of power sources which are highly efficient, clean, and sustainable.

In recent years, the triboelectric nanogenerator (TENG), first invented by the Wang group in 2012 [14], has been quickly developed to be a revolutionary breakthrough in the energy harvesting [15-21] and self-powered systems [22-27]. Based on electrostatic induction and triboelectrification [28], the novel TENG can utilize the Maxwell's displacement current to readily drive electrons to flow through an external circuit and power portable electronic devices. To harvest the ubiquitous mechanical energy from its surroundings, TENGs need to have a simple device design and to be low cost and lightweight. TENGs have also shown the pivotal ability to convert low-frequency mechanical energy from walking, waving, and eye-blinking into electricity. TENGs can readily serve as a sustainable power supply based on four basic operation modes [29], including vertical contact–separation mode [30-32], lateral-sliding mode [33-35], single-electrode mode [36,37], and freestanding triboelectric-layer mode [38]. As an advanced and durable energy source, TENGs have shown promising and significant features that are applied to power units in the micro- and nanoscale [39-44], high-voltage sources [45], self-powered systems [46-50], and blue energy harvesting devices [51-56].

Paper, by far one of the most inexpensive and flexible materials widely used in daily life, was developed more than 2000 years ago in China. Paper and other fiber-based materials are integral components of many objects that are used on a regular basis by the population, which are also available in different compositions, thickness and surface roughness. Most importantly, paper is biocompatible, biodegradable, and environmentally friendly, and has tremendous advantages over the majority of other materials (e.g., it is lightweight, renewable, and air-permeable). Besides, paper is flexible and can be easily folded or bent into 3D structures without causing structural damage.

In the last decades, paper-based electronic devices, such as microfluidic paper-based analytical devices (µPADs) [57-60] and thin-film transistors (TFTs) [61-65] have been widely investigated. Recently, they have also been applied in various energy-related devices [66-68]. Although paper is intrinsically insulating, conductive materials (e.g., metal nanowires, conducting polymers, carbon nanotube (CNT) inks, multiwall carbon nanotube (MWCNT) inks, and reduced graphene oxide) [69-82], can be easily absorbed or used as a coating layer on the surface of the paper due to its wettability and moisture-retention capacity. This provides an efficient method to prepare paper electrodes for TENGs. Paper has also been proven to be a natural TENG friction layer. Due to that, it shows a tendency of easily losing electrons (i.e., electropositive) when contacting a material that can easily gain electrons (i.e., electronegative). Furthermore, due to the high roughness and porous nanofiber structure it can lead to enhanced TENG output performances owing to improved charge-trapping abilities.

Based on the above advantages and conveniences, paper-based TENGs (P-TENGs) have exhibited great potential for many practical applications, leading to a simple yet effective way for the next generation of energy devices and paper electronics. In this review, we try to look back and summarize the latest developments in the field of P-TENGs. Figure 1 schematically shows the theme of this review article and several typical examples in which P-TENGs are used. This paper starts with an overview of TENGs and the corresponding working mechanism of four basic working modes based on charge transfer and on the electron-cloud potential-well model. Regarding surface modification and fabrication methods involving paper, we then highlight the strategies to improve the output performance of P-TENGs. In another section, we give a detailed review on the application of P-TENGs, with two-dimensional patterns and three-dimensional structures, on self-powered sensing devices, human–machine interaction, electrochemistry and highly efficient energy-harvesting systems. To conclude the review, perspectives and proposals regarding future potential applications and research directions are discussed.

Review

Four working modes of TENGs and charge-transfer mechanisms

TENGs, which are emerging and efficient apparatus for energy conversion, have been attracting significant attention from the fields of energy harvesting and self-powered systems. The triboelectric effect [83-85], a type of contact-induced electrification, is the basis of TENGs. It was found that when two different materials are in physical contact, their interfaces become electrically charged. Due to contact electrification (CE, or triboelectrification) [86], opposite charges will be induced when the two materials are separated by a mechanical force, which will correspondingly generate a potential difference between the two materials due to electrostatic induction. If an electrical load is connected through an external circuit, the previously induced potential difference will drive the electrons to flow between

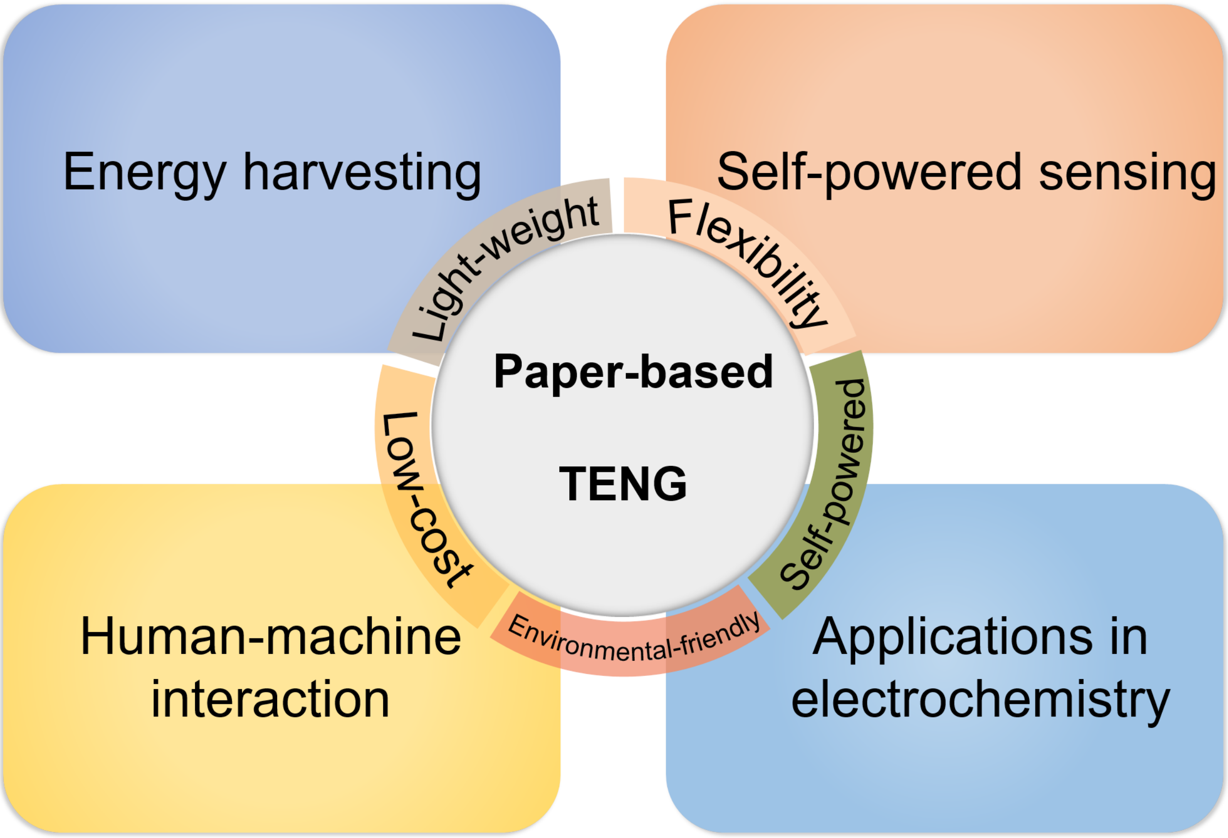

Figure 1: P-TENGs and their applications.

the two materials (through the electrodes and the external circuit). Depending on the circuit configurations and on the variations in the polarization direction, TENGs can have four working modes [87], including vertical contact–separation (CS) mode, in-plane lateral-sliding (LS) mode, single-electrode (SE) mode, and freestanding triboelectric-layer (FT) mode, as shown in Figure 2a.

In the vertical CS mode, a stack of two dielectric films is plated with a metal electrode at the back surface of each layer. When the two dielectric films are vertically separated and periodically contacted due to the application of external forces, a small air gap is formed in the middle and a potential difference is induced between the two electrodes, which can drive the forward/reverse flow of charges via the external circuit. The in-plane LS

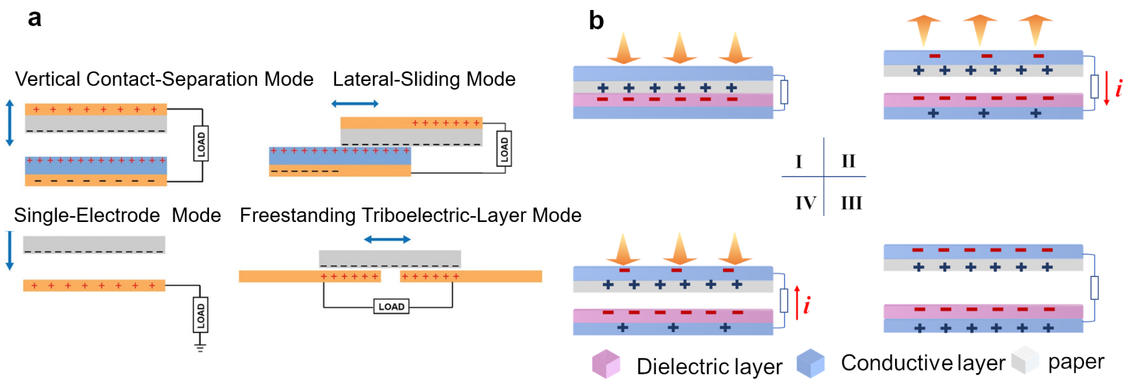

Figure 2: (a) Four working modes of TENGs [87]. Copyright © 2018 WILEY-VCH Verlag GmbH & Co. KGaA, Weinheim. Adapted with permission from Changsheng Wu et al., “Triboelectric Nanogenerator: A Foundation of the Energy for the New Era”, Advanced Energy Materials, John Wiley and Sons. (b) Working mechanism of a TENG based on the vertical contact–separation mode.

mode relies on the relative slippage between the two materials in a horizontal direction parallel to the surface. An alternating current output can be produced during the sliding motions between the top and the bottom layers. This kind of slippage is also common in a variety of rotation-induced sliding modes, which exhibit huge potential for application in high-output TENG devices. Compared with the vertical CS mode and the in-plane LS mode, the SE mode has only one electrode at the bottom, which is connected to ground and taken as the reference electrode. The direction of the induced electric field can be reversely changed during the approximation or separation between the bottom electrode and the upper dielectric materials. The charge exchange will occur between the bottom electrode and ground to balance the induced potential variation. The application scenarios of TENGs with an SE mode are broad, including direct finger/hand/skin touch or body motions. The FT mode uses two unconnected symmetrical electrodes as the reference electrodes. When the top free-standing (i.e., noncontact) dielectric layer moves from one electrode to the other, electrostatic charges will be induced on the two electrodes in sequence. Similar to the SE mode, if one takes one electrode as the reference electrode, the induced charges will flow from the reference electrode to the other electrode through the external load. Thus, the electrical output is induced by the asymmetric charge distribution during the suspending (forward/backward) movements.

Based on the combination effect of triboelectrification and electrostatic induction, the working mechanisms of the four operational modes of TENGs are similar. Taking P-TENGs in the CS mode (most common design in previous works) as a typical representative example, we further systematically analyze the working mechanism of the detailed charge-transfer process. Figure 2b elucidates the charge generation and the electron-transfer process at the friction interfaces (paper/the other dielectric layer) and electrodes (upper/bottom electrode) during one contact–separation cycle of P-TENGs. The electrification occurs at the interfaces between the paper and the other dielectric layer owing to different electronegativities when they come into contact. Different triboelectric charges (positive and negative charges) are induced by the same amount on the surfaces of the friction layers. As there is no electric potential at this stage, there is no electron transfer between the two conductive layers (Figure 2b-I). When the two friction layers start to separate along the vertical direction, opposite charges are induced in the upper and lower conductive electrodes owing to electrostatic induction (Figure 2b-II). As the distance between the two layers increases, the electric potential difference between the two layers enhances, driving the electrons to flow through the external load which generates an instantaneous current. When the two layers are separated by a maximum distance, the positive and negative triboelectric charges become fully equilibrated, resulting in no current flow through the load (Figure 2b-III). When the two layers approach each other, the electrostatic charges are induced and accumulate again, driving the electrons to flow through the load between the two conductive layers in a reverse direction (Figure 2b-IV). Finally, the two friction layers become fully in contact and the whole system returns to the initial state. At this stage, the triboelectric charges are completely balanced and there is no output current.

Although the origin of the contact electrification has been a matter of debate for a long time, no conclusive model to explain this phenomenon has been proposed. Previous studies investigated whether the electron or ion transfer were dominant in the contact-electrification phenomenon. However, the results were highly controversial [88,89]. Xu et al. [90] have proposed that the quantification of the surface charge density at different temperature values is a critical method for investigating this phenomenon. This can be readily explored as an effective tool to identify the transferred charges and the corresponding CE mechanism in TENGs. The results shown in [90] suggest that the electron transfer dominates the CE process. The charge retention ability is attributed to the intrinsic potential barrier heights of the different materials, which can prevent the charge dissipation. As the CE behavior is dependent on the surrounding temperature, Xu et al. [91] have further explored the operation of TENGs at high temperature values. Their results reveal that the thermionic emission of electrons is the main reason for CE and the atomic thermal vibrations strongly influence the CE at increased temperature values.

To better demonstrate the electron-transfer mechanism, which is dominant in CE, Xu et al. have proposed an electron-cloud potential-well model (Figure 3). At the initial state, since the highest occupied energy levels of the two materials (A and B) are different and the individual electron clouds of the materials are separated by a distance *d*, the electrons cannot be transferred between material A and material B. The trapping effect of the potential wells prevents the electrons from escaping (Figure 3-i). Once the material A comes into contact with the material B, their electron clouds collide with one another to form ionic or covalent bonds. The overlap between the electron clouds enable the electrons to spontaneously flow from material A to material B (Figure 3-ii). The majority of the transferred electrons will remain in B even if the material A is separated from the material B by an enlarged energy barrier. This leads to A and B being positively and negatively charged, respectively (Figure 3-iii). As the temperature rises, the transferred electrons in B tend to more easily escape from the potential well and to be thermionically emitted into the air, leading to a gradual decay of the surface charges (Figure 3-iv).

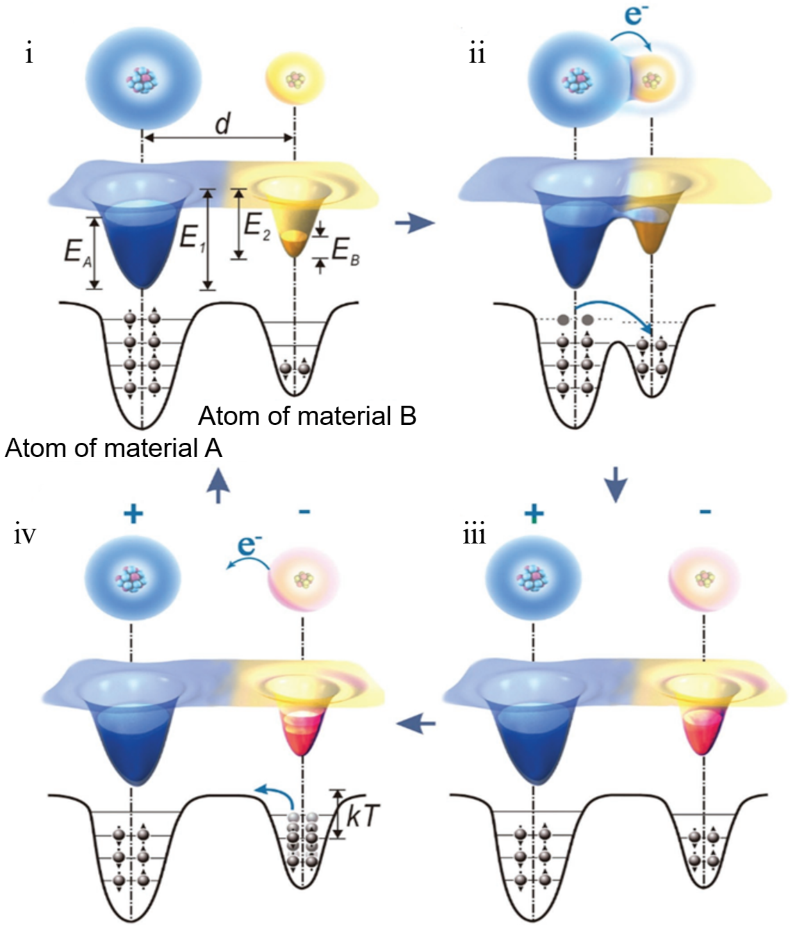

Figure 3: The proposed electron-cloud potential-well model for electron transfer, which is the dominant mechanism of contact electrification [90]. Copyright © 2018 WILEY-VCH Verlag GmbH & Co. KGaA, Weinheim. Adapted with permission from Cheng Xu et al., "On the Electron-Transfer Mechanism in the Contact-Electrification Effect", Advanced Materials, John Wiley and Sons.

Treatment methods for paper and P-TENGs

The electrical properties of paper are critical determinants of the performance of P-TENGs. The original paper structure usually does not meet all the requirements for the desired applications on P-TENG devices. Therefore, corresponding treatment processes (e.g., deposition of conductive materials by laser patterning, screen printing, spray coating, thermal deposition, surface morphology engineering, and chemical modification [46,92-98]) are often applied to convert paper into a conductive electrode or into a charge-enriched friction layer to improve P-TENG output performances. As the TENG output performance closely depends on the triboelectric polarity of the friction layer, the engineering of friction layers with more charges with an opposite polarity induces a larger triboelectric charge density. Since paper is mainly composed of cellulose, which generally shows a tendency of losing electrons (electropositive), it is preferred to pair paper with a friction material that can easily gain electrons (electronegative) according to the triboelectric series [83,99,100].

Figure 4 depicts a paper-based 3D foldable device submitted to a direct laser patterning method, which can convert ink-soaked paper substrates to multifunctional carbide/graphene (MCG) composites [92]. The composites have shown good conductivity even after repeated mechanical bending and folding tests. Moreover, the laser pattering process results in porous MCG structures (with pore sizes ranging from hundreds of nanometers to several microns), which can be used in various applications, such as mechanical energy harvesting devices, chemical sensors, and electrochemical supercapacitors.

Screen printing is a facile, efficient, high-throughput and low-cost printing method [101]. A layer of ink is scraped across the screen surface and, then, extruded through the open pores of a patterned mesh into the substrate. The printing resolution and the pattern thickness depend on the density of the mesh and on the properties of the ink, respectively. Screen printing has been widely used for fabricating conductive electrodes, semiconducting layers of solar cells, and active materials in field-

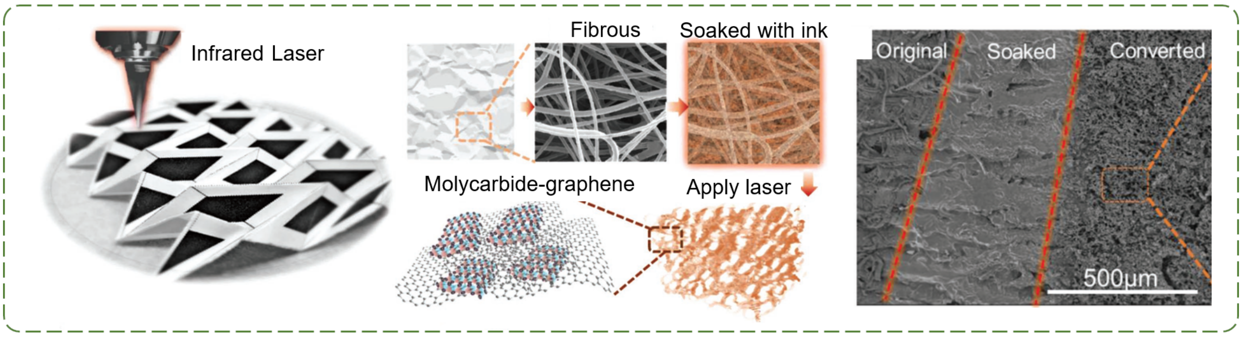

Figure 4: Treatment methods for paper and P-TENGs. Schematic illustration of a simplified MCG composite obtained by a direct laser-writing MCG-patterning process. An SEM image of a paper depicting three regions (from left to right): paper, paper soaked with a Mo–gelatin ink, and paper with converted MCG composites [92]. Copyright © 2018 WILEY-VCH Verlag GmbH & Co. KGaA, Weinheim. Adapted with permission from Xining Zang et al., “Laser-Induced Molybdenum Carbide–Graphene Composites for 3D Foldable Paper Electronics”, Advanced Materials, John Wiley and Sons.

effect transistors (FETs). It is commonly used as a planar printing technique for batch processing. It is also further adaptable to a roll-to-roll process or to rotary screen printing, which enables a facile and high-throughput printing on curved surfaces. The deposition process assisted with soft stencils is another “bottom-up” method for the preparation of functional materials on flexible and irregular surfaces. Even though P-TENGs require flexible conductive materials, metallic materials (e.g., copper, zinc, silver, and gold) are still frequently used as electrodes for flexible electronics due to their excellent electrical conductivity. By using the Kapton tape to attach soft stencils to paper, various metals can be deposited through the stencils by thermal/e-beam evaporation, sputter deposition, or spray deposition. When the stencils are peeled off they can readily leave the metallic patterns on the paper substrate [102] (Figure 5a). In comparison to the conventional printing techniques, vacuum evaporation and vacuum deposition techniques usually allow a better control over the material thickness, yielding more homogeneous structures. The vacuum evaporation is applicable to a variety of metals at a high rate of up to 50 $\text{nm}\cdot\text{s}^{-1}$; however, it requires expensive equipment and high-vacuum conditions. The sputtering can be conducted by using less expensive equipment and under lower vacuum conditions; however, the deposition speed is lower than that of the vacuum evaporation. The thickness of the metal layer obtained by e-beam deposition can be up to several micrometers, which is lower than the thickness of the metal layer obtained by sputter deposition (50–300 μm) [39]. In contrast, the spray coating/deposition with stencil is the most inexpensive process and can be applied at room temperature without any specialized equipment. Figure 5b represents an acoustic energy harvester on a paper substrate with multi-hole electrodes obtained by stencil-assisted vapor deposition [103]. The arrays of small holes with various shapes and distributions are drilled on the stencil via laser cutting, and a layer of copper with thickness of 100 nm is deposited onto the electrode via physical vapor deposition. By combining the stencil-assisted deposition and patterning methods it is possible to apply sophisticated electronic

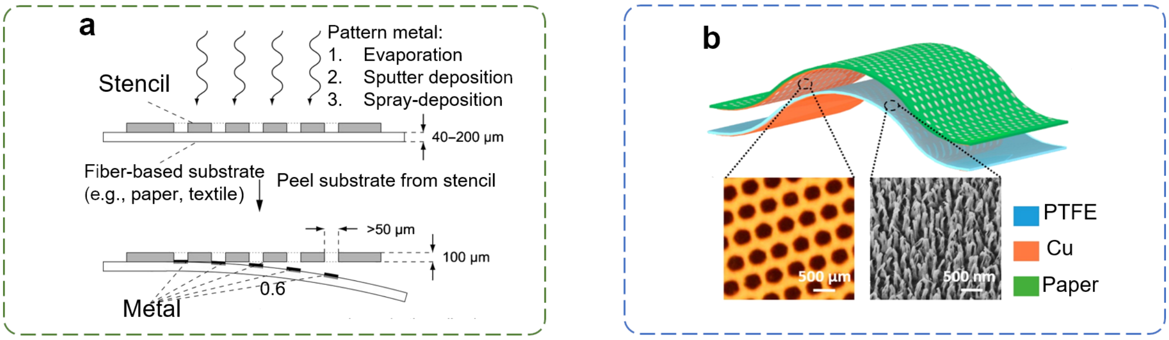

Figure 5: (a) A general scheme for fabricating an electrode on paper substrates [102]. Copyright © 2010 WILEY-VCH Verlag GmbH & Co. KGaA, Weinheim. Adapted with permission from Adam C. Siegel et al., “Foldable Printed Circuit Boards on Paper Substrates”, Advanced Functional Materials, John Wiley and Sons. (b) An acoustic energy harvester with a multi-hole paper electrode obtained by vapor deposition. Adapted with permission from [103], Copyright 2015 American Chemical Society.

devices or e-skins on flexible and arbitrary substrates [75,104-107].

The electronegativity of the friction layer is critical for the triboelectrification properties of TENGs. Surface chemical modification (to introduce electronegative or electropositive functional groups) and micro-/nanostructure engineering (to introduce charge-trapping points to facilitate charge transfer) are effective ways to modulate the electronegativity. The surface modification of the friction materials is performed to implement chemical functionalization by using various molecules [72,93,94,108-113], while surface engineering can be performed by introducing micro-/nanostructured patterns [74,92,114-121] or porous structures [97,122-124]. Feng et al. [93] modified gum wrappers with polydopamine to improve the output voltage of TENGs by approx. 3.5 times in comparison with unmodified TENGs.

Another typical method to prepare nanoscale paper with different electrical properties is by using vacuum filtration (VF) to either obtain dielectric cellulose nanofiber (CNF)- based nanoscale paper or AgNWs-casted conductive paper electrode [125]. The prepared AgNWs/CNF paper is flexible enough to be repeatedly folded and unfolded. When the number of folding/unfolding cycles increases, the sheet resistance of the AgNWs/CNF paper increases only a little, which demonstrates its superior durability and conductivity. VF is a simple and rapid method to cast functional materials onto solution-processable substrates without the need to implement any time-consuming and high-cost processes (e.g., evacuation, thermal/e-beam heating, and radio-frequency sputtering). The conductivity is also easily adjustable by changing the concentration of the conductive precursors (e.g., AgNWs, carbon nanotubes, and reduced graphene oxide).

A special nanoscale paper composed of nanocellulose, which is easy to be synthesized/chemically modified/doped, has attracted great attention in recent years. Generally, cellulose-based composites are used as the electropositive layer, while some common synthetic polymers, such as fluorinated ethylene propylene (FEP), polytetrafluoroethylene (PTFE), and poly(dimethylsiloxane) (PDMS) are used as the electronegative part. As the synthetic polymers have a smooth surface and a dense structure, which are limiting factors for the triboelectric performance of TENG devices, Chen et al. tried to introduce a nitro group into the counter cellulose friction layer to change the triboelectric polarity of cellulose with higher electron-attractive capacity [94]. The hydroxy groups in the cellulose molecules were mostly replaced by nitro groups in order to form a nitrocellulose membrane (NCM), which has a porous structure and a rough surface that improve the triboelectric performance of the constructed TENG. The P-TENGs with a NCM as the negative friction layer have maximum open-circuit voltage (V_{oc}) and short-circuit current (I_{sc}) values of 196.8 V and 31.5 μA, respectively. The NCM-based P-TENG also exhibits good stability and durability and can serve as a sustainable power source. More importantly, the utilization of nanocellulose paper offers an inexpensive, renewable, and biodegradable method to fabricate high-performance P-TENGs through a simple and environmentally friendly approach.

Geometry design of P-TENGs

Two-dimensional patterns

Due to its low cost, lightweight, flexibility, and environmentally benign properties, paper has been extensively applied in disposable and flexible electronics. It is also used to generate various structures owing to its relative toughness and rigidity. Two-dimensional patterns can have a variety of different configurations. The Li group has shown ultrasoft, cuttable and inexpensive P-TENGs for harvesting mechanical energy in various forms [126]. The main materials utilized on those P-TENGs were commercial tissue paper and silver nanowires (Ag NWs), which were key to their feasibility. The P-TENGs were built with two conductive paper pieces as the electrodes, which were sandwiched between two commercial tissue paper pieces. Three basic operation modes were proposed for those P-TENGs, considering diverse movement possibilities. These modes consisted of the vertical CS operation mode, the LS mode and the self-contact (SC) operation mode. One of the critical advantages of using P-TENGs is that the vertical CS mode and the LS mode can generate triboelectric charges with any target object materials. In the self-contact operation mode, the P-TENG is folded such that the polyvinyl chloride (PVC) side faces the paper side.

Three-dimensional structures: origami

Origami (an ancient paper-folding art) was originated in China with the invention of paper and then refined in Japan. Recently, origami has inspired the design of various devices, ranging from macroscopic structures to microscopic materials. Schenk and Guest systematically described the geometry and kinematics of folded shell and cellular metamaterials [127]. The Zhu group used an instant light-driven walking origami-inspired graphene paper to implement programmed vertical and lateral transformations and to improve the performance of many well-designed motions [128]. By using origami-inspired configurations, Yang et al. demonstrated a sophisticated P-TENG for harvesting mechanical energy from various types of human motions, such as stretching, lifting, and twisting [129]. The origami P-TENG could also serve as a self-powered pressure sensor to distinguish, for example, the weight difference between different coins.

Miura-ori, a classic folding structure proposed by Miura, has been applied in the design of certain structures, such as solar sails [130]. Dudte et al. provided a scale-independent optimization algorithm to program the problem of determining generalized Miura-ori tessellations that conform to prescribed surfaces [131]. The flat and folded unit cells of a standard and of a modified Miura-ori structure are depicted in Figure 6a. The complexity of the folding structures is comprised of the basic origami unit cell: four coordinated mountain–valley structures. The basic origami unit cell constitutes the heart of the simplest origami tessellation and can be further engineered into compact and deployable structures of arbitrarily complex geometries. The design of complex origami structures starts with the folding of thin sheets along the creases, which will lead to different geometries in a large scale depending on the thickness and size of the paper sheet. The excellent mechanical properties of the origami structures enable diversified and sophisticated compressions and expansions. Previous research works on paper-based origami mainly focused on the seamless integration of sensing and interactive actuation; however, they lacked to address the concerns regarding paper-based power sources or self-powering strategies. Chen et al. showed the construction of origami P-TENGs as a self-powered paper interface (SPIN) to harvest mechanical energy from contact–separation movements [132] (Figure 6b). The SPIN unit is made of copper tape electrodes, PTFE, and nylon sheet friction layers. The adjustable parameters of the crease patterns, such as shape, size, and orientation, are key to the aesthetics and functionality of the SPIN energy-harvesting units. There are four types of folding structures for an efficient energy harvesting: the stripe fold, the Miura fold, the Yoshimura fold, and the waterbomb fold. The stripe fold is the simplest folding pattern with the maximum displacement in a 1D vertical compression. The Miura fold can be expanded and compressed along multiple axes but it has only one axis of movement due to a negative Poisson ratio. This fold can be compressed in a layered trapezoidal shape along two directions. The Yoshimura fold has a 3D transformation in a spring-like form, which is promising to be explored in different applications. The waterbomb fold is also a basic 2D compression fold used to create unique geometries; yet they are difficult to apply pressure on. The highest V_{oc} value of TENGs is obtained in the stripe fold, followed by decreasing V_{oc} values obtained in the waterbomb, Miura and Yoshimura folds, in this order. As the surface area of each fold is the same, the main reason for the different outputs is attributed to the differences in the maximum separation distance parameter. Since the power density is defined as the power divided by the contact area between two friction layers, the design editor can be used to estimate the potential power generation by the folding structures according to Ohm’s law.

Three-dimensional structures: kirigami

Kirigami is a combination of folding and cutting; therefore, it is different than origami, which only involves the folding of thin planar sheets. The introduction of additional cuts can further enhance the deformability of the resulting structures. Inspired by the art of paper cutting, Wei Wang et al. designed a soft deployable reflector for optical beam steering using kirigami [133]. As shown in Figure 7a, the planar soft deployable structure is made of uniform hollow pockets in which the kirigami reflective films are inlaid. As the axial strain is increased during stretching, the surfaces of the kirigami reflector become parallel. By changing the characteristic angle, the deformation angle of the reflective film and the slit patterning can be controlled.

The kirigami design in TENGs is a highly promising strategy for energy harvesting due to the introduction of more contact/separation spaces. Guo et al. reported a cut-paper-based self-charging power unit (PC-SCPU) by combining TENGs and the SC mode, which is capable of simultaneously harvest and store energy from body movements [39]. Zhou et al. also proposed an

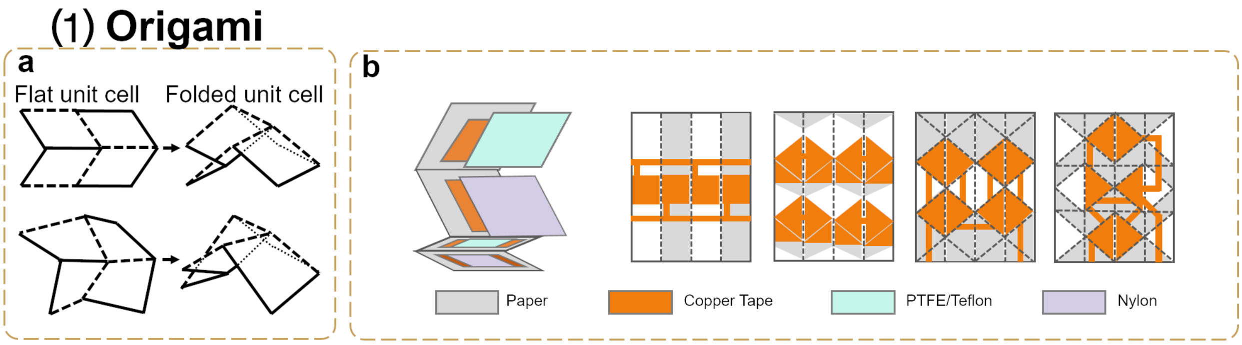

Figure 6: Geometry design of a P-TENG (1) origami: (a) Folded standard (top) and modified (bottom) unit cells. (b) One unit and four different crease pattern designs of SPINs.

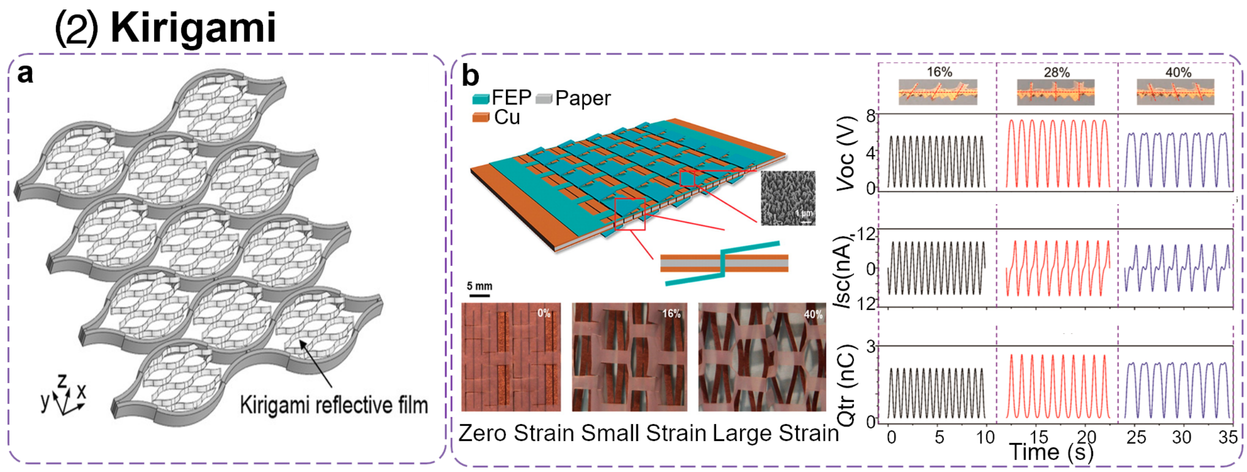

Figure 7: Geometry design of P-TENGs. (2) Kirigami. (a) The profile of the kirigami reflector [133]. Copyright © 2017 WILEY-VCH Verlag GmbH & Co. KGaA, Weinheim. Adapted with permission from Wei Wang et al., “Kirigami/Origami-Based Soft Deployable Reflector for Optical Beam Steering”, Advanced Functional Materials, John Wiley and Sons. (b) An schematic structure and photographs of the different tensile strains of K-TENGs and the typical electrical outputs of K-TENGs. Adapted with permission from [136], Copyright © 2016, American Chemical Society.

all-in-one stretchable self-charging power unit based on folded carbon paper TENGs operating in SC mode [134]. Xia et al. proposed a milk-based P-TENG (MP-TENG) to increase the output performance of TENGs [114]. A lozenge-stacked MP-TENG was designed and fabricated with an enhanced output. Zhang et al. proposed a rhombic-shaped paper-based triboelectric nanogenerator (RP-TENG) that can effectively operate under tensile strain conditions and with an applied contact force [135]. The Wang group developed a highly stretchable interlocking kirigami TENG (K-TENG) based on inelastic paper materials [136]. K-TENGS are capable of harvesting mechanical energy from various types of motions, such as stretching, pressing, and twisting due to the thin cutting film design. The schematic structure of K-TENGs and related photographs are illustrated in Figure 7b. The prepared FEP film with a rectangular kirigami pattern was treated by inductively coupled plasma, in which the parameters of a unit cell were designed to match those of the linear kirigami on paper. The copper-coated paper was chosen as one of the friction layers and as the electrode for the K-TENG, whose horizontal and vertical spacing between the notches was set as 2 mm. The resulting K-TENGs could withstand a tensile strain of up to 200% without breaking. The typical electrical output of a K-TENG under cyclic stretching of up to specific tensile strain values of 16%, 28%, and 40% were tested. When the tensile strain of a given K-TENG was at 16% or 28%, the V_{oc} and the transfered charge (Q_{tr}) increased monotonically with the applied strain, while the I_{sc} only changed direction at the maximum applied strain and at zero strain. When the tensile strain of a K-TENG was at 40%, V_{oc} and Q_{tr} first increased with the applied strain until they reached a fully stretched state, after which both values started to decrease.

Emerging applications of P-TENGs

2D and 3D self-powered sensors based on paper-based TENGs

As a promising technology for self-powered sensing devices, TENGs can directly convert mechanical stimuli into electrical signals without additional transducers. Therefore, TENGs have a great application potential in the fields of active-sensing devices and self-powered sensors [137-144], which require less standby power consumption and simpler control circuits compared to traditional sensors. More recently, P-TENGs have also been employed in a wide range of application scenarios, including acoustic [103], pressure/force/weight [129,145,146], velocity/acceleration [136,147], position [148], anti-theft [149], and temperature [145] sensors. Liu et al. [146] reported a self-powered active P-TENG force sensor with an ionogel-infiltrated paper (IIP) as the electrode, aiming for a flexible all paper-based sensor. The upper ionogel-infiltrated paper-based flexible electrode was adhered to the back side of the filter paper as the upper triboelectrification layer, while the counter friction layer corresponded to the bottom ionogel-infiltrated paper attached inside of the filter paper. The bottom ionogel-infiltrated paper was in contact with the upper pristine filter paper to generate the induced electrostatic charge. In addition, it worked as an electrode conducting the electrons to the external circuit. The all paper-based flexible sensor could detect different impulsive forces without any extra power consumption.

Based on efficient conversion of ambient mechanical energy into electricity, P-TENGs have been extensively utilized in self-powered mechanosensing devices [150] (e.g., pressure, tactile, strain, and force sensors). Some special but also frequently required applications (e.g., humidity and height sensors) have been rarely reported. Recently, Ejehi et al. proposed a self-powered humidity sensor based on a graphene oxide (GO) paper-based TENG [151], which showed an outstanding power density as high as 1.3 W·m^{-2}, a V_{oc} of up to 870 V and a I_{sc} of 1.4 µA·cm^{-2}. GO was chosen to be precipitated on paper in virtue of the reactive oxygen functional groups and due to its high specific surface, which made it a good candidate for both energy harvesting and material storage [152]. Moreover, its intrinsically high mechanical strength enabled the production of a flexible and stable thin layer, which could be used as a free-standing friction layer (also electrode) in TENGs.

In addition to the applications in energy harvesting, GO can also be readily used to monitor the relative humidity (RH) because of the strong interactions between water molecules and oxygen functional groups on its surface. The basis of a GO humidity sensor is the variation of impedance or capacitance owing to the tendency of the water molecules to be adsorbed on the GO surface. The rich functional groups of GO and the flexibility of GO paper deliver the significant potential for a less complicated TENG structure with a high sensitivity and a wide range of humidity detection. The corresponding mechanism of a self-powered GO P-TENG humidity sensor is displayed in Figure 8a. In general, GO P-TENG sensors respond to humidity due to the physical adsorption of water molecules on the surface of the GO layer. In a low RH scenario, water molecules are primarily condensed onto the available active sites of the GO surface, which act as the obstacle for electrostatically induced charges and reduce the contact surface to form a depletion region. As a consequence, the output current of the GO P-TENGs decreases in a low RH condition. As the RH increases, the hydroxy groups of the first physisorbed layer bond to water molecules, through hydrogen bonding, which also permeate into the interlayers of GO. The gradually absorbed water layer creates a uniform barrier layer for the induction of positive charges on the GO surface, which results in the formation of a continuous depletion region and leads to a more rapid current decrease at a higher RH. In order to investigate the electrical performances of the fabricated GO P-TENG as a self-powered humidity sensor, the normalized V_{oc} and I_{sc} of the GO P-TENG were tested, both of which showed an elevated slope when the RH was increased. The response value of the generated voltage reached 400%, while the maximum value for the current response was approx. 700% at a RH = 99% (Figure 8b). To illustrate a more vivid demonstration, the number of LEDs powered by the GO P-TENG decreased with a gradually increasing RH, as shown in Figure 8c. Compared with previously reported TENG-based humidity sensors, in which a TENG is generally used as the external source to power the humidity sensor, the GO P-TENG reviewed here is the first self-powered humidity sensor that utilizes the output performances as sensing signals. The achieved high sensitivity of 500% (*V*/*V*-%RH) is useful for portable/wearable electronics and for potential industrial applications due to its flexibility and lightweight.

Regarding height sensors, Xia et al. proposed a stacked 3D zigzag-structured P-TENG [70], which displayed different output signals depending on the changes in height of a falling object or on the impact when this object came into contact with the P-TENG. To increase the overall output, the paper in the zigzag-structured P-TENG was coated with commercial conductive ink. The ink-coated paper worked as both the functional friction layer and as a supporting structure, while PTFE was used as the other friction layer. The detailed working process is described as follows: at the initial state, a bouncy ball was placed at a certain height. At that stage, the surfaces of PTFE and of the paper of the height sensor were completely separated. When the TENG sensor was compressed by the impact of the falling bouncy ball, the induced triboelectric output could be detected. With the bouncy ball bouncing back up, the PTFE and the supported conductive paper began to separate.

Xia et al. designed a sliding triboelectric nanogenerator based on paper (SP-TENG) for self-powered speed and force sensors [147]. In the initial position, the surfaces of the paper and Teflon tape were completely overlapped and in touch with each other. Because of the triboelectrification, the surfaces of the paper had a positive charge, and the surfaces of the Teflon tape had an equivalent negative charge. When the positively charged top plate started to slide outwards, an induced current was generated. When the top plate started to slide in the opposite direction, the induced current flowed back with the help of external loads in order to maintain the electrostatic equilibrium. When the two plates reached the original position, the charged surfaces went back to a complete interaction setting. The SP-TENG can be used as a force and as a velocity sensor. The output voltage of the SP-TENG is approximately linearly proportional to the velocity.

2D and 3D human–machine interaction devices based on P-TENGs

The rapid development of IoTs and of the 5th generation communication technology aims to increase information exchange and communication through the internet. This will require millions or trillions of sensing nodes and systems to enable a convenient, safe, and sophisticated interaction between humans and electronic devices [153]. Although the power required for the operation of each sensor is down to the microwatt level, the number of these units is usually huge. The most conventional technology for powering IoTs (e.g., traditional chemical batteries) faces a significant challenge due to a limited lifetime

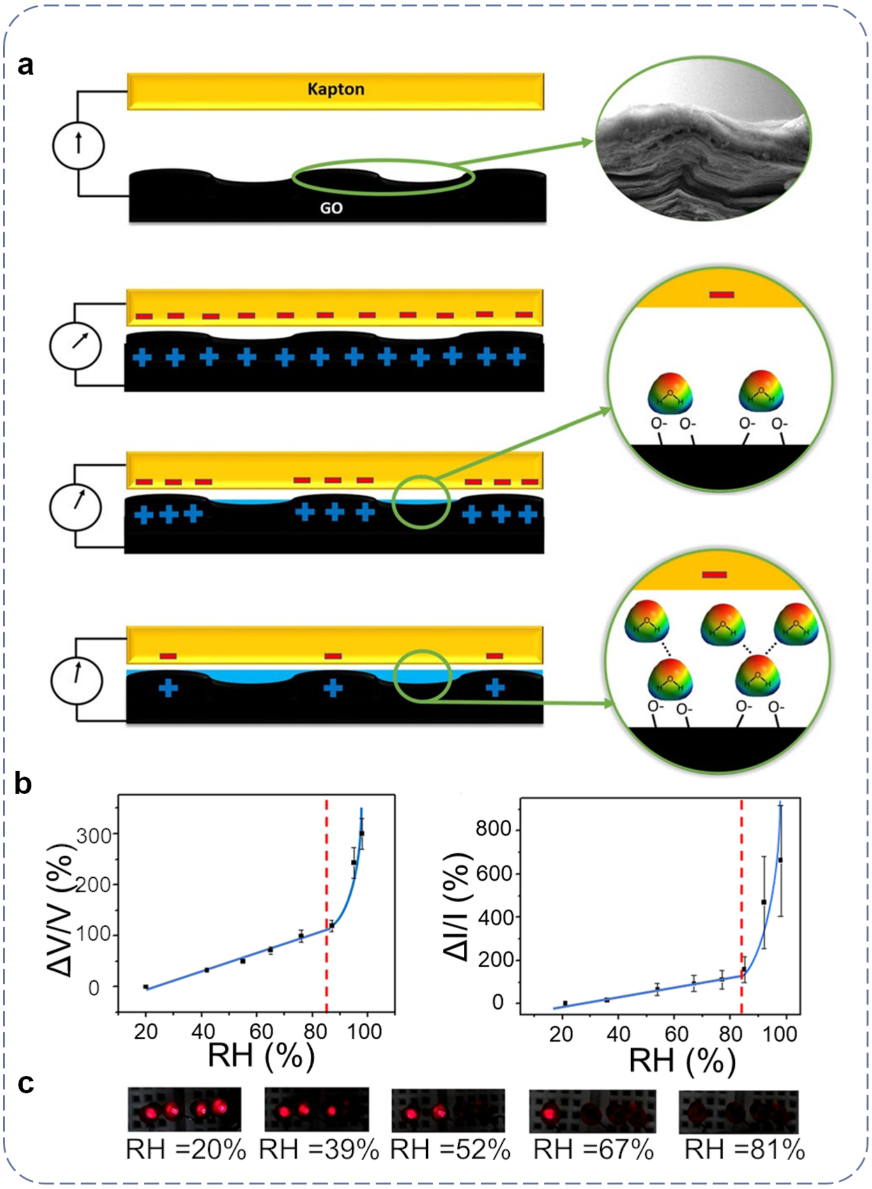

Figure 8: 3D self-powered sensors based on P-TENGs. (a) The sensing mechanism of the self-powered GO paper-based TENG humidity sensor. (b) The response value of the electrical output as a function of RH. (c) The number of LEDs which can be lit by a GO paper-based TENG at different values of RH. Figure 8 is adapted from [151] (© 2020 Faezeh Ejehi et al., published by Springer Nature; distributed under the terms of the Creative Commons Attribution 4.0 International License, https://creativecommons.org/licenses/by/4.0).

and powering distance, and due to the wide demand from the broadly distributed sensor networks. It is, therefore, urgent to investigate self-powered devices in order to promote the development of IoTs. TENG is considered a promising candidate for a self-powered mechanosensing device and it has been successfully employed in human–machine interaction. He et al. developed a wireless human–machine interaction system for document management and a smart system for calculation and reading based on a P-TENG with 2D patterns [154]. A wireless sensing system was also developed by integrating a P-TENG in a single-electrode mode, in which the generated electrical signals were direct responses to external mechanical stimuli. The wireless sensing system could be easily operated by the output voltage generated by the touch between finger and paper, which effectively triggered the processing circuit to produce an infrared (IR) signal. This remote IR signal could be detected by a wireless receiver and read by a computer. When the document was moved, a voltage output was generated due to the separation action, which triggered the remote controller and the IR sensor. Through a signal processor, the relative document number was displayed on the monitor, achieving the document management system.

Another application in human–machine interaction is the paper-based calculator, which was fabricated by using 16 separated squared TENGs as functional keys. It was observed that the corresponding numbers and operative symbols were entered and displayed on the monitor when the relevant functional keys were touched by finger. Notably, the effective working distance to trigger the remote-control circuit was within six meters. The wireless sensing system used a self-powered P-TENG that combines the ultrathin and lightweight features of paper with additional advantages, such as cost-effectiveness and versatility, in applications in which the signal triggered by mechanical motions can be converted into a control signal and readily employed in human–machine interactions.

P-TENGs can also work as tactile sensors to obtain a self-powered paper piano controlled in real time. By properly cutting and folding, a paper piano was obtained by utilizing an array of P-TENGs as an interactive keyboard [94]. In the paper piano, a printed paper substrate with a back Cu electrode was used as one of the friction layers, while a nitrocellulose membrane was used as the other friction layers in the P-TENG device. The P-TENG-based keyboard paired with bridge rectifiers and capacitors was connected to a laptop through a microcontroller. By pressing and releasing the keys of a P-TENG-based keyboard, the capacitors were charged and the voltage of the capacitor connected to the key submitted to press–release cycles was measured. The voltage changes of the capacitor were measured as input signals and recorded by a microcontroller, which could trigger the microcontroller and play music in the computer through the embedded program.

Chen et al. employed a 3D-structured P-TENG and took advantage of the paper creases to implement repetitive push-and-pull movements in promising applications, such as self-powered mechanosensing systems, electronic skins, and human–robot interactions [132]. In that work, a vote-counting button based on the Yoshimura fold was employed as a force and touch sensing device, as shown in Figure 9. This application adapted the nature of the Yoshimura fold, which provides a spring-like feature that can be pressed and recover automatically. By tapping the “voting button”, which was associated with other relevant items, a triboelectric voltage was generated and recognized by the microprocessor in order to evaluate the induced voltage values and to light a corresponding number of LEDs in a strip.

Applications of 2D P-TENGs in self-powered electrochemistry

Metal corrosion is a common phenomenon and a considerable amount of resources are necessary in order to prevent it. Therefore, the development of technologies to protect metals against corrosion has a significant economic importance and has attracted attention from different sectors. Cathodic protection is an effective and a traditional method to keep metals from corrosion. It can be obtained by an external direct current or a by a passive sacrificial anode [155-157]. However, traditional cathodic protection needs external electricity, which is very complex and energy consuming. Assisted with a self-powered system, an ideal cathodic protection system is expected to be sustainably powered by using nanogenerators. This can effectively decrease the usage of traditional methods which are energy consuming and introduce serious environmental problems. Some examples of self-powered systems have been introduced to solve this problem by integrating P-TENGs into an anti-corrosion protection system. Feng et al. have reported P-TENGs that can readily convert kinetic energy into elec-

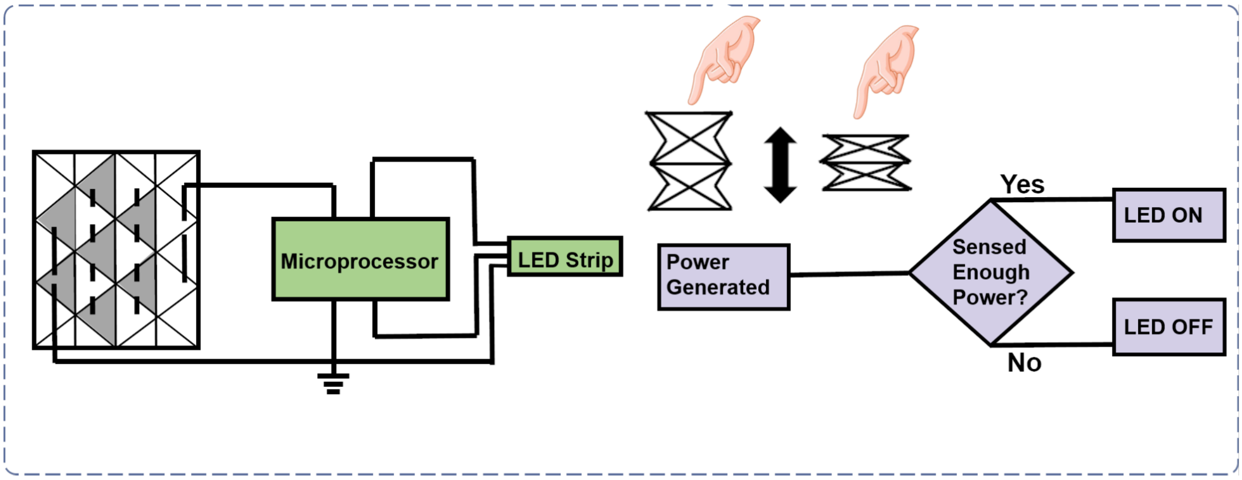

Figure 9: Human–machine interactions based on a 3D P-TENG. Schematic showing a logic flowchart of the Yoshimura fold being used as a voting button in a sensing device.

tricity to protect A3 steel from corrosion and biofouling [93]. A square-shaped A3 steel piece was connected to the cathode and a carbon electrode was connected to the anode, with a P-TENG paired with a rectifier and a capacitor connected in parallel with the electrochemical system. The P-TENG, in this case, was composed of PVDF and paper as the friction layers. The maximum values of V_{oc} and I_{sc} of the P-TENG were 1000 V and 30 mA, respectively. By converting the output form of the alternating current into a direct current with the rectifier, it was possible to efficiently protect the iron electrode from corrosion through the cathodic protection system. The comparative results shown in the photographs of the A3 steel pieces with and without a self-powered cathodic protection system revealed that there were no obvious changes in the morphology and color of the surface of the A3 steel in connection with the TENG. However, the A3 steel without the self-powered protection component was severely corroded. The Tafel plots of A3 steel with and without a cathodic protection showed that with a self-powered cathodic protection provided by the TENG, the A3 steel showed a much lower charge-transfer resistance value and the corresponding Nyquist plot exhibited an arc with a smaller value, which indicated that the TENG-powered cathodic protection system has obvious anticorrosion properties.

Marine fouling, caused by metal contamination and accumulation of biological organisms, is a major challenge for the oceanic ecosystem. With the growing threat to the environment caused by pollution, the search for innovative, highly efficient and cost-effective approaches to curb pollution has attracted much attention [158]. Previous research works have proven that a pulsed electric field can prevent biofouling from adhering to material surfaces [159-161]. Two types of marine algae (*Dunaliella* and *Navicula*) were used as typical indicators to simulate the ecological environment of the marine fouling organisms. Two stainless steel pieces were connected to the anode and to the cathode with a rectifier, and another piece of stainless steel was directly immersed into the algae medium as the blank sample. After introducing the TENG-powered antifouling system, the stainless steel pieces on both the anode and cathode showed good antifouling properties, as indicated by algae density.

An electrochemical reaction is an electron-transferring or flowing process between an electrode and a substance. TENGs can also be used to harvest mechanical energy and drive electropolymerization processes without an external power source to drive the electrochemical reaction. Shi et al. obtained a

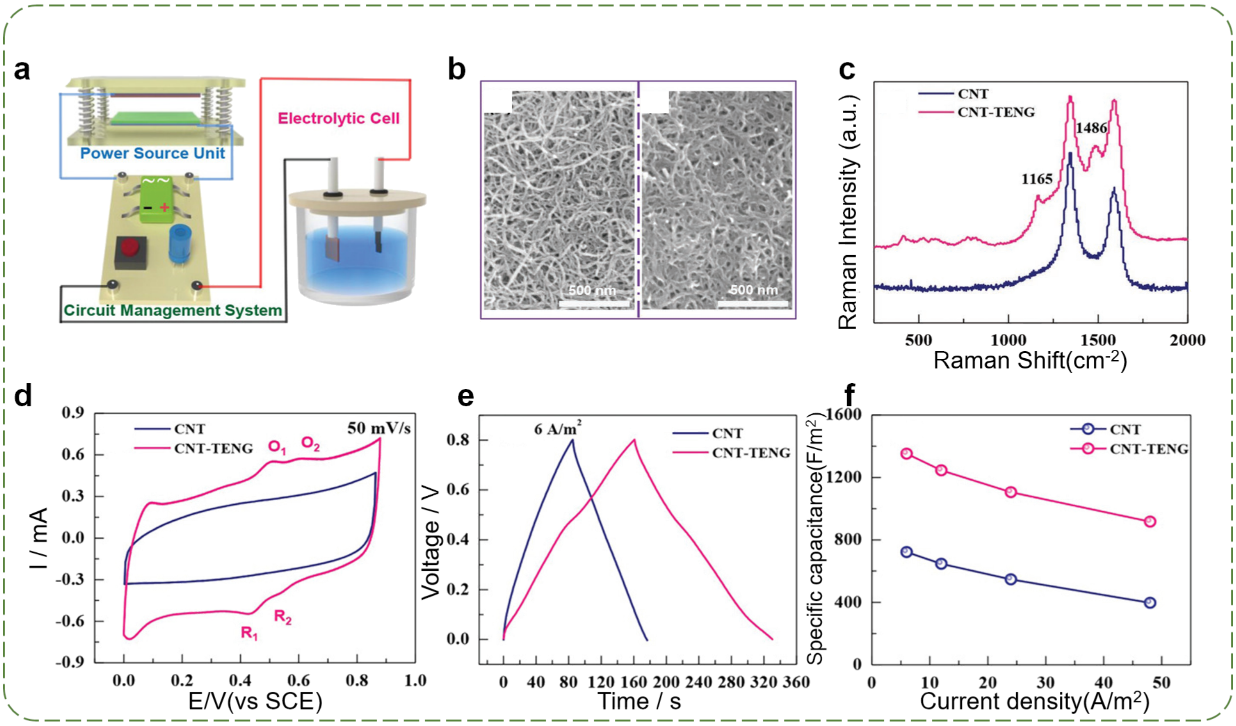

Figure 10: Applications of 2D P-TENGs in a self-powered electrochemical system. (a) Schematic illustration of a TENG electrochemical system and its electrochemical characterization. (b) SEM images of a pristine CNT and of PANI–CNT surfaces. (c) Raman spectroscopy, (d) CV curves, (e) GCD curves, and (f) specific capacitance values of CNT and PANI–CNT electrodes [162]. Copyright © 2019 WILEY-VCH Verlag GmbH & Co. KGaA, Weinheim. Adapted with permission from Kunming Shi et al., “Dielectric Modulated Cellulose Paper/PDMS-Based Triboelectric Nanogenerators for Wireless Transmission and Electropolymerization Applications”, Advanced Functional Materials, John Wiley and Sons.

P-TENG electrochemical system for electropolymerizing polyaniline (PANI) on a CNT electrode. Figure 10a shows the schematic illustration of a TENG electrochemical system (including a TENG, a rectifier and a capacitor), which was used to improve the capacitance of the CNT electrode by PANI electropolymerization [162]. The TENG powering component was comprised of a cellulose/$BaTiO_3$ aerogel paper as the positive friction layer and PDMS as the negative friction layer. The modified CNTs embedded into a thin layer of PANI by the TENG electrochemical system showed a larger diameter compared with the pristine CNTs, as shown in Figure 10b. The electropolymerization of PANI on a CNT electrode is also identified by the Raman spectra in Figure 10c. The electrochemical behavior of CNT and PANI–CNT electrodes were evaluated by using cyclic voltammetry (CV) and galvanostatic charge–discharge characterization (GCD). Compared with the pristine CNT, two pairs of redox peaks appeared in the CV curve of PANI–CNT electrodes at a scan rate of 50 $mV \cdot s^{-1}$ (Figure 10d). The charge–discharge time of the PANI–CNT electrode was almost two times longer than that of the CNT electrode for one cycle (Figure 10e). The PANI–CNT electrode exhibited a larger specific capacitance (approx. 1400 $F \cdot m^{-2}$ under 6 $A \cdot m^{-2}$) in comparison to the CNT electrode under all the applied current densities (Figure 10f). This application of P-TENGs provides a feasible and an effective way to construct self-powered electrochemical systems with a high output performance, enables the application of TENGs in the preparation of electrodes for supercapacitors with high specific capacitance values, and it is promising for large-scale applications in the environmental sciences.

2D and 3D P-TENGs for energy harvesting

Due to its superior performance (i.e., lightweight, low cost, and several material and structural possibilities for their manufacture) P-TENGs have been broadly used as microscale power sources for self-powered systems by harvesting human motion or ambient energy, such as walking, machine vibration, and wave energy. Harvesting low-frequency energy using P-TENGs is of great importance. They have been as used as an acoustic energy harvester and in the field of portable electronics since the beginning of their development. Both 2D patterns and 3D structures based on P-TENGs can be used for energy harvesting and these designed structures are often combined together rather than being mutually exclusive. The electric output performance (i.e., I_{sc}, V_{oc}, Q_{tr} and power density) is virtually important and it is the major figure of merit for energy harvesting. The electric output performance of P-TENGs for energy harvesting and functionalities and a comparison between P-TENGs and polymer-based TENGs are summarized in Table 1 and Table 2, respectively.

Table 1: Summary of output power values for energy harvesting purposes and functionalities in which P-TENGs are applied.

Ref.	Geometry design	Application	
		Electric output (V_{oc}, I_{sc}, Q_{tr}, power density ($mW \cdot m^{-2}$))	Functionality
[49]	2D	5.3×10^5	
[94]	2D	1.61×10^4	self-powered paper piano
[163]	3D (origami)	1.61×10^4	
[147]	2D	1.84×10^4	
[113]	2D	1800	
[68]	2D	906	active sensor
[125]	2D	693	
[46]	2D	398	self-powered sensing system
[162]	2D	352.5	wireless transmission & electropolymerization applications
[154]	2D	285.6	self-powered sensing system
[103]	2D	121	
[80]	2D	72.5	
[82]	2D	64	
[134]	3D (origami)	32.2	
[96]	3D (origami)	29.5	
[147]	3D (origami)	0.583	
[163]	3D (origami)	0.542	
[129]	3D (origami)		pressure sensor
[149]	2D		page mark and anti-theft sensor

Table 1: Summary of output power values for energy harvesting purposes and functionalities in which P-TENGs are applied. (continued)

[126]	2D		action sensor
[145]	2D		temperature & weight sensor
[164]	3D (origami)		height sensor
[146]	2D		active and passive mode sensor
[151]	2D		humidity sensor
[136]	3D (origami)		acceleration & book state sensor
[93]	2D		anticorrosion & antifouling

Table 2: A performance comparison between P-TENGs and traditional polymer-based TENGs.

	Materials	Typical performance				Ref.
		I_{sc}	V_{oc}	Q_{tr}	Power	
traditional polymer-based TENGs	FEP, metal	120 µA	281–560 V	670 nC	7.96 mW	[54-56]
	PTFE, metal	25.97 µA – 1.32 mA	300–400 V	1000 nC	2.84–3 W	[35,53]
	PDMS, CNTs	180 nA	60 V			[81]
	PDMS, liquid metal nanoparticles	12.06 µA	268 V	103.95 nC	0.32 mW	[67]
paper as an electrode (Au Ag Cu Graphite Carbon)	FEP	30 µA	90 V	75 nC·cm^{-3}	–	[39]
	PTFE	2–17 µA	20–110 V	38.4–550 nC	121–906 mW·m^{-2}	[47,69,104,130]
	PDMS	18.6 µA	300 V	79.3 µC·m^{-2}	32.2 mW·m^{-2}	[134]
paper as a friction layer	PDMS & $BaTiO_3$ cellulose paper	8.3 µA	88 V	–	352.5 mW·m^{-2}	[162]
	crepe cellulose & nitrocellulose membrane	31.5 µA	196.8 V	–	16.1 mW·m^{-2}	[94]
	PVDF & polydopamine modified paper	30 µA	100 V	76 µC·m^{-2}	–	[92]
	PTFE & $BaTiO_3$ cellulose paper	forward-poled BC-TENG I_{sc} ≈ 9.8 µA, V_{oc} ≈ 170 V reverse-poled BC-TENG I_{sc} ≈ 1.6 µA, V_{oc} ≈ 44 V				[113]

Due to the advantages of cellulose (i.e., a low cost, lightweight, abundant, and accessible material) cellulose-based materials have also been intensively used, in recent years, in the manufacture of energy-harvesting devices, such as TENGs, (as a positive friction layer or as a direct substrate). P-TENGs exhibiting good stability and durability can be used as a sustainable source to power various portable electronic devices. For example, P-TENGs are able to light up 240 LEDs connected in series through a commercial rectifier bridge. To power relatively high-power electronics, the energy harvested by TENG is generally stored in energy storage devices first. This can be performed by using a bridge rectifier and different types of capacitors. The charged capacitor is then used to power the target electronic devices, such as segmented LED display, liquid crystal display (LCD), and electroluminescence (EL) display units. The cellulose-based P-TENGs have the following electric output performance parameter values: V_{oc} (approx. 196.8 V), I_{sc} (approx. 31.5 µA), and power density of 16.1 W·m^{-2} [94].

As vast amounts of acoustic energy (e.g., from talking, traffic noise, and music) are normally not harvested, Wang group developed an ultrathin and rollable P-TENG for harvesting sound wave energy [103], which is capable of delivering a maximum power density of 121 mW·m^{-2} (volume density of approx.

968 W·m^{-3}) at 800 kΩ under a sound pressure of 117 dB$_{\text{SPL}}$ (Figure 11). The ultrathin P-TENG with a multilayered structure was composed of several thin film materials. Paper was selected as the structural backbone of the TENG (coated with copper, thereby working as an electrification layer) to generate triboelectric charges upon contact with a PTFE membrane. This device can be applied in many scenarios to harvest recycled acoustic mechanical energy from music playing and phone conversations. Compared with traditional acoustic energy harvester, which have a resonance cavity, the presented P-TENG is ultrathin, flexible and rollable. In addition, the ultrathin TENG is fabricated with low-cost, lightweight, and biodegradable paper materials and have a simple structure. The concept and design presented in [103] can be extensively applied to other energy-harvesting or sensing devices, such as wearable and flexible electronics, military surveillance equipment, equipment to reduce jet engine noise, low-cost implantable human ear, and wireless technology applications.

Compared with the structure of 2D patterns, P-TENGs combining origami and kirigami structures are tridimensional and have more flexible structures and, therefore, more application possibilities. As TENGs are more efficient to harvest low-frequency water wave energy, robustness and packaging are of great importance for these applications. Yang et al. [163] designed a non-encapsulated pendulum-like paper-based hybrid nanogenerator to harvest water wave energy. The basic structure of the designed hybrid generator is presented in Figure 12, in which there are two zigzag multilayered P-TENG units with four basic TENGs operating in contact–separation mode on both sides of the mover. P-TENGs operating in soft–hard hybrid mode allows a highly close contact compared with the acrylic-based device. The acrylic plate can further strengthen the toughness of the paper structures and of the zigzag multilayered P-TENG, which can be considered as a spring oscillator. This unique structure revealed superior robustness and a maximum peak power value of up to 22.5 mW of the zigzag multilayered TENGs was ob-

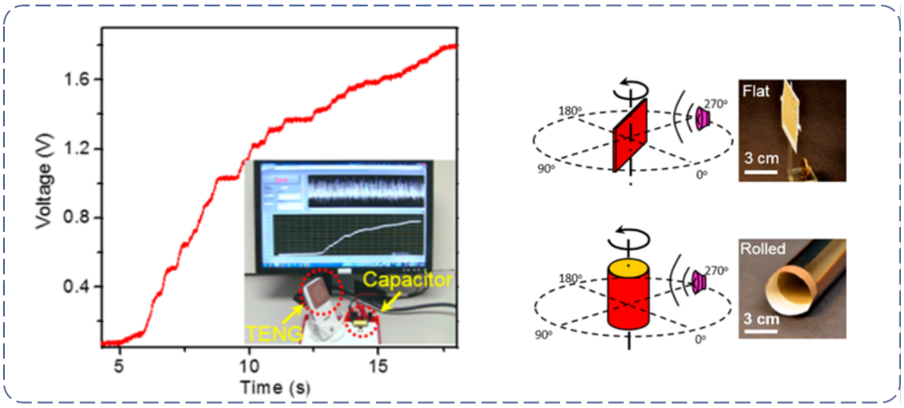

Figure 11: Sound wave energy harvesting by an ultrathin P-TENG. Adapted with permission from [103], Copyright © 2015, American Chemical Society.

Figure 12: Harvesting water wave energy with a hybrid generator [163] Copyright © 2019 WILEY-VCH Verlag GmbH & Co. KGaA, Weinheim. Adapted with permission from Hongmei Yang et al., “A Nonencapsulative Pendulum-Like Paper–Based Hybrid Nanogenerator for Energy Harvesting”, Advanced Energy Materials, John Wiley and Sons.

tained. With the two zigzag multilayered P-TENG superimposed together in parallel, I_{sc} increased to 41.3 μA, while V_{oc} decreased to 567 V and Q_{tr} increased to 551 nC. The charging capability of a 47 μF capacitor by TENGs and EMG was also compared by harvesting mechanical energy from water wave in [163]. Finally, the fabricated device effectively converted the water wave energy into electricity and is able to power more than 220 LEDs, revealing the potential applications in blue energy. The unique structure design of the proposed zigzag multilayered P-TENG broadens the available working frequency ranges by combining multiple modes, avoids the influence on the performance caused by harsh underwater environmental conditions, and reveals superior robustness.

Xia et al. reported a wearable P-TENG for harvesting mechanical energy from the human body [165]. In the study, X-shaped P-TENGs were assembled in cut-paper and origami-paper architectures and, thereby, were capable of providing two working patterns: cut paper and origami paper. The maximum values obtained for X-shaped P-TENGs were: V_{oc} (approx. 326 V), I_{sc} (approx. 45 μA), and power density (542.22 $\mu W \cdot m^{-2}$). The number of X-shaped units influences the P-TENG output. The I_{sc} value increased with an increase in the number of connected working units, whereas V_{oc} decreased owing to the voltage cancelation induced by different working modes. In order to enhance the voltage output, multiple full-wave rectifier bridges were employed in order to connect to each working unit for lighting up 101 high-power blue LEDs. Aside from harvesting energy in multiple directions, the X-shaped P-TENGs can also be stretched and bent due to the special geometry design. The force applied to the device is multi-directional and consistent with the motion of the human body, which allows mechanical energy harvesting from human elbow motions. This straightforward, affordable, multifunctional, and portable P-TENG device seems to enable a sustainable power supply for wearable and flexible electronic systems.

Conclusion

The invention of paper and the discovery of triboelectrification phenomenon are both over 2000 years. Paper is by far one of the most inexpensive and widely used flexible material in daily life. The main advantages of using paper over flexible plastic substrates are the low cost, recyclability, and common use. Paper is flexible and can be easily folded or bent to form 3D structures without causing structural damage. This allows versatile structure designs and makes paper quite suitable for applications in mechanical energy-harvesting devices, such as TENGs. Triboelectrification is the basis of TENGs and it can be explained by an electron-cloud potential-well model and by an electron-emission-dominated charge-transfer mechanism. Therefore, the electrical properties of paper are of vital importance to the performance of TENG devices. Different processes and materials can be applied to paper-based devices. Conductive materials are usually evaporated, deposited, or printed on the paper. By introducing additional functional groups one can also convert the polarity of the paper to achieve a high-performance TENG. Vacuum filtration offers another fast and simple process to fabricate cellulose nanofiber-based TENG. In summary, P-TENGs can combine the merits of lightweight, low cost and flexibility and they exhibit great application potentials in self-powered sensing devices, human–machine interaction, electrochemistry, and energy harvesting.

The use of paper can also be extended to applications such as electronic displays, sensors, and smart packaging. However, low-cost flexible electronics not only require an inexpensive paper substrate, but also a fast and low-cost manufacturing process and the use of inexpensive materials. It can also be applicable to mass production if an appropriate printing technology is used. It is expected that P-TENGs can be readily integrated with other paper-based electronic devices including sensors, microfluidics, and energy storage systems. We have seen a tremendous progress, in recent years, in the field of P-TENGs, which will improve the efficiency of self-powered sensing and energy harvesting devices. However, further progress is needed in the field of electronic materials in terms of stability, performance, processability, fabrication techniques, and methods for making electronic device applications more feasible and accessible.

Funding

This work is financially supported by the National Key Research and Development Program of China (2016YFA0202703), the National Natural Science Foundation of China (52073031, 51605034, 51711540300), the Fundamental Research Funds for the Central Universities (E0EG6801X2), Beijing Nova Program (Z191100001119047), and the “Hundred Talents Program” of the Chinese Academy of Science.

ORCID® iDs

Qijun Sun - https://orcid.org/0000-0003-2130-7389

References

1. Höök, M.; Tang, X. *Energy Policy* **2013,** *52,* 797–809. doi:10.1016/j.enpol.2012.10.046
2. Omer, A. M. *Renewable Sustainable Energy Rev.* **2008,** *12,* 2265–2300. doi:10.1016/j.rser.2007.05.001
3. Chen, G.; Li, Y.; Bick, M.; Chen, J. *Chem. Rev.* **2020,** *120,* 3668–3720. doi:10.1021/acs.chemrev.9b00821
4. Chen, J.; Huang, Y.; Zhang, N.; Zou, H.; Liu, R.; Tao, C.; Fan, X.; Wang, Z. L. *Nat. Energy* **2016,** *1,* 16138. doi:10.1038/nenergy.2016.138

5. Chen, J.; Wang, Z. L. *Joule* **2017,** *1,* 480–521. doi:10.1016/j.joule.2017.09.004
6. Chen, J.; Zhu, G.; Yang, W.; Jing, Q.; Bai, P.; Yang, Y.; Hou, T. C.; Wang, Z. L. *Adv. Mater. (Weinheim, Ger.)* **2013,** *25,* 6094–6099. doi:10.1002/adma.201302397
7. Pu, S.; Fu, J.; Liao, Y.; Ge, L.; Zhou, Y.; Zhang, S.; Zhao, S.; Liu, X.; Hu, X.; Liu, K.; Chen, J. *Adv. Mater. (Weinheim, Ger.)* **2020,** *32,* 1907307. doi:10.1002/adma.201907307
8. Pu, S.; Liao, Y.; Chen, K.; Fu, J.; Zhang, S.; Ge, L.; Conta, G.; Bouzarif, S.; Cheng, T.; Hu, X.; Liu, K.; Chen, J. *Nano Lett.* **2020,** *20,* 3791–3797. doi:10.1021/acs.nanolett.0c00800
9. Zhang, N.; Chen, J.; Huang, Y.; Guo, W.; Yang, J.; Du, J.; Fan, X.; Tao, C. *Adv. Mater. (Weinheim, Ger.)* **2016,** *28,* 263–269. doi:10.1002/adma.201504137
10. Zhang, N.; Huang, F.; Zhao, S.; Lv, X.; Zhou, Y.; Xiang, S.; Xu, S.; Li, Y.; Chen, G.; Tao, C.; Nie, Y.; Chen, J.; Fan, X. *Matter* **2020,** *2,* 1260–1269. doi:10.1016/j.matt.2020.01.022
11. He, G.; Li, Z.; Zhao, J.; Wang, S.; Wu, H.; Guiver, M. D.; Jiang, Z. *Adv. Mater. (Weinheim, Ger.)* **2015,** *27,* 5280–5295. doi:10.1002/adma.201501406
12. Wang, L.; Zhang, B.; Hu, Y.; Li, X.; Zhao, T. *J. Power Sources* **2021,** *482,* 228978. doi:10.1016/j.jpowsour.2020.228978
13. Bharathraj, S.; Adiga, S. P.; Mayya, K. S.; Song, T.; Kim, J.; Sung, Y. *J. Power Sources* **2020,** *474,* 228659. doi:10.1016/j.jpowsour.2020.228659
14. Fan, F.-R.; Tian, Z.-Q.; Lin Wang, Z. *Nano Energy* **2012,** *1,* 328–334. doi:10.1016/j.nanoen.2012.01.004
15. Deng, W.; Zhou, Y.; Zhao, X.; Zhang, S.; Zou, Y.; Xu, J.; Yeh, M.-H.; Guo, H.; Chen, J. *ACS Nano* **2020,** *14,* 9050–9058. doi:10.1021/acsnano.0c04113
16. Jin, L.; Xiao, X.; Deng, W.; Nashalian, A.; He, D.; Raveendran, V.; Yan, C.; Su, H.; Chu, X.; Yang, T.; Li, W.; Yang, W.; Chen, J. *Nano Lett.* **2020,** *20,* 6404–6411. doi:10.1021/acs.nanolett.0c01987
17. Yan, C.; Gao, Y.; Zhao, S.; Zhang, S.; Zhou, Y.; Deng, W.; Li, Z.; Jiang, G.; Jin, L.; Tian, G.; Yang, T.; Chu, X.; Xiong, D.; Wang, Z.; Li, Y.; Yang, W.; Chen, J. *Nano Energy* **2020,** *67,* 104235. doi:10.1016/j.nanoen.2019.104235
18. Zhou, Y.; Deng, W.; Xu, J.; Chen, J. *Cell Rep. Phys. Sci.* **2020,** *1,* 100142. doi:10.1016/j.xcrp.2020.100142
19. Zhou, Z.; Weng, L.; Tat, T.; Libanori, A.; Lin, Z.; Ge, L.; Yang, J.; Chen, J. *ACS Nano* **2020,** *14,* 14126–14133. doi:10.1021/acsnano.0c06949
20. Zou, Y.; Raveendran, V.; Chen, J. *Nano Energy* **2020,** *77,* 105303. doi:10.1016/j.nanoen.2020.105303
21. Zou, Y.; Libanori, A.; Xu, J.; Nashalian, A.; Chen, J. *Research (Washington, DC, U. S.)* **2020,** *2020,* 7158953. doi:10.34133/2020/7158953
22. Meng, K.; Zhao, S.; Zhou, Y.; Wu, Y.; Zhang, S.; He, Q.; Wang, X.; Zhou, Z.; Fan, W.; Tan, X.; Yang, J.; Chen, J. *Matter* **2020,** *2,* 896–907. doi:10.1016/j.matt.2019.12.025
23. Su, Y.; Wang, J.; Wang, B.; Yang, T.; Yang, B.; Xie, G.; Zhou, Y.; Zhang, S.; Tai, H.; Cai, Z.; Chen, G.; Jiang, Y.; Chen, L.-Q.; Chen, J. *ACS Nano* **2020,** *14,* 6067–6075. doi:10.1021/acsnano.0c01804
24. Su, Y.; Yang, T.; Zhao, X.; Cai, Z.; Chen, G.; Yao, M.; Chen, K.; Bick, M.; Wang, J.; Li, S.; Xie, G.; Tai, H.; Du, X.; Jiang, Y.; Chen, J. *Nano Energy* **2020,** *74,* 104941. doi:10.1016/j.nanoen.2020.104941
25. Tat, T.; Libanori, A.; Au, C.; Yau, A.; Chen, J. *Biosens. Bioelectron.* **2021,** *171,* 112714. doi:10.1016/j.bios.2020.112714
26. Zhou, Z.; Chen, K.; Li, X.; Zhang, S.; Wu, Y.; Zhou, Y.; Meng, K.; Sun, C.; He, Q.; Fan, W.; Fan, E.; Lin, Z.; Tan, X.; Deng, W.; Yang, J.; Chen, J. *Nat. Electron.* **2020,** *3,* 571–578. doi:10.1038/s41928-020-0428-6
27. Zhou, Z.; Padgett, S.; Cai, Z.; Conta, G.; Wu, Y.; He, Q.; Zhang, S.; Sun, C.; Liu, J.; Fan, E.; Meng, K.; Lin, Z.; Uy, C.; Yang, J.; Chen, J. *Biosens. Bioelectron.* **2020,** *155,* 112064. doi:10.1016/j.bios.2020.112064
28. Wang, Z. L. *Mater. Today* **2017,** *20,* 74–82. doi:10.1016/j.mattod.2016.12.001
29. Wang, Z. L. *Faraday Discuss.* **2014,** *176,* 447–458. doi:10.1039/c4fd00159a
30. Wang, S.; Lin, L.; Wang, Z. L. *Nano Lett.* **2012,** *12,* 6339–6346. doi:10.1021/nl303573d
31. Wang, M.; Zhang, J.; Tang, Y.; Li, J.; Zhang, B.; Liang, E.; Mao, Y.; Wang, X. *ACS Nano* **2018,** *12,* 6156–6162. doi:10.1021/acsnano.8b02562
32. Zhang, B.; Tang, Y.; Dai, R.; Wang, H.; Sun, X.; Qin, C.; Pan, Z.; Liang, E.; Mao, Y. *Nano Energy* **2019,** *64,* 103953. doi:10.1016/j.nanoen.2019.103953
33. Wang, S.; Lin, L.; Xie, Y.; Jing, Q.; Niu, S.; Wang, Z. L. *Nano Lett.* **2013,** *13,* 2226–2233. doi:10.1021/nl400738p
34. Zhu, G.; Chen, J.; Liu, Y.; Bai, P.; Zhou, Y. S.; Jing, Q.; Pan, C.; Wang, Z. L. *Nano Lett.* **2013,** *13,* 2282–2289. doi:10.1021/nl4008985
35. Zhu, G.; Zhou, Y. S.; Bai, P.; Meng, X. S.; Jing, Q.; Chen, J.; Wang, Z. L. *Adv. Mater. (Weinheim, Ger.)* **2014,** *26,* 3788–3796. doi:10.1002/adma.201400021
36. Yang, Y.; Zhang, H.; Chen, J.; Jing, Q.; Zhou, Y. S.; Wen, X.; Wang, Z. L. *ACS Nano* **2013,** *7,* 7342–7351. doi:10.1021/nn403021m
37. Wang, M.; Zhang, N.; Tang, Y.; Zhang, H.; Ning, C.; Tian, L.; Li, W.; Zhang, J.; Mao, Y.; Liang, E. *J. Mater. Chem. A* **2017,** *5,* 12252–12257. doi:10.1039/c7ta02680c
38. Wang, S.; Xie, Y.; Niu, S.; Lin, L.; Wang, Z. L. *Adv. Mater. (Weinheim, Ger.)* **2014,** *26,* 2818–2824. doi:10.1002/adma.201305303
39. Guo, H.; Yeh, M.-H.; Zi, Y.; Wen, Z.; Chen, J.; Liu, G.; Hu, C.; Wang, Z. L. *ACS Nano* **2017,** *11,* 4475–4482. doi:10.1021/acsnano.7b00866
40. Xia, L.; Long, T.; Li, W.; Zhong, F.; Ding, M.; Long, Y.; Xu, Z.; Lei, Y.; Guan, Y.; Yuan, D.; Zhang, Y.; Jia, C.; Sun, L.; Sun, Q. *Small* **2020,** *16,* 2003321. doi:10.1002/smll.202003321
41. Zhao, C.; Zhang, Q.; Zhang, W.; Du, X.; Zhang, Y.; Gong, S.; Ren, K.; Sun, Q.; Wang, Z. L. *Nano Energy* **2019,** *57,* 440–449. doi:10.1016/j.nanoen.2018.12.062
42. Qin, S.; Zhang, Q.; Yang, X.; Liu, M.; Sun, Q.; Wang, Z. L. *Adv. Energy Mater.* **2018,** *8,* 1800069. doi:10.1002/aenm.201800069
43. Gao, X.; Huang, L.; Wang, B.; Xu, D.; Zhong, J.; Hu, Z.; Zhang, L.; Zhou, J. *ACS Appl. Mater. Interfaces* **2016,** *8,* 35587–35592. doi:10.1021/acsami.6b12913
44. Zhang, N.; Qin, C.; Feng, T.; Li, J.; Yang, Z.; Sun, X.; Liang, E.; Mao, Y.; Wang, X. *Nano Res.* **2020,** *13,* 1903–1907. doi:10.1007/s12274-020-2654-7
45. Chen, X.; Pu, X.; Jiang, T.; Yu, A.; Xu, L.; Wang, Z. L. *Adv. Funct. Mater.* **2017,** *27,* 1603788. doi:10.1002/adfm.201603788
46. Zhang, X. S.; Su, M.; Brugger, J.; Kim, B. *Nano Energy* **2017,** *33,* 393–401. doi:10.1016/j.nanoen.2017.01.053
47. Huang, J.; Yang, X.; Yu, J.; Han, J.; Jia, C.; Ding, M.; Sun, J.; Cao, X.; Sun, Q.; Wang, Z. L. *Nano Energy* **2020,** *69,* 104419. doi:10.1016/j.nanoen.2019.104419

48. Ho, D. H.; Han, J.; Huang, J.; Choi, Y. Y.; Cheon, S.; Sun, J.; Lei, Y.; Park, G. S.; Wang, Z. L.; Sun, Q.; Cho, J. H. *Nano Energy* **2020,** *77,* 105262. doi:10.1016/j.nanoen.2020.105262
49. Mao, Y.; Zhang, N.; Tang, Y.; Wang, M.; Chao, M.; Liang, E. *Nanoscale* **2017,** *9,* 14499–14505. doi:10.1039/c7nr05222g
50. Tang, Y.; Zhou, H.; Sun, X.; Diao, N.; Wang, J.; Zhang, B.; Qin, C.; Liang, E.; Mao, Y. *Adv. Funct. Mater.* **2019,** *30,* 1907893. doi:10.1002/adfm.201907893
51. Chen, J.; Yang, J.; Li, Z.; Fan, X.; Zi, Y.; Jing, Q.; Guo, H.; Wen, Z.; Pradel, K. C.; Niu, S.; Wang, Z. L. *ACS Nano* **2015,** *9,* 3324–3331. doi:10.1021/acsnano.5b00534
52. Jiang, D.; Guo, F.; Xu, M.; Cai, J.; Cong, S.; Jia, M.; Chen, G.; Song, Y. *Nano Energy* **2019,** *58,* 842–851. doi:10.1016/j.nanoen.2019.01.083
53. Li, X.; Tao, J.; Wang, X.; Zhu, J.; Pan, C.; Wang, Z. L. *Adv. Energy Mater.* **2018,** *8,* 1800705. doi:10.1002/aenm.201800705
54. Liu, G.; Guo, H.; Xu, S.; Hu, C.; Wang, Z. L. *Adv. Energy Mater.* **2019,** 1900801. doi:10.1002/aenm.201900801
55. Xiao, T. X.; Liang, X.; Jiang, T.; Xu, L.; Shao, J. J.; Nie, J. H.; Bai, Y.; Zhong, W.; Wang, Z. L. *Adv. Funct. Mater.* **2018,** *28,* 1802634. doi:10.1002/adfm.201802634
56. Zhong, W.; Xu, L.; Wang, H.; An, J.; Wang, Z. L. *Adv. Funct. Mater.* **2019,** *29,* 1905319. doi:10.1002/adfm.201905319
57. Hamedi, M. M.; Ainla, A.; Güder, F.; Christodouleas, D. C.; Fernández-Abedul, M. T.; Whitesides, G. M. *Adv. Mater. (Weinheim, Ger.)* **2016,** *28,* 5054–5063. doi:10.1002/adma.201505823
58. Kalish, B.; Tsutsui, H. *Lab Chip* **2014,** *14,* 4354–4361. doi:10.1039/c4lc00730a
59. Chen, M.; Yang, H.; Rong, L.; Chen, X. *Analyst* **2016,** *141,* 5511–5519. doi:10.1039/c6an00788k
60. Guo, Z. H.; Jiao, Y. C.; Wang, H. L.; Zhang, C.; Liang, F.; Liu, J. L.; Yu, H. D.; Li, C. M.; Zhu, G.; Wang, Z. L. *Adv. Funct. Mater.* **2019,** *29,* 1808974. doi:10.1002/adfm.201808974
61. Hayasaka, K.; Matsui, H.; Takeda, Y.; Shiwaku, R.; Tanaka, Y.; Shiba, T.; Kumaki, D.; Tokito, S. *Adv. Electron. Mater.* **2017,** *3,* 1700208. doi:10.1002/aelm.201700208
62. Mitra, K. Y.; Polomoshnov, M.; Martínez-Domingo, C.; Mitra, D.; Ramon, E.; Baumann, R. R. *Adv. Electron. Mater.* **2017,** *3,* 1700275. doi:10.1002/aelm.201700275
63. Sun, Q.; Kim, J.-H.; Seo, S. *Org. Electron.* **2013,** *14,* 2401–2405. doi:10.1016/j.orgel.2013.06.010
64. Sun, Q.; Seo, S. *Org. Electron.* **2012,** *13,* 384–387. doi:10.1016/j.orgel.2011.11.030
65. Kim, J.-H.; Sun, Q.; Seo, S. *Org. Electron.* **2010,** *11,* 964–968. doi:10.1016/j.orgel.2010.02.015
66. Liu, Y.; Weng, B.; Xu, Q.; Hou, Y.; Zhao, C.; Beirne, S.; Shu, K.; Jalili, R.; Wallace, G. G.; Razal, J. M.; Chen, J. *Adv. Mater. Technol. (Weinheim, Ger.)* **2016,** *1,* 1600166. doi:10.1002/admt.201600166
67. Yang, Y.; Han, J.; Huang, J.; Sun, J.; Wang, Z. L.; Seo, S.; Sun, Q. *Adv. Funct. Mater.* **2020,** *30,* 1909652. doi:10.1002/adfm.201909652
68. Zhong, Q.; Zhong, J.; Hu, B.; Hu, Q.; Zhou, J.; Wang, Z. L. *Energy Environ. Sci.* **2013,** *6,* 1779–1784. doi:10.1039/c3ee40592c
69. Hu, Q.; Wang, B.; Zhong, Q.; Zhong, J.; Hu, B.; Zhang, X.; Zhou, J. *Nano Energy* **2015,** *14,* 236–244. doi:10.1016/j.nanoen.2014.09.036
70. Lu, Y. C.; Wu, H.; Yang, Q. Q.; Ping, J. F.; Wu, J.; Liu, J. *Adv. Sustainable Syst.* **2019,** *3,* 1900012. doi:10.1002/adsu.201900012
71. Zhang, W.; Guo, R.; Sun, J.; Dang, L.; Liu, Z.; Lei, Z.; Sun, Q. *J. Colloid Interface Sci.* **2019,** *553,* 705–712. doi:10.1016/j.jcis.2019.06.048
72. Guo, L.; Zhong, C.; Cao, J.; Hao, Y.; Lei, M.; Bi, K.; Sun, Q.; Wang, Z. L. *Nano Energy* **2019,** *62,* 513–520. doi:10.1016/j.nanoen.2019.05.067
73. Kim, H.; Kim, B. J.; Sun, Q.; Kang, M. S.; Cho, J. H. *Adv. Electron. Mater.* **2016,** *2,* 1600122. doi:10.1002/aelm.201600122
74. Park, J. H.; Sun, Q.; Choi, Y.; Lee, S.; Lee, D. Y.; Kim, Y. H.; Cho, J. H. *ACS Appl. Mater. Interfaces* **2016,** *8,* 15543–15550. doi:10.1021/acsami.6b04340
75. Sun, Q.; Seung, W.; Kim, B. J.; Seo, S.; Kim, S.-W.; Cho, J. H. *Adv. Mater. (Weinheim, Ger.)* **2015,** *27,* 3411–3417. doi:10.1002/adma.201500582
76. Choi, Y.; Sun, Q.; Hwang, E.; Lee, Y.; Lee, S.; Cho, J. H. *ACS Nano* **2015,** *9,* 4354–4361. doi:10.1021/acsnano.5b01791
77. Sun, Q.; Lee, S. J.; Kang, H.; Gim, Y.; Park, H. S.; Cho, J. H. *Nanoscale* **2015,** *7,* 6798–6804. doi:10.1039/c5nr00777a
78. Sun, Q.; Kim, D. H.; Park, S. S.; Lee, N. Y.; Zhang, Y.; Lee, J. H.; Cho, K.; Cho, J. H. *Adv. Mater. (Weinheim, Ger.)* **2014,** *26,* 4735–4740. doi:10.1002/adma.201400918
79. Kim, S.; Choi, Y. J.; Woo, H. J.; Sun, Q.; Lee, S.; Kang, M. S.; Song, Y. J.; Wang, Z. L.; Cho, J. H. *Nano Energy* **2018,** *50,* 598–605. doi:10.1016/j.nanoen.2018.06.010
80. Parandeh, S.; Kharaziha, M.; Karimzadeh, F. *Nano Energy* **2019,** *59,* 412–421. doi:10.1016/j.nanoen.2019.02.058
81. Fan, Y. J.; Meng, X. S.; Li, H. Y.; Kuang, S. Y.; Zhang, L.; Wu, Y.; Wang, Z. L.; Zhu, G. *Adv. Mater. (Weinheim, Ger.)* **2017,** *29,* 1603115. doi:10.1002/adma.201603115
82. Jang, S.; Kim, H.; Oh, J. H. *Nanoscale* **2017,** *9,* 13034–13041. doi:10.1039/c7nr04610c
83. Henniker, J. *Nature* **1962,** *196,* 474. doi:10.1038/196474a0
84. Liu, C.; Bard, A. J. *Nat. Mater.* **2008,** *7,* 505–509. doi:10.1038/nmat2160
85. Baytekin, H. T.; Patashinski, A. Z.; Branicki, M.; Baytekin, B.; Soh, S.; Grzybowski, B. A. *Science* **2011,** *333,* 308–312. doi:10.1126/science.1201512
86. Wang, Z. L.; Wang, A. C. *Mater. Today* **2019,** *30,* 34–51. doi:10.1016/j.mattod.2019.05.016
87. Wu, C.; Wang, A. C.; Ding, W.; Guo, H.; Wang, Z. L. *Adv. Energy Mater.* **2019,** *9,* 1802906. doi:10.1002/aenm.201802906
88. Liu, C.-y.; Bard, A. J. *Chem. Phys. Lett.* **2009,** *480,* 145–156. doi:10.1016/j.cplett.2009.08.045
89. Mizes, H. A.; Conwell, E. M.; Salamida, D. P. *Appl. Phys. Lett.* **1990,** *56,* 1597–1599. doi:10.1063/1.103139
90. Xu, C.; Zi, Y.; Wang, A. C.; Zou, H.; Dai, Y.; He, X.; Wang, P.; Wang, Y.-C.; Feng, P.; Li, D.; Wang, Z. L. *Adv. Mater. (Weinheim, Ger.)* **2018,** *30,* 1706790. doi:10.1002/adma.201706790
91. Xu, C.; Wang, A. C.; Zou, H.; Zhang, B.; Zhang, C.; Zi, Y.; Pan, L.; Wang, P.; Feng, P.; Lin, Z.; Wang, Z. L. *Adv. Mater. (Weinheim, Ger.)* **2018,** *30,* 1803968. doi:10.1002/adma.201803968
92. Zang, X.; Shen, C.; Chu, Y.; Li, B.; Wei, M.; Zhong, J.; Sanghadasa, M.; Lin, L. *Adv. Mater. (Weinheim, Ger.)* **2018,** *30,* 1800062. doi:10.1002/adma.201800062
93. Feng, Y.; Zheng, Y.; Rahman, Z. U.; Wang, D.; Zhou, F.; Liu, W. *J. Mater. Chem. A* **2016,** *4,* 18022–18030. doi:10.1039/c6ta07288g
94. Chen, S.; Jiang, J.; Xu, F.; Gong, S. *Nano Energy* **2019,** *61,* 69–77. doi:10.1016/j.nanoen.2019.04.043

95. Cui, P.; Parida, K.; Lin, M.-F.; Xiong, J.; Cai, G.; Lee, P. S. *Adv. Mater. Interfaces* **2017,** *4,* 1700651. doi:10.1002/admi.201700651
96. Xia, K.; Zhang, H.; Zhu, Z.; Xu, Z. *Sens. Actuators, A* **2018,** *272,* 28–32. doi:10.1016/j.sna.2018.01.054
97. Sahatiya, P.; Kannan, S.; Badhulika, S. *Appl. Mater. Today* **2018,** *13,* 91–99. doi:10.1016/j.apmt.2018.08.009
98. Gao, B.; Wang, X.; Li, T.; Feng, Z.; Wang, C.; Gu, Z. *Adv. Mater. Technol. (Weinheim, Ger.)* **2019,** *4,* 1800392. doi:10.1002/admt.201800392
99. Lee, B. W.; Orr, D. E. The TriboElectric Series. https://www.alphalabinc.com/triboelectric-series/.
100. Zou, H.; Zhang, Y.; Guo, L.; Wang, P.; He, X.; Dai, G.; Zheng, H.; Chen, C.; Wang, A. C.; Xu, C.; Wang, Z. L. *Nat. Commun.* **2019,** *10,* 1427. doi:10.1038/s41467-019-09461-x
101. Liu, J.; Yang, C.; Wu, H.; Lin, Z.; Zhang, Z.; Wang, R.; Li, B.; Kang, F.; Shi, L.; Wong, C. P. *Energy Environ. Sci.* **2014,** *7,* 3674–3682. doi:10.1039/c4ee01995d
102. Siegel, A. C.; Phillips, S. T.; Dickey, M. D.; Lu, N.; Suo, Z.; Whitesides, G. M. *Adv. Funct. Mater.* **2010,** *20,* 28–35. doi:10.1002/adfm.200901363
103. Fan, X.; Chen, J.; Yang, J.; Bai, P.; Li, Z.; Wang, Z. L. *ACS Nano* **2015,** *9,* 4236–4243. doi:10.1021/acsnano.5b00618
104. Kim, J.-H.; Hong, S. H.; Seong, K.-d.; Seo, S. *Adv. Funct. Mater.* **2014,** *24,* 2404–2408. doi:10.1002/adfm.201303478
105. Kang, H.; Zhao, C.; Huang, J.; Ho, D. H.; Megra, Y. T.; Suk, J. W.; Sun, J.; Wang, Z. L.; Sun, Q.; Cho, J. H. *Adv. Funct. Mater.* **2019,** *29,* 1903580. doi:10.1002/adfm.201903580
106. Ho, D. H.; Song, R.; Sun, Q.; Park, W.-H.; Kim, S. Y.; Pang, C.; Kim, D. H.; Kim, S.-Y.; Lee, J.; Cho, J. H. *ACS Appl. Mater. Interfaces* **2017,** *9,* 44678–44686. doi:10.1021/acsami.7b15999
107. Ho, D. H.; Sun, Q.; Kim, S. Y.; Han, J. T.; Kim, D. H.; Cho, J. H. *Adv. Mater. (Weinheim, Ger.)* **2016,** *28,* 2601–2608. doi:10.1002/adma.201505739
108. Xu, S.; Guo, L.; Sun, Q.; Wang, Z. L. *Adv. Funct. Mater.* **2019,** *29,* 1808737. doi:10.1002/adfm.201808737
109. Park, J. H.; Park, K. J.; Jiang, T.; Sun, Q.; Huh, J.-H.; Wang, Z. L.; Lee, S.; Cho, J. H. *Nano Energy* **2017,** *38,* 412–418. doi:10.1016/j.nanoen.2017.05.062
110. Gao, G.; Yu, J.; Yang, X.; Pang, Y.; Zhao, J.; Pan, C.; Sun, Q.; Wang, Z. L. *Adv. Mater. (Weinheim, Ger.)* **2019,** *31,* 1806905. doi:10.1002/adma.201806905
111. Yang, X.; Han, J.; Yu, J.; Chen, Y.; Zhang, H.; Ding, M.; Jia, C.; Sun, J.; Sun, Q.; Wang, Z. L. *ACS Nano* **2020,** *14,* 8668–8677. doi:10.1021/acsnano.0c03030
112. Zhang, G.; Liao, Q.; Zhang, Z.; Liang, Q.; Zhao, Y.; Zheng, X.; Zhang, Y. *Adv. Sci.* **2016,** *3,* 1500257. doi:10.1002/advs.201500257
113. Oh, H.; Kwak, S. S.; Kim, B.; Han, E.; Lim, G.-H.; Kim, S.-W.; Lim, B. *Adv. Funct. Mater.* **2019,** *29,* 1904066. doi:10.1002/adfm.201904066
114. Xia, K.; Zhu, Z.; Zhang, H.; Du, C.; Fu, J.; Xu, Z. *Nano Energy* **2019,** *56,* 400–410. doi:10.1016/j.nanoen.2018.11.071
115. Sadeghi, M.; Delparastan, P.; Pierre, A.; Arias, A. C. *Adv. Electron. Mater.* **2020,** *6,* 1901207. doi:10.1002/aelm.201901207
116. Yang, X.; Hu, G.; Gao, G.; Chen, X.; Sun, J.; Wan, B.; Zhang, Q.; Qin, S.; Zhang, W.; Pan, C.; Sun, Q.; Wang, Z. L. *Adv. Funct. Mater.* **2019,** *29,* 1807837. doi:10.1002/adfm.201807837
117. Zhang, H.; Yu, J.; Yang, X.; Gao, G.; Qin, S.; Sun, J.; Ding, M.; Jia, C.; Sun, Q.; Wang, Z. L. *ACS Nano* **2020,** *14,* 3461–3468. doi:10.1021/acsnano.9b09549
118. Yang, X.; Yu, J.; Zhao, J.; Chen, Y.; Gao, G.; Wang, Y.; Sun, Q.; Wang, Z. L. *Adv. Funct. Mater.* **2020,** *30,* 2002506. doi:10.1002/adfm.202002506
119. Zhang, Q.; Jiang, T.; Ho, D.; Qin, S.; Yang, X.; Cho, J. H.; Sun, Q.; Wang, Z. L. *ACS Nano* **2018,** *12,* 254–262. doi:10.1021/acsnano.7b06126
120. Sun, Q.; Ho, D. H.; Choi, Y.; Pan, C.; Kim, D. H.; Wang, Z. L.; Cho, J. H. *ACS Nano* **2016,** *10,* 11037–11043. doi:10.1021/acsnano.6b05895
121. Chen, Y.; Gao, G.; Zhao, J.; Zhang, H.; Yu, J.; Yang, X.; Zhang, Q.; Zhang, W.; Xu, S.; Sun, J.; Meng, Y.; Sun, Q. *Adv. Funct. Mater.* **2019,** *29,* 1900959. doi:10.1002/adfm.201900959
122. Shi, K.; Huang, X.; Sun, B.; Wu, Z.; He, J.; Jiang, P. *Nano Energy* **2019,** *57,* 450–458. doi:10.1016/j.nanoen.2018.12.076
123. Zhao, J.; Wei, Z.; Zhang, Q.; Yu, H.; Wang, S.; Yang, X.; Gao, G.; Qin, S.; Zhang, G.; Sun, Q.; Wang, Z. L. *ACS Nano* **2019,** *13,* 582–590. doi:10.1021/acsnano.8b07477
124. Gao, G.; Wan, B.; Liu, X.; Sun, Q.; Yang, X.; Wang, L.; Pan, C.; Wang, Z. L. *Adv. Mater. (Weinheim, Ger.)* **2018,** *30,* 1705088. doi:10.1002/adma.201705088
125. Kim, I.; Jeon, H.; Kim, D.; You, J.; Kim, D. *Nano Energy* **2018,** *53,* 975–981. doi:10.1016/j.nanoen.2018.09.060
126. Wu, C.; Kima, T. W.; Sung, S.; Park, J. H.; Li, F. *Nano Energy* **2018,** *44,* 279–287. doi:10.1016/j.nanoen.2017.11.080
127. Schenk, M.; Guest, S. D. *Proc. Natl. Acad. Sci. U. S. A.* **2013,** *110,* 3276–3281. doi:10.1073/pnas.1217998110
128. Mu, J.; Hou, C.; Wang, H.; Li, Y.; Zhang, Q.; Zhu, M. *Sci. Adv.* **2015,** *1,* e1500533. doi:10.1126/sciadv.1500533
129. Yang, P.-K.; Lin, Z.-H.; Pradel, K. C.; Lin, L.; Li, X.; Wen, X.; He, J.-H.; Wang, Z. L. *ACS Nano* **2015,** *9,* 901–907. doi:10.1021/nn506631t
130. Miura, K. *Rep. - Univ. Tokyo, Inst. Space Aeronaut. Sci.* **1969,** *34,* 141–163.
131. Dudte, L. H.; Vouga, E.; Tachi, T.; Mahadevan, L. *Nat. Mater.* **2016,** *15,* 583–588. doi:10.1038/nmat4540
132. Chen, C.; Howard, D.; Zhang, S. L.; Do, Y.; Sun, S.; Cheng, T.; Wang, Z. L.; Abowd, G. D.; Oh, H. SPIN (Self-powered Paper Interfaces). In *Proceedings of the Fourteenth International Conference on Tangible, Embedded, and Embodied Interaction,* 2020; pp 413–442. doi:10.1145/3374920.3374946
133. Wang, W.; Li, C.; Rodrigue, H.; Yuan, F.; Han, M.-W.; Cho, M.; Ahn, S.-H. *Adv. Funct. Mater.* **2017,** *27,* 1604214. doi:10.1002/adfm.201604214
134. Zhou, C.; Yang, Y.; Sun, N.; Wen, Z.; Cheng, P.; Xie, X.; Shao, H.; Shen, Q.; Chen, X.; Liu, Y.; Wang, Z. L.; Sun, X. *Nano Res.* **2018,** *11,* 4313–4322. doi:10.1007/s12274-018-2018-8
135. Zhang, H.; Wang, H.; Zhang, J.; Zhang, Z.; Yu, Y.; Luo, J.; Dong, S. *Sens. Actuators, A* **2020,** *302,* 111806. doi:10.1016/j.sna.2019.111806
136. Wu, C.; Wang, X.; Lin, L.; Guo, H.; Wang, Z. L. *ACS Nano* **2016,** *10,* 4652–4659. doi:10.1021/acsnano.6b00949
137. Dong, B.; Shi, Q.; Yang, Y.; Wen, F.; Zhang, Z.; Lee, C. *Nano Energy* **2021,** *79,* 105414. doi:10.1016/j.nanoen.2020.105414
138. Liu, H.; Fu, H.; Sun, L.; Lee, C.; Yeatman, E. M. *Renewable Sustainable Energy Rev.* **2020,** *137,* 110473. doi:10.1016/j.rser.2020.110473
139. Liu, H.; Zhong, J.; Lee, C.; Lee, S.-W.; Lin, L. *Appl. Phys. Rev.* **2018,** *5,* 041306. doi:10.1063/1.5074184
140. Shi, Q.; Zhang, Z.; He, T.; Sun, Z.; Wang, B.; Feng, Y.; Shan, X.; Salam, B.; Lee, C. *Nat. Commun.* **2020,** *11,* 4609. doi:10.1038/s41467-020-18471-z

141. Wen, F.; He, T.; Liu, H.; Chen, H.-Y.; Zhang, T.; Lee, C. *Nano Energy* **2020,** *78,* 105155. doi:10.1016/j.nanoen.2020.105155
142. Wen, F.; Sun, Z.; He, T.; Shi, Q.; Zhu, M.; Zhang, Z.; Li, L.; Zhang, T.; Lee, C. *Adv. Sci.* **2020,** *7,* 2000261. doi:10.1002/advs.202000261
143. Zhu, M.; He, T.; Lee, C. *Appl. Phys. Rev.* **2020,** *7,* 031305. doi:10.1063/5.0016485
144. Zhu, M.; Yi, Z.; Yang, B.; Lee, C. *Nano Today* **2021,** *36,* 101016. doi:10.1016/j.nantod.2020.101016
145. Karmakar, S.; Kumbhakar, P.; Maity, K.; Mandal, D.; Kumbhakar, P. *Nano Energy* **2019,** *63,* 103831. doi:10.1016/j.nanoen.2019.06.027
146. Liu, H.; Zhao, G.; Wu, M.; Liu, Z.; Xiang, D.; Wu, C.; Cheng, Y.; Wang, H.; Wang, Z. L.; Li, L. *Nano Energy* **2019,** *66,* 104161. doi:10.1016/j.nanoen.2019.104161
147. Xia, K.; Du, C.; Zhu, Z.; Wang, R.; Zhang, H.; Xu, Z. *Appl. Mater. Today* **2018,** *13,* 190–197. doi:10.1016/j.apmt.2018.09.005
148. Zhong, Q.; Zhong, J.; Cheng, X.; Yao, X.; Wang, B.; Li, W.; Wu, N.; Liu, K.; Hu, B.; Zhou, J. *Adv. Mater. (Weinheim, Ger.)* **2015,** *27,* 7130–7136. doi:10.1002/adma.201502470
149. Zhang, L.; Xue, F.; Du, W.; Han, C.; Zhang, C.; Wang, Z. *Nano Res.* **2014,** *7,* 1215–1223. doi:10.1007/s12274-014-0484-1
150. Wang, S.; Lin, L.; Wang, Z. L. *Nano Energy* **2015,** *11,* 436–462. doi:10.1016/j.nanoen.2014.10.034
151. Ejehi, F.; Mohammadpour, R.; Asadian, E.; Sasanpour, P.; Fardindoost, S.; Akhavan, O. *Sci. Rep.* **2020,** *10,* 7312. doi:10.1038/s41598-020-64490-7
152. Zhao, F.; Cheng, H.; Zhang, Z.; Jiang, L.; Qu, L. *Adv. Mater. (Weinheim, Ger.)* **2015,** *27,* 4351–4357. doi:10.1002/adma.201501867
153. Wang, Z. L.; Chen, J.; Lin, L. *Energy Environ. Sci.* **2015,** *8,* 2250–2282. doi:10.1039/c5ee01532d
154. He, X.; Zi, Y.; Yu, H.; Zhang, S. L.; Wang, J.; Ding, W.; Zou, H.; Zhang, W.; Lu, C.; Wang, Z. L. *Nano Energy* **2017,** *39,* 328–336. doi:10.1016/j.nanoen.2017.06.046
155. Cheung, M. M. S.; Cao, C. *Constr. Build. Mater.* **2013,** *45,* 199–207. doi:10.1016/j.conbuildmat.2013.04.010
156. Eltai, E. O.; Scantlebury, J. D.; Koroleva, E. V. *Prog. Org. Coat.* **2012,** *73,* 8–13. doi:10.1016/j.porgcoat.2011.08.012
157. Cao, X.; Jie, Y.; Wang, N.; Wang, Z. L. *Adv. Energy Mater.* **2016,** *6,* 1600665. doi:10.1002/aenm.201600665
158. Lelieveld, J.; Evans, J. S.; Fnais, M.; Giannadaki, D.; Pozzer, A. *Nature* **2015,** *525,* 367–371. doi:10.1038/nature15371
159. Jeong, C. K.; Baek, K. M.; Niu, S.; Nam, T. W.; Hur, Y. H.; Park, D. Y.; Hwang, G.-T.; Byun, M.; Wang, Z. L.; Jung, Y. S.; Lee, K. J. *Nano Lett.* **2014,** *14,* 7031–7038. doi:10.1021/nl503402c
160. Perez-Roa, R. E.; Anderson, M. A.; Rittschof, D.; Orihuela, B.; Wendt, D.; Kowalke, G. L.; Noguera, D. R. *Biofouling* **2008,** *24,* 177–184. doi:10.1080/08927010801975725
161. Amr, A.-G.; Schoenbach, K. H. *IEEE Trans. Plasma Sci.* **2000,** *28,* 115–121. doi:10.1109/27.842878
162. Shi, K.; Zou, H.; Sun, B.; Jiang, P.; He, J.; Huang, X. *Adv. Funct. Mater.* **2019,** *30,* 1904536. doi:10.1002/adfm.201904536
163. Yang, H.; Deng, M.; Tang, Q.; He, W.; Hu, C.; Xi, Y.; Liu, R.; Wang, Z. L. *Adv. Energy Mater.* **2019,** *9,* 1901149. doi:10.1002/aenm.201901149
164. Xia, K.; Zhu, Z.; Zhang, H.; Du, C.; Wang, R.; Xu, Z. *IEEE Trans. Nanotechnol.* **2018,** *17,* 1217–1223. doi:10.1109/tnano.2018.2869934
165. Xia, K.; Zhu, Z.; Zhang, H.; Du, C.; Xu, Z.; Wang, R. *Nano Energy* **2018,** *50,* 571–580. doi:10.1016/j.nanoen.2018.06.019

License and Terms

BEILSTEIN JOURNAL OF NANOTECHNOLOGY

Toward graphene textiles in wearable eye tracking systems for human–machine interaction

Ata Jedari Golparvar[1] and Murat Kaya Yapici*[1,2,3]

Full Research Paper

Open Access

Address:
[1]Faculty of Engineering and Natural Sciences, Sabanci University, TR-34956 Istanbul, Turkey, [2]Sabanci University SUNUM Nanotechnology Research Center, TR-34956 Istanbul, Turkey and [3]Department of Electrical Engineering, University of Washington, Seattle, WA 98195, USA

Email:
Murat Kaya Yapici* - mkyapici@sabanciuniv.edu

* Corresponding author

Keywords:
electrooculography (EOG); flexible electronics; graphene; human–computer interaction (HCI); human–machine interface (HMI); personal assistive device (PAD); wearable smart textile

Beilstein J. Nanotechnol. **2021,** *12,* 180–189.
https://doi.org/10.3762/bjnano.12.14

Received: 19 November 2020
Accepted: 20 January 2021
Published: 11 February 2021

This article is part of the thematic issue "Nanogenerators and flexible electronics".

Guest Editor: Y. Mao

Abstract

The study of eye movements and the measurement of the resulting biopotential, referred to as electrooculography (EOG), may find increasing use in applications within the domain of activity recognition, context awareness, mobile human–computer and human–machine interaction (HCI/HMI), and personal medical devices; provided that, seamless sensing of eye activity and processing thereof is achieved by a truly wearable, low-cost, and accessible technology. The present study demonstrates an alternative to the bulky and expensive camera-based eye tracking systems and reports the development of a graphene textile-based personal assistive device for the first time. This self-contained wearable prototype comprises a headband with soft graphene textile electrodes that overcome the limitations of conventional "wet" electrodes, along with miniaturized, portable readout electronics with real-time signal processing capability that can stream data to a remote device over Bluetooth. The potential of graphene textiles in wearable eye tracking and eye-operated remote object interaction is demonstrated by controlling a mouse cursor on screen for typing with a virtual keyboard and enabling navigation of a four-wheeled robot in a maze, all utilizing five different eye motions initiated with a single channel EOG acquisition. Typing speeds of up to six characters per minute without prediction algorithms and guidance of the robot in a maze with four 180° turns were successfully achieved with perfect pattern detection accuracies of 100% and 98%, respectively.

Introduction

Eye tracking technologies have many applications ranging from behavioral analytics to healthcare. For a brand leader, the prospect of seeing the world literally through consumer's eyes, as opposed to relying on traditional market research methods, is the reason that makes eye tracking a clear winner in understanding the triggering subconscious facts in decision making. In entertainment and virtual reality applications, eye tracking enables a whole new interaction method with contents, and it could also add new security measures through retinal scanning.

In healthcare, eye tracking enables devices to help ease a disabled individual's challenging life using their eye motions. Thousands of people suffer from extreme disabilities such as severe cerebral palsy and amyotrophic lateral sclerosis (ALS), which deprive them of muscular abilities. It is estimated that approximately 450,000 people worldwide are diagnosed with ALS, and in the United States, the incidence of ALS is two per hundred thousand people [1]. Therefore, the advancement of eye tracking technologies is critical for developing assistive devices and human–computer interaction (HCI) platforms for people with disabilities.

Current technologies for eye tracking, however, by being either invasive, expensive, or bulky [2-4] do not address the requirements of a readily usable product in HCI intended for widespread use; and fail to meet the fundamental characteristics of wearability in terms of size miniaturization, low-power operation, ergonomics, and aesthetics. For example, although camera-based eye tracking setups solve the invasivity issue and display long-term functionality, they are hardly affordable due to their hardware (e.g., camera) and image processing requirements. Additionally, in videooculography, the camera has to be positioned at a location suitable to capture eye movements (EMs), which limits the portability of such systems. Therefore, effort has been placed to investigate different methods to utilize EMs in wearable applications.

To this end, electrooculography (EOG) is an economical (a typical EOG setup could be assembled at a cost of under 100 EUR [5]), non-invasive, and reliable method for acquiring biopotential signals around the eyes, and may overcome the limitations of prior technologies. EOG is essentially based on a simple model of the human eye as a dipole with a permanent potential difference between its forward and backward facing spots (i.e., the cornea-retinal potential of 0.4–1.0 mV where the cornea is positive) [6]. This potential difference sets up an electrical field in the tissues surrounding the eye, which generates an electric field [7]. Two electrodes around the eyes can locate the field vector rotation, which creates a more positive charge in the electrode that the cornea is approaching [8]. The biopotentials resulting from eye activity, which are in fact waveforms that relate the dipole fluctuations to the type of eye movement, are referred to as electrooculograms; while the specific technique for recording is known as electrooculography [9]. Electrooculograms also occur in total darkness, when the eyes are closed, even in visually impaired people [10].

So far, several EOG-based rehabilitation systems were developed to mitigate everyday life challenges of and provide some means of communication for people with locked-in syndromes who have extremely limited peripheral mobility but still retain their eye motor coordination [10]. Similarly, basic deliberate eye movements such as saccades (i.e., fast eye movements), fixations (i.e., the duration between two saccades when the gaze is fixated at a point), and blinks have been used for hands-free operation in HCI and human–machine interfaces (HMIs) [11]. With the help of HCI and HMIs one can emulate a computer mouse [12], type using a virtual keyboard [13], drive a wheelchair or control a robotic arm [14], change TV channels [15], and even improve user experience on virtual reality gaming [16] or smartphone operation [17]. Along these lines, in the healthcare domain, as part of a hospital alarm system, EOG-based switches provided immobile patients with a safe and reliable way of signaling an alarm [18]. Other promising studies reported the direct input of numbers, letters of the English alphabet, and Japanese Katakana symbols by eye movements to further help users to communicate complicated messages in a relatively short time [19].

However, despite the various demonstrators of wearable EOG devices in the literature, which prove that EOG is a measurement technique that is reliable, easy to operate, and can be made cosmetically appealing, EOG-based devices still struggle to penetrate the wearables market, and their full potential has not been realized due to limitations of the sensing electrodes [20-22]. The combination of graphene with ordinary textiles presents a viable solution to this limitation [23]. Therefore, this work reports an alternative eye tracking system based on monitoring the ocular biopotential. It demonstrates the first graphene textile-based wearable personal assistive device for interacting with machines and controlling objects. With the developed wearable system prototype, seamless "eye-operated" remote control of objects is achieved, including cursor motion on screen for typing of text and the motion of a four-wheeled car; both of which demonstrate the vast potential of graphene textiles as an enabler of wearable assistive technologies.

Materials and Methods

Synthesis of graphene textiles and electrode preparation

The developed process to synthesize conductive graphene textiles is based on a low-cost and scalable, three-step approach in which conformal layers of graphene were formed on various fabrics including nylon, polyester, cotton, and Kevlar (Figure 1a). The textiles were first dipped into graphene oxide (GO) suspension prepared by the modified Hummer's method, dried to allow for the layering of GO on the textiles, treated by reducing agents (e.g., hydrazine or hydrogen iodide), and rinsed with distilled water to form a stable graphene coating on the textiles. The prepared graphene textiles were then cut into pieces (ca. 3 × 3 cm) and mounted on flexible, polyethylene-based foam paddings, which were sandwiched between metallic snap fasteners in order to establish an electrical connection with the front-end circuitry. In this way, “passive” graphene textile electrodes were formed, which can be directly used to capture surface biopotentials without further modification. Conductivity measurements showed resistance values of the textiles between 1 and 10 kΩ and skin-electrode impedance values from 87.5 kΩ (at 10 Hz) to 11.6 kΩ (at 1 kHz). Additionally, since the operation of the textile electrodes relies on charge flow, moisture and sweat can increase the interface conductivity of the skin electrodes and provide an even better signal-to-noise ratio (SNR) in long-term monitoring applications in contrast to “wet” electrodes, the functionality of which degrades over time [23].

However, one common issue in dry electrodes is the relatively high skin-electrode contact impedance, which causes susceptibility to physical movements and power line interferences resulting in signal distortions. While the flexible, foldable nature of textile electrodes promotes wearability, it can adversely lead to dynamic contact conditions and, thereby, motion artifacts in the acquired signal. A strategy to minimize this effect, which was investigated in this work, is to reduce the impedance of the signal source by utilizing a buffer amplifier, which essentially converts the high-impedance signal to a low-impedance signal. Figure 1b shows the circuit schematic and the components for building “active” graphene textile electrodes. The components are an operational amplifier (OPA2365, Texas Instruments, USA) with a high input impedance, two resistors, and one capacitor. A small-sized printed circuit board (ca. 0.9 × 1.3 cm) was designed and implemented to demonstrate a proof of concept. It allowed for robust integration and an electrical interface between the buffer-circuit components and the graphene textiles to form “active” electrodes.

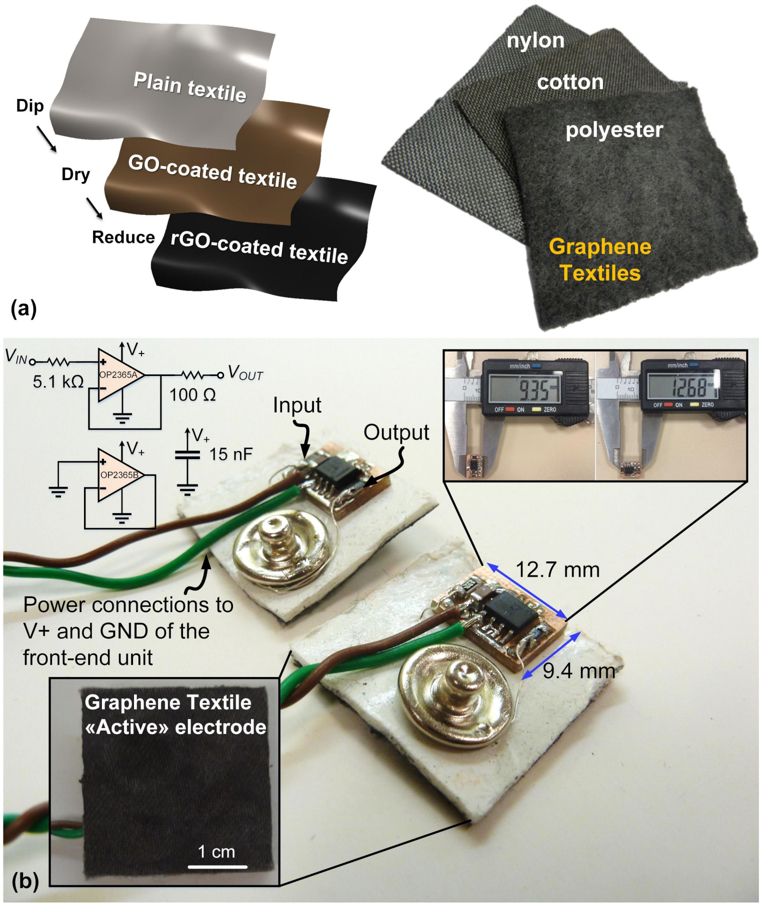

Figure 1: (a) Schematic of the three-step process to obtain conformal graphene coatings on a variety of textiles including nylon, cotton, and polyester; (b) image of the graphene textile “active” electrode with integrated buffer circuitry along with component values and circuit schematic. V_{in} is connected to the graphene textile, and V_{out} is connected to the snap button. Both are used to provide the connection of the “active” textile electrode to the signal acquisition unit; insets show the front side of the electrode assembly with the graphene textile and the dimensions of the miniaturized-PCB on the rear side of the electrode.

Wearable system prototype

One of the fundamental obstacles regarding the actual wearability of electronic systems is the lack of robust integration schemes for the interface between soft sensing electrodes and rigid electronic components. We have addressed this issue by following a system-level design perspective. A miniaturized, battery-powered, portable EOG acquisition unit with wireless data transmission capability was realized and directly integrated into a wearable headband, which also contained the graphene textile electrodes (Figure 2). The electrodes were mounted in a newly introduced manner such that potential crosstalk between channels was eliminated. Also, electrode count and hardware complexity were minimized by removing the vertical acquisition channel without loss of control commands triggered by vertical EMs [24,25]. The readout electronics could be implemented in a small form factor (ca. 4 × 6 cm) that is easily attachable on a wearable custom-made headband. The front half of the headband was kept fairly non-stretchable to maintain the electrode locations on the forehead; while the rear side was made of elastic straps enabling size adjustment to ensure a stable skin–electrode contact.

As shown in the detailed hardware schematic in Figure 2, the circuit has second-order and fourth-order Butterworth high-pass and low-pass filters with cut-off frequencies of 0.5 Hz and 10 Hz, respectively, both based on Sallen–Key topology. The preferred instrumentation amplifier (INA122, Texas Instruments, USA) is specifically designed for battery-powered applications with the capability of running with a single supply. Similarly, the other operation amplifiers used in the design were selected due to their single-supply and rail-to-rail features (OPA2365, Texas Instruments, USA) and are suitable for portable applications. For adjusting the gain in the post-amplification stage, a digitally programmable voltage divider (MAX5421, Maxim, USA) was used so that the gain can be configured at the software level through a graphical user interface (GUI). As a common practice in portable devices nowadays, a lithium-ion/polymer battery with a rating of 3.7 V and 500 mAh was chosen to power the system. The battery charge management circuitry and DC–DC boost converter were based on a MCP73831 (Microchip, USA) and a TPS61090 (Texas Instruments, USA), respectively.

To split the regulated 5 V, a rail splitter (TLE2426, Texas Instruments, USA) was used, which is essentially a voltage divider with a buffer circuitry to prevent it from becoming unbalanced. The currents that can be typically handled by power splitters are small (20–40 mA). Hence, additional buffers with higher current ratings were accommodated in the power management unit as a safety margin, despite the typically low levels of currents drawn by the signal acquisition unit. To adjust the settings and to stream data to a computer, a popular off-the-shelf Bluetooth module (HC06) was used. A custom-designed GUI based on LabVIEW (National Instruments, USA) was implemented at the receiver end, enabling user-friendly operation, calibration, gain adjustment, and event monitoring.

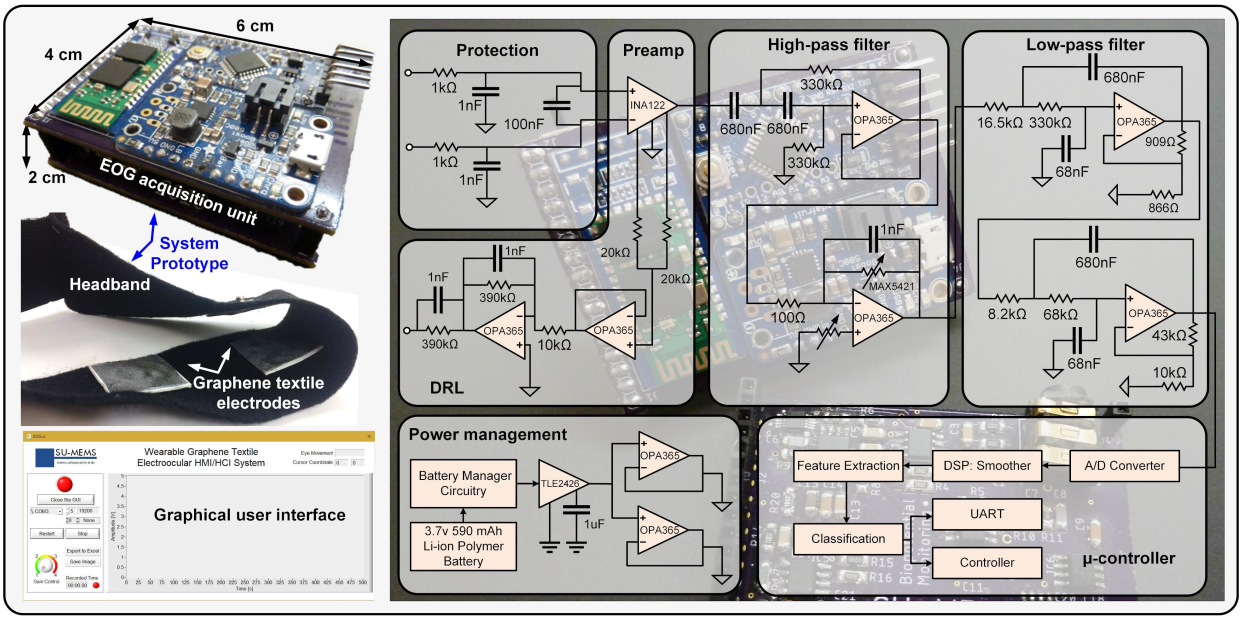

Figure 2: Overview of the system prototype showing the detailed hardware-level schematic of the portable, battery-powered, EOG acquisition unit including on-board filtering and gain stages, power management section, microcontroller unit to process and stream data wirelessly to a computer along with a custom-designed user interface, and the wearable headband with soft graphene textile electrodes.

In the current version of the embedded system, the Bluetooth coverage is ca. 5 m. The power consumption of the circuitry is ca. 80 mW when the Bluetooth device is not paired and ca. 150 mW when it is paired, which allows the battery to run in the paired mode for about 4 h continuously without recharge. These measurements can be further improved by implementing sleep-mode functions to a microcontroller and upgrading the Bluetooth module to a Bluetooth low-energy (BLE) module, such as HM-10, which has low power consumption and offers a higher range up to several tens of meters.

Results and Discussion

Different eye movements along with a detection and classification algorithm having a success rate ranging from 85% up to 100% for detecting eleven different patterns over an hour-long EOG recording experiment [25] were utilized to develop a graphene textile-based wearable eye mouse and a wearable assistive system to control movements of a four-wheeled robot. The wearable eye mouse controlled a cursor on a PC screen and sent *x*–*y* coordinates of the cursor to the GUI. On the computer, the GUI uses the "SetCursorPos" and "mouse_event" functions of the Microsoft Windows User32.dll library to control cursor movement and blink actions, respectively. Swift horizontal eye movements (to the left or right) control the horizontal movement of the cursor in two directions. In contrast, slow eye movements control the cursor motion in vertical directions. Finally, voluntary blinking mimics the mouse click action. When swift or slow eye movements occur, the cursor starts to move in the defined direction at a preconfigured speed until it reaches the edge of the display or until a different eye movement changes the cursor motion. For instance, the cursor will move toward the left side after a swift left eye movement and stop and execute a click action when a blink of the eye occurs. Some additional actions were implemented for better control, such as "cursor stop", which stops the cursor motion at any point without causing a click action. For instance, when the cursor moves, either a swift left or a swift right eye movement can stop the cursor movement. In this way, the user can achieve accurate position control and fine-tune the cursor location when needed. Likewise, the "cursor snap" option was defined to allow for a rapid, discretized transition of the cursor from its existing location to the nearest key in the specified direction of motion.

To evaluate the performance of the graphene textile-based wearable eye mouse, two different tests were carried out. In the first case, a single participant was trained and asked to type a specific word, while the lateral or transverse movements of the cursor on the screen were continuous unless terminated by another command. In the second case, "cursor snap" was activated and five participants were requested to type five randomly selected character sequences of equal length. Figure 3 demonstrates the first testing scenario with the developed eye mouse and the recorded electrooculograms together with their interpretation. The aim here is first to open Microsoft Word Office and the Microsoft Windows virtual keyboard, to write a word, and, finally, to stop the GUI solely by eye movements. The different eye movements and corresponding cursor actions specific to the eye movements are summarized in Table 1, along with a representative sequence of movements needed to type "SUMEMS" and the measured duration for each step.

Speed and initial starting point of the cursor, and several other options are configurable in the GUI settings. In the first trial,

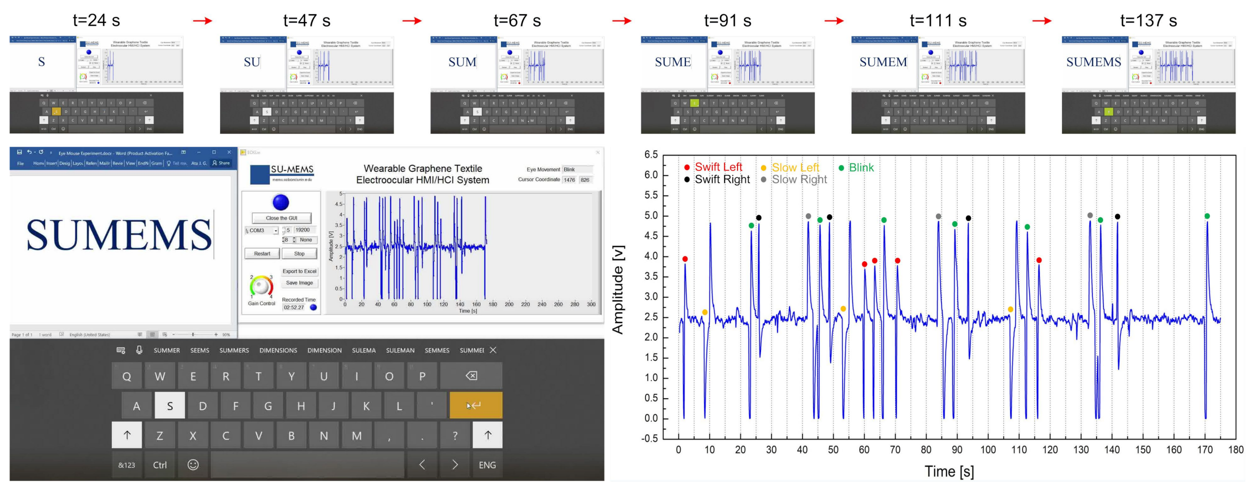

Figure 3: The first testing scenario shows the plot of induced EOG signals with inserted interpretations for each eye movement, which are used to mimic the movements of a mouse cursor to write "SUMEMS" (Sabanci University MEMS Group).

Table 1: Summary of eye movement types with corresponding cursor actions and a representative typing sequence.

Sequence	Type	Action	Duration [s]
1	swift left	left direction	6.5
2	slow left	down direction	14.7
3	blink	click “S”	instantaneous
4	swift right	right direction	15.7
5	slow right	up direction	3.3
6	blink	click “U”	instantaneous
7	swift right	right direction	4.9
8	slow left	down direction	6.1
9	swift left	stop	3.5
10	swift left	left direction	3.0
11	blink	click “M”	instantaneous
12	swift left	left direction	13.7
13	slow right	up direction	5.8
14	blink	click “E”	instantaneous
15	swift right	right direction	13.3
16	slow left	down direction	5.1
17	blink	click “M”	instantaneous
18	swift left	left direction	17.0
19	slow right	up direction	3.4
20	blink	click “S”	instantaneous
21	swift right	right direction	28.9
22	blink	click “Enter”	instantaneous

the cursor speed (pointer speed on screen) was kept slow and set to 1 pixel every 30 ms, which, on average, is translated to one character every ca. 23 s. This resulted in a total typing time of over 2 min for a 6-character word.

The cursor speed was gradually increased in subsequent trials to identify the upper limit on typing speed with the developed wearable eye mouse system. The fundamental constraint on increasing the cursor speed is the inherent transient response of electrooculograms and the detection algorithm to account for this behavior. On the occasion of an eye movement, a certain amount of time is required for the corresponding EOG signal to complete its waveform and reach a steady state, upon which the detection algorithm classifies the performed eye movement and executes the designated action. For instance, considering the case of a blink, which is attributed to the mouse click or “select” action, at cursor speeds above a maximum threshold, there is the possibility that the user attempts to click and select a specific letter but misses it due to the latency in command execution. In our trials with a trained participant, the cursor speed was optimized such that the participant was able to correctly type one character per approx. 10 s, which corresponds to a typing speed of six characters per minute (CPM), a more than two-fold increase in the typing speed compared to the first trial. This is a reasonably good speed for a thresholding-based algorithm approach in which a pattern detection accuracy of up to 100% was achieved, and in alignment with earlier EOG-based spellers, which range from 2.4 to 12 CPM [26].

If the eye mouse is to be used only to facilitate the typing on a virtual keyboard, then, to readily increase the typing speed even for a non-trained user, some software-level realizations can be implemented by applying a fixed coordinate system. That is, the cursor moves only to specific locations of the buttons of the virtual keyboard. For example, in a standard QWERTY keyboard, instead of performing one swift left eye movement to initiate continuous movement of the cursor from letter “A” to letter “K,” one can perform seven swifts left movements to traverse the cursor one at a time to its nearest neighbor in the initiated direction of movement (Figure 4a). Alternatively, five swift right movements can be performed to do the same task but in a comparatively faster way (Figure 4b).

To illustrate this, five volunteers have participated in a study to test the system by writing randomly generated six-letter sequences, summarized in Table 2, together with the typing duration. To train the volunteers, they were shortly briefed about which eye movement corresponds to which action, and they were asked to explore the device before the actual experiment, by trying to write their names. All volunteers reported they felt comfortable using the device shortly within merely 2–3 min.

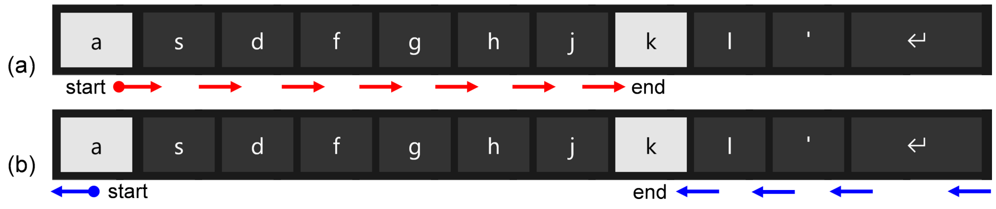

Figure 4: Diagram showing the two possible cursor movement directions to go from letter “A” to “K” in a standard QWERTY keyboard layout; path (a) could be implemented by seven swift left eye movements, and path (b) provides a faster route to reach the same destination by five swift right eye movements.

The shortest typing duration was 55 s, and the longest was 76 s, with an average typing speed of ca. 62 s for six characters or approx. 6 CPM. By implementing letter and word prediction algorithms, a further increase in typing speed can be expected [27].

Table 2: Summary of generated random letter sequences with corresponding typing duration using eye movements.

Subject	Random letter sequence	Duration [s]
1	p h n e x v	55
2	g z n b a y	69
3	l a w x s t	58
4	e m j b c b	53
5	g h e b v z	76

In recent years, there have been many studies on skin-compatible, body-worn devices, collectively referred to as wearable electronics, for applications ranging from energy harvesting to human health and motion monitoring [28-34]. In a second demonstration, we have investigated the potential of the developed graphene textile-based wearable system as an assistive device to remotely control objects, including the steering of a wheelchair using eye movements, which is critical for ALS patients. To show the feasibility of the developed system, the motion of an Arduino-based, custom-designed four-wheeled robot was controlled (Figure 5). In this experiment, eye blink and swift left and right eye movements initiate forward and backward motions, while slow right and left movements enable rotation to the right and left sides.

To record the signals, both the robot and the acquisition unit were paired with a laptop running the previously designed GUI with slight modifications for enabling simultaneous communication of the GUI with robot and EOG acquisition unit. However, in actual usage cases, the laptop can be eliminated by directly connecting the EOG unit to the robot. At the robot end, incoming commands are delivered to a DC motor driver (L298, STMicroelectronics, Switzerland) in the form of pulse-width modulation (PWM) signals with a configured duty cycle value (i.e., speed), which can be changed through settings. To simplify HRI and to improve the user control experience, forward/backward movements and rotation of the robot were preset at a given distance (ca. 15 cm) and a given angle (ca. 45°), both of which can be adjusted in the GUI. Based on this configuration, eye movements were used to steer the robot along the exit path of a maze without crossing the boundaries marked with black tape (Figure 6).

A total of 41 eye movements including 19 swift left EMs (forward), two swift right EMs (backward), seven slow left EMs (turn left), eleven slow right EMs (turn right), and a single blink (forward) action were performed and recorded over a duration of ca. 200 s. Analysis of the extracted video frames along with the recorded EOG waveforms revealed a detection accuracy of approx. 98%. Only one out of 41 eye movements was misinterpreted with the developed system, demonstrating

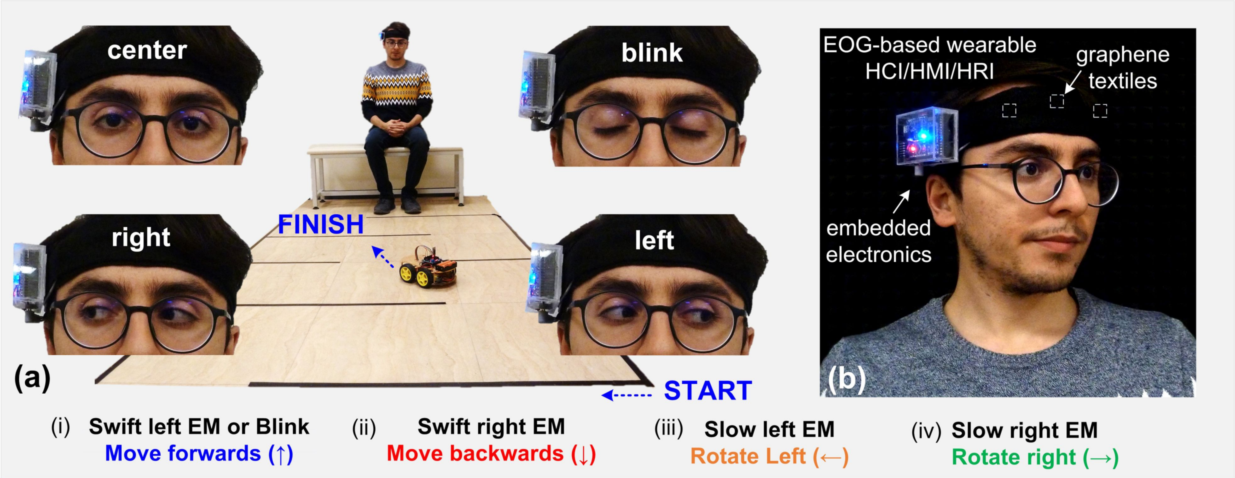

Figure 5: Overview of the second technology demonstrator for the wearable graphene textile-based assistive device for HMI applications. A four-wheeled robot is remotely controlled and steered in a maze. (a) Scenario-specific eye movements (EMs) allow one to steer the robot in different directions as follows: (i) swift left EM or blinking trigger forward motion (↑), (ii) swift right EM triggers backward motion (↓), (iii) slow left EM triggers rotation to the left (←), (iv) slow right EM triggers rotation to the right (→). Insets show images of the eye during different movements. This includes eyes when fixated at the center, while performing a voluntary blink, while performing a right move and fixated at the right, and while performing a left move and fixated at the left; (b) picture of the wearable eye tracker including smart headband with graphene textile electrodes and embedded electronics housed by an acrylic holder all mounted on the head.

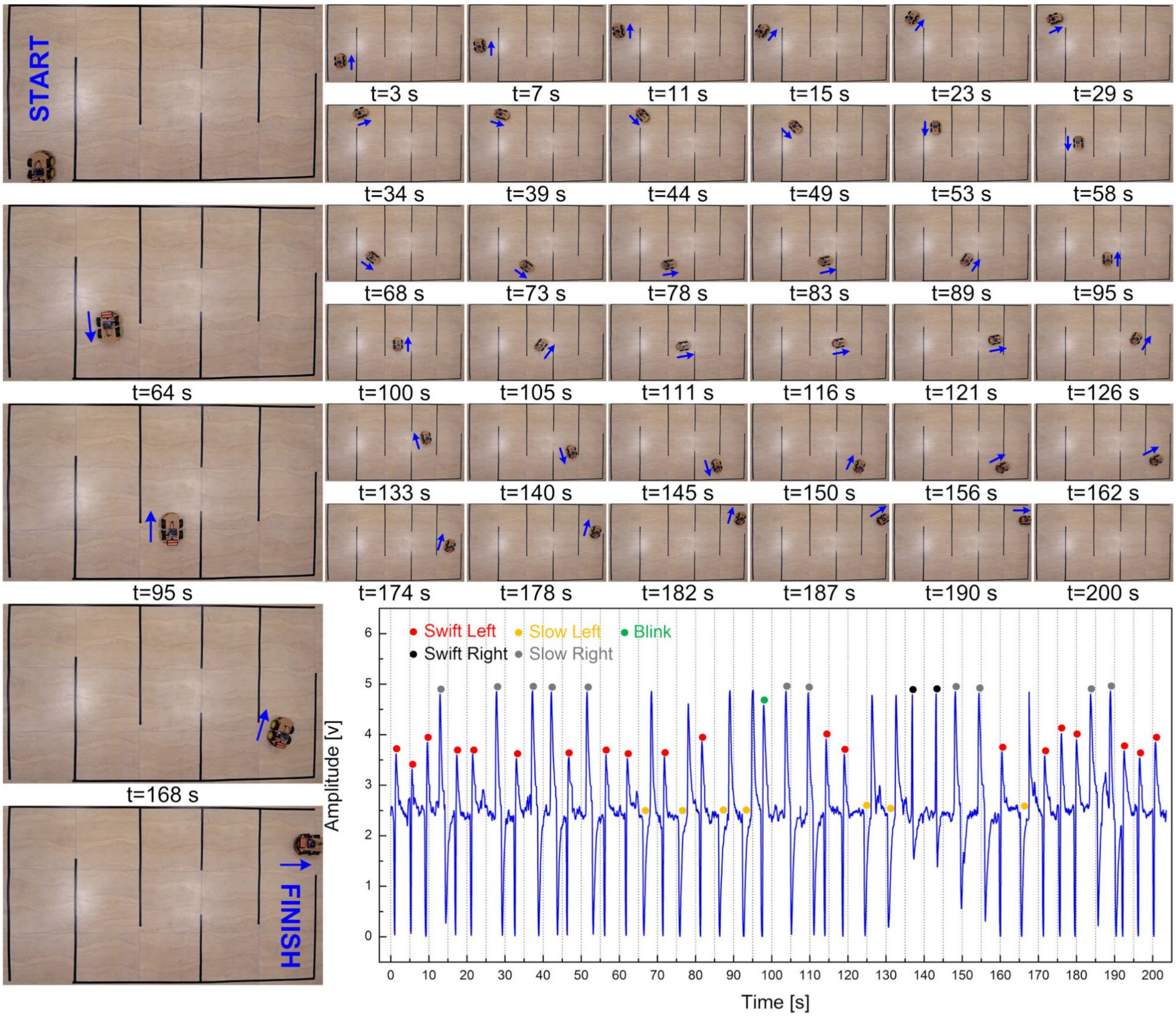

Figure 6: Snapshots of the robot car at different instances and plot of the recorded EOG trace during steering of the robot over a duration of more than 3 min with interpretations for the different eye movements (EMs) labeled in the waveform (video available in Supporting Information File 1).

the near excellent performance of the truly wearable headband prototype for human–robot interaction and control.

Conclusion

In contrast to well-established vision-based gaze tracking, we demonstrate electrooculography (EOG) with truly wearable graphene textiles, enabling an effective, low-cost, low-power, body-worn embedded system with small form factor to monitor and utilize eye movements for the remote control of objects. EOG allows for a recording of ocular biopotentials regardless of ambient lighting conditions, camera line of sight, or the presence of obstacles. Even when the subject's eyes are closed, seamless detection and harnessing of eye movements for object control without the need for a camera is possible. Along with the advantages of being soft and wearable in the form of a smart textile-based accessory with peripheral electronics, the developed EOG system can be utilized in virtual reality environments and serve as a valuable communication platform for people with disabilities such as amyotrophic lateral sclerosis (ALS). In this study, we also demonstrated a proof of concept of "active" graphene textile electrodes and achieved initial results that warrant room for detailed investigation. Additionally, in the current work, the information obtained from EOG remains coarse, the users are static, and signal processing is yet to be optimized for mobile scenarios, which indicates future research directions. We envision that further developments will be possible with the results presented in this work, which lay down the foundations regarding the use of wearable graphene textiles in control applications tailored explicitly to EOG-based human–computer/robot interaction (HCI/HRI).

Supporting Information

Supporting Information File 1

Video showing the steering and control of robot car.
[https://www.beilstein-journals.org/bjnano/content/supplementary/2190-4286-12-14-S1.mp4]

Acknowledgements

This article is based on the M.Sc. thesis of the first co-author. The experimental procedures involving volunteer human subjects described in this research are followed by the ethical principles outlined in the Helsinki Declaration of 1964, as revised in 2013, and participants gave their informed consent for inclusion before they participated in the study. The authors gratefully thank the participants involved in this study.

Funding

This work was supported in part by the Sabanci University research fund.

ORCID® iDs

Ata Jedari Golparvar - https://orcid.org/0000-0002-1107-6380
Murat Kaya Yapici - https://orcid.org/0000-0003-4328-5985

References

1. ALS Association. http://www.alsa.org/about-als/facts-you-should-know.html (accessed Aug 3, 2019).
2. Whitmire, E.; Trutoiu, L.; Cavin, R.; Perek, D.; Scally, B.; Phillips, J.; Patel, S. EyeContact: scleral coil eye tracking for virtual reality. In *Proceedings of the 2016 ACM International Symposium on Wearable Computers,* Association for Computing Machinery: New York, NY, USA, 2016; pp 184–191. doi:10.1145/2971763.2971771
3. Ryan, J. D.; Riggs, L.; McQuiggan, D. A. *J. Visualized Exp.* **2010,** No. 42, e2108. doi:10.3791/2108
4. Pfeiffer, T.; Latoschik, M. E.; Wachsmuth, I. *J. Virtual Reality Broadcast.* **2008,** *5,* No. 16. doi:10.20385/1860-2037/5.2008.16
5. Borghetti, D.; Bruni, A.; Fabbrini, M.; Murri, L.; Sartucci, F. *Comput. Biol. Med.* **2007,** *37,* 1765–1770. doi:10.1016/j.compbiomed.2007.05.003
6. Malmivuo, J.; Plonsey, R. *Bioelectromagnetism: Principles and Applications of Bioelectric and Biomagnetic Fields;* Oxford University Press: New York, 1995. doi:10.1093/acprof:oso/9780195058239.001.0001
7. Häkkinen, V.; Hirvonen, K.; Hasan, J.; Kataja, M.; Värri, A.; Loula, P.; Eskola, H. *Electroencephalogr. Clin. Neurophysiol.* **1993,** *86,* 294–300. doi:10.1016/0013-4694(93)90111-8
8. Abbas, S. N.; Abo-Zahhad, M. Eye Blinking EOG Signals as Biometrics. In *Biometric Security and Privacy;* Jiang, R.; Al-maadeed, S.; Bouridane, A.; Crookes, D.; Beghdadi, A., Eds.; Signal Processing for Security Technologies; Springer International Publishing: Cham, Switzerland, 2017; pp 121–140. doi:10.1007/978-3-319-47301-7_5
9. Soundariya, R. S.; Renuga, R. *Adv. Nat. Appl. Sci.* **2017,** *11,* 38–43.
10. Acar, G.; Ozturk, O.; Golparvar, A. J.; Elboshra, T. A.; Böhringer, K.; Yapici, M. K. *Electronics (Basel, Switz.)* **2019,** *8,* 479. doi:10.3390/electronics8050479
11. Bissoli, A.; Lavino-Junior, D.; Sime, M.; Encarnação, L.; Bastos-Filho, T. *Sensors* **2019,** *19,* 859. doi:10.3390/s19040859
12. Lucena, S.; Conzelmann, P. Computer USB-Mouse Emulation Using EOG. In *Proceedings of the Instrumentation Systems, Circuits and Transducers (INSCIT),* Sao Paulo, Brazil; 2019. doi:10.1109/inscit.2019.8868754
13. Barbara, N.; Camilleri, T. A.; Camilleri, K. P. *Biomed. Signal Process. Control* **2019,** *47,* 159–167. doi:10.1016/j.bspc.2018.07.005
14. Huang, Q.; Chen, Y.; Zhang, Z.; He, S.; Zhang, R.; Liu, J.; Zhang, Y.; Shao, M.; Li, Y. *J. Neural Eng.* **2019,** *16,* 026021. doi:10.1088/1741-2552/aafc88
15. Samann, F. E.; Hadi, M. S. *J. Duhok Univ.* **2018,** *21,* 54–64. doi:10.26682/sjuod.2018.21.1.5
16. Kumar, D.; Sharma, A. Electrooculogram-based virtual reality game control using blink detection and gaze calibration. In *Proceedings of the International Conference on Advances in Computing, Communications and Informatics (ICACCI),* Jaipur, India; 2016. doi:10.1109/icacci.2016.7732407
17. Valeriani, D.; Matran-Fernandez, A. Towards a wearable device for controlling a smartphone with eye winks. In *Proceedings of the Computer Science and Electronic Engineering Conference (CEEC),* Colchester, UK; 2015. doi:10.1109/ceec.2015.7332697
18. Venkataramanan, S.; Prabhat, P.; Choudhury, S. R.; Nemade, H. B.; Sahambi, J. Biomedical instrumentation based on electrooculogram (EOG) signal processing and application to a hospital alarm system. In *Proceedings of the International Conference on Intelligent Sensing and Information,* Chennai, India; 2005. doi:10.1109/icisip.2005.1529512
19. Chang, W.-D.; Cha, H.-S.; Kim, D. Y.; Kim, S. H.; Im, C.-H. *J. NeuroEng. Rehabil.* **2017,** *14,* 89. doi:10.1186/s12984-017-0303-5
20. Golparvar, A. J.; Yapici, M. K. *IEEE Sens. J.* **2018,** *18,* 8971–8978. doi:10.1109/jsen.2018.2868879
21. Homayounfar, S. Z.; Rostaminia, S.; Kiaghadi, A.; Chen, X.; Alexander, E. T.; Ganesan, D.; Andrew, T. L. *Matter* **2020,** *3,* 1275–1293. doi:10.1016/j.matt.2020.07.030
22. Golparvar, A.; Yapici, M. K. Wearable graphene textile-enabled EOG sensing. In *Proceedings of the IEEE Sensors Conferenc,* 2017. doi:10.1109/icsens.2017.8234242
23. Yapici, M. K.; Alkhidir, T.; Samad, Y. A.; Liao, K. *Sens. Actuators, B* **2015,** *221,* 1469–1474. doi:10.1016/j.snb.2015.07.111
24. Yapici, M. K.; Golparvar, A. Wearable graphene textile-based electro-ocular monitoring and object interaction system. US Pat. Appl. 10824230, Nov 3, 2020.
25. Golparvar, A. J.; Yapici, M. K. *J. Electrochem. Soc.* **2019,** *166,* B3184–B3193. doi:10.1149/2.0241907jes

26. Saif, M. B.; Felzer, T. Replacement of the Standard Computer Keyboard and Mouse by Eye Blinks. In *Computers Helping People with Special Needs;* Miesenberger, K.; Bühler, C.; Penaz, P., Eds.; ICCHP 2016. Lecture Notes in Computer Science, Vol. 9769; Springer International Publishing: Cham, Switzerland, 2016; pp 457–463. doi:10.1007/978-3-319-41267-2_64
27. MacKenzie, I. S.; Zhang, X. Eye typing using word and letter prediction and a fixation algorithm. In *Proceedings of the Symposium on Eye tracking research & applications,* Georgia, U.S.; 2008. doi:10.1145/1344471.1344484
28. Tang, Y.; Zhou, H.; Sun, X.; Diao, N.; Wang, J.; Zhang, B.; Qin, C.; Liang, E.; Mao, Y. *Adv. Funct. Mater.* **2020,** *30,* 1907893. doi:10.1002/adfm.201907893
29. Zhang, B.; Tang, Y.; Dai, R.; Wang, H.; Sun, X.; Qin, C.; Pan, Z.; Liang, E.; Mao, Y. *Nano Energy* **2019,** *64,* 103953. doi:10.1016/j.nanoen.2019.103953
30. Cui, X.; Zhao, T.; Yang, S.; Xie, G.; Zhang, Z.; Zhang, Y.; Sang, S.; Lin, Z.-H.; Zhang, W.; Zhang, H. *Nano Energy* **2020,** *78,* 105381. doi:10.1016/j.nanoen.2020.105381
31. Guo, R.; Zhang, H.; Cao, S.; Cui, X.; Yan, Z.; Sang, S. *Mater. Des.* **2019,** *182,* 108025. doi:10.1016/j.matdes.2019.108025
32. Zhu, M.; Lou, M.; Yu, J.; Li, Z.; Ding, B. *Nano Energy* **2020,** *78,* 105208. doi:10.1016/j.nanoen.2020.105208
33. Zhu, M.; Lou, M.; Abdalla, I.; Yu, J.; Li, Z.; Ding, B. *Nano Energy* **2020,** *69,* 104429. doi:10.1016/j.nanoen.2019.104429
34. Lou, M.; Abdalla, I.; Zhu, M.; Wei, X.; Yu, J.; Li, Z.; Ding, B. *ACS Appl. Mater. Interfaces* **2020,** *12,* 19965–19973. doi:10.1021/acsami.0c03670

License and Terms

The definitive version of this article is the electronic one which can be found at:
https://doi.org/10.3762/bjnano.12.14

BEILSTEIN JOURNAL OF NANOTECHNOLOGY

Intracranial recording in patients with aphasia using nanomaterial-based flexible electronics: promises and challenges

Qingchun Wang and Wai Ting Siok*

Review

Open Access

Address:
Department of Linguistics, The University of Hong Kong, Hong Kong, China

Email:
Wai Ting Siok* - siok@hku.hk

* Corresponding author

Keywords:
aphasia; flexible electronics; intracranial electroencephalography (iEEG); language processing; neuroimaging techniques

Beilstein J. Nanotechnol. **2021,** *12,* 330–342.
https://doi.org/10.3762/bjnano.12.27

Received: 31 December 2020
Accepted: 18 March 2021
Published: 08 April 2021

This article is part of the thematic issue "Nanogenerators and flexible electronics".

Guest Editor: Y. Mao

Abstract

In recent years, researchers have studied how nanotechnology could enhance neuroimaging techniques. The application of nanomaterial-based flexible electronics has the potential to advance conventional intracranial electroencephalography (iEEG) by utilising brain-compatible soft nanomaterials. The resultant technique has significantly high spatial and temporal resolution, both of which enhance the localisation of brain functions and the mapping of dynamic language processing. This review presents findings on aphasia, an impairment in language and communication, and discusses how different brain imaging techniques, including positron emission tomography, magnetic resonance imaging, and iEEG, have advanced our understanding of the neural networks underlying language and reading processing. We then outline the strengths and weaknesses of iEEG in studying human cognition and the development of intracranial recordings that use brain-compatible flexible electrodes. We close by discussing the potential advantages and challenges of future investigations adopting nanomaterial-based flexible electronics for intracranial recording in patients with aphasia.

Introduction

Aphasia is an impairment in language and communication, which results from damage to specific brain regions responsible for language [1]. Brain damage can be caused by stroke, tumours, seizures, infection, degeneration, or traumatic brain injury, with stroke being the most common cause of aphasia. According to the US National Aphasia Association, approximately two million members, or 0.6%, of the US population suffer from aphasia, with new cases increasing at a rate of approximately 180,000 per year; also, approximately one third of stroke patients have aphasia. It is projected that by 2030, approximately 4% of US adults will have a stroke [2]. Accordingly, the incidence of aphasia worldwide is expected to increase in the coming decades. Since individuals with aphasia differ greatly in the severity, pattern, and associated lesions of their disorder, it is important to determine the precise location of the lesions and to map the affected brain circuits related to the individuals' language deficits. The scientific study of aphasia, aphasiology, is important not only because it helps in the formulation of the best treatment methods for restoring the lost cognitive functions of individuals with aphasia but also because it provides another window into the brain mechanisms of language.

Over the last century, researchers from multiple disciplines, including biology, psychology, neuroscience, linguistics, and cognitive science, have attempted to understand the nature of aphasia. The research techniques used include classical post-mortem and histological procedures, and modern neuroimaging methods such as positron emission tomography (PET), magnetic resonance imaging (MRI), functional magnetic resonance imaging (fMRI), diffusion tensor imaging (DTI), electroencephalography (EEG), magnetoencephalography (MEG), and intracranial electroencephalography (iEEG). Each of these methods has pros and cons, and each is used to achieve specific results. MRI and DTI provide in vivo measures of brain anatomy and permit direct examination of how anatomical variations may relate to differences in cognitive functioning. DTI is sensitive to the MR signal of water molecules on a micrometre scale to determine water diffusion in different dimensions in terms of magnitude and direction. DTI offers an opportunity to measure the microstructural characteristics of white matter and allows for the examination of how distinct brain regions are correlated. fMRI and PET extend traditional structural imaging to include maps of human brain function that reveal brain regions involved in the performance of a particular cognitive task. PET and fMRI have good spatial resolution and are useful for localising functional brain activation but have poor temporal resolution. In contrast, EEG has good temporal resolution, but its spatial resolution is rather poor. By placing electrodes on the scalp, EEG detects electrical activations of the brain. EEG has been used rather extensively in clinical settings to diagnose conditions such as epilepsy, brain tumours or damage, stroke, seizures, and sleep disorders by detecting aberrant EEG activity [3]. However, the quality of brain signals recorded from deep subcortical regions, such as the insula and hippocampus, remains questionable [4].

Similar to EEG, iEEG also uses electrodes to detect brain neural activity, but the electrodes are either placed on the surface of the brain or implanted inside the brain. With high temporal and spatial resolution, iEEG is an important tool for localising brain regions of interest [5]. However, because of its invasive nature, iEEG signals can only be recorded in patients for presurgical evaluation and functional mapping, and the electrodes must be implanted for clinical but not research purposes. These rules have restricted the location of electrodes that can be placed and have limited our understanding of more complex neural networks such as language processing that require accurate and precise recording of neuronal activity covering almost the whole brain.

The application of novel nanomaterials has the potential to overcome the limitations of conventional electrode arrays. IEEG electrode arrays electroplated with nanoparticles could lower impedance and allow for a closer contact with cortical cells, thereby providing more accurate recordings of cortical activity [6]. Preclinical tests using animals (rats or primates) have shown that nanomaterial-based electronics could boost the spatiotemporal accuracy and resolution of brain imaging signals [7]. In general, iEEG electrode arrays made of nanomaterials are thinner, lighter, and more flexible and sensitive; these characteristics lead to higher spatial and temporal resolution than that of conventional electrode arrays [6,7]. These features make them less harmful to brain tissue [6], indicating their potential application in the human brain.

In this review, we first introduce classical neuropsychological research on aphasia. We then discuss how non-invasive neuroimaging methods have advanced our understanding of the brain mechanisms of language processing and review the findings of iEEG studies. Finally, we discuss the advantages and limitations of iEEG and discuss how novel nanotechnology may facilitate the study of aphasia.

Review

A brief review of classical neuropsychological research on aphasia

The seminal report on aphasia by the French surgeon Paul Broca in 1861 [8] marks the first empirical proof for the functional brain regions of language. Broca observed in his patient, nicknamed Tan, that a brain lesion in the ventroposterior portion of the left frontal lobe would lead to speech production difficulties. Tan had intact language comprehension and mental functions but could only produce the sound "tan". In a later autopsy report of twelve patients with similar symptoms, Broca [9] proposed that the left ventral frontal region was a speech centre for language articulation and production. Broca's proposal was provocative in his time as the brain was believed to function holistically with no localisation of cognitive functions [10]. Inspired by the proposal of his mentor Theodor Meynert that the left superior temporal gyrus (STG) might be important in speech comprehension, the German physician Carl Wernicke [11] also believed that there were localised brain regions for language functions but argued that Broca's area was not the only localised speech centre [12]. Wernicke performed an autopsy on a female patient who suffered from comprehension difficulties (she could not understand others' speech or use the right words for expression) but could speak volubly. He found that the patient had obstruction of the Sylvian artery, and her left STG was damaged. Wernicke termed this type of aphasia *sensory aphasia*, now known as Wernicke's aphasia, as he believed that the STG (or Wernicke's area) was a sensory speech area that stored the sound images of object names (or word pronunciations). Destruction of Wernicke's area leads to difficulty in understanding concepts or word meanings as word pronunciations are lost and could not be used to retrieve word meanings. This loss of word pronunciation also leads to an inability to produce meaningful speech because concepts could not be linked to word pronunciations and could not be translated into motor movements for articulation.

Based on the findings that there were localised regions for speech functions such as motor and sensory speech experience, Wernicke [11] proposed a neurobiological model of language functions that comprises a motor speech centre (i.e., Broca's area) and a sensory speech centre (i.e., Wernicke's area), a pathway connecting the two speech centres, an input pathway from auditory nerves to Wernicke's area, and an output pathway from Broca's area to motor nerves. He also included memory areas for tactile and optical images, both being parts of the concept or semantic network that do not have localised representations but that are distributed over the whole brain. The tactile memory area (for handwriting) has connections with Broca's area, whereas the optical memory area (for reading) has connections with both Wernicke's and Broca's areas. This information-processing type of model outlines a very preliminary framework of language production and comprehension. It depicts the pathways for listening, speaking, reading and writing, and explains how sensory and motor aphasia, alexia (acquired reading disorders) and agraphia (acquired writing disorders) might be caused. Wernicke also differentiated between disorders caused by a lesion in the speech areas and those caused by damage to the pathway connecting the two speech areas. The former leads to a receptive or expressive problem. The latter leads to conduction aphasia, which is a difficulty in speech repetition with intact comprehension and expression. Although Wernicke did not have empirical evidence to support the existence of conduction aphasia when he proposed the model, his prediction led to the discovery of this rare form of aphasia [12].

Wernicke's model was later found to be inadequate in explaining several special types of aphasia, such as pure word deafness (PWD) and transcortical sensory aphasia (TSA). Patients with PWD cannot understand and repeat speech but can understand written texts and speak normally [12]. TSA has symptoms similar to Wernicke's aphasia, except that TSA patients can repeat speech normally [12]. To account for these new types of aphasia, Lichtheim [12] modified Wernicke's model by including a pathway connecting the primary auditory cortex with Wernicke's area and a pathway connecting Broca's area with the motor cortex. He also added a concept centre to the model; the centre represents diffused, interconnected pathways and memory images, as depicted by Wernicke (Figure 1). The Wernicke–Lichtheim model could account for not only mechanisms of normal language comprehension and production but also the causes of the main forms of aphasic syndromes such as motor and receptive aphasia as well as alexia and agraphia. It has also led to the prediction of new aphasic types such as semantic dementia (loss of word meanings).

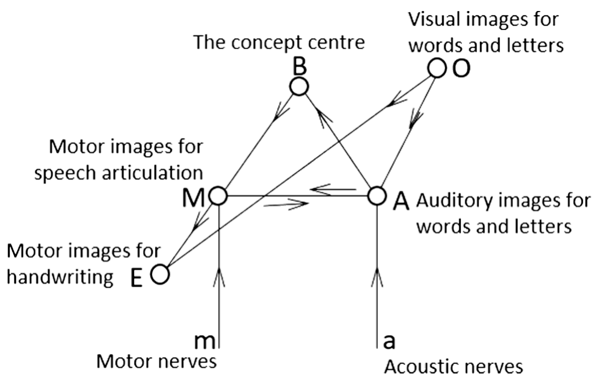

Figure 1: Wernicke's-Lichtheim model (redrawn from [12], Figure 2). A: The Wernicke's area. M: The Broca's area. a: The pathway connecting Broca's area and the motor nerves. m: The pathway connecting the acoustic nerves and Wernicke's area.

With the advancement of techniques for microscopic examination of brain sections (i.e., histology), the associations between brain anatomy and functions became better known. Theodor Meynert pioneered the histological examination of the human brain in 1867 by using a blue dye to observe neuron cells in distinct portions of the cerebral cortex [13]. He observed that different parts of the cerebral cortex had different cell structures and found that sensory input was received at posterior cerebral regions, and motor output was produced at the anterior brain regions [14]. Since then, numerous brain cytoarchitecture maps have been proposed, including Alfred Campbell's brain map with 14 areas [15], Elliot Smith's brain map with 50 areas [16], and Korbinian Brodmann's brain map with 52 areas [17]. Brodmann examined more than 60 mammalian species and divided the cerebral cortex into different areas based on regional variations in cells, labelling each area with a number (from 1 to 52). These regions are now known as Brodmann areas (BAs). Brodmann believed that each area should serve a specific function, and many of them were later found to have a specific role in processing. Although the cortical structure is found to be more complex and heterogeneous than Brodmann suggested, his cytoarchitecture maps remain popular and useful today.

In the last century, neurologists have developed theories of language localisation based on clinical observations and knowledge of the cytoarchitecture of the cerebral cortex. The theories describe typical and atypical language processing mechanisms and offer testable predictions of new aphasic patterns such as conduction aphasia and semantic dementia. Further clinical observations, in turn, provide new data for reinforcing and revising theories. Though many of these neurobiological models have been found to be incorrect and have become obsolete, they still provide a fundamental and schematic understanding of the processing involved in comprehension and production in both auditory and visual modalities. However, interpretations of these findings should be cautious since pathological and healthy brains are different. The language mechanisms deduced from this approach might not reflect the typical brain network. In addition, subjects of those post-mortem brain studies generally had comorbid cognitive or neurological disorders; thus, the brain anomalies observed in them might not be associated with their language deficits.

fMRI and PET studies on language processing

During the last three decades, our understanding of the functional anatomy of language has been extensively enhanced by neuroimaging techniques. These techniques, including PET and fMRI, provide opportunities to observe brain activity noninvasively in healthy people through careful experimental design. For example, neuroimaging studies of English reading have generally shown that adults recruit left-lateralised brain regions during silent or overt reading, including the inferior frontal, occipitotemporal, and temporoparietal regions [18-21]. The left inferior frontal regions (LIFG), that is, Broca's area, and the left posterior superior temporal gyrus (LpSTG), that is, Wernicke's area, serve speech and reading functions. The LIFG, comprising BAs 44, 45, and 47, is involved in multiple functions, including articulatory recoding [22-24], syntactic functions and semantic functions [25], as well as executive functions such as inhibitory control [26,27] and response selection [28]. The LpSTG (or BA 22) is involved in phonemic and rule-based analysis [29,30]. The left angular gyrus (BA 39), the region believed to be a centre for visual word images [31-33], is involved in cross-modal tasks such as visual rhyming and auditory spelling tasks [34,35]. The occipitotemporal region, covering the visual word form area (VWFA), is more activated for written units (either words or letters) than line drawings matching in visual complexity [36,37]. This region is hypothesised to be specialised for orthographic processing [38] and is likely a region that stores visual word images [39], although recent findings have shown that the VWFA is also involved in other cognitive functions, such as attention [40] and nonorthographic visual processing [41]. Though these methods are useful in localising brain functions, they cannot determine the temporal characteristics of signals. Indeed, in recent years, the modular view of brain functions has fallen out of favour, and researchers generally believe that various brain regions function simultaneously and interactively. New analysis methods, such as functional connectivity and dynamic causal modelling, have been used to model dynamic brain networks. To better examine the temporal relation of cortical activities, iEEG would be an ideal method.

Intracranial studies on aphasia

Characteristics of intracranial recording

The iEEG technique provides a promising opportunity to validate and extend current findings from other neuroimaging modalities [42]. The iEEG signal can detect neural activity at the millimetre scale and temporal movement at the millisecond scale. As it provides precise spatial and temporal information about cortical activation and interaction, iEEG is a perfect complement to other invasive or non-invasive neuroimaging methods.

There are two forms of iEEG in terms of the implantation of electrodes. One is called electrocorticography (ECoG), which uses subdural grids or strips of electrodes applied to the cortical surface of the brain. The other is called stereotaxic EEG (sEEG), which uses depth electrodes stereotactically implanted in targeted regions deep inside the brain [42]. Accordingly, ECoG can cover a broader range of brain regions on the cortical surface but may not be used to detect signals from deep brain structures. In contrast, sEEG is advantageous for recording signals from deep brain structures, but electrode placement is more restricted for sEEG than for ECoG. These features cause sEEG to be used less frequently in investigations of higher-level cognitive functions such as language processing. Thus, we focus mainly on studies using ECoG in this review.

ECoG has been used to investigate the onset zone of seizures in patients with epilepsy for decades [43]. This technique was pioneered by neurologists Wilder Penfield and Herbert Jasper in the early 1950s as part of the Montreal Procedure, a special treatment for severe epilepsy. It remains an important method in epilepsy surgeries for preoperative evaluation and functional cortex mapping [44]. ECoG uses strips and grids of electrodes applied to the cortical surface in either subdural or epidural space (Figure 2a) [42]. For example, in a recent iEEG study (Figure 2b), multicontact sensors were implanted in different brain regions to collect data from patients who suffered from pharmacoresistant focal epilepsies [45]. ECoG offers high spatial resolution. The ECoG grid and strip electrodes can cover a large area of the cortex, and as many as 100–200 electrodes can be used [42]. However, in actual applications, the clinical needs of the patients determine the appropriate grid size and electrode placement. Since most epilepsy patients have left temporal lobe or frontal lobe seizures, electrodes are more commonly implanted in the left hemisphere, covering the medial temporal and frontal cortices. Thus, the parietal, occipital, and deeper brain regions, such as the hippocampus and insula, are less frequently covered [42]. This limitation has significantly restricted the use of ECoG in mapping of widely distributed cognitive networks, such as that for language processing.

Compared to metabolic imaging techniques such as fMRI or PET, ECoG has an excellent temporal resolution at the millisecond scale. ECoG data have a typical sampling rate of 1,000–3,000 Hz. This high temporal resolution offers an opportunity to observe the rapid dynamics of neural activities in precisely localized brain regions. ECoG has a much higher signal-to-noise ratio (SNR) than other modalities, such as fMRI or scalp EEG. The SNR of ECoG is 100 times higher than that of scalp EEG due to the reduction of environmental and physiological noise such as muscle contractions or skin potentials [42,46]. ECoG electrodes are characterised by a circular plate shape, with a diameter of 1.2 to 3 mm, and the centres of two adjacent electrodes are approximately 4 to 10 mm apart [42]. These features enable ECoG electrodes to capture the cell population over a relatively large and diverse range.

The abovementioned characteristics of ECoG have made it a promising recording technique for real-time functional brain mapping. It permits real-time functional mapping of cognitive functions and dynamically images neural pathways between brain regions during cognitive processing, in contrast to fMRI and PET, which offer a static image of functional activity without temporal information. In addition to clinical applications, ECoG provides novel interpretations of functional brain localisation. For instance, a study with five epileptic patients implanted with subdural electrodes in their dominant hemisphere of language demonstrated the potential of using ECoG to temporally and spatially segregate complex cognitive functions within a designated brain region [47]. During ECoG recording, these patients performed different cognitive tasks, which included naming pictures, recognising animal sounds, answering questions, naming visual words, and repeating spoken words. The results showed that ECoG could temporally and spatially segregate the cortical subregions within the left posterior inferior frontal gyrus (LPIFG) regarding different cognitive functions. The visual system located in the occipital lobe would be a good candidate for evaluation by ECoG to study its highly modular but interconnected hierarchical networks [48].

iEEG to examine the neuronal representation of reading

As mentioned previously, the ventral occipitotemporal (VOT) region is involved in visual word or orthographic processing

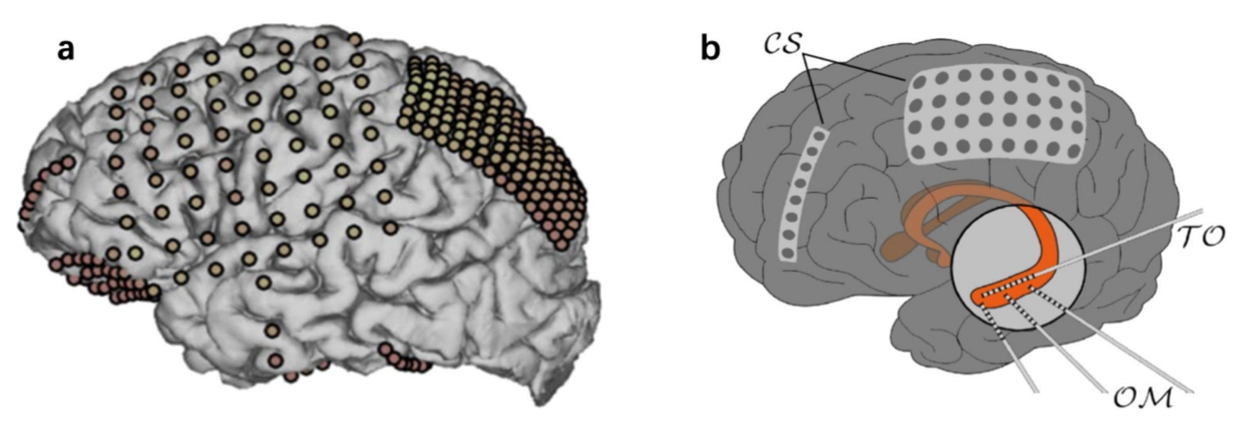

Figure 2: iEEG detects brain activity by implanting electrodes on the cortical surface. (a) Strips and grids of electrodes are used for iEEG recording. Figure 2a was reprinted from [42], Nature Neuroscience, vol. 21, by J. Parvizi; S. Kastner, “Promises and limitations of human intracranial electroencephalography”, Copyright (2018), with permission from Springer Nature. (b) Multicontact sensors could be implanted for iEEG recording. Sensor group cortical surface (CS) are strips and grids of electrodes, and sensor groups trans-occipital (TO) and orthogonal-to-mesial (OM) represent in-depth electrodes. Figure 2b was reprinted from [45], Physiological Measurement, vol. 39, by A. Sanz-Garcia; T. Rings; K. Lehnertz, “Impact of type of intracranial EEG sensors on link strengths of evolving functional brain networks”, article no. 074003, published 13 July 2018, https://doi.org/10.1088/1361-6579/aace94; © Institute of Physics and Engineering in Medicine. Reproduced with permission of IOP Publishing. All rights reserved.

[38,39], although whether this region plays specific roles in visual word identification remains a hotly debated topic [49]. To address this issue, Nobre et al. [50] examined ECoG activity at the VOT cortex of 27 patients with epilepsy during sentence reading, word detection, semantic priming, and object perception. The authors found a region in the posterior fusiform gyrus responding equally to word and nonword strings, likely responsible for prelexical letter integration. In contrast, a region in the anterior fusiform gyrus was sensitive to word lexicality (words > nonwords), semantic content, and context. This region could be responsible for concept representation addressable by visual or multimodal images of words. Both regions showed stronger activity to letter strings than objects, implying their specific role in orthographic processing [50,51].

Based on previous neuroimaging studies with epileptic patients, Cohen et al. [51] proposed the visual word form area (VWFA) hypothesis using behavioural, fMRI, and scalp EEG techniques to evaluate five healthy subjects and two patients who had posterior callosal lesions. They observed from the two patients whose VWFA activity, which occurred 150–160 ms after stimulus onset, could be triggered by words presented in the right visual field (RVF) but not the left visual field (LVF). These patients had posterior callosum damage that disconnected their bilateral visual systems. As a result, the information presented to the LVF could not be transmitted to the left hemisphere for orthographic processing. This suggests that the VWFA specific for orthographic processing is confined to the left hemisphere.

More recent studies have contributed novel findings to support the VWFA hypothesis. Empirical evidence has illustrated that the left mid-fusiform gyrus (lmFG) has a critical role in reading [52,53]. Hirshorn et al. [54] presented iEEG data from four neurological patients with electrodes implanted in their lmFG to demonstrate the involvement of lmFG in word processing (Figure 3a). Four medically intractable epilepsy patients underwent iEEG recordings. The patients viewed three types of visual images (body, word, and phase-scrambled images) and were asked to identify the images that were repeatedly presented. The results showed a strong early-stage sensitivity to word stimuli at 100–400 ms (Figure 3b). Notably, one patient (termed “Patient 1”) underwent surgical removal of tissue around the location of the implanted ventral temporal (VT) electrode. Patient 1 performed multiple naming tasks, including word naming and a set of multiple stimuli pre- and post-surgery at 1.5 weeks, 6 weeks and 3 months. Patient 1 showed reading deficits after the

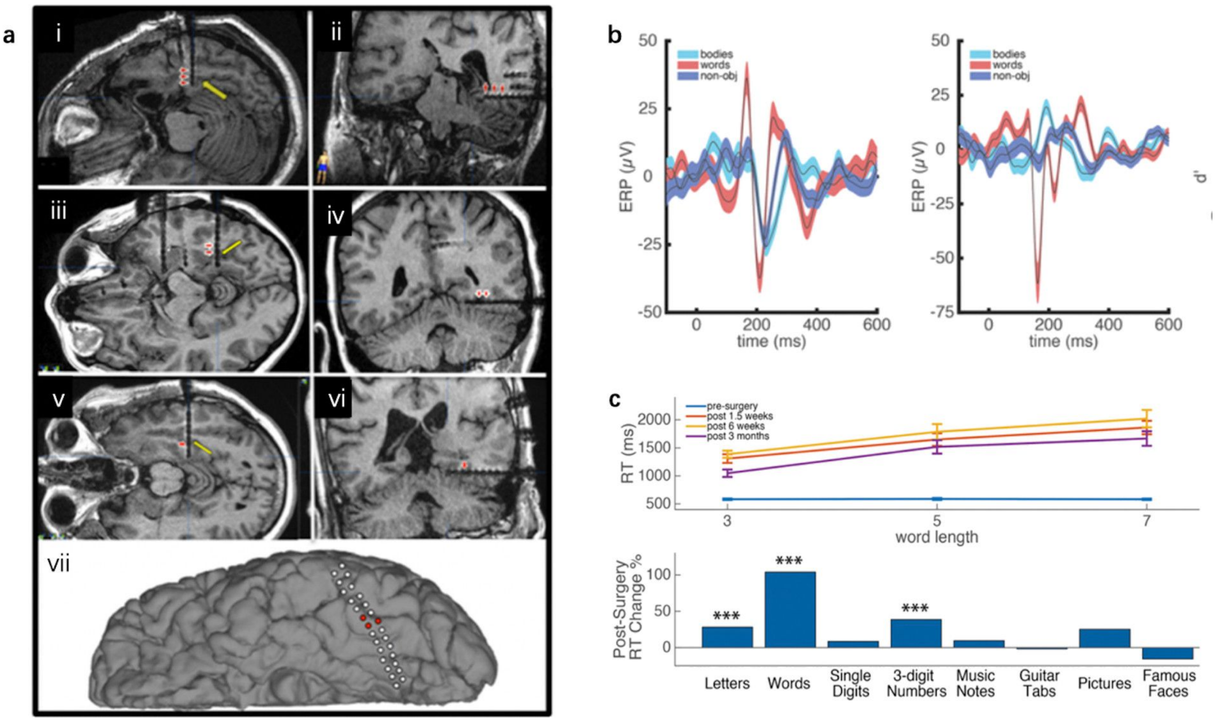

Figure 3: iEEG recording of patients with medically intractable epilepsy. (a) Electrodes were implanted in the ventral temporal cortex of the patients. (b) The signals showed a strong early-stage sensitivity to words at 100–400 ms. (c) The results from the word length and naming task showed that Patient 1 suffered from acquired alexia after surgery. Figure 3 was adapted from [54], Proceedings of the National Academy of Sciences of the United States of America, vol. 113, By E. A. Hirshorn; Y. Li; M. J. Ward; R. M. Richardson; J. A. Fiez; A. S. Ghuman, “Decoding and disrupting left midfusiform gyrus activity during word recognition”, pp 8162–8167, with permission from National Academy of Sciences.

removal of tissues surrounding the VT electrode (Figure 3c). In a follow-up analysis using machine learning methods to examine the patients' iEEG signals at the VWFA responding to words that differed in the degree of visual similarity, the researchers found that, shortly after stimulus onset (from approximately 100 to 430 ms), discriminating between words that shared no letters would activate the VWFA, but discriminating between those that differed by only one letter would not. However, at a later time window (from approximately 360 to 640 ms), discriminating between any two words would activate the VWFA. This pattern of results suggests that the VWFA processes orthographic information dynamically, shifting from a coarse, lexical-based analysis to fine-grained, sublexical-based processing. Thus, the language network is not only widely distributed across brain regions but is also dynamic. IEEG is a useful technique to capture this dynamic nature of language processing.

Successful reading relies on rapid phonological and semantic encoding of written words [55]. Neuroimaging studies of healthy subjects have detected neural activity in the left superior temporal gyrus and the right superior temporal regions when the subjects are processing phonological information [56]. Semantic processing activates more widely distributed brain regions, including the bilateral temporal and inferior frontal areas [57]. Although most of the neuroimaging findings are acquired using non-invasive techniques such as fMRI or PET, iEEG data can substantiate temporal and spatial characteristics of the non-invasive methods. McDonald et al. [58] conducted a multimodal imaging study to investigate word processing in both healthy people and patients with epilepsy. Twelve healthy participants completed a semantics judgement task while being evaluated with fMRI and MEG, and six patients performed the same task while being evaluated with iEEG. The fMRI and MEG results showed spatial concordance within the bilateral occipitotemporal and medial temporal cortex, the left prefrontal cortex, and the left posterior temporal cortex. IEEG recordings were used to validate the fMRI and MEG measurements. Responses from the abovementioned regions supported the time course of the fMRI and MEG results.

Semantics is a broad concept that covers many different types of information and could be modal or modality-specific (e.g., speech). Thus, there are different forms of semantic processing, such as concreteness judgment (abstract vs concrete words), object categorisation (living vs non-living things), meaning relatedness (table–chair vs table–choir) and meaning association (blue–sky). Also, different semantic processing entails different functional networks [57]. Previous neuroimaging research has investigated semantic processing in language production. However, the results derived from these studies are inconsistent because of the influence of the completed task [59], design of the experiment [60], or the object context [61,62]. Some studies have reported that multiple brain regions, such as occipitotemporal region, posterior parietal cortex, and prefrontal cortex, are involved in semantic processing. Nevertheless, other studies have suggested that the left temporal cortex was the main brain region for semantic processing [63].

As it simultaneously provides insight into the spatial and temporal aspects of semantic processing, iEEG is a promising method to reveal the dynamics of natural semantic processing. Khachatryan et al. [64] recorded neural signals from the scalp and cortex of nine epileptic subjects to study the activation of semantic and perceptual priming (Figure 4). Patients completed a semantic judgment task and also behavioural tasks. Scalp EEG data were collected simultaneously with iEEG data, as intracranial recordings can only be implanted in rare brain regions for clinical purposes. Scalp EEG data have shown that the perceptual priming effect is exhibited in early time windows (N100 and P200). In contrast, the semantic priming effect can only be detected in later (N400 and P600) time windows. For the iEEG data, Khachatryan et al. [64] conducted three analyses, including ERP analysis, time-frequency analysis and classification analysis. As shown in Figure 4, ERP analysis suggested that semantic priming occurs more in the left temporal cortex, whereas the distribution of perceptual priming is rather broad. Time–frequency analysis revealed early participation of the right basal occipitotemporal cortex during object processing and engagement of the left temporal cortex for the semantic and perceptual priming effect. Last, the left temporal cortex showed the highest accuracy of semantic priming in the classification analysis. Thus, the study concluded that semantic and perceptual priming could trigger partially overlapping brain regions during visual object processing.

Phonological processing is crucial for efficient reading comprehension and visual word recognition [65]. Extensive neuroimaging research has revealed the precise location of the cortex and the timing of access to phonological information when recognising visual words. Previous neuroimaging studies have documented brain responses to phonological information in the bilateral superior temporal gyri, left lateralised supramarginal gyrus and left lateralised inferior frontal cortex [66,67]. Furthermore, the relative time course of orthographic, phonological, and semantic activation during word identification remains a focus of debate in reading research [68]. Phonological processing is argued to provide the initial access required for word recognition in natural language processing [69]. With high temporal and spatial resolution, iEEG data provide direct information about how and when phonological processing occurs when recognising visual words. Mainy et al. [70]

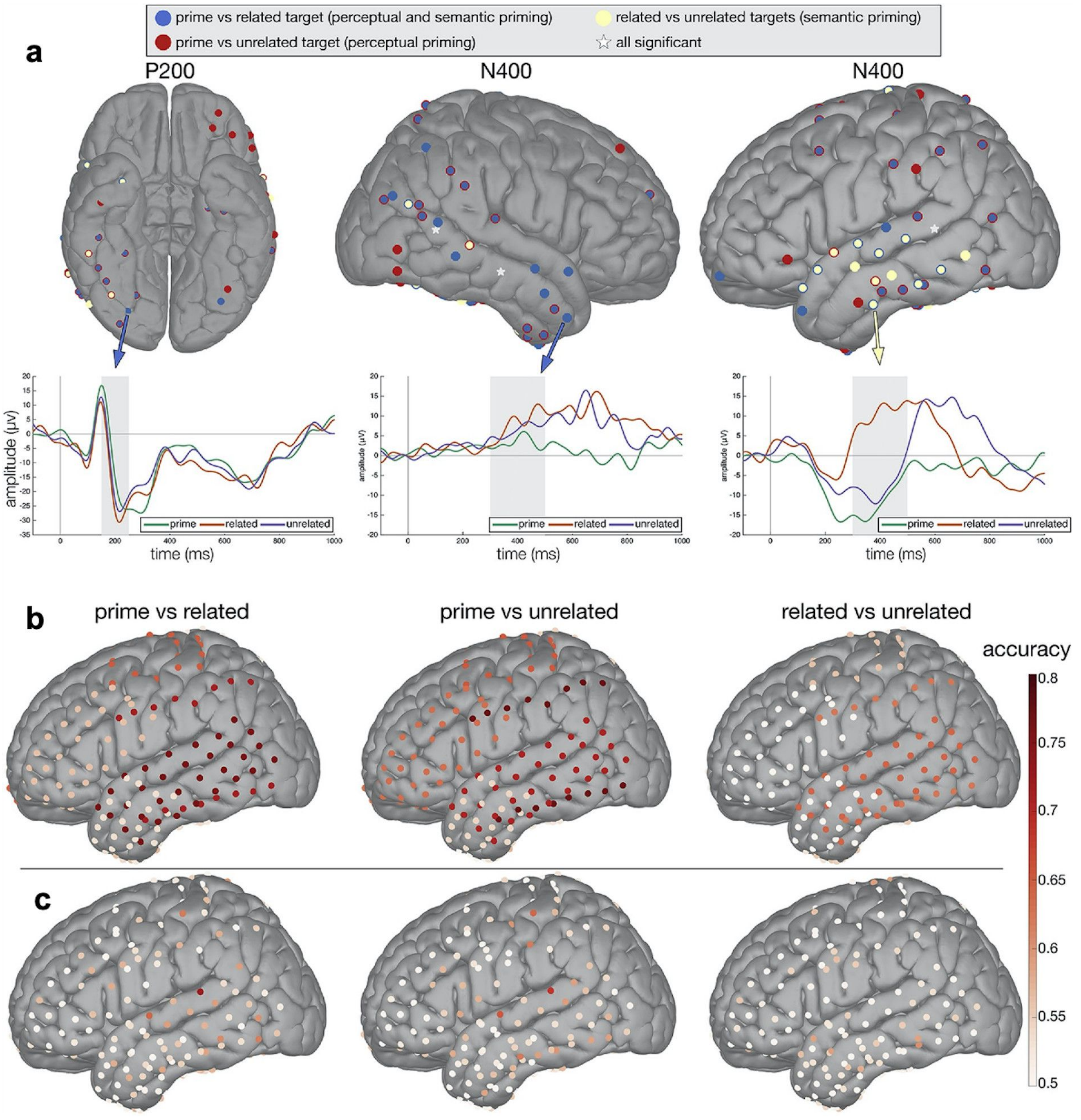

Figure 4: ERP analysis suggests semantic priming centralises in the left temporal cortex, whereas perceptual priming is widespread. (a) ERP analysis suggests the spatial and temporal distribution of semantic and perceptual priming effects. (b) Results of multichannel classification analysis. (c) Results for single channel classification analysis. Figure 4 was reprinted from [64], NeuroImage, vol. 203, by E. Khachatryan; B. Wittevrongel; M. F. Hnazaee; E. Carette; I. Dauwe; A. Meurs; P. Boon; D. van Roost; M. M. Van Hulle, "Semantic and perceptual priming activate partially overlapping brain networks as revealed by direct cortical recordings in humans", article no. 116204, Copyright (2019), with permission from Elsevier.

collected iEEG recordings from ten drug-resistant epileptic patients to reveal the measure of brain activation in the temporal and frontal lobes when processing visual words. To investigate this aspect of phonological processing, patients completed a language decision task involving unreal words while they were evaluated with iEEG. Based on the pattern of gamma-band responses they observed, phonological processing occurred at approximately 400 ms, which was maximally 200 ms after visual analysis. Activations of neuronal populations were observed in the posterior region of Broca's area, the mid and anterior regions of the superior temporal gyrus, and the lateral prefrontal cortex. The results are compatible with previous neuroimaging findings [71,72] and show a clear time course of orthographic, phonological, and semantic processing.

The development of intracranial recordings using flexible electronics

Nanotechnology has facilitated the application of neuroimaging by developing brain-compatible neural devices. A novel device fabricated from soft nanomaterials is capable of accurately measuring cortical activity and obtaining in-depth information from target brain regions [73]. These soft nanomaterials are suitable for the invasive iEEG neuroimaging method to detect neurological disorders. Nanomaterial-based flexible intracranial electrodes have been developed also to improve ECoG measurements [74,75]. For instance, conventional ECoG requires the removal of skull bone, which could result in brain damage. Flexible ECoG electrodes have been developed that can reliably attach to the cortex without removing skull bone, improving the recording signals [76].

Based on a flexible microelectrode array, a wrapping electrode array that can be inserted beneath the skull (iWEBS) was fabricated to map cortical connectivity in a wide region, as presented in Figure 5a. The microelectrode array was made of patterned Au wires passivated with SU-8 photoresist on a flexible polyimide (PI) substrate (Figure 5b). The thickness of iWEBSis was only 14.5 μm with 2 μm SU-8 and 12.5 μm PI layers. The bifurcated flap shape was used to achieve good penetration and attachment to the cortical surface and avoid injuring blood vessels on the brain midline (Figure 5c, left). The width of the Au lines was designed to be 100 μm to reach a low impedance value and enhance the signal-to-noise ratio (Figure 5c, right). The real-time signals of cortical activities in different medical and drug-induced epileptic states were precisely measured when the iWEBS array was used in freely moving mice. Combined with optogenetic mapping techniques, long-range cortical interactions were successfully mapped. The application of these flexible electronics in intracranial recording provides insight and opportunity into the study of patients with challenging neural disorders, including aphasia.

Other than insertable devices, researchers have been developing ultrathin intracranial electrodes that could reduce mechanical brain damage. Moreover, some electronics have been tested in animal models [77-81]. Although the human brain is exceedingly distinct from the mouse brain, given the larger size and more complex network, it is possible to replicate the above-mentioned techniques in humans with technical development.

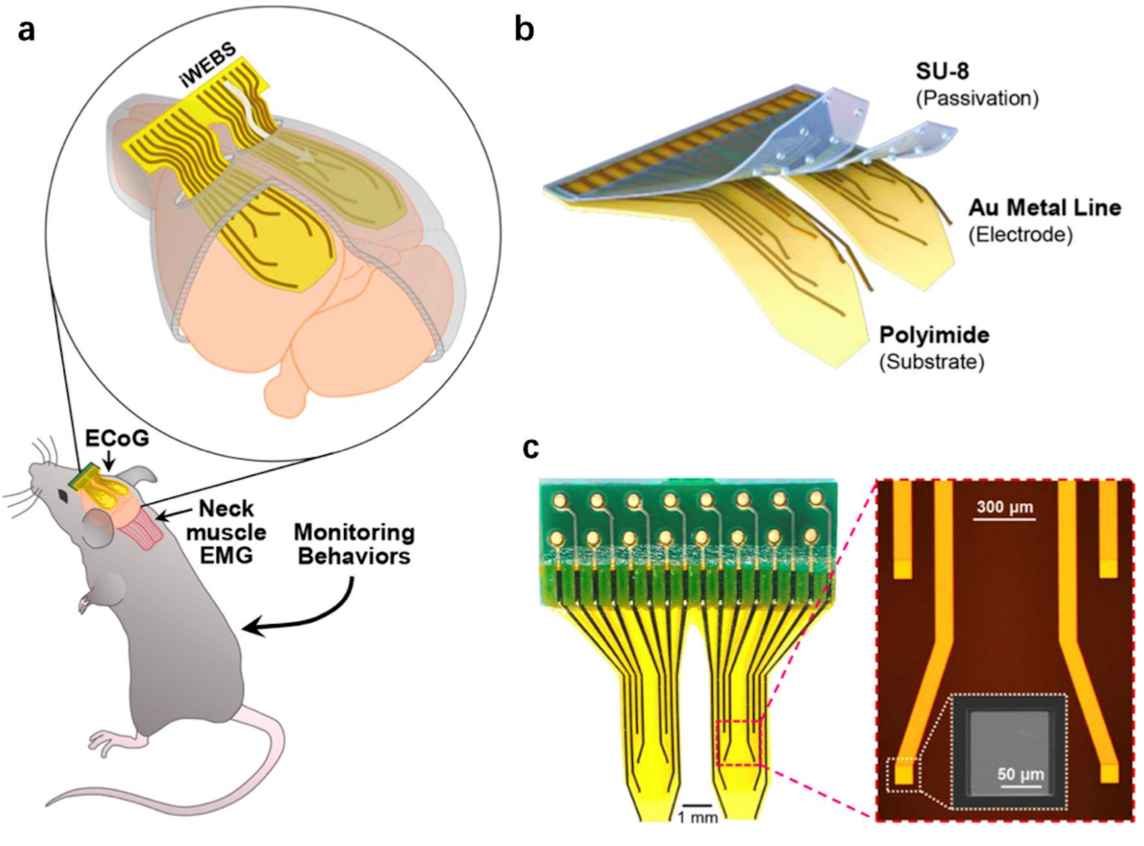

Figure 5: Features of the iWEBS array. (a) Implantation in free-moving mice. (b) Layer components. (c) Structure of recording units. Figure 5 was adapted with permission from [76], Copyright 2016 American Chemical Society.

Moreover, the highly flexible nature of novel electronics allows for the observation of interactions between distant cortical sites. As discussed above, the disconnection of brain regions may also result in aphasia. Compared to conventional intracranial electrodes, novel electronics such as multichannel ECoG microelectrode arrays provide larger coverage of the brain with exceptional thinness and considerable safety improvements [82]. With the facilitation of nanotechnology, it is possible to obtain a precise picture of the brain network of reading.

Conclusion

The iEEG technique is a tool that can be used to investigate the neural mechanisms underlying the reading process. Compared to other neuroimaging methods, such as fMRI or PET, iEEG has the advantage of high temporal and spatial resolution. Therefore, iEEG recording provides reliable anatomical precision with more accurate signals. iEEG is especially crucial for understanding the neural mechanism of reading since real-time recording is important for such sophisticated cognitive function. In addition, iEEG recording provides valuable validation to neuroimaging research of reading processing. Although numerous efforts employing multiple neuroimaging methods have been devoted to the elucidation of the anatomical pathway of reading, some results tend to be inconsistent.

Critical limitations of iEEG must be considered when adopting this method. As discussed above, successful reading relies on complex neural processing, including orthographic, semantic and phonological processing. To examine the neurological pathway of reading at different linguistic levels, an explicit experimental design is required. However, iEEG electrodes can only be implanted for clinical purposes. Restricted by configuration, location, and duration of implantation, language tasks must be concise and brief; such tasks may fail to provide sufficient information to address the issue. The lack of data is another limitation for current iEEG studies. The implantation of electrodes is suitable for a small portion of brain-damaged patients with language deficits. Among these patients, those with severe brain damage cannot complete behavioural tasks that are correlated with neuroimaging data. For epileptic patients, only a few will receive neurosurgical treatment that entails brain ablation and implantation with ECoG electrodes. Some epileptic patients are able to partake in language experiments during surgery and participate in behavioural tasks before or after surgery. Fortunately, clinical institutions, such as the US National Institutes of Health and National Science Foundation, have made efforts to build a common platform that encourages researchers to share data across laboratories. A larger number of participants will be recruited to perform identical tasks, thereby illustrating the research question more thoroughly. Broader usage of iEEG is also limited by technique issues. For instance, an adequate number of electrodes should be implanted to accurately detect neural activity [83]. Nevertheless, conventional electrodes are usually 5–10 mm apart; this spacing does not allow information to be read precisely. Furthermore, due to the limitation of the implanted electrodes, iEEG can only be applied to a small portion of the brain with a focus on certain regions. However, a growing number of neuroimaging studies have shown that multiple brain regions far beyond Broca's area and Wernicke's area are responsible for language processing. Thus, advanced electrodes that are safe and reliably cover a larger range of the brain are required.

As a continuously evolving field, nanotechnology presents a promising strategy to overcome the current technical limitations of the iEEG method. Flexible electronics have been generated that can be invasively implanted in the brain to collect recordings and simulations of neural activities with high quality. For instance, new models are advanced with significantly reduced thickness, which enables reliable contact with the cortex surface. Thus, more accurate recordings can be acquired. Furthermore, long-term implantation has been used in nonhuman primates or rats that presented steady neural decoding for a long time [84]. The development allows for the observation of brain activity in freely moving animals. Researchers are able to investigate the correlation between behaviour and neural networks. The adaption of nanomaterial-based flexible electronics in iEEG recordings offers a great opportunity to overcome current research limitations and reach new milestones in the future.

Notably, most of the products have been tested in animal models at present. Although animal models have provided fundamental descriptions of neural mechanisms in most sensory and cognitive domains, language, particularly reading, is a more sophisticated brain function exclusive to humans. The adaption of novel flexible electrodes that are specific to the human brain is challenged by the distinct differences between the human and animal brains. For instance, the human brain is significantly larger, has more surface area, contains more neurons and is structurally more complex than that of mice. It is unclear whether flexible electrodes can be expanded to cover a larger cortical surface to collect stable and high-quality neural signals. It is also unclear whether enlarged novel electrodes would release excessive heat and cause damage to the brain, especially during long-term implantation. Further investigations are required to design electronics that are compatible with the human brain for intracranial recording. Fortunately, with the advancement of brain imaging technology, it is highly possible to gain a more precise understanding of the neuronal mechanism of language processing. Sustained research progress in neuroimaging and nanomaterials will facilitate further investigation of brain functions. Ultimately, it is only a matter of time before the gap between research and clinical application is closed.

Acknowledgements

The figures in the Graphical Abstract were reprinted with permission from © 2018 IOP Publishing and © 2016 American Chemical Society.

ORCID® iDs

Wai Ting Siok - https://orcid.org/0000-0002-2154-5996

References

1. Damasio, A. R. *N. Engl. J. Med.* **1992,** *326,* 531–539. doi:10.1056/nejm199202203260806
2. Gorelick, P. B. *Lancet Neurol.* **2019,** *18,* 417–418. doi:10.1016/s1474-4422(19)30030-4
3. Niedermeyer, E.; da Silva, F. L. *Electroencephalography: basic principles, clinical applications, and related fields;* Lippincott Williams & Wilkins: Philadelphia, PA, USA, 2005.
4. Lopes da Silva, F. *Neuron* **2013,** *80,* 1112–1128. doi:10.1016/j.neuron.2013.10.017
5. Asano, E.; Juhasz, C.; Shah, A.; Muzik, O.; Chugani, D. C.; Shah, J.; Sood, S.; Chugani, H. T. *Epilepsia* **2005,** *46,* 1086–1097. doi:10.1111/j.1528-1167.2005.05205.x
6. Kumar, A.; Tan, A.; Wong, J.; Spagnoli, J. C.; Lam, J.; Blevins, B. D.; G, N.; Thorne, L.; Ashkan, K.; Xie, J.; Liu, H. *Adv. Funct. Mater.* **2017,** *27,* 1700489. doi:10.1002/adfm.201700489
7. Li, X.; Song, Y.; Xiao, G.; Xie, J.; Dai, Y.; Xing, Y.; He, E.; Wang, Y.; Xu, S.; Zhang, L.; Yu, D.; Tao, T. H.; Cai, X. *Micromachines* **2020,** *11,* 732. doi:10.3390/mi11080732
8. Broca, P. *Bull. Soc. Anat.* **1861,** *6,* 330–357.
9. Broca, P. *Bull. Soc. Anthropol. Paris* **1865,** *6,* 377–393. doi:10.3406/bmsap.1865.9495
10. Wilkins, R. H.; Brody, I. A. *Arch. Neurol. (Chicago)* **1970,** *22,* 279–280. doi:10.1001/archneur.1970.00480210089012
11. Wernicke, C. *Der aphasische Symptomencomplex: eine psychologische Studie auf anatomischer Basis;* Franck und Weigert Verlag: Breslau, Germany, 1874.
12. Lichteim, L. *Brain* **1885,** *7,* 433–484. doi:10.1093/brain/7.4.433
13. Šimić, G.; Hof, P. R. *J. Comp. Neurol.* **2015,** *523,* 5–14. doi:10.1002/cne.23636
14. Meynert, T. *Vierteljahresschr. Psychiatr.* **1867**/**1868**, *1*, 77–93, 198–217; *2*, 88–113.
15. Campbell, A. *J. Laryngol., Rhinol. Otol.* **1903,** *18,* 339–341. doi:10.1017/s1755146300173172
16. Smith, G. E. *J. Anat. Physiol.* **1907,** *41,* 237–254.
17. Brodmann, K. *Vergleichende Lokalisationslehre der Grosshirnrinde;* Barth-Verlag: Leipzig, Germany, 1909.
18. Fiez, J. A.; Balota, D. A.; Raichle, M. E.; Petersen, S. E. *Neuron* **1999,** *24,* 205–218. doi:10.1016/s0896-6273(00)80833-8
19. Horwitz, B.; Rumsey, J. M.; Donohue, B. C. *Proc. Natl. Acad. Sci. U. S. A.* **1998,** *95,* 8939–8944. doi:10.1073/pnas.95.15.8939
20. Price, C. J. *J. Anat.* **2000,** *197,* 335–359. doi:10.1046/j.1469-7580.2000.19730335.x
21. Toro, R.; Fox, P. T.; Paus, T. *Cereb. Cortex* **2008,** *18,* 2553–2559. doi:10.1093/cercor/bhn014
22. Fiez, J. A.; Petersen, S. E. *Proc. Natl. Acad. Sci. U. S. A.* **1998,** *95,* 914–921. doi:10.1073/pnas.95.3.914
23. Pugh, K. R.; Shaywitz, B. A.; Shaywitz, S. E.; Constable, R. T.; Skudlarski, P.; Fulbright, R. K.; Bronen, R. A.; Shankweiler, D. P.; Katz, L.; Fletcher, J. M.; Gore, J. C. *Brain* **1996,** *119,* 1221–1238. doi:10.1093/brain/119.4.1221
24. Shaywitz, S. E.; Shaywitz, B. A.; Pugh, K. R.; Fulbright, R. K.; Constable, R. T.; Mencl, W. E.; Shankweiler, D. P.; Liberman, A. M.; Skudlarski, P.; Fletcher, J. M.; Katz, L.; Marchione, K. E.; Lacadie, C.; Gatenby, C.; Gore, J. C. *Proc. Natl. Acad. Sci. U. S. A.* **1998,** *95,* 2636–2641. doi:10.1073/pnas.95.5.2636
25. Dapretto, M.; Bookheimer, S. Y. *Neuron* **1999,** *24,* 427–432. doi:10.1016/s0896-6273(00)80855-7
26. Bunge, S. A.; Dudukovic, N. M.; Thomason, M. E.; Vaidya, C. J.; Gabrieli, J. D. E. *Neuron* **2002,** *33,* 301–311. doi:10.1016/s0896-6273(01)00583-9
27. Botvinick, M. M.; Braver, T. S.; Barch, D. M.; Carter, C. S.; Cohen, J. D. *Psychol. Rev.* **2001,** *108,* 624–652. doi:10.1037/0033-295x.108.3.624
28. Thompson-Schill, S. L.; Kurtz, K. J.; Gabrieli, J. D. E. *J. Mem. Lang.* **1998,** *38,* 440–458. doi:10.1006/jmla.1997.2559
29. Buchsbaum, B. R.; Hickok, G.; Humphries, C. *Cognit. Sci.* **2001,** *25,* 663–678. doi:10.1207/s15516709cog2505_2
30. Hickok, G.; Poeppel, D. *Trends Cognit. Sci.* **2000,** *4,* 131–138. doi:10.1016/s1364-6613(00)01463-7
31. Déjerine, J. *Mem. Soc. Biol.* **1891,** *3,* 197–201.
32. Hinshelwood, J. *Lancet* **1895,** *146,* 1564–1570. doi:10.1016/s0140-6736(01)98764-1
33. Morgan, W. P. *Br. Med. J.* **1896,** *2,* 1378. doi:10.1136/bmj.2.1871.1378
34. Booth, J. R.; Burman, D. D.; Meyer, J. R.; Lei, Z.; Choy, J.; Gitelman, D. R.; Parrish, T. B.; Mesulam, M. M. *J. Neurolinguist.* **2003,** *16,* 383–405. doi:10.1016/s0911-6044(03)00019-8
35. Booth, J. R.; Burman, D. D.; Meyer, J. R.; Gitelman, D. R.; Parrish, T. B.; Mesulam, M. M. *J. Cognit. Neurosci.* **2004,** *16,* 1234–1249. doi:10.1162/0898929041920496
36. Ben-Shachar, M.; Dougherty, R. F.; Wandell, B. A. *Curr. Opin. Neurobiol.* **2007,** *17,* 258–270. doi:10.1016/j.conb.2007.03.006
37. Szwed, M.; Dehaene, S.; Kleinschmidt, A.; Eger, E.; Valabrègue, R.; Amadon, A.; Cohen, L. *NeuroImage* **2011,** *56,* 330–344. doi:10.1016/j.neuroimage.2011.01.073
38. Dehaene, S.; Cohen, L. *Trends Cognit. Sci.* **2011,** *15,* 254–262. doi:10.1016/j.tics.2011.04.003
39. Dejerine, J. *Mem. Soc. Biol.* **1892,** *4,* 61–90.
40. Chen, L.; Wassermann, D.; Abrams, D. A.; Kochalka, J.; Gallardo-Diez, G.; Menon, V. *Nat. Commun.* **2019,** *10,* 5601. doi:10.1038/s41467-019-13634-z
41. Vogel, A. C.; Petersen, S. E.; Schlaggar, B. L. *Front. Hum. Neurosci.* **2014,** *8,* 88. doi:10.3389/fnhum.2014.00088
42. Parvizi, J.; Kastner, S. *Nat. Neurosci.* **2018,** *21,* 474–483. doi:10.1038/s41593-018-0108-2
43. Martin, S.; Millán, J. d. R.; Knight, R. T.; Pasley, B. N. *Brain Lang.* **2019,** *193,* 73–83. doi:10.1016/j.bandl.2016.06.003
44. Wang, Y.; Yan, J.; Wen, J.; Yu, T.; Li, X. *Front. Neuroinf.* **2016,** *10,* 15. doi:10.3389/fninf.2016.00015
45. Sanz-Garcia, A.; Rings, T.; Lehnertz, K. *Physiol. Meas.* **2018,** *39,* 074003. doi:10.1088/1361-6579/aace94

46. Ball, T.; Kern, M.; Mutschler, I.; Aertsen, A.; Schulze-Bonhage, A. *NeuroImage* **2009,** *46,* 708–716. doi:10.1016/j.neuroimage.2009.02.028
47. Wen, J.; Yu, T.; Li, Y.; Li, X. *J. Clin. Neurosci.* **2017,** *44,* 320–322. doi:10.1016/j.jocn.2017.06.015
48. Van Essen, D.; Anderson, C.; Felleman, D. *Science* **1992,** *255,* 419–423. doi:10.1126/science.1734518
49. Cohen, L. *Proc. Natl. Acad. Sci. U. S. A.* **2016,** *113,* 7938–7940. doi:10.1073/pnas.1608541113
50. Nobre, A. C.; Allison, T.; McCarthy, G. *Nature* **1994,** *372,* 260–263. doi:10.1038/372260a0
51. Cohen, L.; Dehaene, S.; Naccache, L.; Lehéricy, S.; Dehaene-Lambertz, G.; Hénaff, M.-A.; Michel, F. *Brain* **2000,** *123,* 291–307. doi:10.1093/brain/123.2.291
52. Dehaene, S.; Pegado, F.; Braga, L. W.; Ventura, P.; Filho, G. N.; Jobert, A.; Dehaene-Lambertz, G.; Kolinsky, R.; Morais, J.; Cohen, L. *Science* **2010,** *330,* 1359–1364. doi:10.1126/science.1194140
53. Gaillard, R.; Naccache, L.; Pinel, P.; Clémenceau, S.; Volle, E.; Hasboun, D.; Dupont, S.; Baulac, M.; Dehaene, S.; Adam, C.; Cohen, L. *Neuron* **2006,** *50,* 191–204. doi:10.1016/j.neuron.2006.03.031
54. Hirshorn, E. A.; Li, Y.; Ward, M. J.; Richardson, R. M.; Fiez, J. A.; Ghuman, A. S. *Proc. Natl. Acad. Sci. U. S. A.* **2016,** *113,* 8162–8167. doi:10.1073/pnas.1604126113
55. Bouhali, F.; Bézagu, Z.; Dehaene, S.; Cohen, L. *Proc. Natl. Acad. Sci. U. S. A.* **2019,** *116,* 21936–21946. doi:10.1073/pnas.1904184116
56. Démonet, J.-F.; Price, C.; Wise, R.; Frackowiak, R. S. J. *Neurosci. Lett.* **1994,** *182,* 25–28. doi:10.1016/0304-3940(94)90196-1
57. Bookheimer, S. *Annu. Rev. Neurosci.* **2002,** *25,* 151–188. doi:10.1146/annurev.neuro.25.112701.142946
58. McDonald, C. R.; Thesen, T.; Carlson, C.; Blumberg, M.; Girard, H. M.; Trongnetrpunya, A.; Sherfey, J. S.; Devinsky, O.; Kuzniecky, R.; Dolye, W. K.; Cash, S. S.; Leonard, M. K.; Hagler, D. J., Jr.; Dale, A. M.; Halgren, E. *NeuroImage* **2010,** *53,* 707–717. doi:10.1016/j.neuroimage.2010.06.069
59. Harel, A.; Kravitz, D. J.; Baker, C. I. *Proc. Natl. Acad. Sci. U. S. A.* **2014,** *111,* E962–E971. doi:10.1073/pnas.1312567111
60. Thoma, V.; Henson, R. N. *NeuroImage* **2011,** *57,* 513–525. doi:10.1016/j.neuroimage.2011.04.035
61. Bar, M.; Aminoff, E. *Neuron* **2003,** *38,* 347–358. doi:10.1016/s0896-6273(03)00167-3
62. Riès, S. K.; Dhillon, R. K.; Clarke, A.; King-Stephens, D.; Laxer, K. D.; Weber, P. B.; Kuperman, R. A.; Auguste, K. I.; Brunner, P.; Schalk, G.; Lin, J. J.; Parvizi, J.; Crone, N. E.; Dronkers, N. F.; Knight, R. T. *Proc. Natl. Acad. Sci. U. S. A.* **2017,** *114,* E4530–E4538. doi:10.1073/pnas.1620669114
63. Patterson, K.; Nestor, P. J.; Rogers, T. T. *Nat. Rev. Neurosci.* **2007,** *8,* 976–987. doi:10.1038/nrn2277
64. Khachatryan, E.; Wittevrongel, B.; Fahimi Hnazaee, M.; Carrette, E.; Dauwe, I.; Meurs, A.; Boon, P.; van Roost, D.; Van Hulle, M. M. *NeuroImage* **2019,** *203,* 116204. doi:10.1016/j.neuroimage.2019.116204
65. Bradley, L.; Bryant, P. E. *Nature* **1983,** *301,* 419–421. doi:10.1038/301419a0
66. Bles, M.; Jansma, B. M. *BMC Neurosci.* **2008,** *9,* 20. doi:10.1186/1471-2202-9-20
67. Burton, M. W.; LoCasto, P. C.; Krebs-Noble, D.; Gullapalli, R. P. *NeuroImage* **2005,** *26,* 647–661. doi:10.1016/j.neuroimage.2005.02.024
68. Carreiras, M.; Armstrong, B. C.; Perea, M.; Frost, R. *Trends Cognit. Sci.* **2014,** *18,* 90–98. doi:10.1016/j.tics.2013.11.005
69. Wheat, K. L.; Cornelissen, P. L.; Frost, S. J.; Hansen, P. C. *J. Neurosci.* **2010,** *30,* 5229–5233. doi:10.1523/jneurosci.4448-09.2010
70. Mainy, N.; Jung, J.; Baciu, M.; Kahane, P.; Schoendorff, B.; Minotti, L.; Hoffmann, D.; Bertrand, O.; Lachaux, J.-P. *Hum. Brain Mapp.* **2008,** *29,* 1215–1230. doi:10.1002/hbm.20457
71. Salmelin, R. *Clin. Neurophysiol.* **2007,** *118,* 237–254. doi:10.1016/j.clinph.2006.07.316
72. Salmelin, R.; Kujala, J. *Trends Cognit. Sci.* **2006,** *10,* 519–525. doi:10.1016/j.tics.2006.09.007
73. Jeong, Y.-C.; Lee, H. E.; Shin, A.; Kim, D.-G.; Lee, K. J.; Kim, D. *Adv. Mater. (Weinheim, Ger.)* **2020,** *32,* 1907522. doi:10.1002/adma.201907522
74. Kim, J. H.; Lee, G. H.; Kim, S.; Chung, H. W.; Lee, J. H.; Lee, S. M.; Kang, C. Y.; Lee, S.-H. *Biosens. Bioelectron.* **2018,** *117,* 436–443. doi:10.1016/j.bios.2018.06.035
75. Zátonyi, A.; Fedor, F.; Borhegyi, Z.; Fekete, Z. *J. Neural Eng.* **2018,** *15,* 054003. doi:10.1088/1741-2552/aacf71
76. Park, A. H.; Lee, S. H.; Lee, C.; Kim, J.; Lee, H. E.; Paik, S.-B.; Lee, K. J.; Kim, D. *ACS Nano* **2016,** *10,* 2791–2802. doi:10.1021/acsnano.5b07889
77. Chung, J. E.; Joo, H. R.; Fan, J. L.; Liu, D. F.; Barnett, A. H.; Chen, S.; Geaghan-Breiner, C.; Karlsson, M. P.; Karlsson, M.; Lee, K. Y.; Liang, H.; Magland, J. F.; Pebbles, J. A.; Tooker, A. C.; Greengard, L. F.; Tolosa, V. M.; Frank, L. M. *Neuron* **2019,** *101,* 21–31. doi:10.1016/j.neuron.2018.11.002
78. Xie, C.; Liu, J.; Fu, T.-M.; Dai, X.; Zhou, W.; Lieber, C. M. *Nat. Mater.* **2015,** *14,* 1286–1292. doi:10.1038/nmat4427
79. Wei, X.; Luan, L.; Zhao, Z.; Li, X.; Zhu, H.; Potnis, O.; Xie, C. *Adv. Sci.* **2018,** *5,* 1700625. doi:10.1002/advs.201700625
80. Fu, T.-M.; Hong, G.; Zhou, T.; Schuhmann, T. G.; Viveros, R. D.; Lieber, C. M. *Nat. Methods* **2016,** *13,* 875–882. doi:10.1038/nmeth.3969
81. Luan, L.; Wei, X.; Zhao, Z.; Siegel, J. J.; Potnis, O.; Tuppen, C. A.; Lin, S.; Kazmi, S.; Fowler, R. A.; Holloway, S.; Dunn, A. K.; Chitwood, R. A.; Xie, C. *Sci. Adv.* **2017,** *3,* e1601966. doi:10.1126/sciadv.1601966
82. Tolstosheeva, E.; Gordillo-González, V.; Biefeld, V.; Kempen, L.; Mandon, S.; Kreiter, A.; Lang, W. *Sensors* **2015,** *15,* 832–854. doi:10.3390/s150100832
83. Nagahama, Y.; Schmitt, A. J.; Nakagawa, D.; Vesole, A. S.; Kamm, J.; Kovach, C. K.; Hasan, D.; Granner, M.; Dlouhy, B. J.; Howard, M. A., III; Kawasaki, H. *J. Neurosurg.* **2018,** 1–13. doi:10.3171/2018.1.jns171808
84. Ashmore, R. C.; Endler, B. M.; Smalianchuk, I.; Degenhart, A. D.; Hatsopoulos, N. G.; Tyler Kabara, E. C.; Batista, A. P.; Wang, W. Stable online control of an electrocorticographic brain-computer interface using a static decoder. Aug 28–Sept 1, 2012; 2012 Annual International Conference of the IEEE Engineering in Medicine and Biology Society: San Diego, CA, USA, 2012; pp 1740–1744. doi:10.1109/embc.2012.6346285

License and Terms

BEILSTEIN JOURNAL OF NANOTECHNOLOGY

A stretchable triboelectric nanogenerator made of silver-coated glass microspheres for human motion energy harvesting and self-powered sensing applications

Hui Li[1,2], Yaju Zhang[1], Yonghui Wu[1], Hui Zhao[2], Weichao Wang[1], Xu He[*3]
and Haiwu Zheng[*1]

Full Research Paper

Open Access

Address:
[1]School of Physics and Electronics, Henan University, Kaifeng 475004, China, [2]School of Mechanical and Automotive Engineering, Henan Key Laboratory for Advanced Silicon Carbide Materials, Kaifeng University, Kaifeng, 475004, China and [3]Defense Key Disciplines Lab of Novel Micro-nano Devices and System Technology, Chongqing University, Chongqing, 400044, China

Email:
Xu He* - hexhorizon@126.com; Haiwu Zheng* - zhenghaiw@ustc.edu

* Corresponding author

Keywords:
human motion energy; silver-coated glass microsphere; single-electrode mode; triboelectric nanogenerator; wearable

Beilstein J. Nanotechnol. **2021,** *12,* 402–412.
https://doi.org/10.3762/bjnano.12.32

Received: 31 December 2020
Accepted: 12 April 2021
Published: 03 May 2021

This article is part of the thematic issue "Nanogenerators and flexible electronics".

Guest Editor: Y. Mao

Abstract

Wearable triboelectric nanogenerators (TENGs) have recently attracted great interest because they can convert human biomechanical energy into sustainable electricity. However, there is a need for improvement regarding the output performance and the complex fabrication of TENG devices. Here, a triboelectric nanogenerator in single-electrode mode is fabricated by a simple strategy, which involves a sandwich structure of silicone rubber and silver-coated glass microspheres (S-TENG). The S-TENG exhibits a remarkable performance in harvesting human motion energy and as flexible tactile sensor. By optimizing the device parameters and operating conditions, the maximum open-circuit voltage and short-circuit current of the S-TENG can reach up to 370 V and 9.5 µA, respectively. The S-TENG with good stretchability (300%) can be produced in different shapes and placed on various parts of the body to harvest mechanical energy for charging capacitors and powering LED lights or scientific calculators. In addition, the good robustness of the S-TENG satisfies the needs of reliability for flexible tactile sensors in realizing human–machine interfaces. This work expands the potential application of S-TENGs from wearable electronics and smart sensing systems to real-time robotics control and virtual reality/augmented reality interactions.

Introduction

Traditional batteries cannot provide a durable and reliable power supply for small portable electronic devices, personalized healthcare, and Internet-of-Things (IoT) devices [1-6]. Thanks to the progress in low-power technology, the power consumption of microelectronic devices has dropped to the level of micro- or nanowatts, which makes the use of environmentally friendly energy a good and practical strategy. Multiple sources of energy could be used, such as wind energy [7], solar energy [8], thermal energy [9], electromagnetic energy [10], and mechanical energy [11], among which mechanical energy is created almost everywhere. Mechanical energy has many obvious advantages over other energy forms, such as high energy density, wide distribution, and simple acquisition. Regarding this, it is desirable to develop wearable devices that convert mechanical energy from human body motion into electricity [12].

Triboelectric nanogenerators (TENGs), with a wide range of material choices and simple device structures, capture the energy of human motion in real time [13]. This form of energy conversion can not only provide sustainable power for electronic systems, but also provide reliable solutions for active sensing and human–computer interfaces [14]. A stretchable TENG with double-helix structure was previously designed. It consisted of silver-coated glass microspheres (SCGMs) and silicone rubber as stretchable conductive thread (SCT) and a silicone rubber-coated SCT as the other triboelectric thread [15]. This TENG can convert the biomechanical energy from human joint motions. The elastomer matrix guarantees that the TENG can be applied in stretchable electronic systems. The TENG generates an open-circuit voltage of 3.82 V and a short-circuit current of 65.8 nA. There are two more references focused on stretchable TENGs utilizing SCGMs to harvest biomechanical energy [16,17]. Zhang et al. invented a closed-structure TENG made of stretchable materials for harvesting human motion energy and monitoring [17]. It can produce an open-circuit voltage up to 150 V and an optimal instantaneous power density of 44.6 mW/m^2. From the abovementioned references [15,16], it can be seen that the output performance remains to be improved despite the complex fabrication procedure of the TENG devices. More recently, Qian et al. proposed a nylon-regulated TENG in contact-separated working mode, whose open-circuit voltage and short-circuit current can reach up to 1.17 kV and 138 μA, respectively [16]. Although this is a tremendous advancement in output performance, the contact-separated working mode with double electrodes makes it difficult to connect the current conducting wires to moving objects when trying to harvest mechanical energy. Besides, the organic–inorganic composites prepared by embedding relatively hard SCGMs into a soft silicone rubber matrix reduce the stretchability of the TENG devices, which is adverse regarding wearables. Therefore, further investigations to enhance the stretchability of TENGs by innovative design are still required.

In this work, we developed a single-electrode mode, stretchable triboelectric nanogenerator (S-TENG) using a simple strategy. The single-electrode mode enables the TENG to scavenge energy from the irregular mechanical motion of a free object, independent of electrode position and shape [18,19]. The S-TENG with sandwich structure consists of silicone rubber and SCGMs. The latter are either used as electrode or triboelectric layer. The S-TENG can charge commercial capacitors and power LED lights and scientific calculators and has three distinct advantages. These advantages are: (a) It can be made into multiple shapes and placed on various parts of the body to harvest mechanical energy, requires only a simple fabrication process, (b) it shows stable output and long working life, which provides sustainable electricity, and (c) due to the unique structural design of the device and the high elasticity of the silicone rubber, the S-TENG can be stretched easily to 300% to realize a conformal assembly in stretchable electronic systems. The distinct advantages of the S-TENG indicate broad application prospects in wearable electronics and smart sensing systems.

Results and Discussion

Figure 1a is the schematic of the structural design of the S-TENG. The device is composed of three layers, that is, the top layer and the bottom layer of silicone rubber and the middle layer of SCGMs. The scanning electron microscopy (SEM) image (Figure 1b) and the energy dispersive X-ray spectroscopy (EDS) measurement (Figure 1c) show that the SCGMs are evenly dispersed across the silicone rubber. Figure 1d presents the flow chart for the fabrication of the S-TENG. Silicone rubber and SCGMs are filled in a 3D-printed mold and cured. After that, the device is removed from the mold.

The S-TENG can be cut into different shapes for possible applications. The device can be stretched to 300% of the initial length (Video 1, Supporting Information File 1). Also, it can be rolled and twisted easily, as shown in Figure 1e.

Figure 2a illustrates the electricity generation mechanism of the single-electrode mode S-TENG, which is based on a conjunction of contact triboelectrification and electrostatic induction [2,20-23]. In the initial state (Figure 2a-I), the frictional layer and the S-TENG are in balance without potential difference. When the frictional layer contacts the silicone rubber (Figure 2a-II), the positive charges in the frictional layer are equal to the negative charges in the silicone rubber. Once the surfaces of frictional layer and silicon rubber are separating (Figure 2a-III), the negative charges on the silicone rubber surface drive the electrons of the SCGMs to flow to ground, generating a reverse triboelectric potential. When frictional layer and silicone rubber are entirely separated, the electrostatic equilibrium between the SCGMs and ground is re-established, no output signal can be observed (Figure 2a-IV). When the frictional layer is close to the silicone rubber, the electrons will

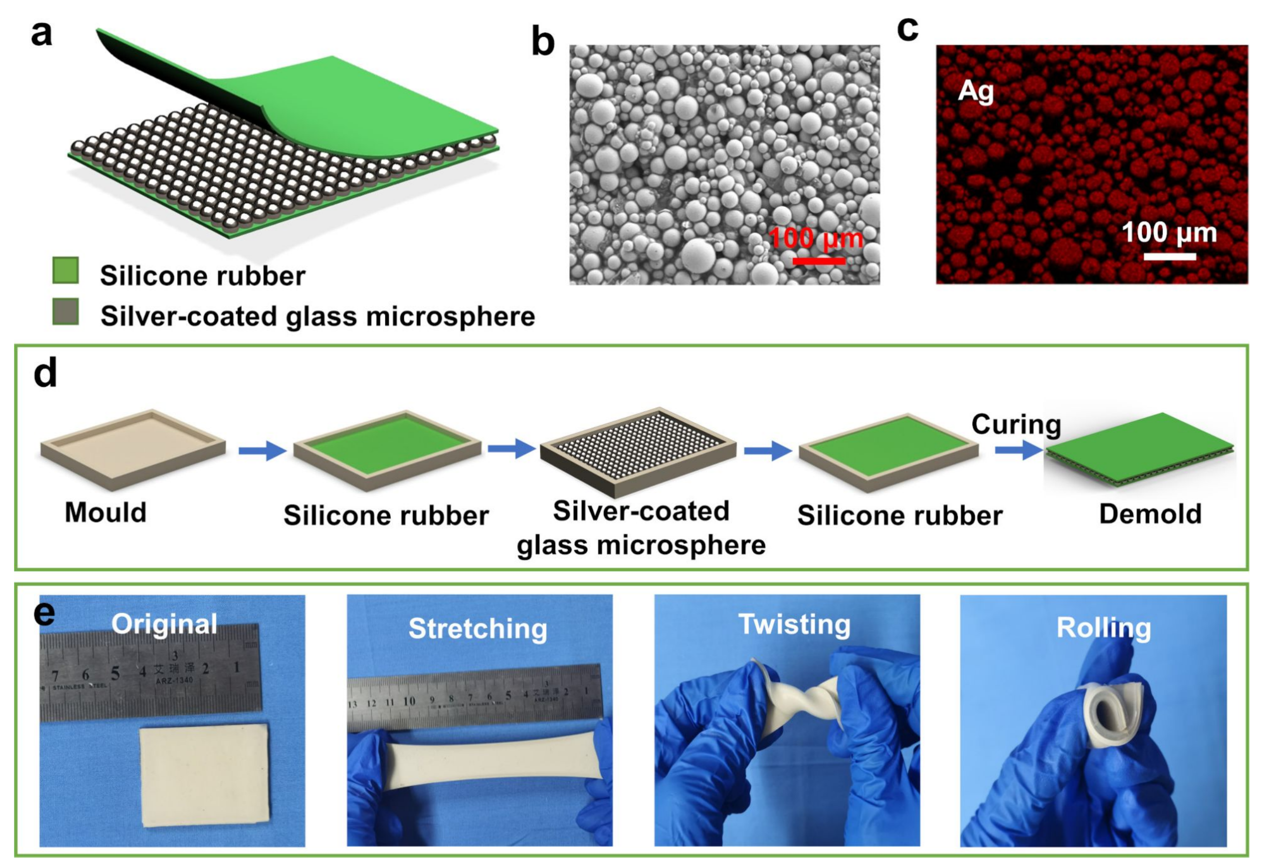

Figure 1: (a) The structural design of the single-electrode mode TENG. (b) SEM and (c) EDS measurements of the SCGM surface. (d) Flow chart for the fabrication process of the S-TENG. (e) Photographs of the S-TENG (original, stretched, twisted and rolled).

transfer from ground to the SCGMs and generate a positive potential through the triboelectric effect. Finally, the charge distributions of the two surfaces return to the initial stage.

In order to measure the electrical output of the S-TENG, a piece of 30 × 40 mm^2 was stuck onto an acrylic plate that was fixed on a linear motor. With the linear motor, displacement and motion frequency of the other triboelectric layer relative to the silicon rubber can be controlled. The open-circuit voltage (V_{OC}) peaks remain unchanged when the frequency varies from 1 to 2.5 Hz (Figure 2b-I). The short-circuit current (I_{SC}) increases from 1 to 4.2 μA when the frequency goes from 1 to 2.5 Hz (Figure 2b-II). The peak values of V_{OC} and I_{SC} go up to nearly 200 V and 4.2 μA, respectively, at 2.5 Hz, as shown in Figure 2c-I and 2c-II. Based on Maxwell's displacement current, with the increasing number of contact/separation cycles during a unit of time, the charge movement rate between electrode and ground is increasing. Therefore, the I_{SC} of the S-TENG can be increased at high frequencies.

The size plays a crucial role regarding the electrical output of the S-TENG. The output of the S-TENG was studied while changing the size from 10 × 10 mm^2 to 80 × 80 mm^2. As shown in Figure 3a and Figure 3b, under a force of 50 N, both V_{OC} and I_{SC} increase when the contact area increases. When the contact area is 80 × 80 mm^2, V_{OC} and I_{SC} reach up to about 370 V and 9.5 μA, respectively. The S-TENG can be used as a large wearable device. With bigger contact area, more charges and, consequently, higher I_{SC} values are generated. V_{OC} and I_{SC} both increase proportionally to the contact area from 10 × 10 mm^2 to 50 × 50 mm^2. However, V_{OC} and I_{SC} of 80 × 80 mm^2 are not proportionally increased. This may be attributed to the fact that the large device collapses easily in a non-uniform manner. Specifically, the upper and lower surfaces may not contact or separate efficiently, which causes the actual contact area to be smaller than expected [17].

Different devices were prepared by adjusting the ratio between silicone rubber and SCGMs (1:1, 1:1.5, 1:2, 1:2.5). As can be seen from Figure 3c and Figure 3d, when the mass ratio between silicone rubber and SCGMs is 1:1.5, V_{OC} and I_{SC} reach the largest values of 250 V and 6 μA, respectively, under a force of 150 N. As the content of SCGMs continues to increase,

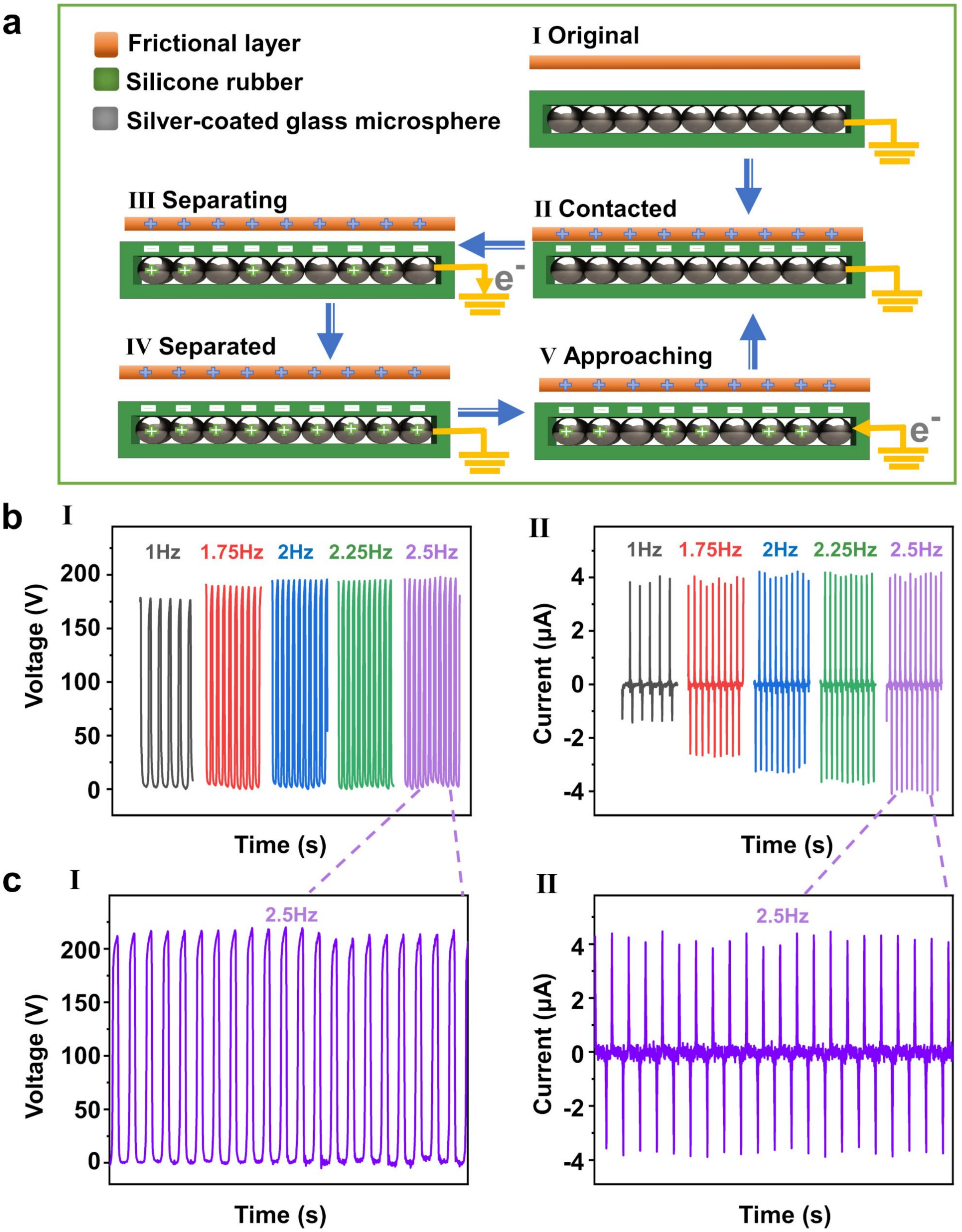

Figure 2: (a) Schematic of the working principle of the S-TENG. (b-I) Open-circuit voltage and (b-II) short-circuit current of the S-TENG at different motion frequencies and an applied force of 90 N. Magnified curves of (c-I) open-circuit voltage and (c-II) short-circuit current when tapping at a motion frequency of 2.5 Hz.

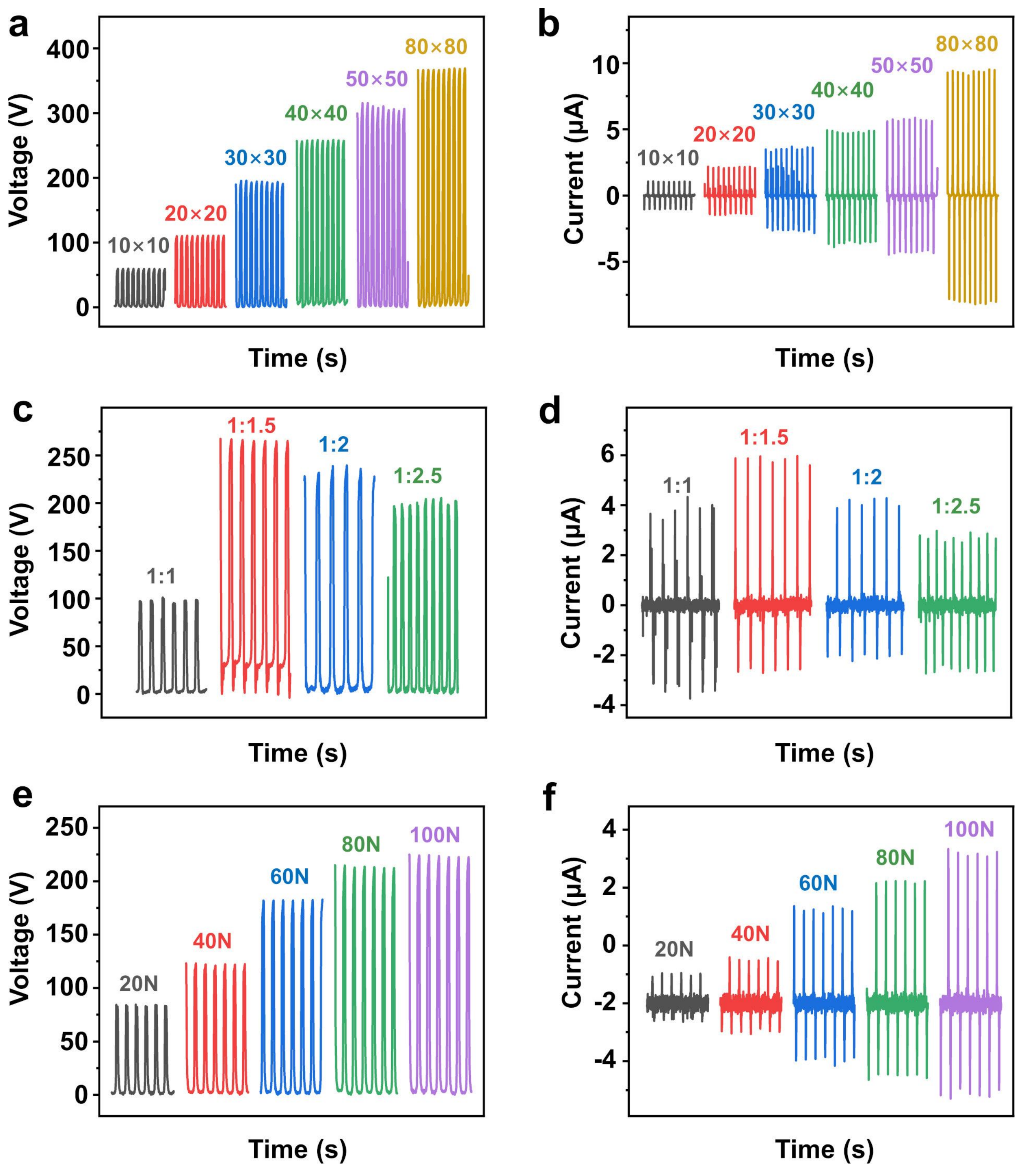

Figure 3: Open-circuit voltage and short-circuit current of the S-TENG (a, b) as functions of the contact area, (c, d) as function of the ratio between silicone rubber and silver-coated glass microspheres, and (e, f) as function of the applied force.

V_{OC} and I_{SC} gradually decrease. The larger amount of SCGMs causes less air in the same volume. Hence, there is less friction between silicone rubber and SCGMs.

The applied force is another factor that impacts V_{OC} and I_{SC}. As shown in Figure 3e and Figure 3f, when the applied force is increased from 20 to 100 N, the V_{OC} values increase from 85 to

225 V and the I_{SC} values rise from 1 to 5.3 μA. The reason is that the stronger compressive force leads to an intensification of friction and the generation of more charges. A similar trend is observed for V_{OC}, as expected.

Because of the mismatch between AC and DC systems a full-wave rectifier circuit was introduced to the setup. Figure 4a shows the voltage of different capacitors (2.2, 4.7, 10, and 33 μF) as function of the charging time with the rectified

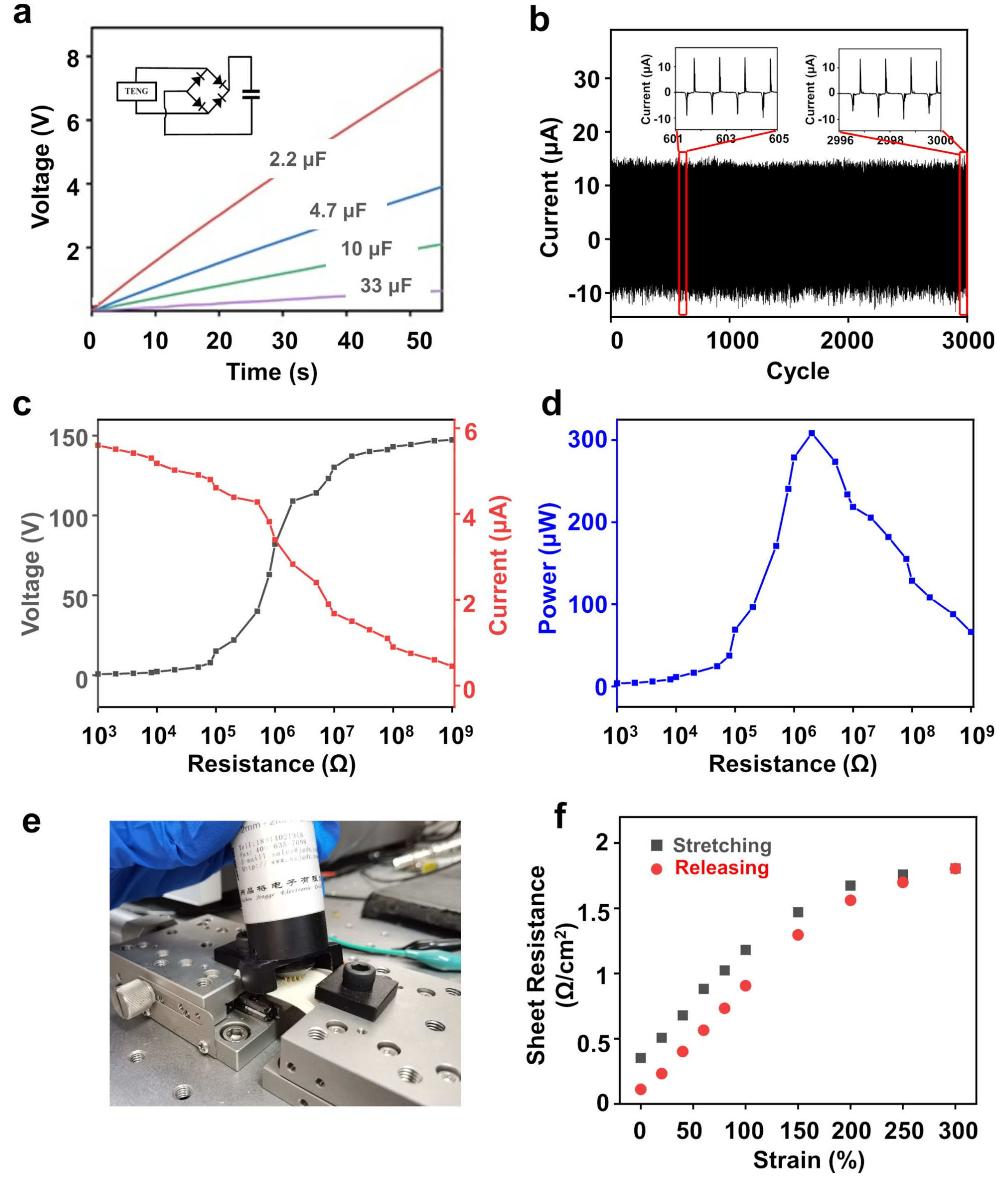

Figure 4: (a) Voltage of different capacitors (2.2, 4.7, 10, and 33 μF) as function of the charging time with the rectified S-TENG output. The inset shows the circuit diagram of the charging system. (b) Cyclic stability of the S-TENG for about 3000 cycles. The inset shows enlarged vies of the middle and the last five cycles. (c) Voltage/current trends and (d) output power of the S-TENG under different load resistances. The maximum power is 308 μW under an external load resistance of 2 MΩ. (e) Photograph of the custom-made resistance test platform. (f) Sheet resistance under tensile strain from 0 to 300%.

S-TENG output. The voltage reaches a saturation value of 14 V for charging a 2.2 μF capacitor.

Reliability is a key parameter considering the practical application of the S-TENG. As depicted in Figure 4b, the I_{SC} values of the device do not decline after 3000 cycles for 25 min, demonstrating the long-term stable operation of the S-TENG on the human body. The impedance matching experiment was designed to measure the powering capability of the S-TENG with different resistances. Figure 4c,d shows the relationship between load resistance and I_{SC}, V_{OC}, and power of the S-TENG (30 × 40 mm^2). With the resistance in parallel changing from 1000 Ω to 1 GΩ, V_{OC} increases from 0.6 to 147 V and I_{SC} decreases from 5.6 to 0.45 μA. The output power (blue line) is calculated as $P = U{\cdot}I$. The instantaneous power can achieve a peak value of 308 μW (V_{OC} = 109 V and I_{SC} = 2.8 μA) with an external load resistance of 2 MΩ. As can be seen from Figure 4e and Figure 4f, the resistance linearly increases from 0.35 to 1.18 Ω/cm^2 when the tensile strain reaches 300%. In the process, the thickness of the SCGM layer becomes thinner and the resistance of the S-TENG increases linearly. When the S-TENG is further stretched, the slope of the curve falls again because the relative variation of the SCGM layer decreases. After releasing the strain, the resistance is recovered at 0.11 Ω/cm^2 resulting from a hysteresis in the rearrangement of the SCGMs. Although the curves between sheet resistance and tensile strain have different shapes, the resistance value before and after stretching is of the same order, exhibiting the excellent flexibility and mechanical robustness of the S-TENG.

Applications of S-TENG

Charging performance and monitoring human motion

The electrical output of S-TENGs has been used to power small electronic components [17]. In Video 2 (Supporting Information File 2) the S-TENG is connected to a linear motor. 235 LEDs connected in series can be lit up after rectification of the output. Because of the video frame rate, some LEDs that light up are not captured. Figure 5a and Video 3 (Supporting Information File 3) show that a scientific calculator is powered on after padding the S-TENG for eight seconds. If the S-TENG device continued to generate electrical output, the calculator would work for a longer time when needed. Figure 5b and Video 4 (Supporting Information File 4) show that LEDs showing the word “HENU” are lit when they are connected to the S-TENG.

The S-TENG can be put into shoes to monitor human movement [24]. An S-TENG device with a diameter of 50 mm and a thickness of 3 mm is suitable to be worn regularly. As shown in Video 5 (Supporting Information File 5), the primary movement of a human being is recorded. The current of the S-TENG for walking and jumping is 1.5 and 2 μA, respectively, as shown in Figure 5c. Two forward electrical signals can be captured every one second during walking. From the graph, the backward-signal I_{SC} generated by the three exercise modes is higher than the forward-signal I_{SC}. The air mixed with SCGMs of the S-TENG is squeezed during the process of stamping continuously. Thus, the S-TENG cannot be recovered to the original state. Different motions produce different signals. The I_{SC} generated by jumping is higher than that generated by walking, due to the larger applied force under intense exercise conditions.

The S-TENG device can be potentially applied to harvest energy from different human motions and yield motion statistics. These data can be used for the analysis of physical exertion and exercise intensity by using a micro-processing unit that includes analog-to-digital conversion and wireless transmission. From the number of steps a person takes each day, the number of calories burned through exercise can be estimated. A person can keep trying to lose weight using the device. Also, the S-TENG device can monitor the rehabilitation training of post-op patients who need to avoid excessive physical training that may be harmful to heart or lung. It can also be used to check heartbeat and breathing rate, which are low-intensity movements, for comprehensive health analysis and evaluation [17].

The S-TENG can be placed in different positions of the human body to harvest motion energy with stimulation from another triboelectric layer, such as clothing or the hand. An S-TENG with an area of 100 × 100 mm^2 was placed on the waist of a person. As shown in Figure 5d and Video 6 (Supporting Information File 6), the S-TENG can light up 235 LEDs by the continuously padding the device in single-electrode contact-separation mode. The S-TENG also can be placed on elbow and knee joints and harvest body motion energy for wearable devices [25].

Sensing applications

The S-TENG provides an effective power source for electronic devices. Another potential application for the S-TENG is as flexible tactile sensor that can serve as electronic skin for a more comfortable interactive experience between humans and external objects by sensing all kinds of information, such as size, shape, and texture [26,27]. The flexible tactile sensor can generate electrical signals in response to different mechanical stimuli for the self-supply with energy. An S-TENG with an area of 20 × 20 mm^2 was placed on each of five fingertips, as exhibited in Figure 6a. When the thumb touches index finger, middle finger, ring finger and small finger in turn, the resulting

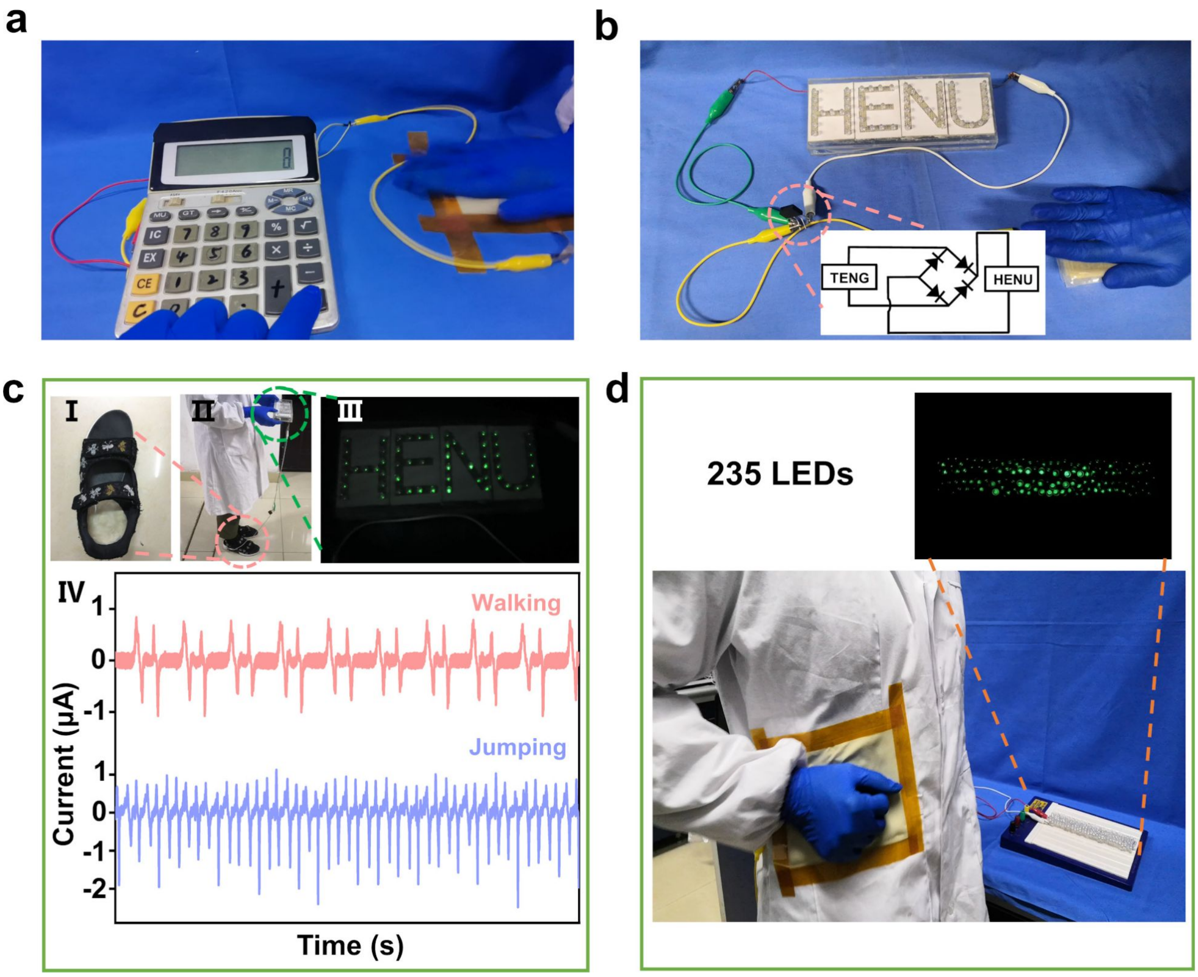

Figure 5: Optical image of the power supplied by padding the S-TENG with the hand for (a) a calculator and (b) LEDs showing "HENU". The inset shows the circuit diagram of the rectifier. (c) Demonstration of the S-TENG to detect human motion; (I, II) the position of the S-TENG in a shoe, and (III) powered LEDs; (IV) current output of the S-TENG during the two different motions. (d) The S-TENG can be fixed at the waist of a human and can light up 235 LEDs.

I_{SC} is 1, 1.2, 0.8, and 0.3 μA, respectively, as depicted in Figure 6b.

A single-electrode S-TENG was installed on the finger of a robotic hand [26], as shown in Figure 6c,d and Video 7 and Video 8 (Supporting Information File 7, Supporting Information File 8). An electrical signal is generated when the robot touches an object. When the output signal passes through the signal-processing circuit, the digital waveform can be obtained. The current level (high or low) indicates whether finger and object are in contact. Further data processing can realize basic contact perception. Figure 6e shows the circuit diagram of the signal-processing unit.

Experimental

In this work, a simple method for fabricating a TENG is proposed. First, a layer of cured silicone rubber film (Smoth-on, Ecoflex 00-20) was prepared. Gel A and gel B were mixed together with a volume ratio of 1:1 in a container for 5 min. Then the mixture was poured into a mold with rectangular groove (30 × 40 mm^2) manufactured by a 3D printer, and a vacuuming operation was performed for 5 min to eliminate any entrapped air. After curing for 30 min at 50 °C, the rectangular silicone sheet was peeled off from the mold slowly. Second, SCGMs (diameter of 30 μm, Shenzhen Changxinda Shielding Materials Co. LTD) with good electrical conductivity were spread evenly over the surface. Finally, different films were prepared by adjusting the ratio between silicone and rubber/SCGMs (1:1, 1:1.5, 1:2, 1:2.5).

Characterization and measurements

The values of V_{OC} and I_{SC} were measured by using an electrometer (Keithley 6514) and the data acquisition device. The force was applied by a linear motor (Linmot E1100) and a force

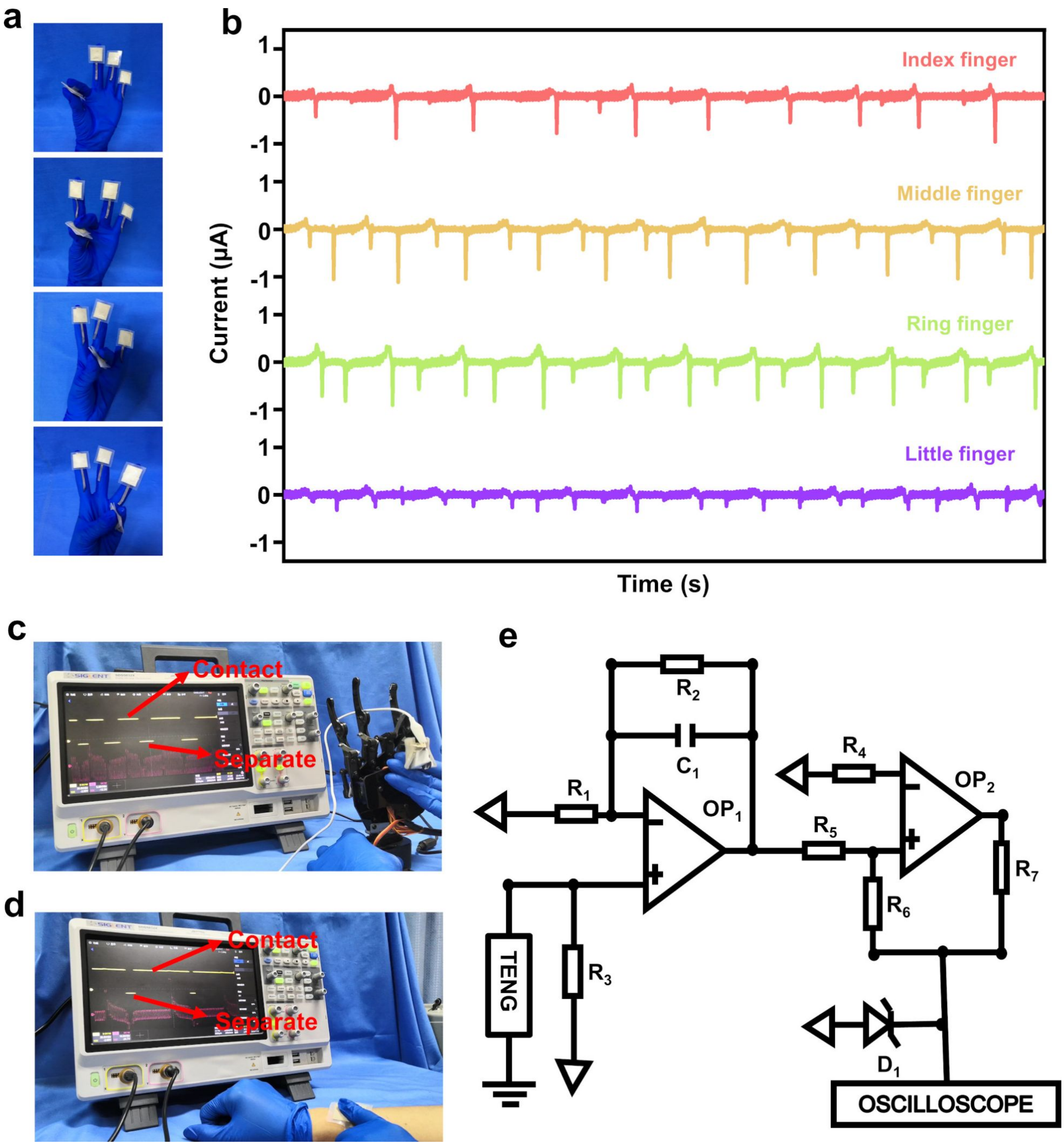

Figure 6: (a) The position of the S-TENGs on the fingers. (b) Current output of the thumb touching the other fingers. (c, d) Potential application of the S-TENG in robotic sensing. (e) The circuit diagram of the signal processing unit.

detector. The TENG was attached onto the fixed end of a linear motor. Sensing measurements used LabVIEW programs to record information. The sheet resistance of the flexible SCGM/silicone rubber electrode was measured using the M-3 Mini four-probe tester. SEM (JSM-7001F) was used for morphology characterization of the surface of the SCGMs.

Conclusion

In summary, an easily manufactured, inexpensive and stretchable single-electrode mode S-TENG was designed and fabricated, of which the electrode was made of a conductive fabric. The top and bottom layers of the sandwich structure are silicone rubber and the middle layer are SCGMs both as conducting layer and frictional layer. The peak values of V_{OC} and I_{SC} of the S-TENG are nearly 200 V and 4.2 μA at a frequency of 2.5 Hz. Moreover, the device has good long-term stability with almost no degradation of the electrical output after 3000 cycles. In addition, the S-TENG can light up 235 LEDs and power a commercial calculator by padding the S-TENG with the hand. The S-TENG device can be made into various shapes and sizes, and can be freely placed on different parts of body to harvest human motion energy. It has been proven that the device is suitable for wearable energy harvesting. A large-scale device could be used to power portable electronic devices.

Supporting Information

Supporting Information File 1

Video S1: Stretchability of the S-TENG.
[https://www.beilstein-journals.org/bjnano/content/supplementary/2190-4286-12-32-S1.mp4]

Supporting Information File 2

Video S2: Power LEDs.
[https://www.beilstein-journals.org/bjnano/content/supplementary/2190-4286-12-32-S2.mp4]

Supporting Information File 3

Video S3: Power a calculator.
[https://www.beilstein-journals.org/bjnano/content/supplementary/2190-4286-12-32-S3.mp4]

Supporting Information File 4

Video S4: Light up letters of “HENU”.
[https://www.beilstein-journals.org/bjnano/content/supplementary/2190-4286-12-32-S4.mp4]

Supporting Information File 5

Video S5: Placement in a shoe.
[https://www.beilstein-journals.org/bjnano/content/supplementary/2190-4286-12-32-S5.mp4]

Supporting Information File 6

Video S6: Attachment to the waist.
[https://www.beilstein-journals.org/bjnano/content/supplementary/2190-4286-12-32-S6.mp4]

Supporting Information File 7

Video S7: Robotic sensing.
[https://www.beilstein-journals.org/bjnano/content/supplementary/2190-4286-12-32-S7.mp4]

Supporting Information File 8

Video S8: Human–computer interaction.
[https://www.beilstein-journals.org/bjnano/content/supplementary/2190-4286-12-32-S8.mp4]

Funding

This work was supported by the National Natural Science Foundation of China (Nos. 51872074 and 52072111), the Program for Innovative Research Team in Science and Technology in University of Henan Province (19IRTSTHN019), first-class discipline cultivation project of Henan University (2019YLZDJL06, 2019YLZDYJ04 and 2019YLZDYJ14) and the Candidates for the Training Program of Young Backbone Teachers in Henan Province of China (No.2018GGJS266) and the Scientific and Technological Project in Henan Province of China (212102210025).

References

1. Fan, F.-R.; Tian, Z.-Q.; Lin Wang, Z. *Nano Energy* **2012,** *1,* 328–334. doi:10.1016/j.nanoen.2012.01.004
2. Wang, Z. L. *ACS Nano* **2013,** *7,* 9533–9557. doi:10.1021/nn404614z
3. Wang, Z. L.; Chen, J.; Lin, L. *Energy Environ. Sci.* **2015,** *8,* 2250–2282. doi:10.1039/c5ee01532d
4. Wang, Z. L.; Wu, W. *Angew. Chem., Int. Ed.* **2012,** *51,* 11700–11721. doi:10.1002/anie.201201656
5. Xu, C.; Song, Y.; Han, M.; Zhang, H. *Microsyst. Nanoeng.* **2021,** *7,* 25. doi:10.1038/s41378-021-00248-z
6. Tang, Y.; Zhou, H.; Sun, X.; Diao, N.; Wang, J.; Zhang, B.; Qin, C.; Liang, E.; Mao, Y. *Adv. Funct. Mater.* **2019,** *30,* 1907893. doi:10.1002/adfm.201907893
7. Rahman, M. T.; Salauddin, M.; Maharjan, P.; Rasel, M. S.; Cho, H.; Park, J. Y. *Nano Energy* **2019,** *57,* 256–268. doi:10.1016/j.nanoen.2018.12.052
8. Duan, J.; Hu, T.; Zhao, Y.; He, B.; Tang, Q. *Angew. Chem., Int. Ed.* **2018,** *57,* 5746–5749. doi:10.1002/anie.201801837
9. Choi, D.; Yoo, D.; Kim, D. S. *Adv. Mater. (Weinheim, Ger.)* **2015,** *27,* 7386–7394. doi:10.1002/adma.201503802
10. Zhang, B.; Chen, J.; Jin, L.; Deng, W.; Zhang, L.; Zhang, H.; Zhu, M.; Yang, W.; Wang, Z. L. *ACS Nano* **2016,** *10,* 6241–6247. doi:10.1021/acsnano.6b02384
11. Lin, Z.; Zhang, B.; Zou, H.; Wu, Z.; Guo, H.; Zhang, Y.; Yang, J.; Wang, Z. L. *Nano Energy* **2020,** *68,* 104378. doi:10.1016/j.nanoen.2019.104378
12. Wang, H.; Han, M.; Song, Y.; Zhang, H. *Nano Energy* **2020,** *81,* 105627. doi:10.1016/j.nanoen.2020.105627
13. Sala de Medeiros, M.; Chanci, D.; Moreno, C.; Goswami, D.; Martinez, R. V. *Adv. Funct. Mater.* **2019,** *29,* 1904350. doi:10.1002/adfm.201904350
14. Li, X.; Jiang, C.; Zhao, F.; Lan, L.; Yao, Y.; Yu, Y.; Ping, J.; Ying, Y. *Nano Energy* **2019,** *61,* 78–85. doi:10.1016/j.nanoen.2019.04.025
15. Zhu, J.; Wang, X.; Xing, Y.; Li, J. *Nanoscale Res. Lett.* **2019,** *14,* 247. doi:10.1186/s11671-019-3085-9

16. Qian, J.; He, J.; Qian, S.; Zhang, J.; Niu, X.; Fan, X.; Wang, C.; Hou, X.; Mu, J.; Geng, W.; Chou, X. *Adv. Funct. Mater.* **2020,** *30,* 1907414. doi:10.1002/adfm.201907414
17. Zhang, Z.; Du, K.; Chen, X.; Xue, C.; Wang, K. *Nano Energy* **2018,** *53,* 108–115. doi:10.1016/j.nanoen.2018.08.011
18. Mule, A. R.; Dudem, B.; Patnam, H.; Graham, S. A.; Yu, J. S. *ACS Sustainable Chem. Eng.* **2019,** *7,* 16450–16458. doi:10.1021/acssuschemeng.9b03629
19. Cui, C.; Wang, X.; Yi, Z.; Yang, B.; Wang, X.; Chen, X.; Liu, J.; Yang, C. *ACS Appl. Mater. Interfaces* **2018,** *10,* 3652–3659. doi:10.1021/acsami.7b17585
20. Yang, Y.; Zhang, H.; Lin, Z.-H.; Zhou, Y. S.; Jing, Q.; Su, Y.; Yang, J.; Chen, J.; Hu, C.; Wang, Z. L. *ACS Nano* **2013,** *7,* 9213–9222. doi:10.1021/nn403838y
21. Wang, Z. L. *Mater. Today* **2017,** *20,* 74–82. doi:10.1016/j.mattod.2016.12.001
22. Martella, C.; Mennucci, C.; Lamperti, A.; Cappelluti, E.; Buatier de Mongeot, F.; Molle, A. *Adv. Mater. (Weinheim, Ger.)* **2018,** *30,* 1705615. doi:10.1002/adma.201705615
23. Wang, M.; Zhang, N.; Tang, Y.; Zhang, H.; Ning, C.; Tian, L.; Li, W.; Zhang, J.; Mao, Y.; Liang, E. *J. Mater. Chem. A* **2017,** *5,* 12252–12257. doi:10.1039/c7ta02680c
24. Yao, M.; Xie, G.; Gong, Q.; Su, Y. *Beilstein J. Nanotechnol.* **2020,** *11,* 1590–1595. doi:10.3762/bjnano.11.141
25. Guan, X.; Xu, B.; Wu, M.; Jing, T.; Yang, Y.; Gao, Y. *Nano Energy* **2021,** *80,* 105549. doi:10.1016/j.nanoen.2020.105549
26. Dong, B.; Yang, Y.; Shi, Q.; Xu, S.; Sun, Z.; Zhu, S.; Zhang, Z.; Kwong, D.-L.; Zhou, G.; Ang, K.-W.; Lee, C. *ACS Nano* **2020,** *14,* 8915–8930. doi:10.1021/acsnano.0c03728
27. Jeon, S.-B.; Kim, W.-G.; Park, S.-J.; Tcho, I.-W.; Jin, k.-K.; Han, J.-K.; Kim, D.; Choi, Y.-K. *Nano Energy* **2019,** *65,* 103994. doi:10.1016/j.nanoen.2019.103994

License and Terms

The definitive version of this article is the electronic one which can be found at:
https://doi.org/10.3762/bjnano.12.32

BEILSTEIN JOURNAL OF NANOTECHNOLOGY

Simulation of gas sensing with a triboelectric nanogenerator

Kaiqin Zhao[1,2], Hua Gan[3], Huan Li[4], Ziyu Liu[*1] and Zhiyuan Zhu[*2]

Full Research Paper

Open Access

Address:
[1]School of Microelectronics, Fudan University, Shanghai 200433, China, [2]Chongqing Key Laboratory of Nonlinear Circuits and Intelligent Information Processing, Southwest University, Chongqing 400715, China, [3]No.29 Research Institute of CETC, Chengdu 610036, China and [4]Ocean College, Zhejiang University, Zhejiang 316021, China

Email:
Ziyu Liu* - liuziyu@fudan.edu.cn; Zhiyuan Zhu* - zyuanzhu@swu.edu.cn

* Corresponding author

Keywords:
gas; sensor; triboelectric nanogenerator (TENG)

Beilstein J. Nanotechnol. **2021,** *12,* 507–516.
https://doi.org/10.3762/bjnano.12.41

Received: 28 December 2020
Accepted: 20 May 2021
Published: 28 May 2021

This article is part of the thematic issue "Nanogenerators and flexible electronics".

Guest Editor: Y. Mao

Abstract

Safety concerns require the frequently check for leaks in gas pipelines. Also, in coal mines the type gases permeating from the ground need to be monitored. Triboelectric nanogenerators (TENGs) can be applied for gas sensing without external power supply. In this paper, a two-dimensional model of a TENG was established, and a gas jet a rectangular cross section was added between two triboelectric materials. The TENG could generate distinguishable electrical signals according to the different types of gas and the different gas injection areas. This work contributes to the area of self-powered gas sensing.

Introduction

With economic development and social progress, there is an increasing demand for wearable [1-4], medical [5], and portable electronic devices [6,7]. The power supply is an important part of modern electronic equipment. A traditional battery has the disadvantages of short work life and heavy pollution. Therefore, it is extremely urgent to find a green and sustainable power supply for microelectronic devices.

Triboelectric nanogenerators (TENGs) can collect and convert different forms of energy (e.g., human motion [8-10], vibration [11], rotation [12], wind [13], and water [14]) into electric energy [15-17], thus expanding the range of energy production to a more microscopic scale [18] and improving the rate of utilization [19]. Characterized by low cost, light weight, environmental safety, and high conversion efficiency under low frequency, TENGs can provide continuous power supply for wearable devices [20], medical devices, and microelectronic systems [21]. In addition, triboelectric nanogenerators can also be used as sensors [22]. TENGs, originally proposed by Prof. Zhongling Wang [23], are microgenerators that convert mechanical energy into electrical energy based on the triboelectric effect [24]. In most TENG simulations, a triboelectric polymer material is in direct contact with an electrode layer with very small separation distance (less than 1 mm) [25], and the effective contact area of the friction material is increased by texturing its surface [26,27] to improve its electrical output. This setup is widely applied in vertical contact separation mode [28,29], sliding mode [30,31], single electrode mode [32-34], and independent layer mode [35]. In order to explain the charge transfer process between two friction materials in contact, various models have been proposed and explored, such as electron cloud model [36-38], ion transfer model [39], and material transfer model [40].

It is attractive that, in addition to providing power for electronic devices, TENGs can also be used as self-powered sensors for pressure, vibration, speed, chemicals, and body motion. Regarding leaks in gas pipelines or harmful gases in underground coal mines, it is necessary to detect the presence of a specific gas or the content of gas in ambient air. Therefore, gas sensors are usually indispensable in safety systems. Ordinary sensors need to be charged externally, and once the power is used up, the gas sensor loses its function. TENGs generate electricity that can be used for developing self-powered gas sensors.

In this paper, in order to explore the sensing of different gases by TENGs, a gas jet of rectangular cross section was added to the two-dimensional model of a TENG. The TENG generates electrical signals depending on the type of gas and the cross section of the gas injection area. Further, in order to eliminate the inevitable topological change during the actual movement of the TENG, an air gap was established in COMSOL to construct the two-dimensional model of the TENG. Based on the assumption that the surface charge density of the triboelectric nanogenerator is constant, the potential was calculated by using finite element methods and the Poisson equation of static electricity, and the influence of the change in the shape of the triboelectric material was simulated.

Results and Discussion

Triboelectric nanogenerators generate electricity through contact electrification and electrostatic induction. Contact electrification refers to the electron transfer between two different materials in contact because the atoms are so close together. An electric field is generated after friction electrification, and electrostatic induction is caused by the electric field. The charge flow of a TENG is shown in Figure 1. When the two triboelectric materials contact each other, different charges are generated on the surface. When they are separated, the induced electrons of the upper surface electrode will flow to the lower surface electrode, forming a current flow. When the two triboelectric materials approach, the electrons of the electrode on the lower surface will flow back to the electrode on the upper surface, forming a downward current until the two triboelectric materials contact each other.

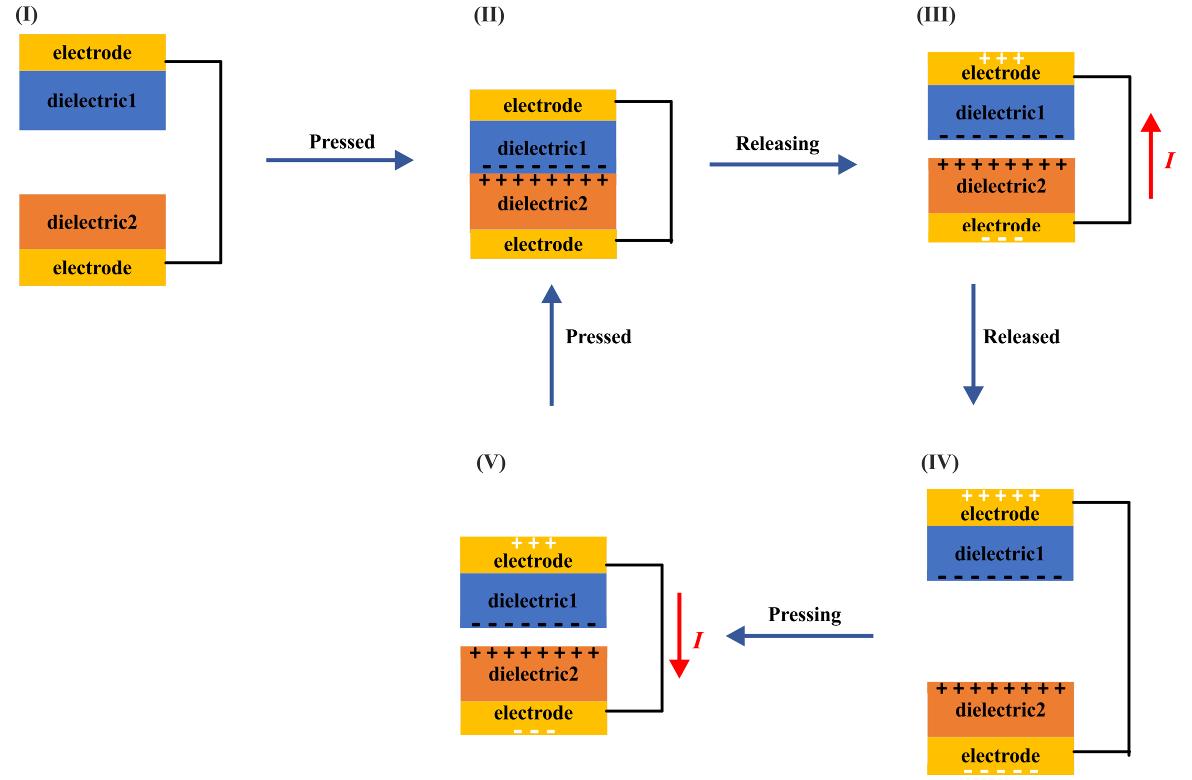

Figure 1: Charge flow in a triboelectric nanogenerator.

A simplified model of a two-dimensional TENG was set up in COMSOL (Figure 2). Two rectangles represent the triboelectric materials with different dielectric constants. The length and width are set as 50 mm and 0.1 mm, respectively. By changing the distance (*ds*), we simulate the process of the triboelectric materials approaching and moving away from each other. Figure 3a is the surface potential distribution diagram of the triboelectric materials of a TENG at a distance of 1 mm. Due to the influence of the relative permittivity, the material with the lower relative permittivity is negatively charged, while the other triboelectric material is positively charged. When the distance between the two dielectric materials varies, the field intensity caused by the charge also varies. The corresponding electric potential decreases with decreasing distance and increases with increasing distance. Figure 3b is the electric potential distribution diagram when the distance is 0.1 mm. In the simulation, we measured the potential difference between the outer surfaces of the two dielectric materials as *ds* is gradually increased from 0.1 to 1 mm, as shown in Figure 3c, which also reflects the influence of the distance between the two triboelectric materials on the potential.

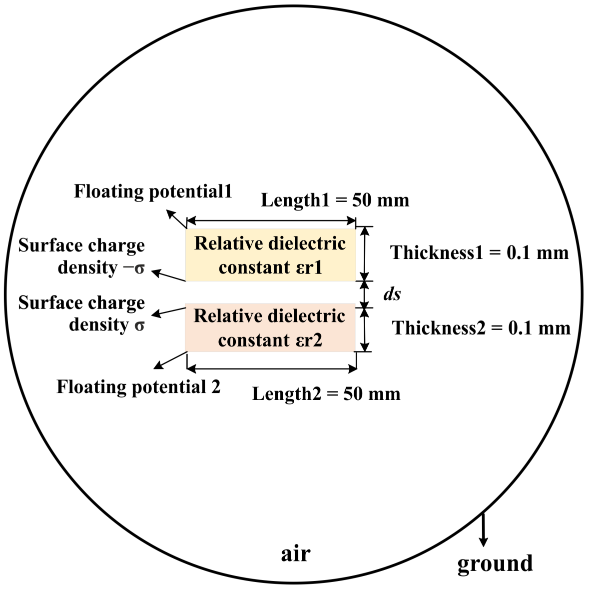

Figure 2: Two-dimensional model of a contact separation TENG.

In practice, it is difficult to directly test the influence of the shape of the triboelectric material on the electric potential due to the influence of various factors. Here, we set the shape of the upper triboelectric material to be an isosceles triangle and a right-angled triangle, the height is set to 1 mm, and the other parameters are the same as in Figure 2, as shown in Figure 4.

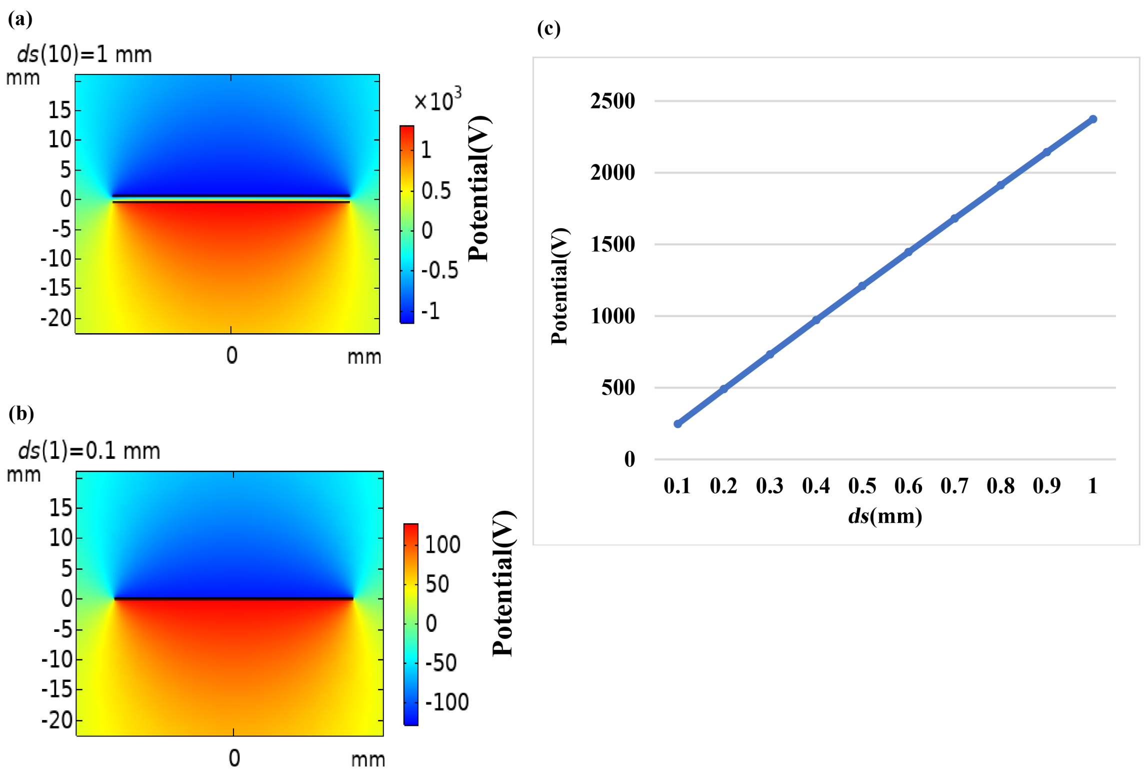

Figure 3: Simulation diagram for (a) *ds* = 1 mm and (b) *ds* = 0.1 mm. (c) Potential difference between the outer surfaces of the upper and the lower triboelectric materials as a function of *ds*.

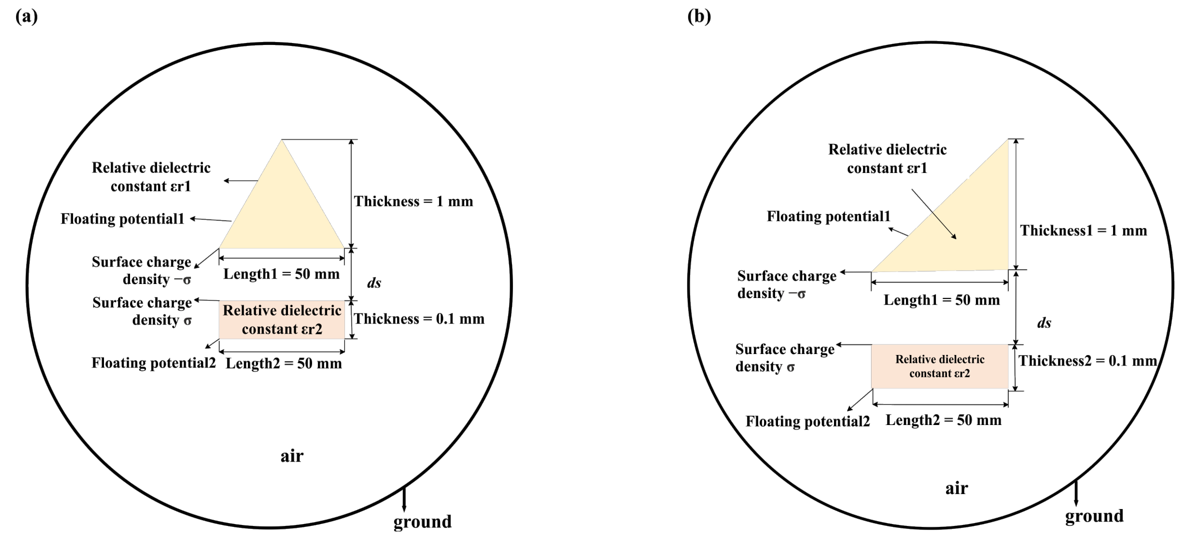

Figure 4: Two-dimensional TENG model with (a) isosceles triangle and (b) right-angled triangle TENG model.

The three models were simulated and compared in COMSOL while ignoring edge effects. As can be seen from Figure 5a–c, the electric potential of the rectangle and the isosceles triangles is symmetrically distributed along the central axis, while that of the right-angled triangle is asymmetrically distributed. Figure 5b shows that the two sides of the isosceles triangle have the same potential. According to Figure 5c, the potential distribution at the hypotenuse of the right-angled triangle is different from that at the side perpendicular to the horizontal plane. The potentials at the hypotenuse and the right side of the right-angled triangle were simulated for *ds* values of 0.1, 0.2, 0.3, 0.4, 0.5, 0.6, 0.7, 0.8, 0.9, and 1 mm, and the potential difference was calculated. Figure 5d shows that the electric potentials at the hypotenuse and the right side of the triangle increase with an increase of *ds*. Also, the potential difference increases. Therefore, if an external circuit can be built, then the load can be directly connected to the right side and the hypotenuse of the right-angled triangle and the transfer of electrons can be driven by the potential difference between the two sides. Figure 5e,f shows the electric potential in the simulation of rectangle, isosceles triangle, and right-angled triangle. The electric potentials obtained for the three models are basically the same, but it can be found that the electric potential calculated for the rectangular TENG is higher than those calculated for the triangles. Figure 5f is the potential difference obtained by subtracting the potential of the isosceles triangle TENG and that of the hypotenuse of the right-angled triangle TENG. The potential difference is all positive, and the potential difference increases as *ds* increases. The potential of the hypotenuse of the right-angled triangle TENG is smaller than that of the right-angled side, but as the distance *ds* increases, the gap between the potentials of the two sides decreases until the potential of the hypotenuse is greater than that of the right-angled side. It can be concluded that the rectangular TENG is economical and can achieve good electronic output.

We considered designing a TENG-based gas sensor that could be used to detect different gases under real-life conditions. When, in contact separation mode, two triboelectric materials approach or move away from each other, other substances, such as water vapor, carbon dioxide, and other gases, can pass through the gap. We present a simulation with water vapor under ideal conditions, that is, the surface charge density may be changed during the experiment. A simplified two-dimensional sensor model is shown in Figure 6a. A rectangular gas injection area was added to the model in Figure 2. It was used to study the influence of gas type and gas injection area on the electrical potential of the TENG. The potential distribution obtained from COMSOL is shown in Figure 6b.

The injection of carbon dioxide into the air gap of the TENG was simulated to quantitatively analyze the gas injection area. The effect on the TENG potential was first considered as a function of the gas injection area (indicated here by the side length of the rectangle) and the distance between the two triboelectric materials, as shown in Figure 7a. When gas injection area changes, the TENG potential also changes slightly. Figure 7b–d shows that, with constant distance between the two triboelectric materials, an increase in the size of the gas injection area leads to a decrease of the electric potential, suggesting that the TENG gas sensor can be used to measure the size of a gas leak.

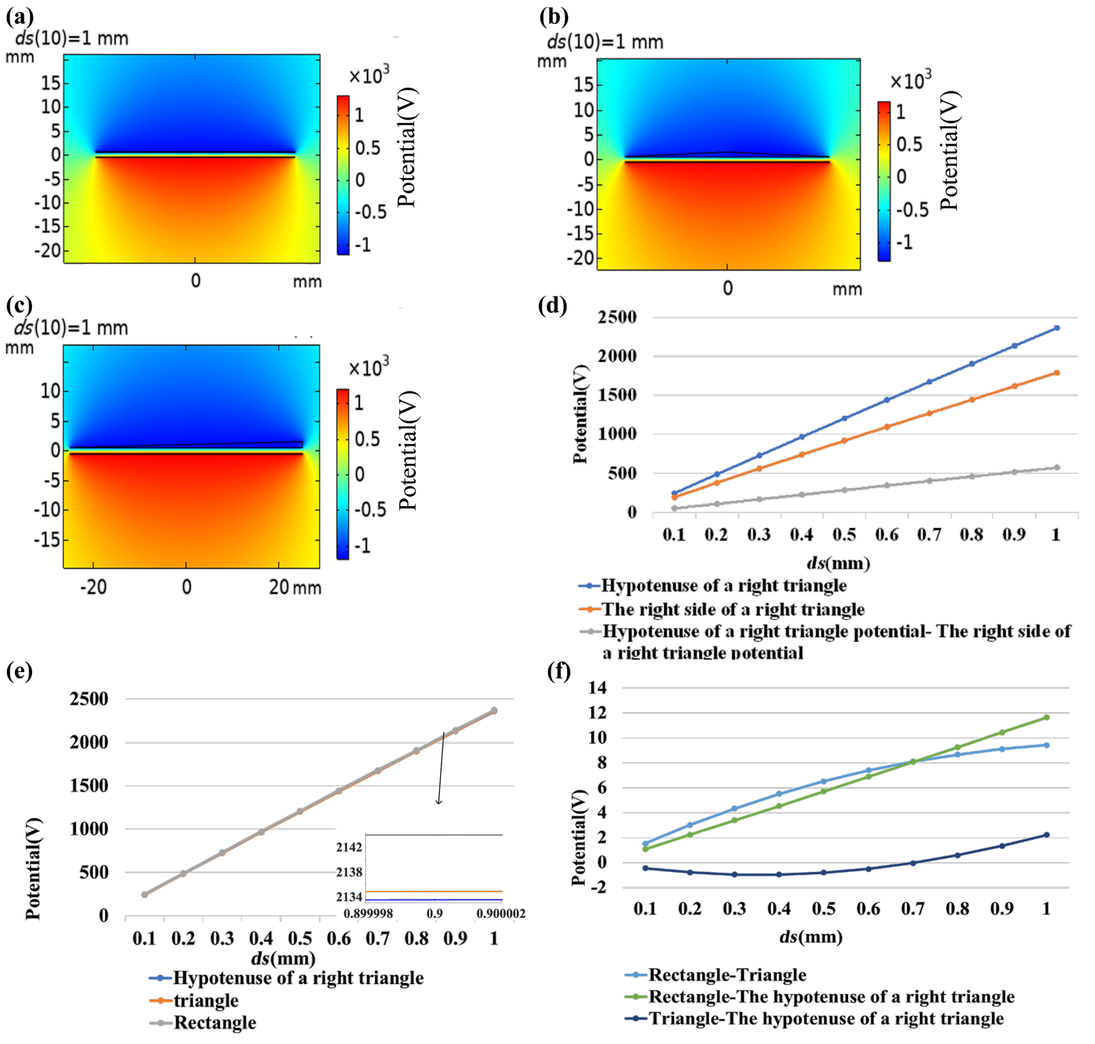

Figure 5: Comparison of shapes. (a) Potential distribution diagram of a rectangular TENG. (b) Potential distribution diagram of an isosceles triangle TENG. (c) Potential distribution diagram of a right-angled triangle TENG. (d) Outer boundary potential and potential difference of a right-angled triangle TENG. (e) Potential of the three shapes of TENG. (f) Potential difference of the three shapes of TENG.

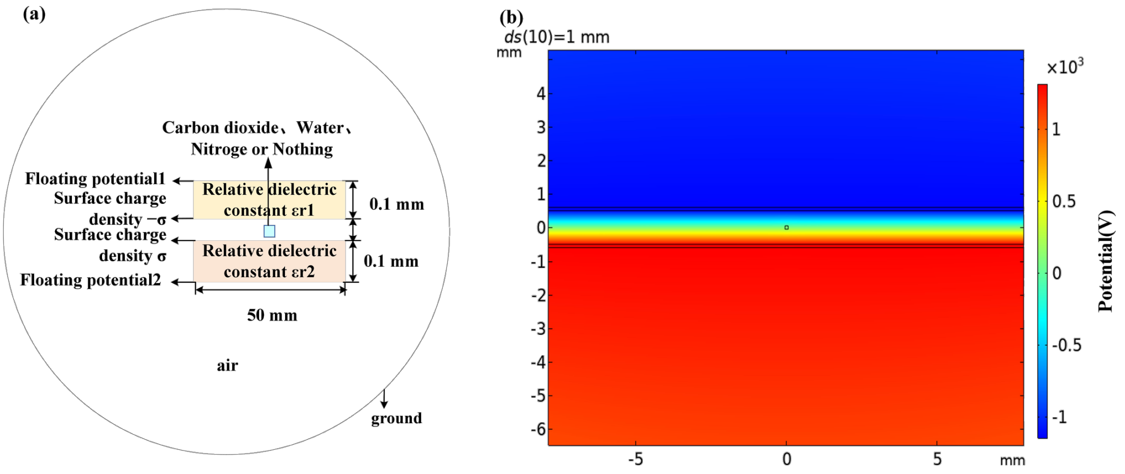

Figure 6: (a) TENG with a gas jet between two triboelectric materials. (b) TENG potential distribution diagram with gas jet.

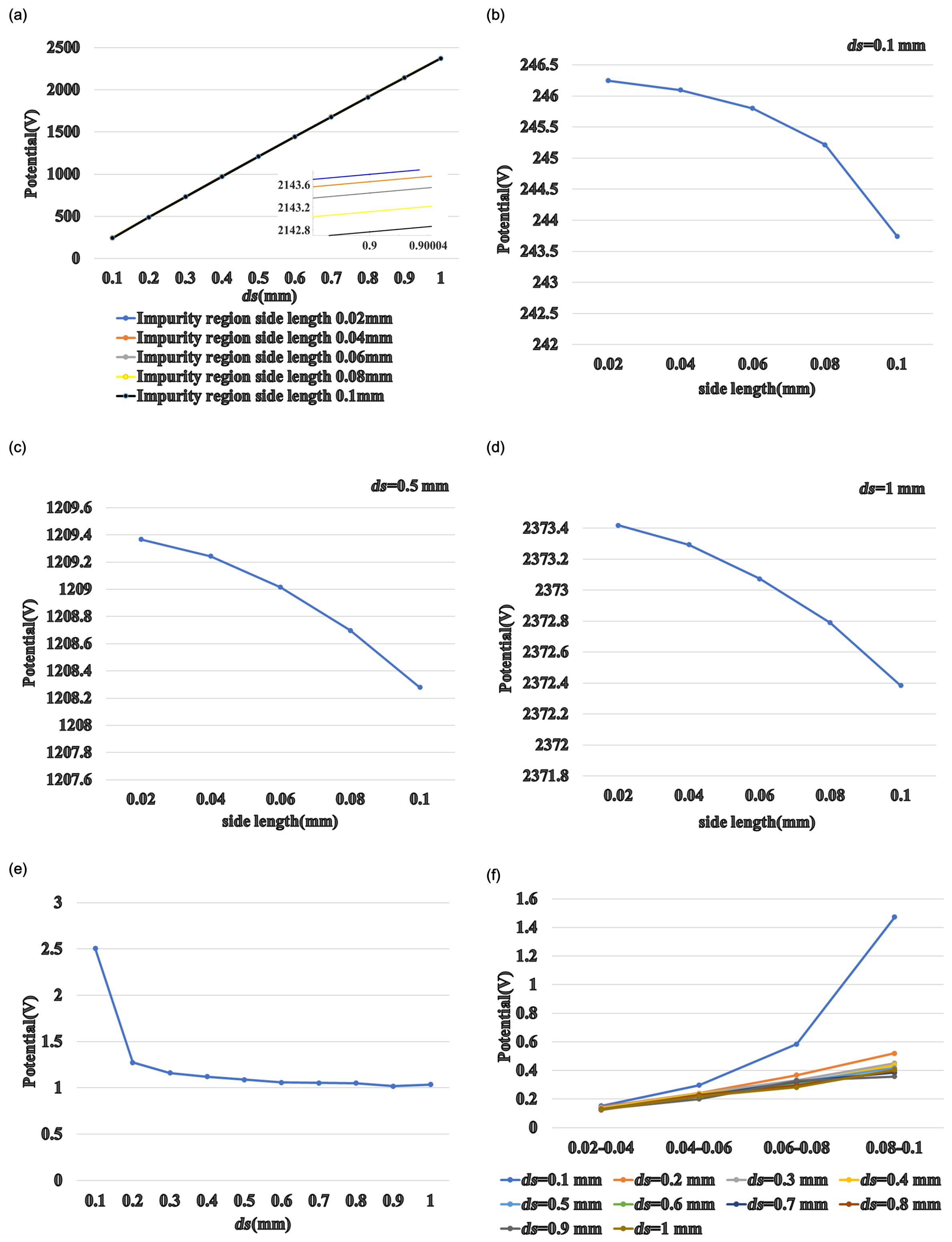

Figure 7: (a) The potential of the TENG varies with distance *ds* for different sizes of the gas injection area. The TENG potential as a function of the gas injection area with (b) *ds* = 0.1 mm, (c) *ds* = 0.5 mm, and (d) *ds* = 1 mm. (e) TENG potential difference as a function of *ds*. (f) TENG potential difference of rectangular cross sections with different side lengths.

Figure 7e shows the TENG potential as a function of the distance *ds*. For *ds* = 0.1 mm, the difference in TENG potential is the largest (approximately 2.5 V). When *ds* increases, the potential difference between a gas injection area of 0.02 mm and a gas injection area of 0.1 mm decreases, eventually reaching 1 V. This suggests that when the distance between the two triboelectric materials is large enough relative to the size of the gas injection area, the size of the gas injection area has little effect on the sensing function. Therefore, if the gas injection area needs to be measured, it should be first estimated, then an appropriate TENG distance *ds* needs to be found.

The potential differences of the TENG with a rectangular gas injection area with different side lengths are compared in Figure 7f. The curves are closer to a quadratic function when *ds* = 0.1 mm. Based on the knowledge of differential derivation in mathematics, Figure 7b can be speculated to be a cubic curve. The curves of the four potential differences are closer to linear curves for *ds* = 0.2–1.0 mm. Similarly, it can be inferred that Figure 7c and Figure 7d are curves of a quadratic function.

We compared the TENG with carbon dioxide, water vapor, and nitrogen as injection gases. Figure 8 shows the potential difference of the TENG with different gases at the same distance *ds*. The potential values of the TENG with carbon dioxide and water vapor are similar. The potential of the TENG with nitrogen is significantly higher. Without any gas, the potential of the TENG is even higher. It is noted that the relative dielectric constants of these three gases are different. That of carbon dioxide is the largest, followed by those of water vapor and nitrogen, which explain the results shown in Figure 8. It can also be concluded from these figures that the difference in power potential between the four types of TENG decreases with the increase of *ds*.

Figure 9a is the schematic diagram of an isosceles triangle TENG with a gas jet. Figure 9b is the corresponding simulation of the potential. In order to compare the effects of the two shapes of TENG on sensing different gases, we simulate the TENG with gas jets when *ds* is 0.1 mm, 0.5 mm, and 1 mm, as shown in Figure 9c–e. It can be seen from these three figures that a small distance between the triboelectric materials is helpful for distinguishing different gases. It is noted that water or humidity can degrade the surface charge density of the electrification surfaces in an actual experiment. We will carry out further investigations in the future.

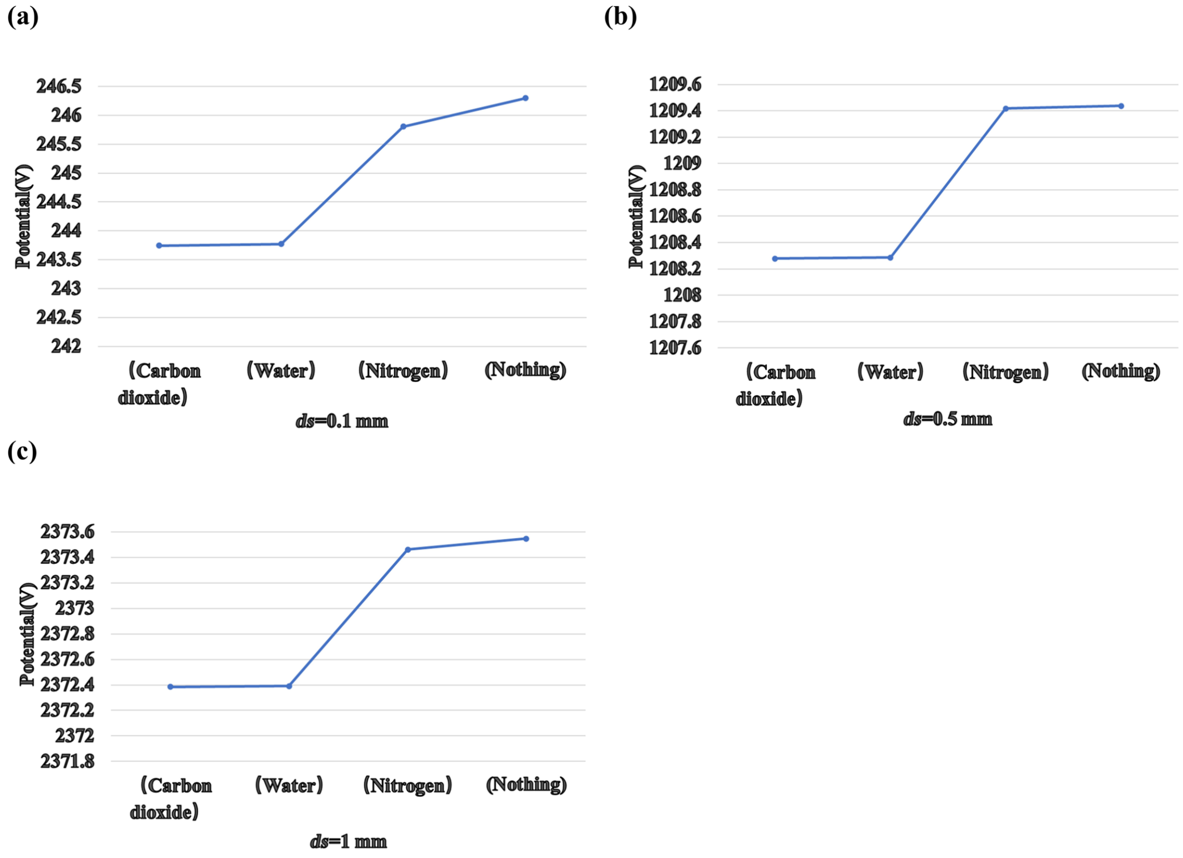

Figure 8: (a) The potential of TENG with different injected gases at (a) *ds* = 0.1 mm, (b) *ds* = 0.5 mm, and (c) *ds* = 1 mm.

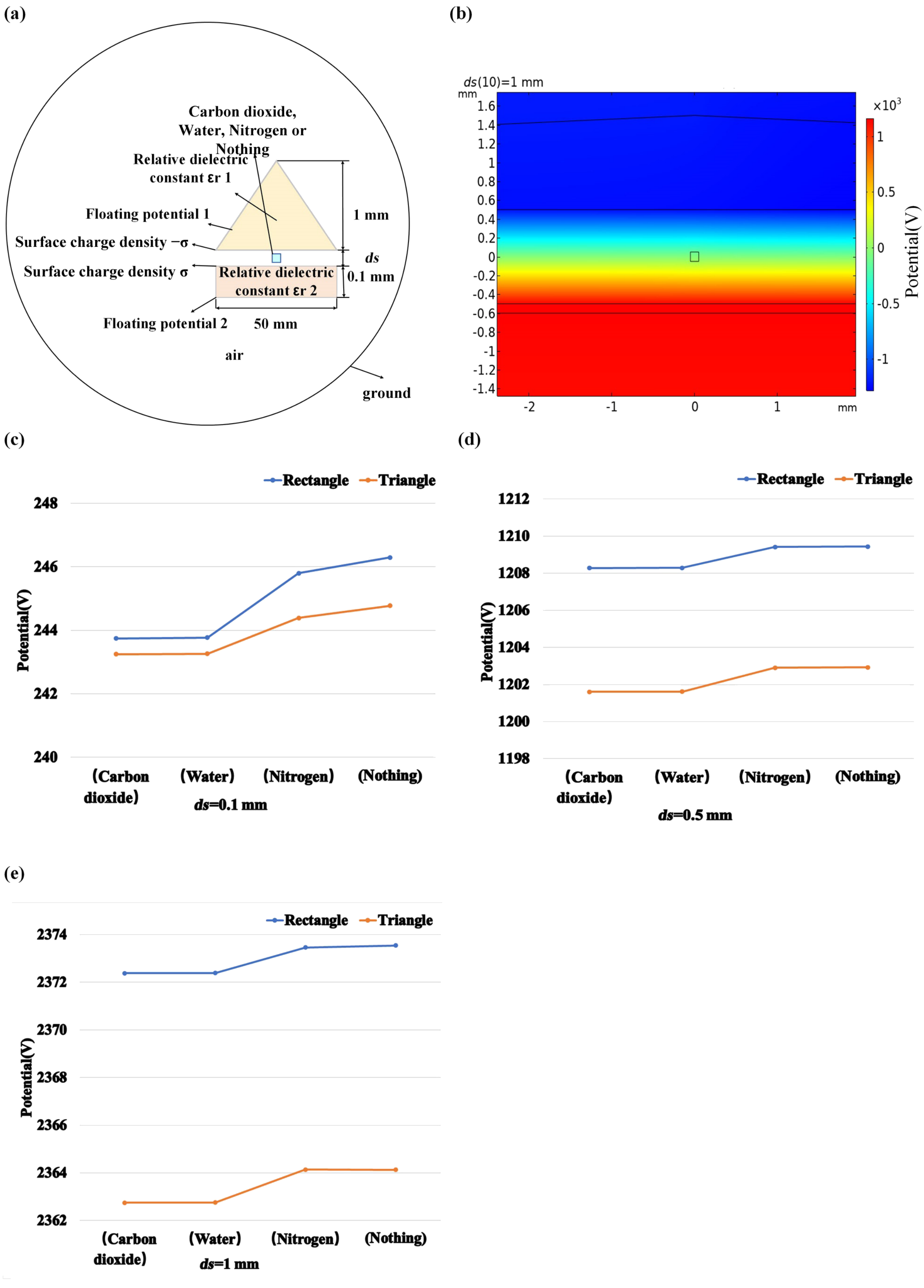

Figure 9: (a) Schematic diagram of an isosceles triangle TENG with injected gases. (b) Simulation of the TENG potential. (c–e) Potential diagram of the two shapes of TENGs with different injected gases at the same distance *ds*.

Conclusion

Simulations of three differently shaped TENGs were carried out in this paper. In order to investigate the sensing of different gases with sensors based on these TENGs, an injected gas jet with rectangular cross section was added to the two-dimensional model of the TENG. The size of the gas jet influences the potential of the TENG. However, when the distance between the triboelectric materials is large enough, a change of the gas jet cross section has only little effect on the TENG potential. The simulation results also show that the type of gas influences the potential of the TENG depending on the relative permittivity of the gas. This work is helpful for the development of self-powered TENG-bases gas sensors.

Funding

This research was supported by Zhejiang Provincial Natural Science Foundation of China (Grant No. LY20F040004), the Fundamental Research Funds for the Central Universities (Grant No. SWU019040, 2020jd001), National Natural Science Foundation of China (Grant No. 61804132, 62074132) and Zhoushan Municipal Government.

References

1. Xu, S.; Zhang, Y.; Jia, L.; Mathewson, K. E.; Jang, K.-I.; Kim, J.; Fu, H.; Huang, X.; Chava, P.; Wang, R.; Bhole, S.; Wang, L.; Na, Y. J.; Guan, Y.; Flavin, M.; Han, Z.; Huang, Y.; Rogers, J. A. *Science* **2014,** *344,* 70–74. doi:10.1126/science.1250169
2. Zhang, X.-S.; Han, M.; Kim, B.; Bao, J.-F.; Brugger, J.; Zhang, H. *Nano Energy* **2018,** *47,* 410–426. doi:10.1016/j.nanoen.2018.02.046
3. Li, X.; Lin, Z.-H.; Cheng, G.; Wen, X.; Liu, Y.; Niu, S.; Wang, Z. L. *ACS Nano* **2014,** *8,* 10674–10681. doi:10.1021/nn504243j
4. Kenry; Yeo, J. C.; Lim, C. T. *Microsyst. Nanoeng.* **2016,** *2,* 16043. doi:10.1038/micronano.2016.43
5. Araci, I. E.; Su, B.; Quake, S. R.; Mandel, Y. *Nat. Med.* **2014,** *20,* 1074–1078. doi:10.1038/nm.3621
6. Harris, K. D.; Elias, A. L.; Chung, H.-J. *J. Mater. Sci.* **2016,** *51,* 2771–2805. doi:10.1007/s10853-015-9643-3
7. Xiang, Z.; Yen, S.-C.; Sheshadri, S.; Wang, J.; Lee, S.; Liu, Y.-H.; Liao, L.-D.; Thakor, N. V.; Lee, C. *Adv. Mater. (Weinheim, Ger.)* **2016,** *28,* 4472–4479. doi:10.1002/adma.201503423
8. Lee, C.; Kim, M.; Kim, Y. J.; Hong, N.; Ryu, S.; Kim, H. J.; Kim, S. *Int. J. Control, Autom. Syst.* **2017,** *15,* 3–15. doi:10.1007/s12555-016-0462-3
9. Wang, M.; Zhang, J.; Tang, Y.; Li, J.; Zhang, B.; Liang, E.; Mao, Y.; Wang, X. *ACS Nano* **2018,** *12,* 6156–6162. doi:10.1021/acsnano.8b02562
10. Wang, M.; Zhang, N.; Tang, Y.; Zhang, H.; Ning, C.; Tian, L.; Li, W.; Zhang, J.; Mao, Y.; Liang, E. *J. Mater. Chem. A* **2017,** *5,* 12252–12257. doi:10.1039/c7ta02680c
11. Luo, J.; Wang, Z.; Xu, L.; Wang, A. C.; Han, K.; Jiang, T.; Lai, Q.; Bai, Y.; Tang, W.; Fan, F. R.; Wang, Z. L. *Nat. Commun.* **2019,** *10,* 5147. doi:10.1038/s41467-019-13166-6
12. Wang, Z. L.; Chen, J.; Lin, L. *Energy Environ. Sci.* **2015,** *8,* 2250–2282. doi:10.1039/c5ee01532d
13. Lin, H.; He, M.; Jing, Q.; Yang, W.; Wang, S.; Liu, Y.; Zhang, Y.; Li, J.; Li, N.; Ma, Y.; Wang, L.; Xie, Y. *Nano Energy* **2019,** *56,* 269–276. doi:10.1016/j.nanoen.2018.11.037
14. Lin, Z.-H.; Cheng, G.; Wu, W.; Pradel, K. C.; Wang, Z. L. *ACS Nano* **2014,** *8,* 6440–6448. doi:10.1021/nn501983s
15. Parida, K.; Bhavanasi, V.; Kumar, V.; Bendi, R.; Lee, P. S. *Nano Res.* **2017,** *10,* 3557–3570. doi:10.1007/s12274-017-1567-6
16. Mao, Y.; Zhang, N.; Tang, Y.; Wang, M.; Chao, M.; Liang, E. *Nanoscale* **2017,** *9,* 14499–14505. doi:10.1039/c7nr05222g
17. Wang, Z.; Liu, W.; He, W.; Guo, H.; Long, L.; Xi, Y.; Wang, X.; Liu, A.; Hu, C. *Joule* **2021,** *5,* 441–455. doi:10.1016/j.joule.2020.12.023
18. Li, Z.; Chen, J.; Yang, J.; Su, Y.; Fan, X.; Wu, Y.; Yu, C.; Wang, Z. L. *Energy Environ. Sci.* **2015,** *8,* 887–896. doi:10.1039/c4ee03596h
19. Wang, Z. L.; Song, J. *Science* **2006,** *312,* 242–246. doi:10.1126/science.1124005
20. Ning, C.; Tian, L.; Zhao, X.; Xiang, S.; Tang, Y.; Liang, E.; Mao, Y. *J. Mater. Chem. A* **2018,** *6,* 19143–19150. doi:10.1039/c8ta07784c
21. Ding, W.; Wang, A. C.; Wu, C.; Guo, H.; Wang, Z. L. *Adv. Mater. Technol. (Weinheim, Ger.)* **2019,** *4,* 1800487. doi:10.1002/admt.201800487
22. Tang, Y.; Zhou, H.; Sun, X.; Diao, N.; Wang, J.; Zhang, B.; Qin, C.; Liang, E.; Mao, Y. *Adv. Funct. Mater.* **2020,** *30,* 1907893. doi:10.1002/adfm.201907893
23. Fan, F.-R.; Tian, Z.-Q.; Wang, Z. L. *Nano Energy* **2012,** *1,* 328–334. doi:10.1016/j.nanoen.2012.01.004
24. Niu, S.; Wang, Z. L. *Nano Energy* **2015,** *14,* 161–192. doi:10.1016/j.nanoen.2014.11.034
25. Wang, Z. L.; Lin, L.; Chen, J.; Niu, S.; Zi, Y. *Triboelectric Nanogenerators;* Springer International Publishing: Cham, Switzerland, 2016. doi:10.1007/978-3-319-40039-6
26. Jiang, T.; Chen, X.; Yang, K.; Han, C.; Tang, W.; Wang, Z. L. *Nano Res.* **2016,** *9,* 1057–1070. doi:10.1007/s12274-016-0997-x
27. Cheng, G.-G.; Jiang, S.-Y.; Li, K.; Zhang, Z.-Q.; Wang, Y.; Yuan, N.-Y.; Ding, J.-N.; Zhang, W. *Appl. Surf. Sci.* **2017,** *412,* 350–356. doi:10.1016/j.apsusc.2017.03.255
28. Chung, J.; Lee, S.; Yong, H.; Moon, H.; Choi, D.; Lee, S. *Nano Energy* **2016,** *20,* 84–93. doi:10.1016/j.nanoen.2015.12.006
29. Yang, W.; Wang, X.; Li, H.; Wu, J.; Hu, Y. *Nano Energy* **2018,** *51,* 241–249. doi:10.1016/j.nanoen.2018.06.066
30. Seol, M.-L.; Han, J.-W.; Moon, D.-I.; Yoon, K. J.; Hwang, C. S.; Meyyappan, M. *Nano Energy* **2018,** *44,* 82–88. doi:10.1016/j.nanoen.2017.11.067
31. Jing, Q.; Zhu, G.; Bai, P.; Xie, Y.; Chen, J.; Han, R. P. S.; Wang, Z. L. *ACS Nano* **2014,** *8,* 3836–3842. doi:10.1021/nn500694y
32. Gogurla, N.; Roy, B.; Park, J.-Y.; Kim, S. *Nano Energy* **2019,** *62,* 674–681. doi:10.1016/j.nanoen.2019.05.082
33. Zhang, B.; Tang, Y.; Dai, R.; Wang, H.; Sun, X.; Qin, C.; Pan, Z.; Liang, E.; Mao, Y. *Nano Energy* **2019,** *64,* 103953. doi:10.1016/j.nanoen.2019.103953
34. Mao, Y.; Geng, D.; Liang, E.; Wang, X. *Nano Energy* **2015,** *15,* 227–234. doi:10.1016/j.nanoen.2015.04.026
35. Paosangthong, W.; Wagih, M.; Torah, R.; Beeby, S. *Nano Energy* **2019,** *66,* 104148. doi:10.1016/j.nanoen.2019.104148
36. Willatzen, M.; Wang, Z. L. *Nano Energy* **2018,** *52,* 517–523. doi:10.1016/j.nanoen.2018.08.015
37. Lin, S.; Xu, C.; Xu, L.; Wang, Z. L. *Adv. Funct. Mater.* **2020,** *30,* 1909724. doi:10.1002/adfm.201909724
38. Wang, Z. L.; Wang, A. C. *Mater. Today* **2019,** *30,* 34–51. doi:10.1016/j.mattod.2019.05.016

39. McCarty, L. S.; Whitesides, G. M. *Angew. Chem., Int. Ed.* **2008,** *47,* 2188–2207. doi:10.1002/anie.200701812
40. Baytekin, H. T.; Patashinski, A. Z.; Branicki, M.; Baytekin, B.; Soh, S.; Grzybowski, B. A. *Science* **2011,** *333,* 308–312. doi:10.1126/science.1201512

License and Terms

The definitive version of this article is the electronic one which can be found at:
https://doi.org/10.3762/bjnano.12.41

BEILSTEIN JOURNAL OF NANOTECHNOLOGY

Nanogenerator-based self-powered sensors for data collection

Yicheng Shao[1], Maoliang Shen[1], Yuankai Zhou[1], Xin Cui[2,3,4], Lijie Li[5]
and Yan Zhang*[1,2,3,4]

Review

Address:
[1]School of Physics, University of Electronic Science and Technology of China, Chengdu 610054, China, [2]College of Chemistry and Chemical Engineering, Center on Nanoenergy Research, School of Physical Science and Technology, Guangxi University, Nanning 530004, China, [3]Beijing Institute of Nanoenergy and Nanosystems, Chinese Academy of Sciences, Beijing 100083, China, [4]College of Nanoscience and Technology, University of Chinese Academy of Sciences, Beijing 100049, China and [5]Multidisciplinary Nanotechnology Centre, College of Engineering, Swansea University, Swansea, SA1 8EN, UK

Email:
Yan Zhang* - zhangyan@uestc.edu.cn

* Corresponding author

Keywords:
data collection; Internet of Things; nanogenerator; self-powered sensor; wearable device

Beilstein J. Nanotechnol. **2021,** *12,* 680–693.
https://doi.org/10.3762/bjnano.12.54

Received: 01 January 2021
Accepted: 22 June 2021
Published: 08 July 2021

This article is part of the thematic issue "Nanogenerators and flexible electronics".

Guest Editor: Y. Mao

Abstract

Self-powered sensors can provide energy and environmental data for applications regarding the Internet of Things, big data, and artificial intelligence. Nanogenerators provide excellent material compatibility, which also leads to a rich variety of nanogenerator-based self-powered sensors. This article reviews the development of nanogenerator-based self-powered sensors for the collection of human physiological data and external environmental data. Nanogenerator-based self-powered sensors can be designed to detect physiological data as wearable and implantable devices. Nanogenerator-based self-powered sensors are a solution for collecting data and expanding data dimensions in a future intelligent society. The future key challenges and potential solutions regarding nanogenerator-based self-powered sensors are discussed.

Introduction

Self-powered sensor systems can harvest and convert environmental energy to electricity, which enables sensor operation without external power source [1,2]. Nanogenerators (NGs) can effectively harvest energy various low-frequency mechanical motions from the environment. NG-based self-powered sensors act as data collection units for traffic [3-11], meteorological environment [12-21], human movement [22-27], viscera [28-30], body fluid composition [31-39], biological nerve impulses [40], and gas sensors [18-20]. Self-powered sensors based on NGs can analyze objects from a new perspective. The materials of NG come from a wide range of sources, such as wood [41,42], paper [43-46], waste milk carton [15], and skin [47-49]. Thus, low-cost self-powered sensors can be deployed on a large scale and are a good candidate for data sources for the Internet of things (IoT), big data, and artificial intelligence (AI).

NGs can be used as both pressure sensors and as energy supplies. Triboelectric nanogenerators (TENGs) were used as electronic skin for pressure detection and material identification [50,51]. Pressure sensors based on piezoelectric nanogenerators (PENGs) were used to detect tiny pressure deviations from water droplets [52,53], wind flow [53-56], or even human pulse waveforms [57,58]. NG-based self-powered sensors can be applied in traffic monitoring [3,59-61], and road and bridge monitoring [4,59]. Data regarding the driving status of vehicles, the operating status of vehicle components, and the driver usage habits are related to the safety of vehicle driving and the experience of the driver [5-11].

The principle of operation of TENGs is the triboelectrification/contact electrification (CE) process [62-64]. TENGs have four working modes: the common vertical contact-separation mode, the single-electrode mode, the contact-sliding mode, and the freestanding-triboelectric-layer mode [2,65]. TENGs can be made of many different materials with low manufacturing cost, environmental friendliness, and low maintenance cost. TENG-based sensors can collect multidimensional and large-scale data, which are a novel data source for big data and AI. Especially, TENGs are good candidates for designing AI sensors [66]. TENGs can be used as an energy source for traditional sensors to collect tiny amounts of energy from the environment, such as from liquid droplets [67]. The performance of TENGs can be improved through material optimization and charge-accumulation strategies [4,62,64,68,69]. In addition, TENGs can be directly used as sensors. For example, TENGs can collect irregular and low-frequency wave energy to generate electricity from blue energy [70]. Self-powered sensors based on TENGs can collect hydrological data such as wave information [12,13], water quality [14,15], and ion concentration [16,17,71], which can be used for weather forecasting, disaster warning, and water quality protection. In addition, long-term monitoring and collection of hydrological data can also provide a certain reference for the design of sterilization and algae removal [72], wastewater treatment [73,74], and electrochemical corrosion protection of metal surfaces and battery cathodes [56,75,76]. TENG-based special flexible pressure sensors can be placed on the surface of human skin to monitor the physiological activities of the human body, such as joint bending, extension, and body rotation [22-26,77].

Figure 1 shows the application NG-based self-powered sensors in the collection of human physiological and of environmental

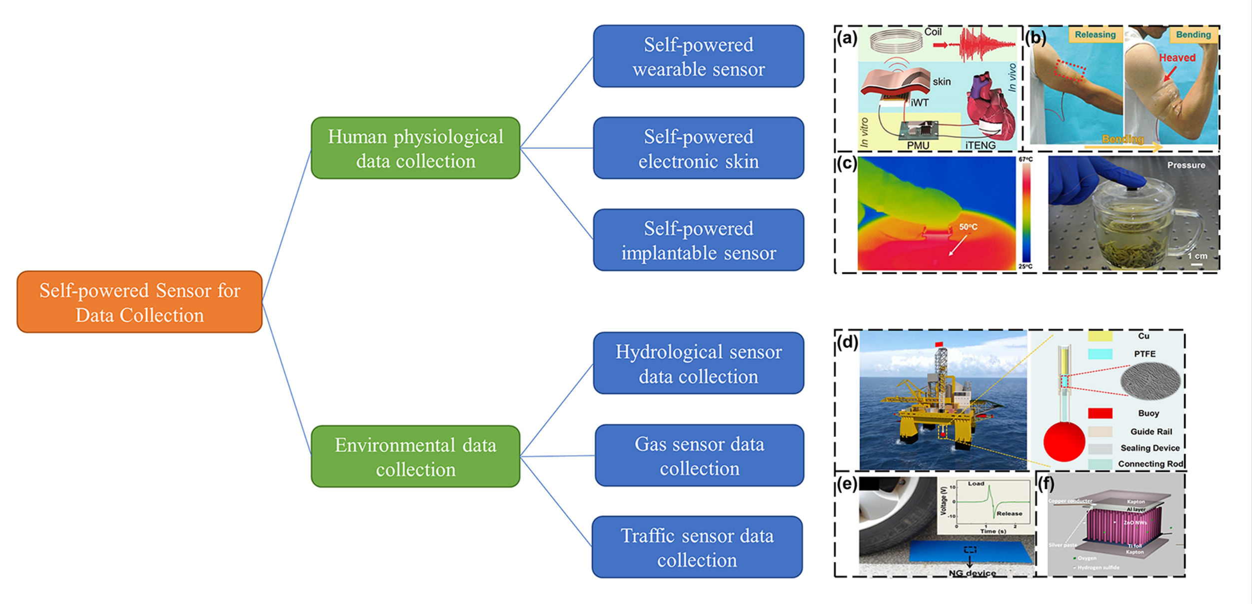

Figure 1: The development of nanogenerator-based self-powered sensors in the collection of human physiological data and of environmental data. Figure 1a was reproduced with permission from [28], Copyright 2016 American Chemical Society. Figure 1b is adapted from [22]. Copyright © 2018 WILEY-VCH Verlag GmbH & Co. KGaA, Weinheim. Used with permission from Zhen Wen et al., “TA Wrinkled PEDOT:PSS Film Based Stretchable and Transparent Triboelectric Nanogenerator for Wearable Energy Harvesters and Active Motion Sensors”, Advanced Functional Materials, John Wiley and Sons. Figure 1c is reproduced from [51] (© 2020 Yang Wang et al., some rights reserved; exclusive licensee American Association for the Advancement of Science. No claim to original U.S. Government Works. Distributed under a Creative Commons Attribution License 4.0 (CC BY) https://creativecommons.org/licenses/by/4.0/). Figure 1d reproduced with permission from [12], Copyright 2016 American Chemical Society. Figure 1e was reproduced from [3], Nano Energy, vol. 2, by L. Lin, Y. Hu, C. Xu, Y. Zhang, R. Zhang, X. Wen, Z. L. Wang, “Transparent flexible nanogenerator as self-powered sensor for transportation monitoring“, pages no. 75–81, Copyright (2012), with permission from Elsevier. Figure 1f was republished from [18] (X. Xue et al., “Surface free-carrier screening effect on the output of a ZnO nanowire nanogenerator and its potential as a self-powered active gas sensor”, Nanotechnology, vol. 24, no. 22, 225501, published on 30 April 2013, https://doi.org/10.1088/0957-4484/24/22/225501 © 2013 IOP Publishing Ltd. Publishing. Reproduced with permission via Copyright Clearance Center. All rights reserved.

data. On this basis, developments and challenges of future NG-based self-powered sensors in data-driven intelligent systems are proposed.

Review

Human physiological data collection based on self-powered sensors

Self-powered wearable sensors and electronic skin

Self-powered wearable sensors to collect human motion data can provide a data set for medical diagnosis and rehabilitation, sports training, human motion recognition, respiratory monitoring, and human 3D motion modeling [78-80]. These data can be used for real-time detection of human health or human–computer interaction [81,82]. Wen et al. [22] manufactured a transparent and stretchable wrinkled (maximum strain approximately 100%) TENG (WP-TENG) based on a poly(3,4-ethylenedioxythiophene):poly(4-styrenesulfonate) (PEDOT:PSS) electrode and installed the WP-TENG-based self-powered motion sensor at different positions of a human arm. The WP-TENG was placed on the skin above the muscles of the arm, as shown in Figure 2a. When the arm is bent, the muscles stretch the sensor to a larger contact area, and a voltage variation is generated by the sensor. An output voltage of about 23 V is generated. When the arm is released, the voltage returns to zero. The peak voltage varies with the bending angle of the elbow, as shown in Figure 2b, and the frequency of joint motion, as shown in Figure 2c. The self-powered motion sensor can obtain the bending angle of the elbow joint through the peak voltage output, and monitor the motion frequency in real time by counting the peaks. Furthermore, self-powered motion sensors can be used for gesture recognition [78,83,84]. The combination of a self-powered motion sensor and a back-end data processing system based on machine learning (ML) can realize sign language recognition for people with language impairment. Zhou et al. [84] fabricated a stretchable sensor for sign language recognition. The stretchable sensor is installed on a glove by using a flexible material. When the fingers move, each finger generates an electrical signal. These signals are classified by using ML algorithms to obtain the text, and finally the text is converted into speech output. The method of ML processing uses a principal component analysis (PCA) algorithm for feature extraction and a support vector machine (SVM) algorithm for gesture recognition, with a recognition accuracy of 98.63% and recognition time of less than 1s. The front-end sensor could be replaced by a more advanced self-powered pressure/touch sensor based on PENGs/TENGs, which combined with back-end ML technology, can help disabled people to live and communicate normally. Self-powered motion sensors can also collect the weak mechanical energy generated in other physiological activities of the human body, such as heartbeat, breathing, and vocal cords [85,86]. Without external power supply, the back-end data processing technology can realize real-time detection and early warning of human health [87]. For example, voice can be recognized by vocal cord vibration, which can be recorded with a biosensor attached to the skin of the throat. Voice print recognition and speech recognition can be realized by employing back-end data processing technology [88].

PENG/TENG-based self-powered sensors are flexible and highly sensitive, which can reduce inconveniences of a sensor system during physical training [41]. Back-end intelligent analysis technology can be used to quickly detect the large amount of data collected to reconstruct muscle movement and accurately obtain exercise habits. For example, the movements of athletes can be detected and identified in real time using AI classification techniques [89]. Big data analysis technology can monitor the training status of athletes in real time and provide training suggestions [83].

TENGs have high sensitivity, and a slight strain can cause the output signal of TENGs to change. Self-powered sensors based on TENGs are feasible signal monitoring sensors for facial activity, breathing, vocal cord vibration, heartbeat, and other small physiological activities. Small physiological signals, such as facial activity data, can be used for monitoring the driver status to prevent non-hazardous driving and improve driving safety. In 2018, Meng et al. [10] proposed a TENG-based self-powered pressure sensor that can detect situations such as the driver stepping on the accelerator or blinking. In 2020, Lu et al. [11] further proposed a transparent stretchable self-powered sensor based on a polyacrylamide TENG (PL-TENG), which is used to detect driver fatigue and distraction while driving and then to alert the driver. Different actions of the driver, such as winking, opening mouth, nodding, and turning neck will cause the PL-TENG to output electrical signals with corresponding features. The output voltage can be processed by a recurrent neural network (RNN) and judged by multiple sensors to improve the driving safety. The TENG-based self-powered pressure sensor is more sensitive, more stable, and less costly than the near-infrared illuminator, with far-reaching implications for traffic safety.

TENG-based electronic skin has more functions. Inspired by the plasticity of human skin nerve signals, the researchers proposed a single-electrode TENG (SE-TENG) as an intelligent neuromorphic sensor using reduced graphene oxide [90]. Reduced graphene oxide can act as electronic trap, and the output information of the sensor contains real-time stimulation information and information about previous stimulations. The sensor can generate voltage pulses similar to biological mechanoreceptors

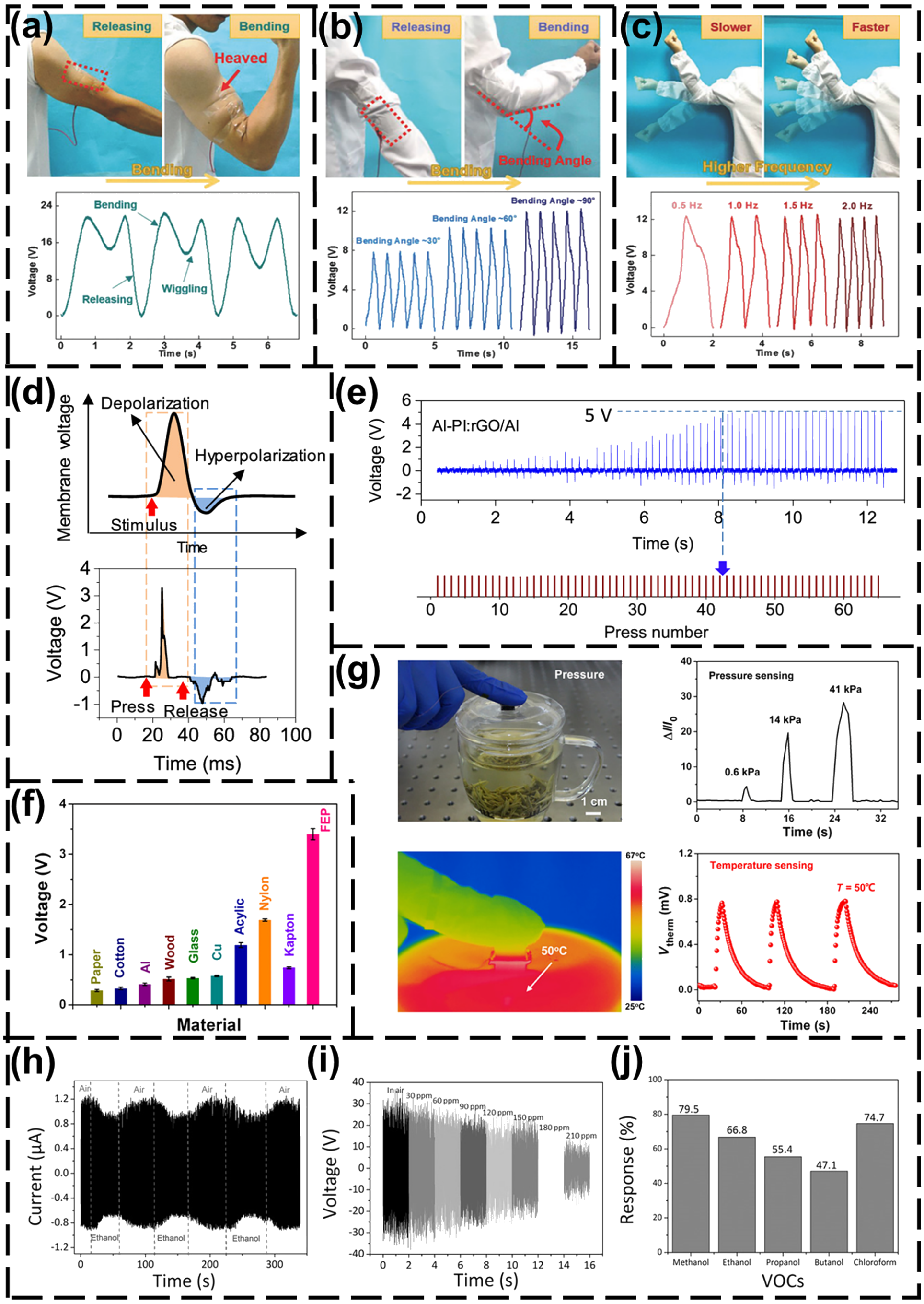

Figure 2: NG-based self-powered wearable sensor and electronic skin for data collection. (a) A schematic diagram of a WP-TENG-based motion sensor installed on the arm to detect the motion state, and the voltage signal generated by sensor when the arm is bent and released [22]. Figure 2a–c was reproduced from [22] (for permission, please see the caption of Figure 1b). (b) The sensor is installed on the elbow to detect different bending angles of the elbow. Voltage signals of different magnitudes are generated when the elbow is bent at different angles [22]. (c) The sensor is installed on the elbow. The elbow is bent and released at different frequencies and the voltage signals are generated at different frequencies [22]. (d) The biologic potential generated by external pressure and an intelligent neuromorphic sensor [90]. Figure 2d and Figure 2e were reprinted with permission from [90], Copyright 2020 American Chemical Society. (e) The output of the sensor changing with the increase of pressure times [90]. (f) The output voltage generated when in contact with different materials [51]. Figure 2f and Figure 2g were reproduced from [51] (for permission, please see the caption of Figure 1c) (g) A multi-functional self-powered sensor detects pressure and temperature and generates output signals [51]. (h) The output current of smelling electronic skin exposed to air and ethanol at a concentration of 60 ppm [91]. Figure 2h–j was reproduced from [91]. Copyright © 2016 WILEY-VCH Verlag GmbH & Co. KGaA, Weinheim. Used with permission from Xinyu Xue et al., “Outputting Olfactory Bionic Electric Impulse by PANI/PTFE/PANI Sandwich Nanostructures and their Application as Flexible, Smelling Electronic Skin”, Advanced Functional Materials, John Wiley and Sons. (i) The output voltage of smelling electronic skin as the ethanol concentration increases [91]. (j) The response of smelling electronic skin to several volatile organic compounds [91].

under external pressure, as shown in Figure 2d. The upper panel of Figure 2d is the biological action potential, and the lower panel of Figure 2d is the voltage pulse generated by the sensor. The output monotonously increases with pressure. The output voltage reaches a saturation value after a certain number of sensor actuations, as shown in Figure 2e. This intelligent neuromorphic sensor that mimics synaptic enhancement and memory can be used as a human skin tactile sensing solution, providing rich data for artificial intelligence. Wang et al. proposed a hydrophobic polytetrafluoroethylene film and sponge-like graphene/polydimethylsiloxane composite material to prepare a multifunctional self-powered sensor [51]. The sensor can infer the performance of the material through the difference in the output of the electrical signal generated by contact with different materials, as shown in Figure 2f. The sensor can also measure pressure and temperature as shown in Figure 2g.

Electronic skin can also collect composition information of substances in the air. Xue et al. proposed a TENG-based smelling electronic skin that generates electrical impulses when exposed to gas flow or pressure [91]. The material of the electronic skin can react with volatile organic compounds (VOCs) in the air, such as ethanol, as shown in Figure 2h. In addition to detecting whether the air contains VOCs, the output open-circuit voltage of the smelling electronic skin is also negatively correlated with the concentration of the VOCs, as shown in Figure 2i. The smelling electronic skin responds to a variety of VOCs, such as methanol, propanol, butanol, and chloroform, as shown in Figure 2j.

Self-powered implantable sensors

Physiological data can be used for health monitoring. When analyzing the components in body fluids, such as glucose, external sensors will lose accuracy due to interference from other components in body fluids [92]. An internal blood glucose sensor would be more reliable. Given the many possible TENG materials, materials with good biocompatibility can used for implantable self-powered physiological sensors. The sensors can be powered by the mechanical energy from the biological activity of the organism, and provide physiological data. An implantable heart monitoring sensor based on a TENG can work stably for a long time, providing a solution for long-term heart monitoring. Zheng et al. proposed an implantable TENG (iTENG) to realize wireless heart monitoring in vivo [28]. The iTENG is not cytotoxic. The packaging material of the iTENG showed good biocompatibility in mouse fibroblasts. The iTENG was implanted between heart and pericardium of a Yorkshire pig to monitor the heartbeat signal. The iTENG can be driven by heartbeat movement, collect the heartbeat signal and send it wirelessly to the data-receiving end outside the body, as shown in Figure 3a. The output voltage is synchronous with the electrocardiogram (ECG) signal, as shown in Figure 3b. The iTENG provided a stable electrical signal output for more than 72 h in this case.

The changes of endocardial pressure (EP) have important clinical significance for patients with impaired heart function. The self-powered endocardial pressure sensor (SEPS) converts the energy of blood flow into electrical energy in the heart, which is used to detect changes in EP in real time [29]. The SEPS was implanted in the left atrium of a Yorkshire pig. Figure 3c shows the output voltages during cardiac contraction and relaxation. The changes in the output voltage signal are completely synchronous with the changes in the femoral arterial pressure (FAP) and ECG signals. After epinephrine is injected, the FAP rises, while the peak value of the SEPS output voltage slowly decreases, as shown in Figure 3d. The opposite trends of the two are synchronous, so the output voltage of SEPS can be used as an indicator of epinephrine efficiency. The SEPS can accurately monitor the EP of the ventricle in real time. Through sudden changes in the EP, life-threatening arrhythmias can be detected in a timely manner.

Compared with the heart, the physiological activity of the gastrointestinal tract is weaker. Traditional TENGs are affected by the heart and respiration, and it is difficult to obtain accurate information on the physiological activity of the gastrointestinal tract. Cheng et al. proposed an asymmetrical and ultrasensitive TENG (ATNG), which can monitor tiny gastrointestinal movements and collect gastrointestinal data [30]. The ATNG was implanted into the abdominal cavity of a rabbit, and the duodenal peristalsis signal of the rabbit was monitored, as shown in Figure 3e. Comparison with the frequency-domain transform of the traditional TENG output signal implanted in the same position shows that the 0.58 Hz signal captured by the traditional TENG is a breathing signal. The ATNG can capture the gastrointestinal movement signal with the small 0.32 Hz intestinal movement signal and eliminate the interference of breathing. Under anesthesia, glucose solution was injected into the stomach of the rabbit. After 5 min, the gastrointestinal peristalsis becomes intense, and after 10 min, the peristaltic recovery becomes smooth (Figure 3f). It shows that the ATNG can monitor the weak activity of the gastrointestinal tract of a rabbit and can provide data on weak physiological activities.

An important indicator of human health is the composition of body fluids. The large amount of mechanical energy generated by the human body can also be used to drive a self-powered body fluid sensor to collect body fluid data [31-38]. In addition to the real-time detection of body fluids by self-powered technology, the self-powered technology can be used to deliver drugs to the patient according to changes in the chemical com-

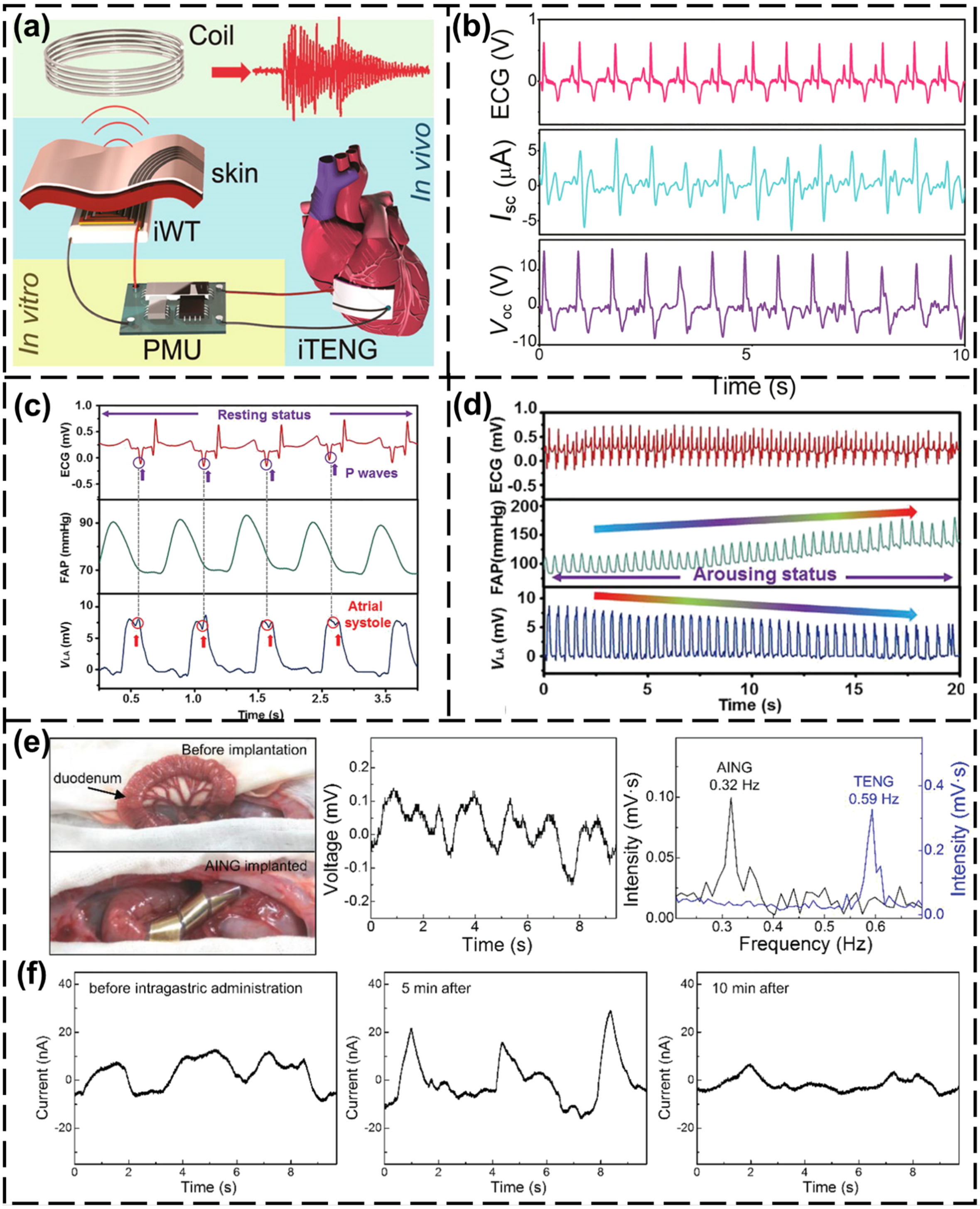

Figure 3: Self-powered implantable sensors in vivo. (a) Structure of heart data sensor based on an iTENG, implantable wireless transmitter (IWT) and power management unit (PMU) [28]. (b) Comparison of the output of the iTENG and ECG signal [28]. Figure 3a,b was reproduced with permission from [28] (for permission, please see the caption of Figure 1a). (c) Correspondence between ECG, FAP, and SEPS output signals [29]. Figure 3c,d was reproduced from [29]. Copyright © 2018 WILEY-VCH Verlag GmbH & Co. KGaA, Weinheim. Used with permission from Zhou Li et al., “Transcatheter Self-Powered Ultrasensitive Endocardial Pressure Sensor”, Advanced Functional Materials, John Wiley and Sons. (d) The change of ECG, FAP, and SEPS output voltage after epinephrine injection [29]. (e) When the ATNG is implanted in rabbits, the activity of the rabbit intestines causes changes in output signal of the ATNG [30]. Figure 3e,f were reproduced from [30]. Copyright © 2020 WILEY-VCH Verlag GmbH & Co. KGaA, Weinheim. Used with permission from Zhong Lin Wang et al., “Mechanically Asymmetrical Triboelectric Nanogenerator for Self -Powered Monitoring of In Vivo Microscale Weak Movement”, Advanced Functional Materials, John Wiley and Sons. (f) The electrical signal generated by the activity of the intestine after glucose injection under anesthesia [30].

position of the body fluids [93,94]. This self-powered experiential health management and treatment system is a development direction of future medicine. Zhang et al. [31] developed a self-powered implantable blood glucose meter based on the piezo-enzymatic-reaction coupling effect of GOx@ZnO (GOx: glucose oxidase) nanowires. By collecting the mechanical energy generated by human movement, the output voltage provided information about blood glucose concentration. As shown in Figure 4a, the output voltage of the self-powered blood glucose meter is inversely proportional to the glucose concentration. After implanting the device in a mouse, the output of the device changes with the blood glucose concentration, as shown in Figure 4b, which proves the feasibility of the device to collect blood glucose data.

Sweat data analysis is one of the directions to analyze the physical state of athletes. For example, lactic acid levels in the sweat of athletes are analyzed to determine whether they are tired and engaged in aerobic or anaerobic exercise. Guan et al. [37] proposed a self-powered analyzer that can detect changes in lactic acid in sweat. As shown in Figure 4c, the output voltage of the analyzer is proportional to the lactic acid concentration. The analyzer attached to the surface of human body uses the evaporation of sweat during human exercise to generate electricity, and its output performance is affected by the concentration of lactic acid in the sweat, as shown in Figure 4d. According to the change of output voltage data, big data analysis can be performed on the exercise status of the athlete. Training status and exercise intensity information can be obtained in real time. This is a new solution for big data sensing in sports. The mechanical energy generated by blood flow or body motion also can drive sensors for monitoring various indicators of body fluids. Pan et al. [35] proposed a self-powered blood pressure sensor that uses mechanical energy and biochemical energy. The fiber nanogen-

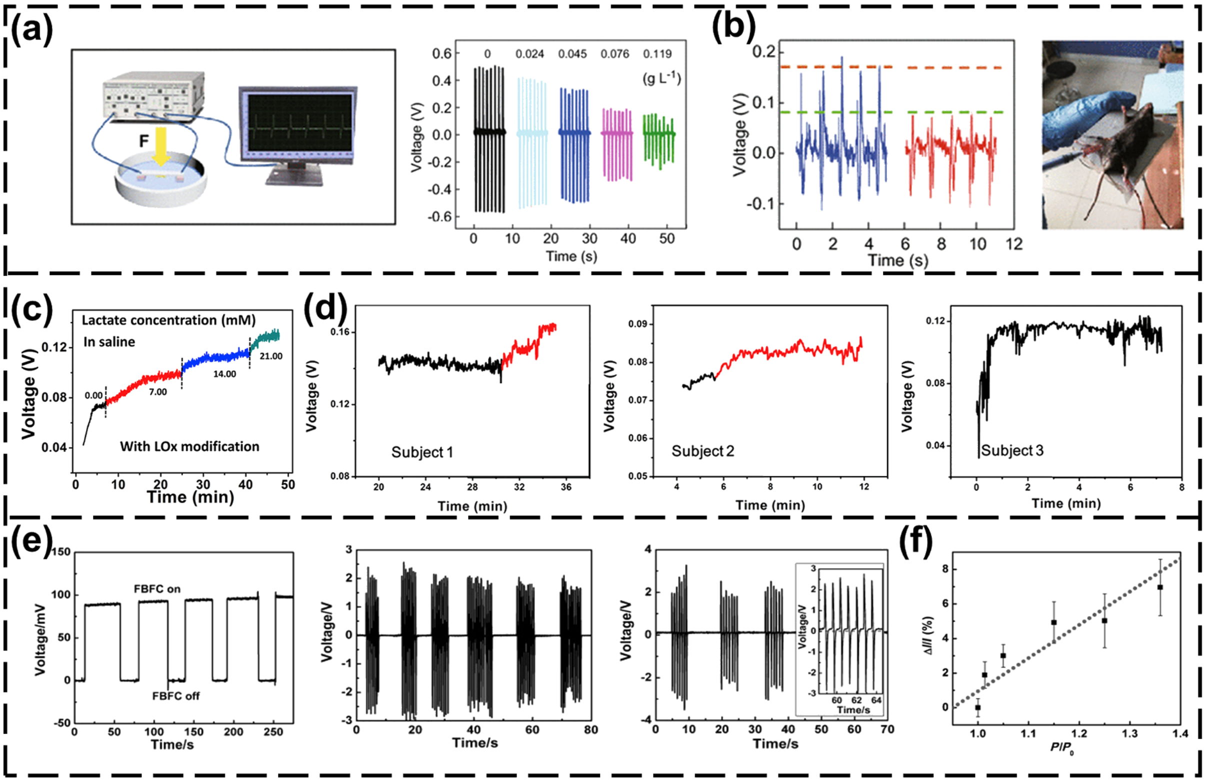

Figure 4: Structure and performance of self-powered body fluid sensors. (a) The system composition of the implantable skin-like glucometer and the voltage output in different concentrations of glucose [31]. Figure 4a,b was reproduced from [31] (© 2018 W. Zhang et al., published by Springer Nature, distributed under the terms of the Creative Commons Attribution 4.0 International License, https://creativecommons.org/licenses/by/4.0). (b) Implantable skin-like glucometer implanted in a mouse and the voltage output of the device under different blood glucose concentrations [31]. (c) The output voltage performance of sweat-evaporation-biosensing sensors in different concentrations of lactic acid [37]. Figure 4c,d was adapted from [37], Nano Energy, vol. 59, by H. Guan, T. Zhong, H. He, T. Zhao, L. Xing, Y. Zhang, X. Xue, "A self-powered wearable sweat-evaporation-biosensing analyzer for building sports big data", pages no. 754–761, Copyright (2019), with permission from Elsevier. (d) Real-time voltage output generated by the sweat-evaporation-biosensing sensor when three people are cycling [37]. (e) The FBFC converts glucose to produce DC output, the FNG produces AC output from the same periodic pressure, and the hybrid system output of FBFC and FNG in series [35]. Figure 4e,f was reproduced from [35]. Copyright © 2011 WILEY-VCH Verlag GmbH & Co. KGaA, Weinheim. Used with permission from Caofeng Pan et al., "Fiber-Based Hybrid Nanogenerators for/as Self-Powered Systems in Biological Liquid", Angewandte Chemie International Edition, John Wiley and Sons. (f) Output of the hybrid system under different pressures [35].

erator (FNG) and the fiber biofuel cell (FBFC) are fully integrated on a single carbon fiber. The FNG converts the periodically applied pressure in the liquid into an alternating current (AC) output, and the FBFC converts glucose in the blood into electrical energy to generate a direct current (DC) output. Figure 4e shows the output performance of FBFC and FNG, and the output performance of two devices in series. The output of FNG as a pressure sensor with pressure changes is shown in Figure 4f. The output is proportional to the pressure. By collecting mechanical energy and biochemical energy in the environment of the human body, this sensor can stably and continuously collect pressure data from human blood vessels and other body fluid environments. The NGs can be used for human health monitoring and blood pressure data analysis.

Environmental data collection based on self-powered sensors

Environmental sensors can be used for collecting and processing data of electricity and gas maintenance, vehicle safety, and weather forecasting. The collection of environmental data requires real-time, long-term monitoring. Compared with traditional sensors, self-powered sensors based on PENGs/TENGs can convert mechanical energy into electricity. At the same time, they can also obtain environmental information. PENG/TENG-based self-powered sensors can be placed on roads and bridges, which can be powered by mechanical energy from traffic flow and bridge vibration. Self-powered sensors can be used to collect real-time data of vehicle speed, acceleration and tire status. Self-powered sensors can collect hydrological and meteorological data, providing powerful data tools for ambient intelligence in the future, such as improving driving safety, accurate weather forecasts, and disaster warning.

Self-powered hydrological and gas sensors

Zhang et al. reported a triboelectric ocean-wave spectrum sensor (TOSS) [12]. The structure of the device is shown in Figure 5a. The TOSS collects wave data from a buoy. While ocean waves move the buoy up and down, charges are generated in a TENG, as shown in Figure 5b. The generated charges are linearly correlated with the wave heights, as shown in Figure 5c. From this linear relationship, the wave height data can be obtained, including period and speed of waves.

Environmentally friendly, portable, easy-to-deploy, and low-cost TENGs are novel devices for water quality monitoring. Zhou et al. proposed the use of waste materials to make an arc-shaped TENG (AS-TENG) [15]. The AS-TENG can provide energy for a pH sensor in water. The system can trigger an alarm when the pH value is lower than 5. Lee et al. proposed a based Hg^{2+} ion sensor based on ZnO nanowires and carbon nanotubes for detecting toxic pollutants [17]. The ZnO nanowire (NW) array acted as power source. When Hg^{2+} ions were detected, the system powered a light-emitting diode (LED). Li et al. designed a self-powered heavy metal ion triboelectric nanosensor [16]. By adding three ligand molecules to the surface of nanoporous anodic aluminum oxide, the detection sensitivity for Cu^{2+}, Pb^{2+}, and Cr^{3+} reached 0.005×10^{-6}, 0.003×10^{-6}, and 0.004×10^{-6} M, respectively. The self-powered tribo-nanosensor generates different output voltages according to the ion concentration, as shown in Figure 5d. The TENGs are a low-cost and environmentally friendly solution for detecting heavy metal ions. The kinetic energy generated by the flow of waste water is converted into electricity through a water-driven triboelectric nanogenerator (WD-TENG). Thus, heavy metal ions in waste water can be removed without external power consumption. The self-powered sensor collects water quality information such as ion concentration in the water as a data source for hydrological analysis.

PENG/TENG-based pressure sensors can accurately sense pressure changes through the output response signal. Gas molecules can be adsorbed on the surface of piezoelectric/triboelectric materials, causing changes in the carrier density [95]. Thus, the gas concentration can be obtained from the output voltage of the PENG/TENGs. The output of a PENG based on ZnO NWs is largely influenced by the surface carrier density on the surface of the nanowires. The adsorption of gas molecules can change the surface carrier density by the shielding effect, so the output of the sensor is very sensitive to the gas concentration. Compared with traditional metal oxide semiconductor (MOS) gas sensors, the PENG/TENG-based self-powered gas sensor has a lower power consumption, requires no heating, and exhibits high stability and high sensitivity.

In 2013, Xue et al. proposed a ZnO NWs PENG-based self-powered gas sensor [18]. The response of the unpackaged PENG sensor was studied under exposure to oxygen (O_2), hydrogen sulfide (H_2S) gas, and water vapor. The sensitivity to H_2S gas was as low as 100 ppm. The design of the whole self-powered sensor system consists of three parts. A ZnO NW array as the piezoelectric energy generation module, Ti foil and Al layer as electrodes, and kapton boards as supporting frame. Under the same deformation conditions, the sensitivity S of a PENG/TENG can be simply defined as:

$$S[\%] = \frac{V_a - V_g}{V_g} \times 100\%, \qquad (1)$$

where V_a is the piezoelectric output voltage in dry air (the concentration of the gas to be measured is 0 ppm), and V_g is the piezoelectric output voltage during exposure to the test gas. The

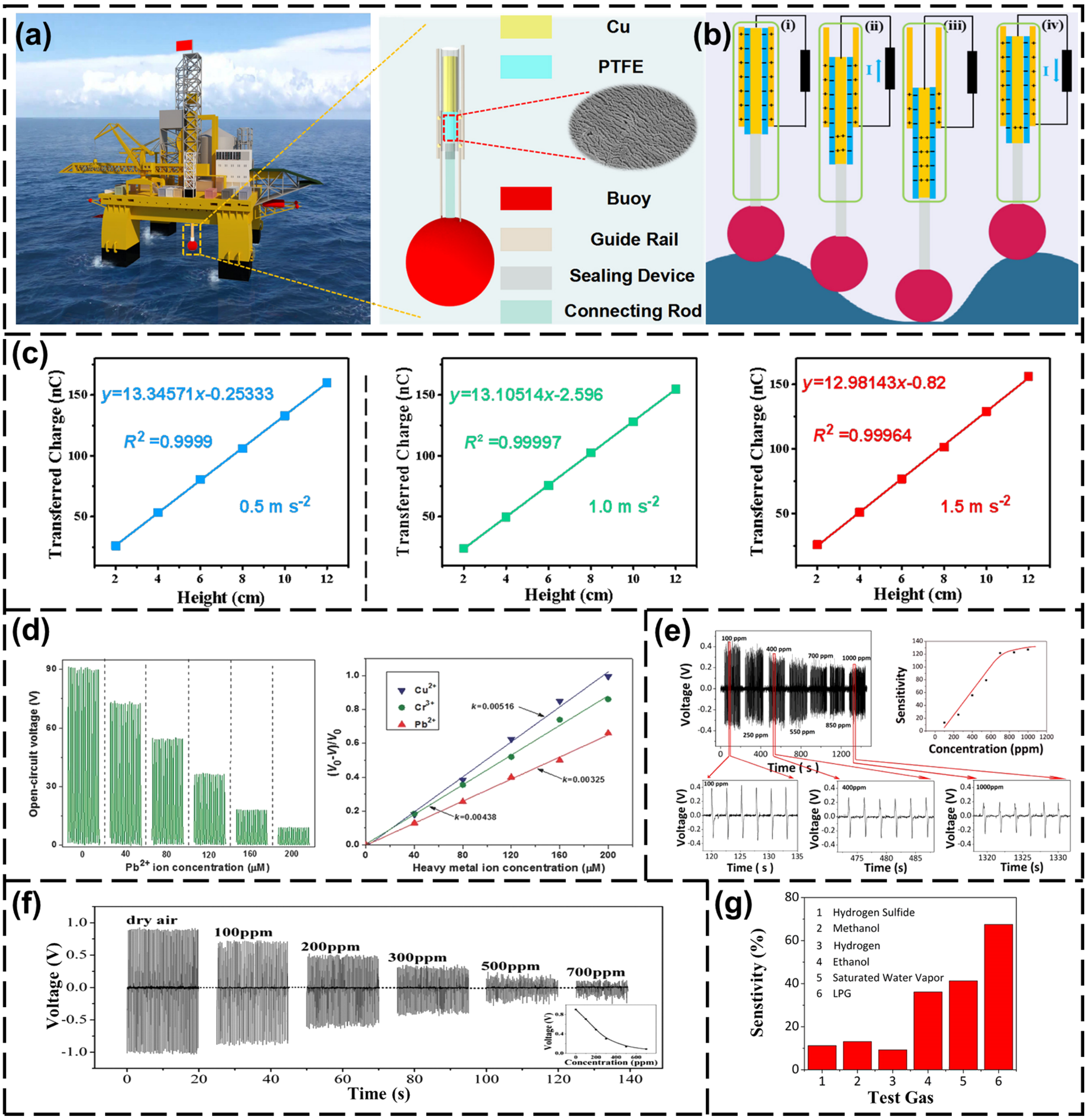

Figure 5: Self-powered hydrological and gas sensor for environmental data collection. (a) The appearance structure of TOSS [12]. Figure 5a–c was reproduced with permission from [12] (for permission, please see the caption of Figure 1d). (b) The principles of TOSS to obtain sea wave information [12]. (c) Relationship between wave height and transferred charges under different accelerations [12]. (d) Output voltage of the self-powered tribo-nanosensor under different heavy metal ion concentrations [16]. Figure 5d was reproduced from [16]. Copyright © 2016 WILEY-VCH Verlag GmbH & Co. KGaA, Weinheim. Used with permission from Zhaoling Li et al., “Triboelectrifcation-Enabled Self-Powered Detection and Removal of Heavy Metal Ions in Wastewater”, Advanced Materials, John Wiley and Sons. (e) Output voltage of the self-powered sensor under different H_2S gas concentrations at room temperature. The sensitivity *S* varies with H_2S gas concentration [18]. Figure 5e was reproduced from [18] (for permission, please see the caption of Figure 1f). (f) Piezoelectric output voltage relationship of the device when In_2O_3/ZnO NW is exposed to dry air and H_2S gas of various concentrations at room temperature [20]. Figure 5f was reproduced with permission from [20], Copyright 2014 American Chemical Society. (g) Sensitivity of $ZnSnO_3$/ZnO NW-based SPGS to H_2S, H_2, ethanol, methanol, LPG, and saturated moisture at 4000 ppm [21]. Figure 5g was reproduced with permission from [21], Copyright 2015 American Chemical Society.

sensitivity of above ZnO-based self-powered sensor is 127.3% under 1000 ppm H_2S. The piezoelectric output of sensor decreased with increase of the concentration of the tested gas, as shown in Figure 5e. In 2016, a self-powered gas sensor based on a NiO/ZnO heterojunction nanowire array showed high sensitivity and fast response [19]. At room temperature, the piezoelectric voltage of the NiO/ZnO NW array was reduced from 0.388 V (in dry air) to 0.061 V (at 1000 ppm H_2S), and the response was approximately 10 times that of naked the ZnO NW array. An In_2O_3/ZnO heterostructure was prepared the sensitivity of which was 925% [20]. Figure 5f shows the piezoelectric output voltage of In_2O_3/ZnO NW array exposed to dry air and H_2S gas of various concentrations at room temperature. Compared with the gas adsorption reaction of ZnO material, the conversion of In_2O_3/ZnO to In_2S_3/ZnO has a stronger regulating effect on the piezoelectric filtration of free carriers.

A ZnO-based self-powered gas sensor (SPGS) can be used to detect H_2S, NH_3 [96,97], ethanol [91,98-100], CO_2 [101,102] and other gases [103-105]. A $ZnSnO_3$/ZnO NW-based PENG was used to detect liquefied petroleum gas (LPG) with high sensitivity, selectivity, and reliability [21]. The sensitivity of $ZnSnO_3$/ZnO (1 h) NWs in 4000 ppm H_2S, H_2, ethanol, methanol, LPG, and saturated water vapor was measured. The sensitivity of $ZnSnO_3$/ZnO NW for LPG is much higher than for other gases, as shown in Figure 5g. Modaresinezhad et al. used a DC nanogenerator based on ZnO nanosheets as room-temperature self-powered humidity sensor [103].

This new type of self-powered gas sensors will be an important development direction for the next generation of gas sensors [95]. In addition, the above self-powered sensors show that they are easier to deploy and consume less power than traditional MOS gas sensors. Because of this, self-powered sensors can be deployed in large numbers, and a large number of self-powered sensors will generate a massive amount of data. Through big data and AI analysis the back-end data processing capability can be enhanced. Moreover, AI technology can also enhance the performance of sensor.

Traffic sensors

PENGs are also applicable in intelligent transportation systems. Self-powered vehicle sensors based on PENGs/TENGs can collect the signal of force changes when the vehicle status changes. In 2011, Hu et al. [5] proposed a flexible PENG that was attached to a vehicle tire. During rotation of the tire, the electrical pulses were generated by the PENG. These electrical signals can be used as sensor outputs to calculate the vehicle speed and provide energy for an external system. The PENG consisted of top and bottom Cr/Au electrodes, ZnO NWs on the electrodes and a flexible polyester substrate. Figure 6a shows the PENG fixed to the inner surface of the tire with adhesive tape. The output voltage of the PENG changed with the deformation of the tire during rolling. Figure 6b shows the output open-circuit voltage during tire movement. Speed information of the vehicle can be obtained from the output voltage.

Speed and acceleration sensors based on PENGs/TENGs were used to detect the driving status. Acceleration information can be obtained from the tire movement of the vehicle. Zhang et al. proposed a self-powered acceleration sensor based on liquid-metal triboelectric nanogenerator (LM-TENG), which can directly detect horizontal and vertical accelerations [6]. When a vehicle crashes, the force and position data of the vehicle can be obtained through the acceleration sensor. This acceleration sensor can be used to detect the acceleration of a vehicle climbing uphill. This application can provide data support for the vertical motion information for future 3D car navigation. A driving safety warning system can detect the tire pressure to determine whether the vehicle has too high or unbalanced load [7]. To detect the state of wheels at high friction and at high speed, sensors based on a harsh-environmental TENG (he-TENG) can be included in a self-powered smart brake system. TENG-based vehicle sensors can collect data on driving habits, such as the frequency of using brake pedal and accelerator pedal under different road conditions [8]. Thus, TENG-based warning and brake systems may be designed for future autonomous vehicles.

Intelligent transportation is emerging with the development of IoT technology [106]. Traditional sensor networks are powered by batteries or energy grids. Thus, the deployment and maintenance of sensors will bring challenges for intelligent transportation systems. PENGs/TENGs can gain energy from vibrations without the need for an energy grid. In 2013, Lin et al. [3] proposed a transparent and flexible PENG (TFNG) based on a flexible polydimethylsiloxane (PDMS) substrate and ZnO NWs. It could be deployed on the road for speed and weight detection, as well as collecting mechanical energy from rolling wheels to power a LCD. Figure 6c shows the output voltage signal when the wheel runs over the TFNG. The output of TFNG has good durability, as shown in Figure 6d. The principle of measuring vehicle speed and weight is shown in Figure 6e. Two TFNGs with a distance of $\Delta S = 0.6$ m were placed on the road. When the vehicle passed the TFNGs, two peak waveforms were generated. The speed can be calculated from the peak time difference Δt between two waveforms: $v = \Delta S/\Delta t$. Figure 6f shows the output voltage at vehicle speeds of 1 and 1.5 m/s. The output voltage of the TFNG is proportional to the weight of the vehicle, as shown in Figure 6g. A TENG-based self-powered sensor can also be deployed to detect bridge vibrations [68]. When the bridge vibrations are within the safety limit, the TENG generates AC signals for power supply and analysis of vibration characteristics. When the vibration exceeds a threshold, the output signal becomes a DC signal and an alarm is triggered.

To sum up, self-powered sensors based on NGs have great prospects as intelligent traffic sensors, and they show excellent performance in traffic monitoring. Abundant sensor data can

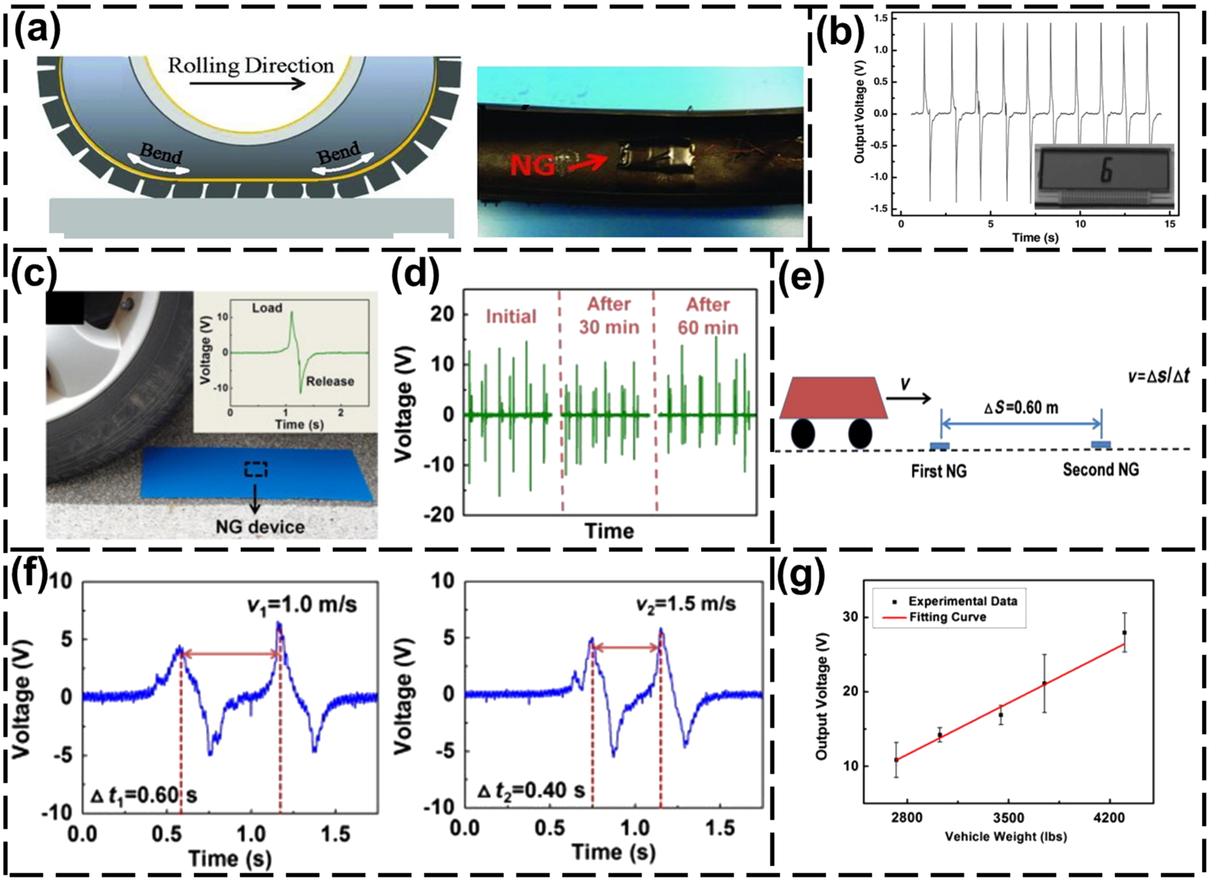

Figure 6: NG-based self-powered traffic sensor. (a) PENG attached to a tire with adhesive tape [5]. Figure 6a,b was reproduced from [5]. Copyright © 2011 WILEY-VCH Verlag GmbH & Co. KGaA, Weinheim. Used with permission from Youfan Hu et al., “A Nanogenerator for Energy Harvesting from a Rotating Tire and its Application as a Self-Powered Pressure/Speed Sensor”, Advanced Materials, John Wiley and Sons. (b) The output voltage of a PENG and the LCD powered by the PENG when the tire rotates [5]. (c) The voltage output after the sensor is pressed by the wheel once [3]. Figure 6c–g was reproduced from [3], (for permission, please see the caption of Figure 1e). (d) After being rolled over by wheels for an extended period of time, the output voltage of the TFNG changes only slightly [3]. (e) Schematic diagram of measuring speed via a TFNG [3]. (f) Voltage output of the TFNG as a function of the time at different vehicle speeds [3]. (g) Relationship between vehicle weight and output voltage of the TFNG [3].

establish smart transportation and improve driving safety and convenience. Also they are the basis of data for autonomous driving.

Key challenges and potential solutions for future self-powered sensors

In the future, NG-based self-powered sensors can be used in the collection of external environment data and human physiological data. NG-based self-powered sensors are good candidates for “smart dust”, which requires independent continuous work and the collection massive data [107]. We propose several key challenges and directions for the future development of NG-based self-powered sensors:

1. Application-specific integrated circuits (ASICs) designed for TENG sensors. The energy, such as mechanical energy, chemical energy, thermal energy, and light energy, that can be gained from the environment maybe limited and random. TENG sensors require ASICs with fast power-up, high performance and low energy consumption. The key properties of the ASICs should be ultra-short power-on time and ultrafast processing, while the performance should be higher than that of traditional ICs. Thus, the ASICs will have a smaller average power consumption. It is necessary to design energy management, information processing, and communications ASICs for TENG applications.

2. The embedded operating system based on adaptive energy unit. The random energy from the environment makes it difficult for TENG sensors to work continuously. A low-power high-performance sampling algorithm could collect the main data. It is necessary to develop new theories and algorithms for TENG sensors. The embedded operating system would be based on these new theories and algorithms, which effectively control information and energy flows.

3. AI for TENG-based self-powered sensors. The bottleneck of the self-powered systems is the quality of data due to the randomness of the energy from the environment. AI algorithms could learn the complete information features and complete the missing information in the TENG sensor data. AI algorithms for energy management are also an important topic for TENG applications.

4. New communication systems designed for TENG sensors. TENG-based self-powered sensors have great advantages for large-scale deployment. The transmission of massive data will rise challenges. Efficient and low-power communication systems are necessary. Another solution is compressing data for communication, which reduces the scale of data transmission.

Funding

The authors are thankful for the support from University of Electronic Science and Technology of China (ZYGX2015KYQD063), Swansea University, SPARC II project, and Thousand Talents program for a pioneer researcher and his innovation team, China.

ORCID® iDs

Lijie Li - https://orcid.org/0000-0003-4630-7692
Yan Zhang - https://orcid.org/0000-0002-7329-0382

References

1. Wu, Z.; Cheng, T.; Wang, Z. L. *Sensors* **2020,** *20,* 2925. doi:10.3390/s20102925
2. Gao, Q.; Cheng, T.; Wang, Z. L. *Extreme Mech. Lett.* **2021,** *42,* 101100. doi:10.1016/j.eml.2020.101100
3. Lin, L.; Hu, Y.; Xu, C.; Zhang, Y.; Zhang, R.; Wen, X.; Lin Wang, Z. *Nano Energy* **2013,** *2,* 75–81. doi:10.1016/j.nanoen.2012.07.019
4. Li, S.; Liu, D.; Zhao, Z.; Zhou, L.; Yin, X.; Li, X.; Gao, Y.; Zhang, C.; Zhang, Q.; Wang, J.; Wang, Z. L. *ACS Nano* **2020,** *14,* 2475–2482. doi:10.1021/acsnano.9b10142
5. Hu, Y.; Xu, C.; Zhang, Y.; Lin, L.; Snyder, R. L.; Wang, Z. L. *Adv. Mater. (Weinheim, Ger.)* **2011,** *23,* 4068–4071. doi:10.1002/adma.201102067
6. Zhang, B.; Wu, Z.; Lin, Z.; Guo, H.; Chun, F.; Yang, W.; Wang, Z. L. *Mater. Today* **2020,** *43,* 37–44. doi:10.1016/j.mattod.2020.10.031
7. Wen, J.; Chen, B.; Tang, W.; Jiang, T.; Zhu, L.; Xu, L.; Chen, J.; Shao, J.; Han, K.; Ma, W.; Wang, Z. L. *Adv. Energy Mater.* **2018,** *8,* 1801898. doi:10.1002/aenm.201801898
8. Xie, Z.; Zeng, Z.; Wang, Y.; Yang, W.; Xu, Y.; Lu, X.; Cheng, T.; Zhao, H.; Wang, Z. L. *Nano Energy* **2020,** *68,* 104360. doi:10.1016/j.nanoen.2019.104360
9. Askari, H.; Khajepour, A.; Khamesee, M. B.; Wang, Z. L. *Nano Energy* **2019,** *66,* 104103. doi:10.1016/j.nanoen.2019.104103
10. Meng, X.; Cheng, Q.; Jiang, X.; Fang, Z.; Chen, X.; Li, S.; Li, C.; Sun, C.; Wang, W.; Wang, Z. L. *Nano Energy* **2018,** *51,* 721–727. doi:10.1016/j.nanoen.2018.07.026
11. Lu, X.; Zheng, L.; Zhang, H.; Wang, W.; Wang, Z. L.; Sun, C. *Nano Energy* **2020,** *78,* 105359. doi:10.1016/j.nanoen.2020.105359
12. Zhang, C.; Liu, L.; Zhou, L.; Yin, X.; Wei, X.; Hu, Y.; Liu, Y.; Chen, S.; Wang, J.; Wang, Z. L. *ACS Nano* **2020,** *14,* 7092–7100. doi:10.1021/acsnano.0c01827
13. Xu, M.; Wang, S.; Zhang, S. L.; Ding, W.; Kien, P. T.; Wang, C.; Li, Z.; Pan, X.; Wang, Z. L. *Nano Energy* **2019,** *57,* 574–580. doi:10.1016/j.nanoen.2018.12.041
14. Bai, Y.; Xu, L.; He, C.; Zhu, L.; Yang, X.; Jiang, T.; Nie, J.; Zhong, W.; Wang, Z. L. *Nano Energy* **2019,** *66,* 104117. doi:10.1016/j.nanoen.2019.104117
15. Zhou, Z.; Li, X.; Wu, Y.; Zhang, H.; Lin, Z.; Meng, K.; Lin, Z.; He, Q.; Sun, C.; Yang, J.; Wang, Z. L. *Nano Energy* **2018,** *53,* 501–507. doi:10.1016/j.nanoen.2018.08.055
16. Li, Z.; Chen, J.; Guo, H.; Fan, X.; Wen, Z.; Yeh, M.-H.; Yu, C.; Cao, X.; Wang, Z. L. *Adv. Mater. (Weinheim, Ger.)* **2016,** *28,* 2983–2991. doi:10.1002/adma.201504356
17. Lee, M.; Bae, J.; Lee, J.; Lee, C.-S.; Hong, S.; Wang, Z. L. *Energy Environ. Sci.* **2011,** *4,* 3359–3363. doi:10.1039/c1ee01558c
18. Xue, X.; Nie, Y.; He, B.; Xing, L.; Zhang, Y.; Wang, Z. L. *Nanotechnology* **2013,** *24,* 225501. doi:10.1088/0957-4484/24/22/225501
19. Qu, Z.; Fu, Y.; Yu, B.; Deng, P.; Xing, L.; Xue, X. *Sens. Actuators, B* **2016,** *222,* 78–86. doi:10.1016/j.snb.2015.08.058
20. Zang, W.; Nie, Y.; Zhu, D.; Deng, P.; Xing, L.; Xue, X. *J. Phys. Chem. C* **2014,** *118,* 9209–9216. doi:10.1021/jp500516t
21. Fu, Y.; Nie, Y.; Zhao, Y.; Wang, P.; Xing, L.; Zhang, Y.; Xue, X. *ACS Appl. Mater. Interfaces* **2015,** *7,* 10482–10490. doi:10.1021/acsami.5b01822
22. Wen, Z.; Yang, Y.; Sun, N.; Li, G.; Liu, Y.; Chen, C.; Shi, J.; Xie, L.; Jiang, H.; Bao, D.; Zhuo, Q.; Sun, X. *Adv. Funct. Mater.* **2018,** *28,* 1803684. doi:10.1002/adfm.201803684
23. Yu, J.; Hou, X.; Cui, M.; Shi, S.; He, J.; Sun, Y.; Wang, C.; Chou, X. *Sci. China Mater.* **2019,** *62,* 1423–1432. doi:10.1007/s40843-019-9446-1
24. Roy, K.; Ghosh, S. K.; Sultana, A.; Garain, S.; Xie, M.; Bowen, C. R.; Henkel, K.; Schmeiβer, D.; Mandal, D. *ACS Appl. Nano Mater.* **2019,** *2,* 2013–2025. doi:10.1021/acsanm.9b00033
25. Yi, F.; Lin, L.; Niu, S.; Yang, P. K.; Wang, Z.; Chen, J.; Zhou, Y.; Zi, Y.; Wang, J.; Liao, Q.; Zhang, Y.; Wang, Z. L. *Adv. Funct. Mater.* **2015,** *25,* 3688–3696. doi:10.1002/adfm.201500428
26. Wang, S.; Fang, Y.; He, H.; Zhang, L.; Li, C.; Ouyang, J. *Adv. Funct. Mater.* **2021,** *31,* 2007495. doi:10.1002/adfm.202007495
27. Li, X.; Lin, Z.-H.; Cheng, G.; Wen, X.; Liu, Y.; Niu, S.; Wang, Z. L. *ACS Nano* **2014,** *8,* 10674–10681. doi:10.1021/nn504243j
28. Zheng, Q.; Zhang, H.; Shi, B.; Xue, X.; Liu, Z.; Jin, Y.; Ma, Y.; Zou, Y.; Wang, X.; An, Z.; Tang, W.; Zhang, W.; Yang, F.; Liu, Y.; Lang, X.; Xu, Z.; Li, Z.; Wang, Z. L. *ACS Nano* **2016,** *10,* 6510–6518. doi:10.1021/acsnano.6b02693
29. Liu, Z.; Ma, Y.; Ouyang, H.; Shi, B.; Li, N.; Jiang, D.; Xie, F.; Qu, D.; Zou, Y.; Huang, Y.; Li, H.; Zhao, C.; Tan, P.; Yu, M.; Fan, Y.; Zhang, H.; Wang, Z. L.; Li, Z. *Adv. Funct. Mater.* **2019,** *29,* 1807560. doi:10.1002/adfm.201807560
30. Cheng, B.; Ma, J.; Li, G.; Bai, S.; Xu, Q.; Cui, X.; Cheng, L.; Qin, Y.; Wang, Z. L. *Adv. Energy Mater.* **2020,** *10,* 2000827. doi:10.1002/aenm.202000827
31. Zhang, W.; Zhang, L.; Gao, H.; Yang, W.; Wang, S.; Xing, L.; Xue, X. *Nano-Micro Lett.* **2018,** *10,* 32. doi:10.1007/s40820-017-0185-x
32. Xue, X.; Qu, Z.; Fu, Y.; Yu, B.; Xing, L.; Zhang, Y. *Nano Energy* **2016,** *26,* 148–156. doi:10.1016/j.nanoen.2016.05.021

33. Lei, Y.; Zhao, T.; He, H.; Zhong, T.; Guan, H.; Xing, L.; Liu, B.; Xue, X. *Smart Mater. Struct.* **2019,** *28,* 105001. doi:10.1088/1361-665x/ab3901
34. Yang, W.; Han, W.; Gao, H.; Zhang, L.; Wang, S.; Xing, L.; Zhang, Y.; Xue, X. *Nanoscale* **2018,** *10,* 2099–2107. doi:10.1039/c7nr08516h
35. Pan, C.; Li, Z.; Guo, W.; Zhu, J.; Wang, Z. L. *Angew. Chem., Int. Ed.* **2011,** *50,* 11192–11196. doi:10.1002/anie.201104197
36. Zhao, T.; Zheng, C.; He, H.; Guan, H.; Zhong, T.; Xing, L.; Xue, X. *Smart Mater. Struct.* **2019,** *28,* 085015. doi:10.1088/1361-665x/ab2624
37. Guan, H.; Zhong, T.; He, H.; Zhao, T.; Xing, L.; Zhang, Y.; Xue, X. *Nano Energy* **2019,** *59,* 754–761. doi:10.1016/j.nanoen.2019.03.026
38. Zhang, W.; Guan, H.; Zhong, T.; Zhao, T.; Xing, L.; Xue, X. *Nano-Micro Lett.* **2020,** *12,* 105. doi:10.1007/s40820-020-00441-1
39. Li, H.; Zhao, L.; Meng, J.; Pan, C.; Zhang, Y.; Zhang, Y.; Liu, Z.; Zou, Y.; Fan, Y.; Wang, Z. L.; Li, Z. *Nano Today* **2020,** *33,* 100873. doi:10.1016/j.nantod.2020.100873
40. Zhao, L.; Li, H.; Meng, J.; Wang, A. C.; Tan, P.; Zou, Y.; Yuan, Z.; Lu, J.; Pan, C.; Fan, Y.; Zhang, Y.; Zhang, Y.; Wang, Z. L.; Li, Z. *Adv. Funct. Mater.* **2020,** *30,* 1907999. doi:10.1002/adfm.201907999
41. Luo, J.; Wang, Z.; Xu, L.; Wang, A. C.; Han, K.; Jiang, T.; Lai, Q.; Bai, Y.; Tang, W.; Fan, F. R.; Wang, Z. L. *Nat. Commun.* **2019,** *10,* 5147. doi:10.1038/s41467-019-13166-6
42. Hao, S.; Jiao, J.; Chen, Y.; Wang, Z. L.; Cao, X. *Nano Energy* **2020,** *75,* 104957. doi:10.1016/j.nanoen.2020.104957
43. Zhang, L.; Xue, F.; Du, W.; Han, C.; Zhang, C.; Wang, Z. *Nano Res.* **2014,** *7,* 1215–1223. doi:10.1007/s12274-014-0484-1
44. Xia, K.; Du, C.; Zhu, Z.; Wang, R.; Zhang, H.; Xu, Z. *Appl. Mater. Today* **2018,** *13,* 190–197. doi:10.1016/j.apmt.2018.09.005
45. Jo, S.; Kim, I.; Jayababu, N.; Roh, H.; Kim, Y.; Kim, D. *ACS Sustainable Chem. Eng.* **2020,** *8,* 10786–10794. doi:10.1021/acssuschemeng.0c02542
46. Mao, Y.; Zhang, N.; Tang, Y.; Wang, M.; Chao, M.; Liang, E. *Nanoscale* **2017,** *9,* 14499–14505. doi:10.1039/c7nr05222g
47. Dhakar, L.; Pitchappa, P.; Tay, F. E. H.; Lee, C. *Nano Energy* **2016,** *19,* 532–540. doi:10.1016/j.nanoen.2015.04.020
48. Yang, Y.; Zhang, H.; Lin, Z.-H.; Zhou, Y. S.; Jing, Q.; Su, Y.; Yang, J.; Chen, J.; Hu, C.; Wang, Z. L. *ACS Nano* **2013,** *7,* 9213–9222. doi:10.1021/nn403838y
49. Chen, H.; Song, Y.; Cheng, X.; Zhang, H. *Nano Energy* **2019,** *56,* 252–268. doi:10.1016/j.nanoen.2018.11.061
50. Lin, L.; Xie, Y.; Wang, S.; Wu, W.; Niu, S.; Wen, X.; Wang, Z. L. *ACS Nano* **2013,** *7,* 8266–8274. doi:10.1021/nn4037514
51. Wang, Y.; Wu, H.; Xu, L.; Zhang, H.; Yang, Y.; Wang, Z. L. *Sci. Adv.* **2020,** *6,* eabb9083. doi:10.1126/sciadv.abb9083
52. Fan, F.-R.; Lin, L.; Zhu, G.; Wu, W.; Zhang, R.; Wang, Z. L. *Nano Lett.* **2012,** *12,* 3109–3114. doi:10.1021/nl300988z
53. Lee, J.-H.; Yoon, H.-J.; Kim, T. Y.; Gupta, M. K.; Lee, J. H.; Seung, W.; Ryu, H.; Kim, S.-W. *Adv. Funct. Mater.* **2015,** *25,* 3203–3209. doi:10.1002/adfm.201500856
54. Wang, Z. L.; Chen, J.; Lin, L. *Energy Environ. Sci.* **2015,** *8,* 2250–2282. doi:10.1039/c5ee01532d
55. Hu, Y.; Yang, J.; Jing, Q.; Niu, S.; Wu, W.; Wang, Z. L. *ACS Nano* **2013,** *7,* 10424–10432. doi:10.1021/nn405209u
56. Zhu, H. R.; Tang, W.; Gao, C. Z.; Han, Y.; Li, T.; Cao, X.; Wang, Z. L. *Nano Energy* **2015,** *14,* 193–200. doi:10.1016/j.nanoen.2014.11.041
57. Akiyama, M.; Morofuji, Y.; Kamohara, T.; Nishikubo, K.; Tsubai, M.; Fukuda, O.; Ueno, N. *J. Appl. Phys.* **2006,** *100,* 114318. doi:10.1063/1.2401312
58. Wang, J.; Shi, J.; Deng, X.; Xie, L.; Jiang, J.; Tang, J.; Liu, J.; Wen, Z.; Sun, X.; Liu, K.; Fang, Y. *Nano Energy* **2020,** *78,* 105348. doi:10.1016/j.nanoen.2020.105348
59. Zhang, B.; Chen, J.; Jin, L.; Deng, W.; Zhang, L.; Zhang, H.; Zhu, M.; Yang, W.; Wang, Z. L. *ACS Nano* **2016,** *10,* 6241–6247. doi:10.1021/acsnano.6b02384
60. Askari, H.; Asadi, E.; Saadatnia, Z.; Khajepour, A.; Khamesee, M. B.; Zu, J. *Nano Energy* **2017,** *32,* 105–116. doi:10.1016/j.nanoen.2016.12.024
61. Yao, M.; Xie, G.; Gong, Q.; Su, Y. *Beilstein J. Nanotechnol.* **2020,** *11,* 1590–1595. doi:10.3762/bjnano.11.141
62. Nie, J.; Ren, Z.; Xu, L.; Lin, S.; Zhan, F.; Chen, X.; Wang, Z. L. *Adv. Mater. (Weinheim, Ger.)* **2020,** *32,* 1905696. doi:10.1002/adma.201905696
63. Xu, C.; Zi, Y.; Wang, A. C.; Zou, H.; Dai, Y.; He, X.; Wang, P.; Wang, Y.-C.; Feng, P.; Li, D.; Wang, Z. L. *Adv. Mater. (Weinheim, Ger.)* **2018,** *30,* 1706790. doi:10.1002/adma.201706790
64. Li, S.; Nie, J.; Shi, Y.; Tao, X.; Wang, F.; Tian, J.; Lin, S.; Chen, X.; Wang, Z. L. *Adv. Mater. (Weinheim, Ger.)* **2020,** *32,* 2001307. doi:10.1002/adma.202001307
65. Wang, Z. L. *Faraday Discuss.* **2014,** *176,* 447–458. doi:10.1039/c4fd00159a
66. Zhou, Y.; Shen, M.; Cui, X.; Shao, Y.; Li, L.; Zhang, Y. *Nano Energy* **2021,** *84,* 105887. doi:10.1016/j.nanoen.2021.105887
67. Nie, J.; Wang, Z.; Ren, Z.; Li, S.; Chen, X.; Lin Wang, Z. *Nat. Commun.* **2019,** *10,* 2264. doi:10.1038/s41467-019-10232-x
68. Li, S.; Fan, Y.; Chen, H.; Nie, J.; Liang, Y.; Tao, X.; Zhang, J.; Chen, X.; Fu, E.; Wang, Z. L. *Energy Environ. Sci.* **2020,** *13,* 896–907. doi:10.1039/c9ee03307f
69. Lei, R.; Shi, Y.; Ding, Y.; Nie, J.; Li, S.; Wang, F.; Zhai, H.; Chen, X.; Wang, Z. L. *Energy Environ. Sci.* **2020,** *13,* 2178–2190. doi:10.1039/d0ee01236j
70. Wang, Z. L.; Jiang, T.; Xu, L. *Nano Energy* **2017,** *39,* 9–23. doi:10.1016/j.nanoen.2017.06.035
71. Jeon, S.-B.; Seol, M.-L.; Kim, D.; Park, S.-J.; Choi, Y.-K. *Adv. Electron. Mater.* **2016,** *2,* 1600006. doi:10.1002/aelm.201600006
72. Jiang, Q.; Jie, Y.; Han, Y.; Gao, C.; Zhu, H.; Willander, M.; Zhang, X.; Cao, X. *Nano Energy* **2015,** *18,* 81–88. doi:10.1016/j.nanoen.2015.09.017
73. Li, Z.; Chen, J.; Zhou, J.; Zheng, L.; Pradel, K. C.; Fan, X.; Guo, H.; Wen, Z.; Yeh, M.-H.; Yu, C.; Wang, Z. L. *Nano Energy* **2016,** *22,* 548–557. doi:10.1016/j.nanoen.2016.03.002
74. Chen, S.; Wang, N.; Ma, L.; Li, T.; Willander, M.; Jie, Y.; Cao, X.; Wang, Z. L. *Adv. Energy Mater.* **2016,** *6,* 1501778. doi:10.1002/aenm.201501778
75. Guo, W.; Li, X.; Chen, M.; Xu, L.; Dong, L.; Cao, X.; Tang, W.; Zhu, J.; Lin, C.; Pan, C.; Wang, Z. L. *Adv. Funct. Mater.* **2014,** *24,* 6691–6699. doi:10.1002/adfm.201401168
76. Cui, S.; Zheng, Y.; Liang, J.; Wang, D. *Chem. Sci.* **2016,** *7,* 6477–6483. doi:10.1039/c6sc02562e
77. Shi, C.; Zou, Z.; Lei, Z.; Zhu, P.; Zhang, W.; Xiao, J. *Sci. Adv.* **2020,** *6,* eabd0202. doi:10.1126/sciadv.abd0202
78. Yang, S.; Cui, X.; Guo, R.; Zhang, Z.; Sang, S.; Zhang, H. *Beilstein J. Nanotechnol.* **2020,** *11,* 1655–1662. doi:10.3762/bjnano.11.148
79. Dong, J.; Chen, L.; Yang, Y.; Wang, X. *Beilstein J. Nanotechnol.* **2020,** *11,* 1847–1853. doi:10.3762/bjnano.11.166

80. Wang, M.; Zhang, J.; Tang, Y.; Li, J.; Zhang, B.; Liang, E.; Mao, Y.; Wang, X. *ACS Nano* **2018,** *12,* 6156–6162. doi:10.1021/acsnano.8b02562
81. Zhang, B.; Tang, Y.; Dai, R.; Wang, H.; Sun, X.; Qin, C.; Pan, Z.; Liang, E.; Mao, Y. *Nano Energy* **2019,** *64,* 103953. doi:10.1016/j.nanoen.2019.103953
82. Tang, Y.; Zhou, H.; Sun, X.; Diao, N.; Wang, J.; Zhang, B.; Qin, C.; Liang, E.; Mao, Y. *Adv. Funct. Mater.* **2020,** *30,* 1907893. doi:10.1002/adfm.201907893
83. Kim, K. K.; Ha, I.; Kim, M.; Choi, J.; Won, P.; Jo, S.; Ko, S. H. *Nat. Commun.* **2020,** *11,* 2149. doi:10.1038/s41467-020-16040-y
84. Zhou, Z.; Chen, K.; Li, X.; Zhang, S.; Wu, Y.; Zhou, Y.; Meng, K.; Sun, C.; He, Q.; Fan, W.; Fan, E.; Lin, Z.; Tan, X.; Deng, W.; Yang, J.; Chen, J. *Nat. Electron.* **2020,** *3,* 571–578. doi:10.1038/s41928-020-0428-6
85. Chen, X.; Shao, J.; An, N.; Li, X.; Tian, H.; Xu, C.; Ding, Y. *J. Mater. Chem. C* **2015,** *3,* 11806–11814. doi:10.1039/c5tc02173a
86. Chen, X.; Li, X.; Shao, J.; An, N.; Tian, H.; Wang, C.; Han, T.; Wang, L.; Lu, B. *Small* **2017,** *13,* 1604245. doi:10.1002/smll.201604245
87. Chen, X.; Parida, K.; Wang, J.; Xiong, J.; Lin, M.-F.; Shao, J.; Lee, P. S. *ACS Appl. Mater. Interfaces* **2017,** *9,* 42200–42209. doi:10.1021/acsami.7b13767
88. Yang, J.; Chen, J.; Su, Y.; Jing, Q.; Li, Z.; Yi, F.; Wen, X.; Wang, Z.; Wang, Z. L. *Adv. Mater. (Weinheim, Ger.)* **2015,** *27,* 1316–1326. doi:10.1002/adma.201404794
89. Hassan, M. M.; Uddin, M. Z.; Mohamed, A.; Almogren, A. *Future Gener. Comput. Syst.* **2018,** *81,* 307–313. doi:10.1016/j.future.2017.11.029
90. Wu, C.; Kim, T. W.; Park, J. H.; Koo, B.; Sung, S.; Shao, J.; Zhang, C.; Wang, Z. L. *ACS Nano* **2020,** *14,* 1390–1398. doi:10.1021/acsnano.9b07165
91. Xue, X.; Fu, Y.; Wang, Q.; Xing, L.; Zhang, Y. *Adv. Funct. Mater.* **2016,** *26,* 3128–3138. doi:10.1002/adfm.201505331
92. Vashist, S. K. *Anal. Chim. Acta* **2012,** *750,* 16–27. doi:10.1016/j.aca.2012.03.043
93. Song, P.; Kuang, S.; Panwar, N.; Yang, G.; Tng, D. J. H.; Tjin, S. C.; Ng, W. J.; Majid, M. B. A.; Zhu, G.; Yong, K.-T.; Wang, Z. L. *Adv. Mater. (Weinheim, Ger.)* **2017,** *29,* 1605668. doi:10.1002/adma.201605668
94. Cui, Q.; Le, T.-H.; Lin, Y.-J.; Miao, Y.-B.; Sung, I.-T.; Tsai, W.-B.; Chan, H.-Y.; Lin, Z.-H.; Sung, H.-W. *Nano Energy* **2019,** *66,* 104120. doi:10.1016/j.nanoen.2019.104120
95. Shen, M.-L.; Zhang, Y. *Acta Phys. Sin.* **2020,** *69,* 170701. doi:10.7498/aps.69.20200784
96. Cui, S.; Zheng, Y.; Zhang, T.; Wang, D.; Zhou, F.; Liu, W. *Nano Energy* **2018,** *49,* 31–39. doi:10.1016/j.nanoen.2018.04.033
97. Wang, S.; Xie, G.; Tai, H.; Su, Y.; Yang, B.; Zhang, Q.; Du, X.; Jiang, Y. *Nano Energy* **2018,** *51,* 231–240. doi:10.1016/j.nanoen.2018.06.041
98. Zhao, Y.; Lai, X.; Deng, P.; Nie, Y.; Zhang, Y.; Xing, L.; Xue, X. *Nanotechnology* **2014,** *25,* 115502. doi:10.1088/0957-4484/25/11/115502
99. Lin, Y.; Deng, P.; Nie, Y.; Hu, Y.; Xing, L.; Zhang, Y.; Xue, X. *Nanoscale* **2014,** *6,* 4604–4610. doi:10.1039/c3nr06809a
100. Meng, J.; Li, H.; Zhao, L.; Lu, J.; Pan, C.; Zhang, Y.; Li, Z. *Nano Lett.* **2020,** *20,* 4968–4974. doi:10.1021/acs.nanolett.0c01063
101. Wang, H.; Wu, H.; Hasan, D.; He, T.; Shi, Q.; Lee, C. *ACS Nano* **2017,** *11,* 10337–10346. doi:10.1021/acsnano.7b05213
102. Zhao, K.; Gu, G.; Zhang, Y.; Zhang, B.; Yang, F.; Zhao, L.; Zheng, M.; Cheng, G.; Du, Z. *Nano Energy* **2018,** *53,* 898–905. doi:10.1016/j.nanoen.2018.09.057
103. Modaresinezhad, E.; Darbari, S. *Sens. Actuators, B* **2016,** *237,* 358–366. doi:10.1016/j.snb.2016.06.097
104. Zhang, L.; Li, H.; Xie, Y.; Guo, J.; Zhu, Z. *Beilstein J. Nanotechnol.* **2020,** *11,* 1394–1401. doi:10.3762/bjnano.11.123
105. Zhang, D.; Xu, Z.; Yang, Z.; Song, X. *Nano Energy* **2020,** *67,* 104251. doi:10.1016/j.nanoen.2019.104251
106. Zhang, J.; Wang, F.-Y.; Wang, K.; Lin, W.-H.; Xu, X.; Chen, C. *IEEE Trans. Intell. Transp. Syst.* **2011,** *12,* 1624–1639. doi:10.1109/tits.2011.2158001
107. Ilyas, M.; Mahgoub, I. *Smart Dust: Sensor Network Applications, Architecture and Design;* CRC press: Boca Raton, FL, USA, 2006.

License and Terms

The definitive version of this article is the electronic one which can be found at: https://doi.org/10.3762/bjnano.12.54